frontiers | Research Topics

Smart wearable devices in healthcare—methodologies, applications, and algorithms

Edited by
Chang Yan, Ming Zeng, Hong Zeng, Aiguo Song and Lei Zhang

Published in
Frontiers in Neuroscience

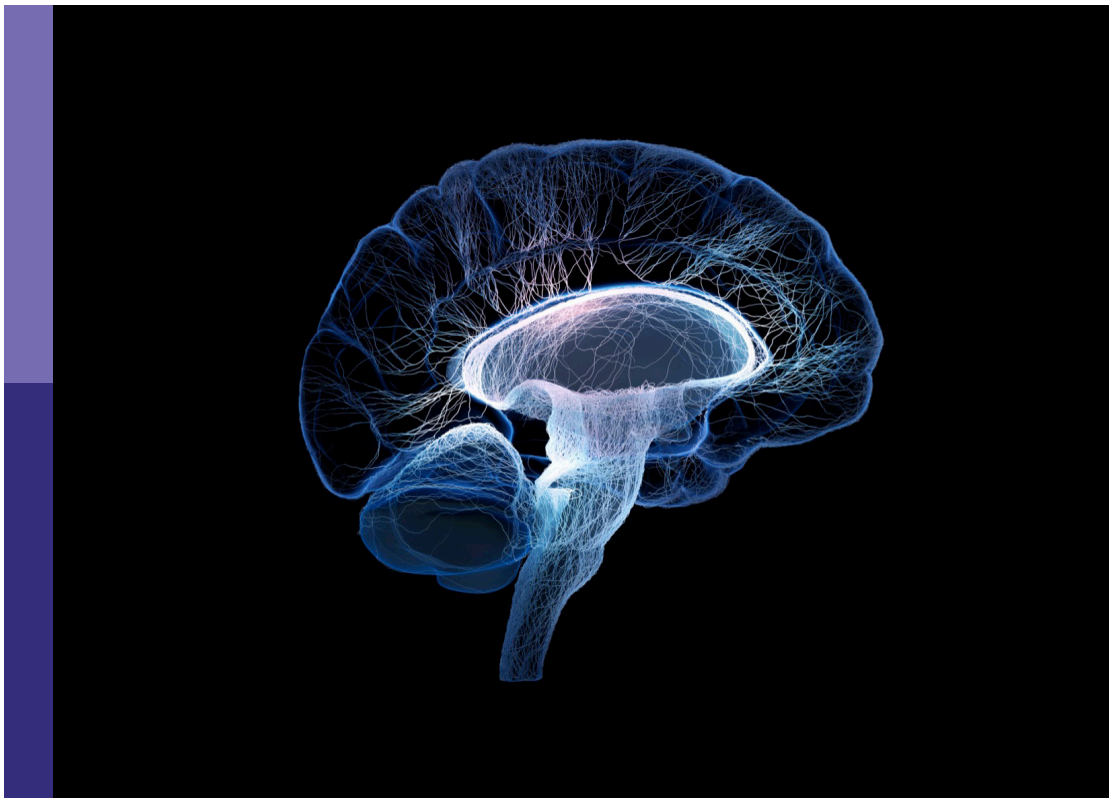

ISSN 1664-8714
ISBN 978-2-8325-4008-4
DOI 10.3389/978-2-8325-4008-4

About Frontiers

Frontiers is more than just an open access publisher of scholarly articles: it is a pioneering approach to the world of academia, radically improving the way scholarly research is managed. The grand vision of Frontiers is a world where all people have an equal opportunity to seek, share and generate knowledge. Frontiers provides immediate and permanent online open access to all its publications, but this alone is not enough to realize our grand goals.

Frontiers journal series

The Frontiers journal series is a multi-tier and interdisciplinary set of open-access, online journals, promising a paradigm shift from the current review, selection and dissemination processes in academic publishing. All Frontiers journals are driven by researchers for researchers; therefore, they constitute a service to the scholarly community. At the same time, the *Frontiers journal series* operates on a revolutionary invention, the tiered publishing system, initially addressing specific communities of scholars, and gradually climbing up to broader public understanding, thus serving the interests of the lay society, too.

Dedication to quality

Each Frontiers article is a landmark of the highest quality, thanks to genuinely collaborative interactions between authors and review editors, who include some of the world's best academicians. Research must be certified by peers before entering a stream of knowledge that may eventually reach the public - and shape society; therefore, Frontiers only applies the most rigorous and unbiased reviews. Frontiers revolutionizes research publishing by freely delivering the most outstanding research, evaluated with no bias from both the academic and social point of view. By applying the most advanced information technologies, Frontiers is catapulting scholarly publishing into a new generation.

What are Frontiers Research Topics?

Frontiers Research Topics are very popular trademarks of the *Frontiers journals series*: they are collections of at least ten articles, all centered on a particular subject. With their unique mix of varied contributions from Original Research to Review Articles, Frontiers Research Topics unify the most influential researchers, the latest key findings and historical advances in a hot research area.

Find out more on how to host your own Frontiers Research Topic or contribute to one as an author by contacting the Frontiers editorial office: frontiersin.org/about/contact

Smart wearable devices in healthcare—methodologies, applications, and algorithms

Topic editors

Chang Yan — Southeast University, China
Ming Zeng — Facebook, United States
Hong Zeng — Southeast University, China
Aiguo Song — Southeast University, China
Lei Zhang — Nanjing Normal University, China

Citation

Yan, C., Zeng, M., Zeng, H., Song, A., Zhang, L., eds. (2023). *Smart wearable devices in healthcare—methodologies, applications, and algorithms*. Lausanne: Frontiers Media SA. doi: 10.3389/978-2-8325-4008-4

Topic Editor Ming Zeng Ph.D. was employed by the Facebook Company (now Meta). The remaining authors declare that the research was conducted in the absence of any commercial or financial relationships that could be construed as a potential conflict of interest.

Table of contents

frontiers | Frontiers in Neuroscience

TYPE Original Research
PUBLISHED 06 February 2023
DOI 10.3389/fnins.2023.1121902

OPEN ACCESS

EDITED BY
Chang Yan,
Southeast University, China

REVIEWED BY
Sagar Nagpal,
East Tennessee State University, United States
Liting Zhang,
Shandong Provincial Hospital, China

*CORRESPONDENCE
Xinge Jiang
✉ jiangxe2003@sina.com
Hua Wu
✉ wuhua@sdjtu.edu.cn

SPECIALTY SECTION
This article was submitted to Neuroprosthetics, a section of the journal Frontiers in Neuroscience

RECEIVED 12 December 2022
ACCEPTED 09 January 2023
PUBLISHED 06 February 2023

CITATION
Sun Z, Jiang X, Wu H and Liu F (2023) Variation of peripheral pulse transit time with internal vascular pressure changes induced by arm movement. *Front. Neurosci.* 17:1121902. doi: 10.3389/fnins.2023.1121902

Variation of peripheral pulse transit time with internal vascular pressure changes induced by arm movement

Zhiwei Sun[1], Xinge Jiang[1]*, Hua Wu[1]* and Feifei Liu[2]

[1]School of Information Science and Electrical Engineering, Shandong Jiaotong University, Jinan, China, [2]School of Science, Shandong Jianzhu University, Jinan, China

Pulse transit time (PTT) and blood pressure (BP) are widely used to quantify arterial characteristics. Arm position influences arterial BP and peripheral PTT. This study aims to quantify the relationship between PTT changes with internal vascular pressure variations induced by the arm moving. With left arm at horizontal position as reference and the right arm moving from 90 to 45, 0, −45, and −90° respectively, PTT difference was calculated by the difference of the pulse foot between right arm and left arm within the same heartbeat. The change in the BP was calculated from the gravitational effect with the measured arm length. Our results showed that the change in PTT with arm elevating is more obvious than that with arm lowering, indicating the different relationship between PTT changes due to the internal BP changes. This can help in understanding the inherent physiological/pathological mechanism of cardiovascular system.

KEYWORDS

arterial blood pressure, pulse transit time, hydrostatic principle, arm position, arterial properties

1. Introduction

A common method to reflect the performance of the cardiovascular system includes extraction of the information contained in radial artery pressure waveforms (Liu et al., 2013, 2014). We used arterial blood pressure (BP) as an important indicator to reflect the performance of arteries. Previous studies demonstrated that the value of BP measurement was influenced by the arm position. Netea et al. (2003), Fouladi et al. (2018), and Pan et al. (2019) showed that the BP values recorded with the left arm above and below the level of the right atrium decreased with the lifting of the arm but increased with the lowering of the arm, which was explained to be the effect of hydrostatic forces (Merendino, 1961; Webster et al., 1984). However, recent studies showed that the hydrostatic theory is not the only explanation for the change in BP along the arm. Gavish and Gavish (2011, 2013) found that the changes in both systolic blood pressure (SBP) and diastolic blood pressure (DBP) showed high linear correlations with the length of the arm. However, the systolic rate is lower than the diastolic rate with the right arm lifting.

The PTT is a widely-used measurement for quantifying arterial properties (Zheng and Murray, 2011; Mol et al., 2020). Recently, PTT is also used as a new technique for BP measurement (Atef et al., 2017; Cho and Park, 2021). The relationship between BP and PTT has

been widely studied. Pereira (Schaanning and Skjaervold, 2020) reported that the PTT deduced from different locations can be used to measure BP by studying the relationship between BP and PTT in the static arm. Patzak et al. (2015) concluded that PTT showed a linear relationship in the low BP ranges while it showed an exponential relationship in the high BP ranges in the situation where the BP increased with the intravenous administration of dobutamine. Liu and Zhang (2006) studied the relationship between the PTT variations and the changes in the BP induced by the right arm lifting. The authors also reported that the PTT increased and the radial mean arterial pressure (MAP) gradually decreased with the arm lifting. Foo et al. (2005) studied the PTT changes induced by the different limb positions, in which the right or left arm was randomly selected for lifting and/or the right or left leg was randomly selected for lowering. Their studies showed that the mean PTT value increased with the arm lifting, while the mean PTT value decreased with the leg lowering. Previous studies showed that different arm position involves different muscles or muscles in different states. The relationship between PTT and BP may be different because of arm lifting or lowering (Siu et al., 2016). To make this clearer, we investigated the relationship between the changes in the PTT and the changes in the internal vascular pressure induced by arm movement.

2. Methods

2.1. Volunteers and setting

According to the Declaration of Helsinki (1989) by the World Medical Association, 22 healthy volunteers (13 men and 9 women) aged between 21 and 46 years were recruited from Shandong Jiaotong University, Jinan, China. The study received ethical permission from the Research Ethics Committee of the Affiliated Hospital of Shandong First Medical University, China (No. 2022001). All subjects provided their written informed consent.

The design of this study has been described in detail in our previous study (Jiang et al., 2017). Briefly, the design of the study is that the left arm was placed at the horizontal position as a reference and the right arm was moved at five different positions (90, 45, 0, −45, and −90°). To reduce the impact of intravascular physiological changes caused by the acute setting of arm position change, there were two identical repeat sessions in the whole measurement process for radial artery pulses. In one session, the measurement position sequence of the moving arm was 90, 45, 0, −45, and −90°, whereas, in the other session, the sequence was −90, −45, 0, 45, and 90°. At each session, the radial artery pulses were recorded when the signals were stable at each position (mostly, the moving arm was held at each position for 10–20 s before the measurement). Then, 10 successive radial artery pulse segments were obtained simultaneously from both arms. SBP and DBP were measured at the beginning and the end of the study and then MAP was calculated. Each subject's arm length (the distance between the clavicle and the radial artery) was measured and listed in Table 1.

2.2. Calculation of MAP changes and PTT differences

In this study, the difference between the half value of the arm length (the distance between the clavicle and the radial artery) and 10 cm (the distance from the clavicle to the shoulder) was considered as each subject's midpoint of the arm. The actual changes in blood pressure induced by the arm movements were calculated individually for each subject by using the lowering/lifting vertical distance from the midpoint of the arm and the hydrostatic principle (Zheng and Murray, 2009). For example, if the arm length measured from the clavicle to the radial artery was 64 cm, the effective arm length was considered 54 cm and the midpoint of the arm was the point on the effective arm 27 cm. With the arm lowering and lifting at 90 and 45°, respectively, the lowering/lifting vertical distances from the midpoint of the arm were 27 and 19.1 cm with increasing/decreasing blood pressure at 19.4 and 13.7 mm Hg, respectively.

PTT difference is equal to the difference in the pulse felt between the right arm and the left arm within the same heartbeat. As an example of calculating the PTT difference, Figure 1 shows the PTT difference with the left arm at the horizontal position as a reference and the right arm at 90°. Each subject's PTT differences at each position were calculated from 10 consecutive heartbeats.

The paired t-test was used to examine the effect of arm position on blood pressure and PTT, and a $p < 0.05$ was considered statistically significant.

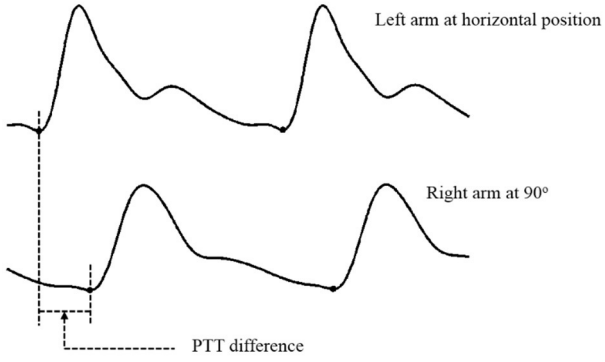

FIGURE 1
An example of calculating the PTT difference with the left arm at the horizontal position as a reference and the right arm at 90°.

TABLE 1 Arm length of the 22 subjects studied.

Subject's no.	1#	2#	3#	4#	5#	6#	7#	8#	9#	10#	11#
Arm length (cm)	64.6	66.5	69.0	66.5	65.0	68.0	65.7	71.0	66.9	65.4	65.4
Subject's no.	12#	13#	14#	15#	16#	17#	18#	19#	20#	21#	22#
Arm length (cm)	67.0	69.0	64.2	62.4	69.0	62.4	65.0	63.2	58.9	61.6	63.6

#The sequence number of the subject.

TABLE 2 The overall means and SDs of MAP and PTT differences with the right arm at five positions.

Position	90°	45°	0°	−45°	−90°
MAP (mm Hg)	66 ± 8*	71 ± 8*	86 ± 8	100 ± 8*	106 ± 8*
PTT differences (ms)	19 ± 7*	13 ± 7*	2 ± 5	−1 ± 5*	−2 ± 5*

*Significant statistical difference compared with 0°.

3. Results

3.1. Mean blood pressure and PTT differences at different positions

Table 2 presents the overall means and standard deviations (SDs) of MAP and PTT differences with the right arm at five positions. The paired *t*-test was performed with a PTT difference of the non-horizontal level and a PTT difference of the horizontal level, respectively. Figure 2A shows the means and SDs of MBP with the right arm at five positions to the horizontal level. The changes in the arm position caused a significant effect on BP (all $p < 0.01$), and the variations of MAP were large with the arm below the horizontal level while small with the arm above the horizontal level (Figure 2A). Figure 2B shows the means and SDs of the PTT differences with the right arm at five positions to the horizontal level. The arm position caused a significant effect on PTT ($p < 0.01$ at 90, 45, −45, and −90°; $p > 0.05$ at 0°), which implies that the PTT differences were large with the right arm above the horizontal level while small with the right arm below the horizontal level.

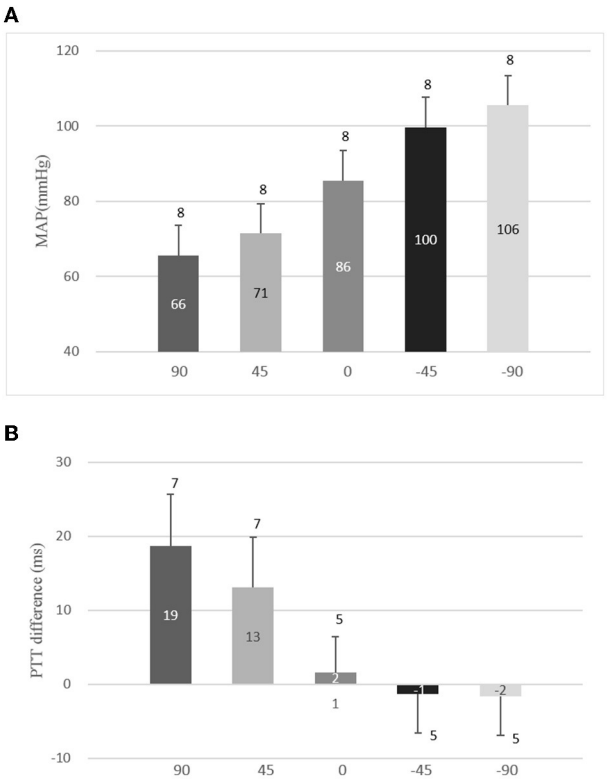

FIGURE 2
Means and standard deviations (SDs) of mean arterial pressure (MAP) and pulse transit time (PTT) differences with the right arm at different positions. **(A)** Means and SDs of MBP with the right arm at five positions to the horizontal level and **(B)** means and SDs of PTT differences with the right arm at five positions to the horizontal level.

3.2. PTT changes with different MAP induced by various arm positions

The changes in the PTT were calculated from the PTT differences of the right arm at positions 90, 45, −45, and −90° min those at 0°, respectively. The relationship between the changes in the PTT and a corresponding MAP with the arm positioned at 90, 45, −45, and −90° are depicted in Figure 3. With the arm moving at 90, 45, −45, and −90°, the changes in PTT were 17.1 ± 6.1, 11.4 ± 5.8, −3.0 ± 3.0, and −3.3 ± 2.6 ms and decreased, while the changes in MBP were 65.6 ± 8.0, 71.4 ± 8.0, 99.7 ± 8.0, and 105.5 ± 8.0 mm Hg and increased. Table 3 lists the rate of the means and SDs of the changes in the PTT and the linear regression equations with the right arm moving from 90 to −90° for each subject. As the rate was calculated with difference between the value with the right arm at a higher position and the value with the right arm at a lower position, the mean rates of the changes in the PTT shown in Table 3 were negative. However, if the rate was calculated with the difference between the value with the arm at a lower position and the value with the arm at a higher position, the rate shown in Table 3 would be positive. In this study, absolute values of the rate were used to identify the relationship between the changes in PTT and changes in the MAP induced by right arm movement. Table 3 points that the rates of changes in the PTT with the arm above the heart level (from 90 to 45° and from 45 to 0°) are larger (1.19 and 0.79) than those (0.21 and 0.06) with the arm below the heart level (from 0 to −45° and from −45 to −90°).

4. Discussion

We investigated the relationship between the changes in the PTT and the changes in the MAP induced by the right arm lifting and lowering, and we found that (1) when the arm was positioned at 45 and 90°, the changes in the PTT increased while the BP decreased and (2) when the arm was positioned at −45 and −90°, the changes in the PTT increased and the BP increased. These results indicated that there were different relationships between PTT variations and MAP changes induced by different right arm positions. At 90° and 45°, the changes in the PTT were 17.1 and 11.4 with a rate of −1.19 ± 0.60 and −0.79 ± 0.39, respectively, while, at −45° and −90°, the changes in the PTT were −3.0 and −3.3 with the rate of −0.21 ± 0.23 and −0.06 ± 0.27, respectively.

Our results are consistent with the studies of Foo et al. (2005) and Liu and Zhang (2006), which showed that the changes in PTT increased and the BP decreased during the arm lifting. However, the research of Liu and Zhang only involves arm lifting and not arm lowering. Foo et al. also studied the relationship between PTT and BP induced by limb lifting and lowering. Lifting of one of the arms or lowering of one of the legs was used in the study of Foo et al., while we used the same arm to study the relationship between the changes in PTT and the changes in the BP induced by the right arm liftingor lowering. We found that there are different relationships between PTT changes and BP changes with the arm lifting or lowering at

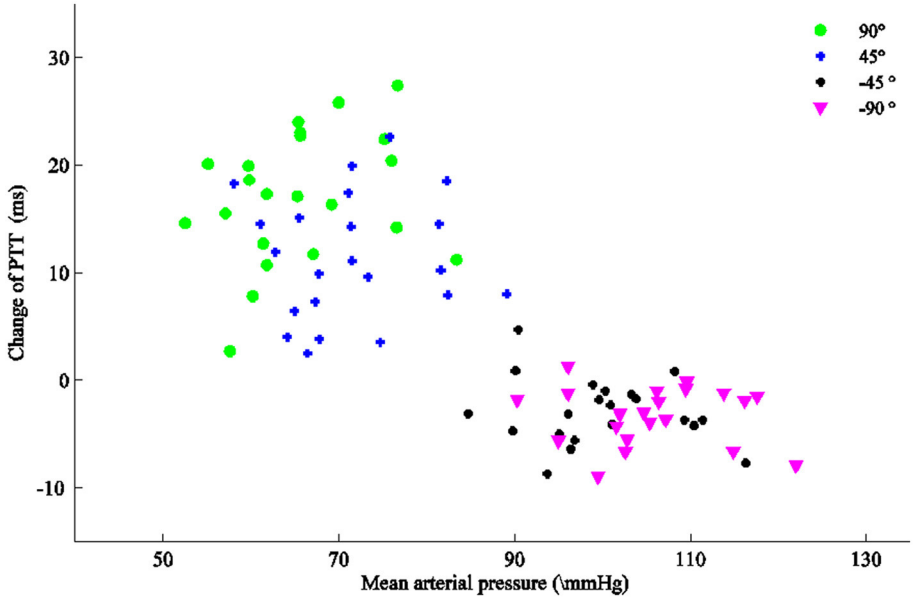

FIGURE 3
Relationship between each subject's changes in the pulse transit time (PTT) and corresponding mean arterial pressure (MAP) with the arm at 90, 45, −45, and −90°, respectively.

TABLE 3 The means and SDs of the rate of changes in the PTT (ms) and linear regression equations with the right arm moving from 90 to −90° for each subject.

Position	From 90° to 45°	From 45° to 0°	From 0° to −45°	From −45° to −90°
Mean ± SD90% CI	−1.19 ± 0.60	−0.79 ± 0.39	−0.21 ± 0.23	−0.06 ± 0.27
	(−2.17, −0.20)	(−1.43, −0.14)	(−0.59, 0.16)	(−0.51, 0.39)
Position	90°	45°	−45°	−90°
Linear regression equation	$y = 0.21x + 3.29$ $(R^2 = 0.076)$	$y = 0.04x + 8.78$ $(R^2 = 0.003)$	$y = -0.07x + 3.86$ $(R^2 = 0.031)$	$y = -0.03x - 0.27 (R^2 = 0.008)$

the same height relative to the level of the right atrium. With the arm lowering from the same height, the change in the PTT is smaller than that of the arm lifting. Zheng et al. (2007) and Zheng and Murray (2009) also indicated the relationship between internal vascular pressure and PTT with the arm at a different position. The data from Zheng and Murray's study are also in agreement with our data although they were not clearer.

This distinct result indicates that the effects of the physiological structure on PTT are different when lifting or lowering the arm. The reason may be partly due to different muscle states corresponding to different movements (Siu et al., 2016).

This study has several limitations. First, the sample involved only 22 subjects. The small sample size limits obtaining statistically significant results for a wide population. Second, when calculating the length of the midpoint of the arm, it was not accurate that 10 cm is considered to be the distance from the clavicle to the shoulder for all subjects, and the values of MBP with the arm positioned at 90, 45, −45, and −90° were estimated by the linear hydrostatic principle using the midpoint of the arm but not to the direct measuring. These values will cause some errors in calculating the changes in MBP. Finally, this study only involved healthy people and did not involve the diseased population.

5. Conclusion

This study demonstrated that there are different relationships between changes in PTT and changes in BP induced by right arm lifting or lowering at the same height relative to the level of the right atrium. Changes in PTT were larger during the arm lifting than the arm lowering with the approximate linear change in MBP. Future research should focus on the relationship between changes in PTT and changes in BP induced by arm movement for patients with a certain disease, which may thus be potentially useful for clinical applications.

Data availability statement

The raw data supporting the conclusions of this article will be made available by the authors, without undue reservation.

Ethics statement

The studies involving human participants were reviewed and approved by the Medical Ethics Committee of Jinshoulder, Lumbar,

and Leg Pain Hospital Affiliated to Shandong First-Medical University. The patients/participants provided their written informed consent to participate in this study.

Author contributions

ZS is responsible for data acquisition, programming, and thesis writing. XJ is responsible for experimental scheme design, data sorting, and paper modification. HW is responsible for the design of experimental equipment and the revision of papers. FL is responsible for guiding the experimental procedure. All authors contributed to the article and approved the submitted version.

Funding

This study was supported by the National Natural Science Foundation of China (Grant No. 82072014 and 61901114), the National Key R&D Program of China (Grant No. 2019YFE010670), the Shandong Province Natural Science Foundation (Grant No. ZR2020MF028), and the Key R&D Program of Shandong Province (Grant No. 2020CXGC010110).

Acknowledgments

The authors thank the Southeast–Lenovo Wearable Heart–Sleep–Emotion Intelligent Monitoring Lab for their support.

Conflict of interest

The authors declare that the research was conducted in the absence of any commercial or financial relationships that could be construed as a potential conflict of interest.

Publisher's note

References

Atef, M., Xiyan, L., Wang, G., Lian, Y. (2016). "PTT based continuous-time non-invasive blood pressure system," in *IEEE International Midwest Symposium on Circuits and Systems* (IEEE), 1–4. doi: 10.1109/MWSCAS.2016.7870022

Cho, H. S., and Park, Y. J. (2021). Measurement of pulse transit time using ultra-wideband radar. *Technol. Health Care* 29, 859–868. doi: 10.3233/THC-202626

Foo, J. Y., Wilson, S. J., Williams, G. R., Harris, M. A., and Cooper, D. M. (2005). Pulse transit time changes observed with different limb positions. *Physiol. Meas.* 26, 1093. doi: 10.1088/0967-3334/26/6/018

Fouladi, B., Joshi, H., and Edgell, H. (2018). Cardiovascular and autonomic responses to passive arm or leg movement in men and women. *Eur. J. Appl. Physiol.* 119, 551–559. doi: 10.1007/s00421-018-4030-9

Gavish, B., and Gavish, L. (2011). Blood pressure variation in response to changing arm cuff height cannot be explained solely by the hydrostatic effect. *J. Hypertens.* 29, 2099–2104. doi: 10.1097/HJH.0b013e32834ae315

Gavish, B., and Gavish, L. (2013). Simple determination of the systolic-diastolic pressure relationship from blood pressure readings taken at different arm heights. *Blood Press. Monit.* 18, 144. doi: 10.1097/MBP.0b013e328361c8fd

Jiang, X., Wei, S., Zheng, D., Liu, F., Zhang, S., Zhang, Z., et al. (2017). Change of bilateral difference in radial artery pulse morphology with one-side arm movement. *Artery Res.* 19, 1–8. doi: 10.1016/j.artres.2017.04.008

Liu, C., Tao, Z., Zhao, L., Chang, F., Liu, C., Wei, S., et al. (2014). Modelling arterial pressure waveforms using Gaussian functions and two-stage particle swarm optimizer. *Biomed Res. Int.* 2014, 923260. doi: 10.1155/2014/923260

Liu, C., Zheng, D., Murray, A., and Liu, C. (2013). Modeling carotid and radial artery pulse pressure waveforms by curve fitting with Gaussian functions. *Biomed. Signal Process. Control.* 8, 449–454. doi: 10.1016/j.bspc.2013.01.003

Liu, Y., and Zhang, Y. (2006). *Pulse Transit Time and Arterial Blood Pressure at Different Vertical Wrist Positions*. Available online at: https://citeseerx.ist.psu.edu/document?repid=rep1&type=pdf&doi=848f9debbc19a7be9f3995c3e695863370c7db12

Merendino, J. (1961). Importance of the position of the arm on the level of arterial blood pressure. *JAMA.* 175, 51. doi: 10.1001/jama.1961.63040010010015c

Mol, A., Meskers, C., Niehof, S. P., Maier, A. B., and van Wezel, R. J. A. (2020). Pulse transit time as a proxy for vasoconstriction in younger and older adults. *Exp. Gerontol.* 135, 110938. doi: 10.1016/j.exger.2020.110938

Netea, R. T., Lenders, J. P., and Thien, T. (2003). Both body and arm position significantly influence blood pressure measurement. *J. Hum. Hypertens.* 17, 459–462. doi: 10.1038/sj.jhh.1001573

Pan, F., He, P., Chen, F., Pu, X., Zhao, Q., and Zheng, D. (2019). Deep learning-based automatic blood pressure measurement: evaluation of the effect of deep breathing, talking, and arm movement. *Ann. Med.* 51, 397–403. doi: 10.1080/07853890.2019.1694170

Patzak, A., Mendoza, Y., Gesche, H., and Konermann, M. (2015). Continuous blood pressure measurement using the pulse transit time: comparison to intra-arterial Measurement. *Blood Press.* 24, 217–221. doi: 10.3109/08037051.2015.1030901

Schaanning, S. G., and Skjaervold, N. K. (2020). Rapid declines in systolic blood pressure are associated with an increase in pulse transit time. *PLoS ONE.* 15, 1–16. doi: 10.1371/journal.pone.0240126

Siu, A., Schinkel-Ivy, A., and Drake, J. D. (2016). Arm position influences the activation patterns of trunk muscles during trunk range-of-motion movements. *Hum. Mov. Sci.* 49, 267–276. doi: 10.1016/j.humov.2016.07.010

Webster, J., Newnham, D., Petrie, J. C., and Lovell, H. G. (1984). Influence of arm position on measurement of blood pressure. *Br. Med. J.* 288, 1574–1575. doi: 10.1136/bmj.288.6430.1574

Zheng, D., Allen, J., and Murray, A. (2007). Non-invasive in vivo assessment of changes in peripheral arterial properties with estimation of arterial volume compliance. *Physiol. Meas.* 28, 1317. doi: 10.1088/0967-3334/28/10/015

Zheng, D., and Murray, A. (2009). Non-invasive quantification of peripheral arterial volume distensibility and its non-linear relationship with arterial pressure. *J. Biomechanic.* 42, 1032–1037. doi: 10.1016/j.jbiomech.2009.02.011

Zheng, D., and Murray, A. (2011). Peripheral arterial volume distensibility: significant differences with age and blood pressure measured using applied external pressure. *Physiol. Meas.* 32, 499. doi: 10.1088/0967-3334/32/5/001

frontiers | Frontiers in Neuroscience

TYPE Methods
PUBLISHED 08 March 2023
DOI 10.3389/fnins.2023.1153386

OPEN ACCESS

EDITED BY
Chang Yan,
Southeast University, China

REVIEWED BY
Guohun Zhu,
The University of Queensland, Australia
Xinyu Yang,
University of Leicester, United Kingdom

*CORRESPONDENCE
Feifei Liu
✉ liufeifei19@sdjzu.edu.cn
Shengxiang Xia
✉ xias@sdjzu.edu.cn

SPECIALTY SECTION
This article was submitted to Neuroprosthetics, a section of the journal Frontiers in Neuroscience

RECEIVED 29 January 2023
ACCEPTED 20 February 2023
PUBLISHED 08 March 2023

CITATION
Ren Y, Liu F, Xia S, Shi S, Chen L and Wang Z (2023) Dynamic ECG signal quality evaluation based on persistent homology and GoogLeNet method. *Front. Neurosci.* 17:1153386. doi: 10.3389/fnins.2023.1153386

Dynamic ECG signal quality evaluation based on persistent homology and GoogLeNet method

Yonglian Ren[1], Feifei Liu[1,2]*, Shengxiang Xia[1]*, Shuhua Shi[1], Lei Chen[3] and Ziyu Wang[1]

[1]School of Science, Shandong Jianzhu University, Jinan, China, [2]Center for Engineering Computation and Software Development, Shandong Jianzhu University, Jinan, China, [3]School of Science and Technology, Shandong University of Traditional Chinese Medicine, Jinan, China

Cardiovascular disease is a serious health problem. Continuous Electrocardiograph (ECG) monitoring plays a vital role in the early detection of cardiovascular disease. As the Internet of Things technology continues to mature, wearable ECG signal monitors have been widely used. However, dynamic ECG signals are extremely susceptible to contamination. Therefore, it is necessary to evaluate the quality of wearable dynamic ECG signals. The topological data analysis method (TDA) with persistent homology, which can effectively capture the topological information of high-dimensional data space, has been widely studied. In this study, a brand-new quality assessment method of wearable dynamic ECG signals was proposed based on the TDA with persistent homology method. The point cloud of an ECG signal was constructed, and then the complex sequence was generated and displayed as a persistent barcode. Finally, GoogLeNet based on the transfer learning model with a 10-fold cross-validation method was used to train the classification model. A total of 12-leads ECGs Dataset and single-lead ECGs Dataset, established based on the 2011 PhysioNet/CinC challenge dataset, were both used to verify the performance of this method. In the study, 773 "acceptable" and 225 "unacceptable" signals were used as 12-leads ECGs Dataset. We relabeled 12,000 ECG signals in the challenge dataset, and treated them as single-lead ECGs Dataset after empty lead detection and balance datasets. Compared with the traditional ECG signal quality assessment method mainly based on waveform characteristics and time-frequency characteristics, the performance of the quality assessment method proposed. In this study, the classification performance of the proposed method are fairly great, *mAcc* = 98.04%, *F*1 = 98.40%, *Se* = 97.15%, *Sp* = 98.93% for 12-leads ECGs Dataset and *mAcc* = 98.55%, *F*1 = 98.62%, *Se* = 98.37%, *Sp* = 98.85% for single-lead ECGs Dataset.

KEYWORDS

quality assessment, persistent homology, point cloud, complex sequence, persistent barcode

Introduction

Heart disease is a serious threat to human health. According to the World Health Report 2021, by 2019, cancer, cardiovascular disease (CVD), diabetes, and chronic respiratory disease will be the main killers of human beings. Therefore, the prevention, diagnosis, and treatment of CVD have become important issues worldwide. With the rapid development of networks, big data, the Internet of Things, and artificial intelligence, wearable ECG monitoring equipment (Redmond et al., 2012; Viegas et al., 2016) has been widely used. Realize real-time and long-term monitoring of human ECG signals. However, ECG signal is a weak physiological signal that is easy to be interfered, leading to obvious defects in recording signal quality. Therefore, it is necessary to conduct effective signal quality assessment when monitoring wearable ECG equipment.

There are the following research methods for ECG signal quality evaluation, which are based on PhysioNet/CinC competition data in 2011. Zaunseder et al. (2011) based on the frequency domain characteristics of ECG signals, used indicators related to the power spectrum combined with decision trees to classify ECG signals. The classification accuracy was 90.4%; Kalkstein et al. (2011) used a combined machine learning algorithm of K-nearest neighbor and random forest for ECG signal quality assessment and obtained 91.2% classification accuracy on the test set; Xia et al. (2011) studied the time domain, frequency domain, autocorrelation, cross-correlation, and other indicators of ECG time series, formed a matrix with the results of these indicators, and used the spectral radius of the regular matrix to classify ECG signals. With the rapid development of deep learning, researchers began to apply deep learning to cardiovascular disease classification. For example, Alqudah et al. (2022) sent the extracted ECG spectrum features to different convolutional neural network (CNN) architectures to classify the MIT-BIH arrhythmia database. Al-Issa and Alqudah (2022) developed a heart diagnostic system combining CNN and Long Short-Term Memory (LSTM) components to distinguish five heart valve diseases. Obeidat and Alqudah (2021) used a hybrid lightweight one-dimensional depth learning model, which combines convolutional CNN and LSTM methods for ECG classification.

Topological data analysis method is a data analysis framework based on algebraic topology tools (Carlsson, 2009). The purpose of adopting the TDA method is to apply data analysis, algebraic topology, computational geometry, computer science, statistics, etc., to find a shape like structure in the data to analyze the complex topology and geometry of the data (Edelsbrunner and Harer, 2010). These data are usually represented as a point cloud in Euclidean space. Persistent homology (Zomorodian and Carlsson, 2005) is the main concept that allows multiscale data analysis and is also a basic mathematical tool of TDA. Persistent homology is calculated by simple complex, and its output results usually include persistent barcode and persistent diagram. In this study, Vietoris-Rips (VR) complex and SubLevel-Set (SLS) complex are selected, and detailed in Section "2. Basic terminology."

Topological data analysis method methods have been applied to wearable ECG signal analysis [see (Chung et al., 2021) for an example] based on the persistence diagram obtained by VR filtering and SLS filtering. This is used to construct persistence statistics for heart rate variability analysis and its classification in sleep-wake. Reference (Dindin et al., 2020) used the TDA method to detect arrhythmias through a modular multichannel neural network for binary classification. The classification accuracy obtained in the test set was 90% on average, and the average test accuracy in multiclassification was 80.5%. Reference (Ignacio et al., 2019) demonstrated how to map ECGs onto high-dimensional point clouds through delayed embedding to extract topological features and finally apply random forests for classification. Study (Graff et al., 2021) examined when persistence diagram was obtained by SLS filtering, and a set of indicators was extracted to distinguish the RR interval of healthy subjects and stroke patients. In addition (Yan et al., 2019) applied TDA to reconstruct a signal point cloud to extract persistent landscape features to classify heart rate variability. The accuracy of a normal heartbeat was 100%, of ventricular beating was 97.13%, of supraventricular beating was 94.27%, and of fusion beating was 94.27%. Although the TDA method has been applied to the processing and classification of ECG signals, to the best of our knowledge, research on the quality assessment of ECG signals using TDA is still lacking.

Traditional ECG signal quality evaluation methods mostly rely on the setting of ECG signal feature extraction classifier. In recent years, the deep learning method has been widely used in many fields because of its powerful functions. More and more researchers apply the deep learning method to the quality evaluation of ECG signals. However, the deep learning method has poor interpretability and cannot explore the high-dimensional spatial characteristics of ECG signals. ECG is an electrical activity process that reflects the excitation of the heart. It is not enough to extract features from the basic function of the heart and its pathological research. Topological data analysis method can solve this problem. In this study, persistent homology can be used to construct point clouds through folded signals, extract topological features, and comprehensively reflect the damage of heart valves.

In this study, a brand-new quality assessment method of wearable dynamic ECG signals was proposed based on the TDA with persistent homology method, so as to reduce the workload of medical staff and reduce the rate of miscarriage of justice. In this study, the features captured by the topological data analysis method is topological and spatial information of high-dimensional data space. First, the point cloud of an ECG signal was constructed, and then the complex sequence was generated and displayed as a persistent barcode. Topological and spatial information was converted into the persistent barcode.

In Section "2. Basic terminology," we introduce VR filtration, SLS filtration, and persistent homology related concepts. The dataset adopted in this study and the constructed model are accepted in detail in Section "**3. Model**." In Section "4. Results," we present the results for different classifications. Model performance based on ECG quality assessment and comparison with other quality assessment methods is discussed in detail in Section "5. Discussion."

Basic terminology

Vietoris-Rips filtration

Common complexes include Alpha complex, *Čech* complex, lazy witness complex, VR complex and so on. In this study, VR complex is selected for the following reasons: (a) when using

Alpha complex, the lack of monotonicity may introduce significant computational costs and even make it unusable in some cases. (b) In the calculation, VR complex is easier to calculate than $\hat{C}ech$ complex. Because VR complex can be stored as a picture, that is, only 0-dimensional and 1-dimensional complex need to be stored, and all high-dimensional complex need not be stored like $\hat{C}ech$ complex. (c) The lazy witness complex is to randomly select the number of points in a group of point clouds. Compared with VR complex, it has randomness and is suitable for the point cloud structure with a large amount of data. Assume that VR filtering represents the distance between two points in the metric space Z. The VR complex sequence VR (Z, ∈) is defined as follows: (1) The vertex set is Z. (2) For vertices a and b, if d (a, b) ≤ ∈, then the edge (ab) is included in VR (Z, ∈). (3) If all edges of VR (Z, ∈) are simplexes, then it contains simplexes of higher dimensions. The filtering of the VR complex can be regarded as filtration of the (n-1) dimensional simplex, as shown in **Figure 1**.

SubLevel-Set filtration

The definition of the SLS is as follows: We define a time series of ECG signals as a continuous function, where T is the length of the time series and is a real-valued function called the α-level subset. For each α∈R,

$$f_\alpha := f^{-1}(-\infty,\alpha)\{t \in [0, T] | f(x) \leq \alpha\} \quad (1)$$

According to the formula $\alpha_1 \leq \alpha_2, f_{\alpha_1} \subseteq f_{\alpha_2}$, therefore, for any increasing sequence of a filter is formed. The filtering process is shown in **Figure 2** below.

Persistence homology

Persistent homology is a method to compute spatial topological features at different spatial resolutions. More persistent features are detected across a wide range of spatial scales. The space must first be represented as a simplicial complex, and a distance function on the underlying space corresponds to a filtering of a simplicial complex, which is a nested sequence of increasing subsets.

When $0 \leq i \leq j \leq n$, the inclusio $K_i \to K_j$ induces a homomorphism $f_p^{i,j} : H_p(K_i) \to H_p(K_j)$ on the simplicial homology groups for each dimension p. The p^{th} persistent homology groups are the images of these homomorphisms, and the p^{th} persistent Betti numbers $p = 0$ are the ranks of those groups. Persistent Betti numbers for coincide with the size function, which is a predecessor of persistent homology.

Topological data analysis method methods extract information from the topological and geometric properties of the data point cloud. In this study, we first construct a data point cloud for each time series using the sliding window method to construct a complex sequence for a point cloud dataset and filter the complex sequence $\phi = K_0 \subset K_1 \subset \ldots \subset K_n = K$. Topological features will appear and disappear during the construction of complex filtering. The persistence diagram proposed by Edelsbrunner et al. (2000) and the persistence barcode proposed by Carlsson et al. (2005) are tools for visualizing topological features that can visually display persistent homology. There is an equivalence relationship between them. The persistence diagram was encoded from the k-dimensional homology α information in all scales. A homology α was a point, which represent the birth and death time of the corresponding topological features. A barcode is a finite set of intervals that are bounded below. Intuitively, the intervals denote the life-times of a non-trivial loop in a growing complex. The left endpoint signifies the birth of a new topological attribute, and the right endpoint signals its death. The longer the interval, the more important the topological attribute, as it insists on being a feature of the complex.

Model

Based on 2011 PhysioNet/CinC challenge data, we constructed 12-leads ECGs Database and single-lead ECGs Database. For the two databases, we use VR filtration method to obtain persistent barcodes and SLS filtration method to obtain persistent diagrams. When using VR filtration method, this study uses the sliding window method to construct the point cloud of the ECG signal. Finally, the GoogLeNet based on the transfer learning method is applied for classification. The flow diagram of this study is shown in **Figure 3**.

The data

Data were drawn from the PhysioNet Challenge 2011 dataset where binary labels were available, on 1,000 12-lead ECGs indicating whether the entire recording was acceptable or unacceptable. These data supporting the development and evaluation of challenge entries were collected by the Sana Project (Celi et al., 2009) and are freely available through PhysioNet (Goldberger et al., 2000). Patient age, sex, weight, and possibly other relevant information were included in the challenge data. The full diagnostic bandwidth is 0.05–100 Hz. Leads were recorded simultaneously for 10 s, sampled at 500 Hz at 16-bit resolution. Among the 1,000 signals, 773 were marked as "acceptable" and 225 were "unacceptable," and 2 were "indeterminate."

A total of 12-leads ECGs dataset

In this study, 773 "acceptable" and 225 "unacceptable" signals were used as 12-leads ECGs Dataset. Whereas the "acceptable," "indeterminate," and "unacceptable" classification criteria for the entire 12 channels. For example, many "acceptable" ECGs have a channel with complete noise or even a flat line. Therefore, we constructed single-lead ECGs Dataset.

Single-lead ECGs quality assessment dataset construction

According to Silva et al. (2011), study (Liu et al., 2018) adopts the scoring criteria of five signal quality levels of 10-s ECG segments. A total of 9,941 "acceptable" and 2,059 "unacceptable" 10-s ECG segments were found. With empty lead detection, 1,071 10-s ECG segments were detected from the disqualified group. Hence, only 988 "unacceptable" fragments were found. It can be

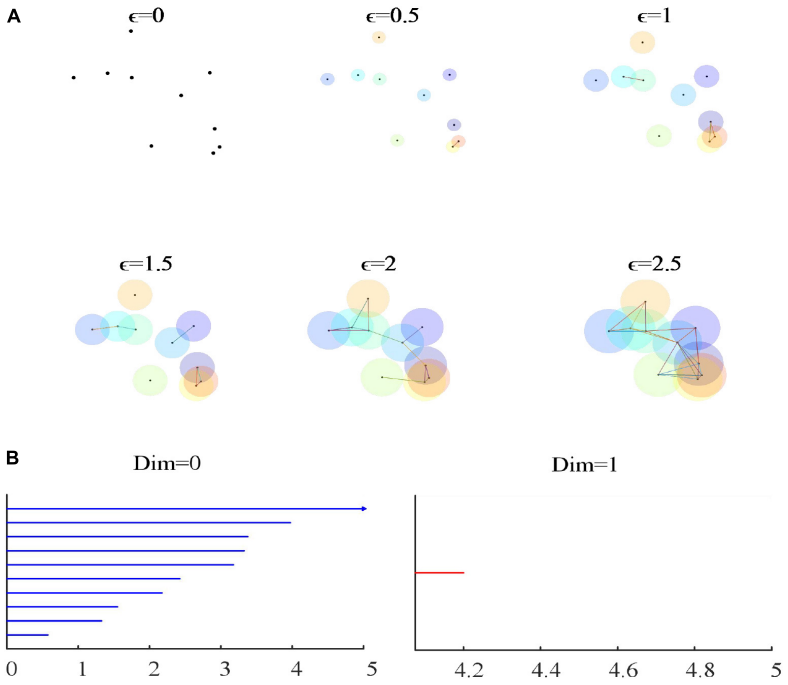

FIGURE 1
(A) The filtering process of the VR complex. **(B)** The 0-dimensional and 1-dimensional persistence barcode of VR filtration. As ϵ continues to increase, an increasing number of simplicial complexes are formed. In **(B)**, blue is a 0-dimensional persistence barcode, and red is a 1-dimensional persistence barcode. The abscissa of the persistence barcode picture represents 2ϵ. When ϵ = 0, there are 10 connected components; when ϵ = 1, there are seven connected components; when ϵ = 2, there are two connected branches; and when ϵ = 2.05 to ϵ = 2.1, there is a hole.

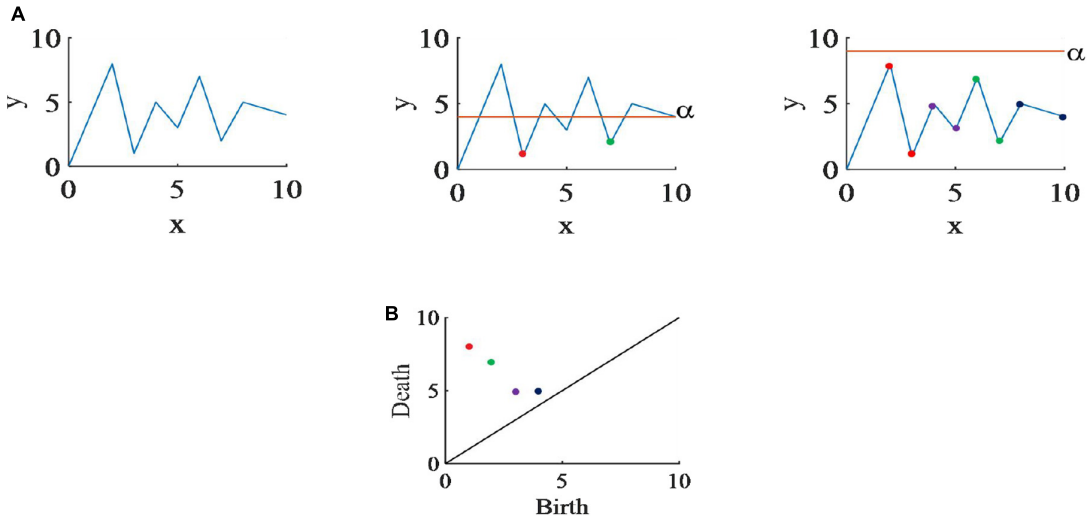

FIGURE 2
(A) The SLS filtering process of randomly generated time series. When α scans a node that it considers to be a local minimum, it saves the value of that node as the birth point of the slot, and the trough of death is determined by the lowest. Since the global minimum will not disappear, its death time is infinite. **(B)** The persistence diagram of this time series.

seen that the "acceptable" and "unacceptable" signals are seriously unbalanced, and this study generates additional noisy records to balance the problem of uneven data.

We used the Physical Network Noise Stress Test Database (Moody et al., 1984) (NSTDB) noise samples, which contain samples for three types of noise: *bw*, *em*, and *ma*. *Bw* contains baseline drift noise; *em* contains electrode motion artifacts, as well as substantial baseline drift and muscle noise; and *ma* contains mostly muscle noise. These three noise samples have two leads. This study adds *gaussian* noise with only one lead data, and the signal-to-noise ratio of the noise is −10 dB. We added four different noises to the 7,882 "acceptable" ECG signals: 2,252 noise data with *bw*, *em*, and *ma* noise and 1,126 with *gaussian* noise. There is no possibility of adding two different noises to one signal. There

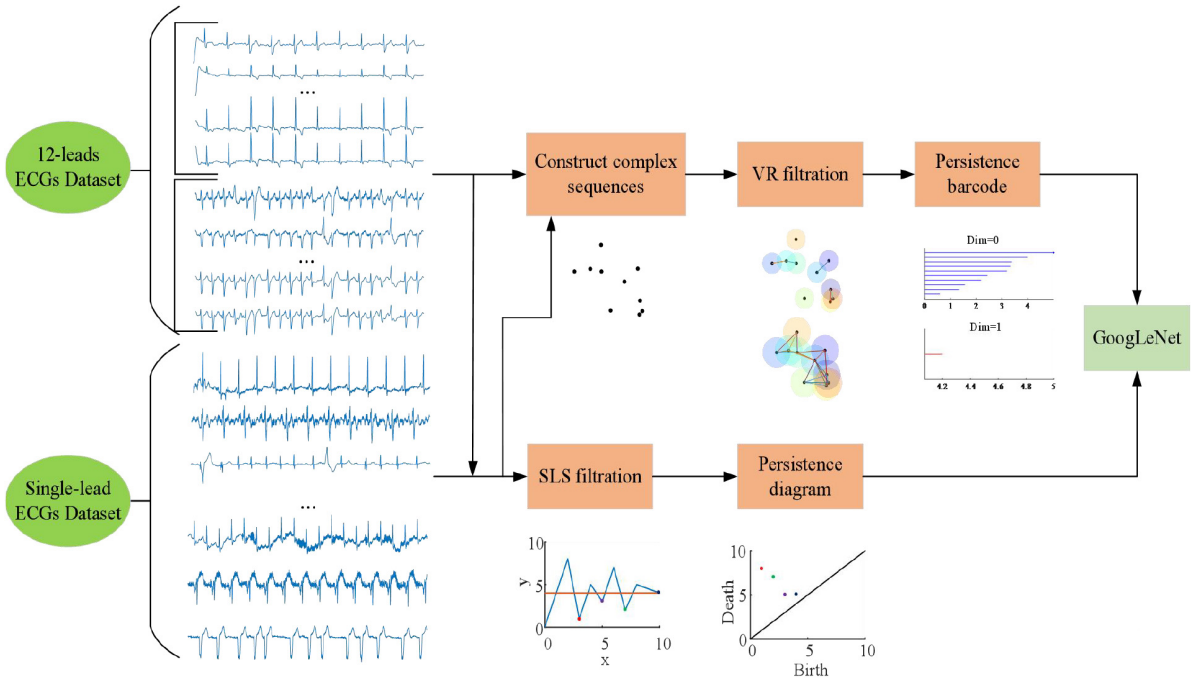

FIGURE 3
Flow diagram of this study.

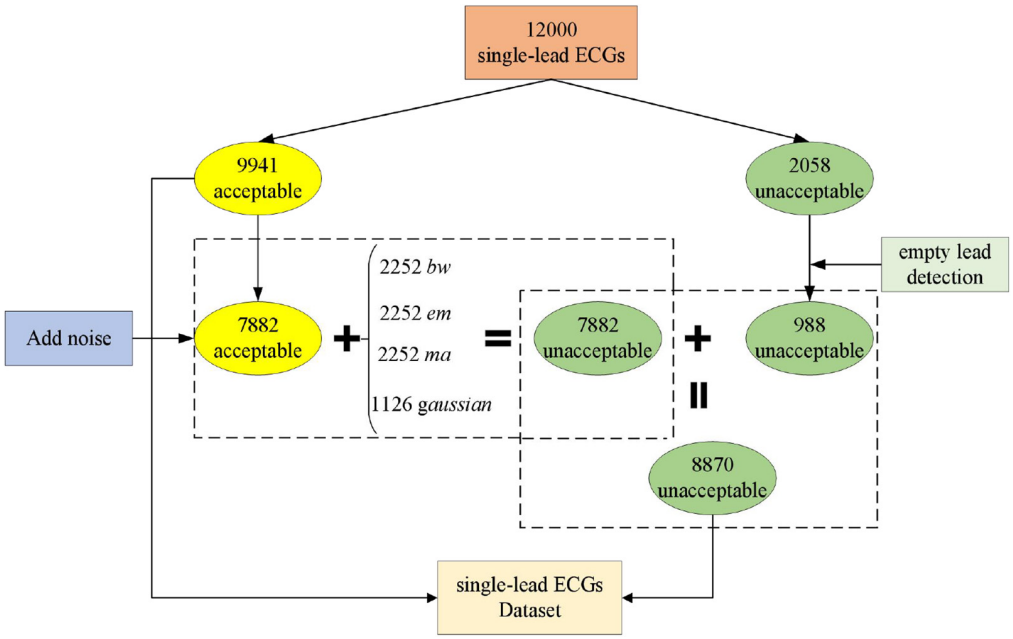

FIGURE 4
Construction process of single-lead ECGs Dataset.

are 9,941 "acceptable" signals and 8,870 "unacceptable" signals. As shown in the Figure 4.

Electrocardiograph signal processing

The ECG signals of "acceptable" and "unacceptable" were normalized by Mapminmax function. Mapminmax is a function of MATLAB, which is mainly used to normalize data. It converts all data into numbers between (−1, 1), so as to eliminate the difference in the number of data in each dimension. The algorithm is as follows:

It is assumed that x has only finite real values and that the elements of each row are not all equal. *ymin* is the minimum value we expect after normalization. *ymax* is the maximum value we expect after normalization, and the normalized matrix is marked

as y.

$$y = \frac{(ymax - ymin)(x - xmin)}{(xmax - xmin)} + ymin \tag{2}$$

Filtration of ECG signal

Topological data analysis method studies shapes constructed from invariant datasets under continuous deformation (such as tension and torsion). We use VR filtration and SLS filtration methods to analyze ECG signals, and use persistence barcode and persistence diagram to display the topological characteristics of ECG signals. In VR filtration method, a point cloud was structure by the sliding window method. In the process of $\in$ becoming larger, points are connected with each other, and "hole" and "void" may appear and disappear, which means that the topological characteristics will appear and disappear. SLS filtration method directly looks for birth value and death value on the waveform of ECG signal. In order to see the difference between persistent barcodes more intuitively and clearly, we take a 3-s ECG signal segment in Figure 5 as an example. Figure 5 shows the three-dimensional scatter (A), persistence barcode (B), and persistence diagram (C) of 3-s "acceptable" and "unacceptable" ECG segments.

In this study, for 12-leads ECGs Dataset, the point cloud structure of sliding windows with five lengths of 1, 2, 3, 4, and 5 s and dimensions of 120, 60, 36, 24, and 24 are established. For single-lead ECGs Dataset, the point cloud structure of sliding windows with five lengths of 0.1, 0.2, 0.3, 0.4, and 0.5 s and dimensions of 100, 50, 33, 25, and 20 are established. When a signal cannot meet the length of a sliding window, we discard it. For the 12-leads dataset, when the sliding window length is 0.1 s, the point cloud dimension of one signal is 120, and the point cloud dimension of 12-leads signals is 1,200. For a single-lead dataset, if the sliding window length is 1 s, the point cloud dimension is 10. According to the experimental results, we know that the larger the dimension of the point cloud, the better the result. However, when the point cloud dimension is too large, it will cause a certain amount of calculation and time loss. Therefore, in this study, we control the size of the sliding window to control the dimension of the two data sets within 120, which can not only maintain the accuracy of the results, but also reduce unnecessary waste of time.

Sliding window method to construct point cloud and VR filtration of ECG signal

At present, the application of ECG signal quality assessment based on persistent homology is lacking. In this study, the sliding window method is used to establish the point cloud dataset. Given a set of time series $x(x_1, x_2, \ldots, x_n)$, construct a matrix,

$$\begin{bmatrix} x_1, \ldots, x_t \\ x_{t+1}, \ldots, x_{2t} \\ \ldots \\ x_{(d-1)t+1}, \ldots, x_{dt} \end{bmatrix}, dt \leq \mathrm{n},\ d > 0, t > 0, n > 0 \tag{3}$$

Where d is the dimension, t is the size of the sliding window, and n is the length of the time series. At that time, a point that does not meet the size of a window is discarded. Through experiments, the window size is continuously adjusted to find an optimal window size so that the classification accuracy is the best.

The process of constructing VR complex is reconstruct the point cloud from the time series of ECG signals. Each point is surrounded by a ball with a diameter of $2\in$. During the change of radius $\in$, holes will appear and disappear. The following is an example of intercepting a 3-s ECG signal to reconstruct the three-dimensional scatter of the point cloud dataset to better visualize the spatial structure of the point cloud. As shown in Figures 5A, B, the length of the sliding window is 1 s, and the dimension is three.

SubLevel-Set filtration of ECG signal

SubLevel-Set filtering method maps time series data to its peak and trough pairs to express information about data smoothness and volatility. First, we model the time series of ECG signals as a graph with multiple nodes, each connected to two neighbors (except the ends). Then selecting α, α value is swept from $-\infty$ to $+\infty$, to identify troughs and match them to peaks as it increases. When α is swept passed a node that it identifies as a local minimum, it saves the value of that node as the birth of that trough. The death of a trough is given by the lowest α value. Finally, the algorithm terminates when all node values are smaller than α. We select two acceptable ECG signals and two unacceptable ECG signals and use the SLS filtration method to generate persistence diagram, as shown in Figure 5C below.

Evaluation method

We select the following evaluation indicators to obtain the classification accuracy: sensitivity (Se), specificity (Sp), $F1$, accuracy (Acc) and correction accuracy ($mAcc$), which are defined as follows:

Se: The number predicted to be positive and correct, the proportion of the total number of actual positives.

$$Se = \frac{\mathrm{TP}}{(\mathrm{TP} + \mathrm{FN})} \times 100\% \tag{4}$$

Sp: The number predicted to be negative and correct, the proportion of the total number of actual negatives.

$$Sp = \frac{\mathrm{TN}}{(\mathrm{TN} + \mathrm{FP})} \times 100\% \tag{5}$$

$F1$: The harmonic values of the precision rate and recall rate.

$$F1 = \frac{\mathrm{TP}}{\mathrm{TP} + 0.5(\mathrm{FR} + \mathrm{FN})} \times 100\% \tag{6}$$

Acc: Number of correct predictions, accounting for the total number.

$$Acc = \frac{\mathrm{TP} + \mathrm{TN}}{\mathrm{TP} + \mathrm{TN} + \mathrm{FR} + \mathrm{FN}} \times 100\% \tag{7}$$

$mAcc$

$$mAcc = \frac{(Se + Sp)}{2} \times 100\% \tag{8}$$

Among them, TP: "acceptable" signal is correctly predicted as an "acceptable" signal by the model; TN: "unacceptable" signal is correctly predicted as an "unacceptable" signal by the model; FP: "unacceptable" signal is incorrectly predicted as an "acceptable" signal by the model; FN: "acceptable" signal is predicted as an "unacceptable" signal by the model's signal.

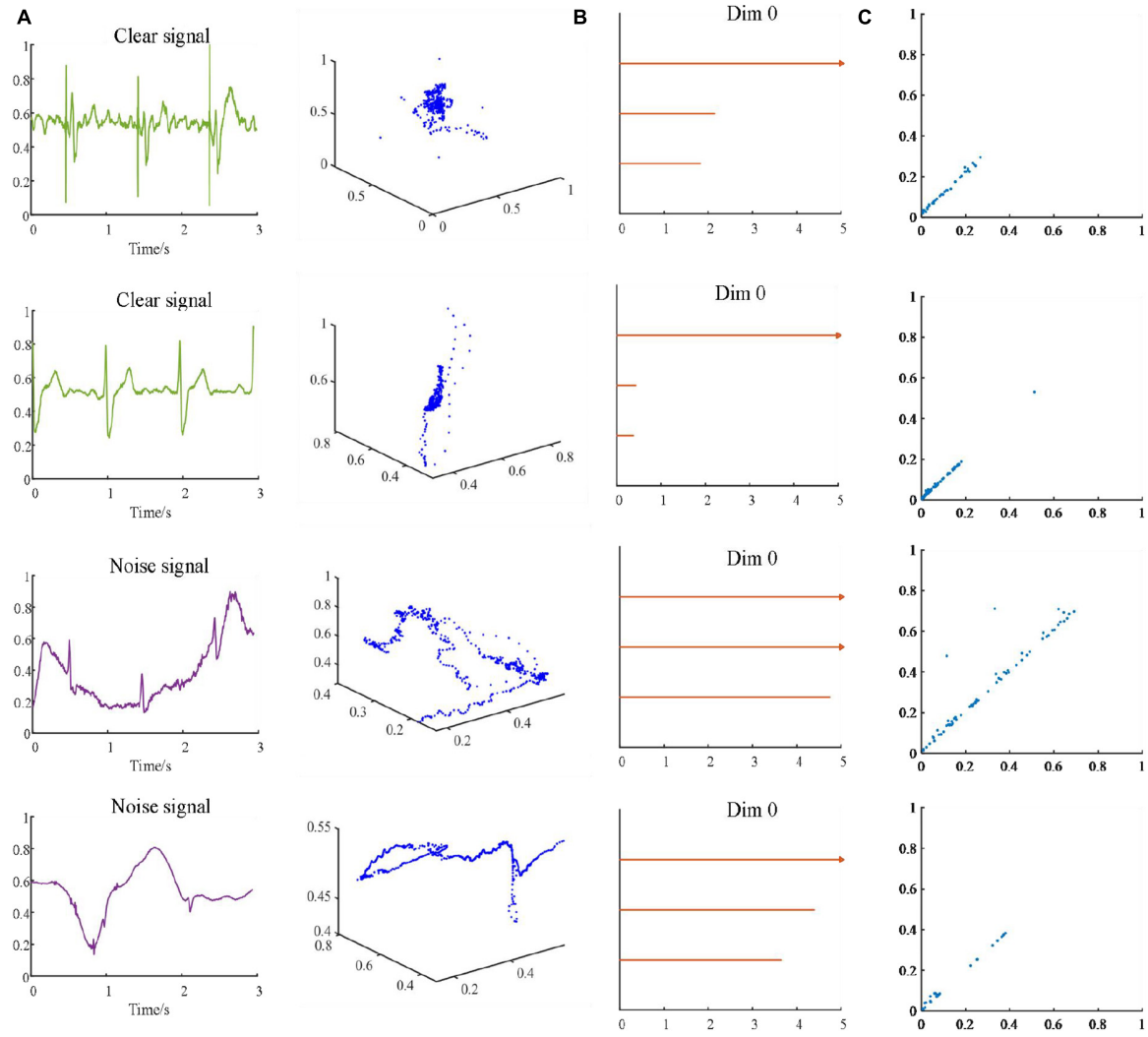

FIGURE 5
Two clean and two noisy ECG signals and its corresponding use of the sliding window method to establish three-dimensional scatter **(A)** and persistence barcode **(B)**. Persistence diagram obtained by the SLS-filtration method **(C)**.

Results

In this study, a quality assessment method of wearable dynamic ECG signals was proposed based on the persistent homology method and GoogLeNet (Assari et al., 2022) method. The performances of VR and SLS filtration were considered. We put the 224 × 224 × 3 persistent barcode pictures or persistent diagram pictures obtained by the persistent homology method into GoogLeNet for classification. For VR filtration, the influences of the sliding windows length for the point cloud structure was also explored. Tenfold cross-validation is applied to test classification performance. All the segments were randomly divided into 10 groups.

Results of 12-leads ECGs dataset

Table 1 and Figure 6 displayed the results of 12-leads ECGs Dataset. For VR filtration, the length of sliding windows was set to 1, 2, 3, 4, and 5 s, respectively. As shown in Table 1, the classification result of SLS filtration method is the best, $mAcc = 98.04\%$. The result of VR filtration method with sliding window of 1 s is the relatively high, $mAcc = 95.16\%$. As the length of sliding windows increasing, the classifying performances decrease. In the Figure 6, the Box-plot and normal distribution curve of all results were given. The boxplot shows the mean and variance of 10-fold cross-validation results, while the normal distribution curve shows how the results distribute.

Results of single-lead ECGs dataset

Table 2 and Figure 7 displayed the results of single-lead ECGs Dataset. For VR filtration, the point cloud structure of sliding windows with five lengths of 0.1, 0.2, 0.3, 0.4, and 0.5 s were established, respectively. In the Figure 7, the Box-plot and normal distribution curve of all results were also given. As shown in Table 2, the experimental results for the VR filtration show that

TABLE 1 Classification results of VR and SLS filtration methods in 12-leads ECGs Dataset.

	SW = 1 s	SW = 2 s	SW = 3 s	SW = 4 s	SW = 5 s	SLS
mAcc (%)	95.16 ± 0.20	93.11 ± 0.19	91.75 ± 0.21	90.22 ± 0.29	89.78 ± 0.26	**98.04 ± 0.11**
F1 (%)	95.60 ± 0.09	93.88 ± 0.08	92.06 ± 0.08	91.58 ± 0.18	90.85 ± 0.17	**98.40 ± 0.06**
Se (%)	92.02 ± 0.14	89.25 ± 0.35	85.90 ± 0.11	85.78 ± 0.23	84.41 ± 0.24	**97.15 ± 0.11**
Sp (%)	98.31 ± 0.41	96.98 ± 0.42	97.51 ± 0.43	94.67 ± 0.42	95.16 ± 0.33	**98.93 ± 0.23**

Bold values represent the data with the best results.

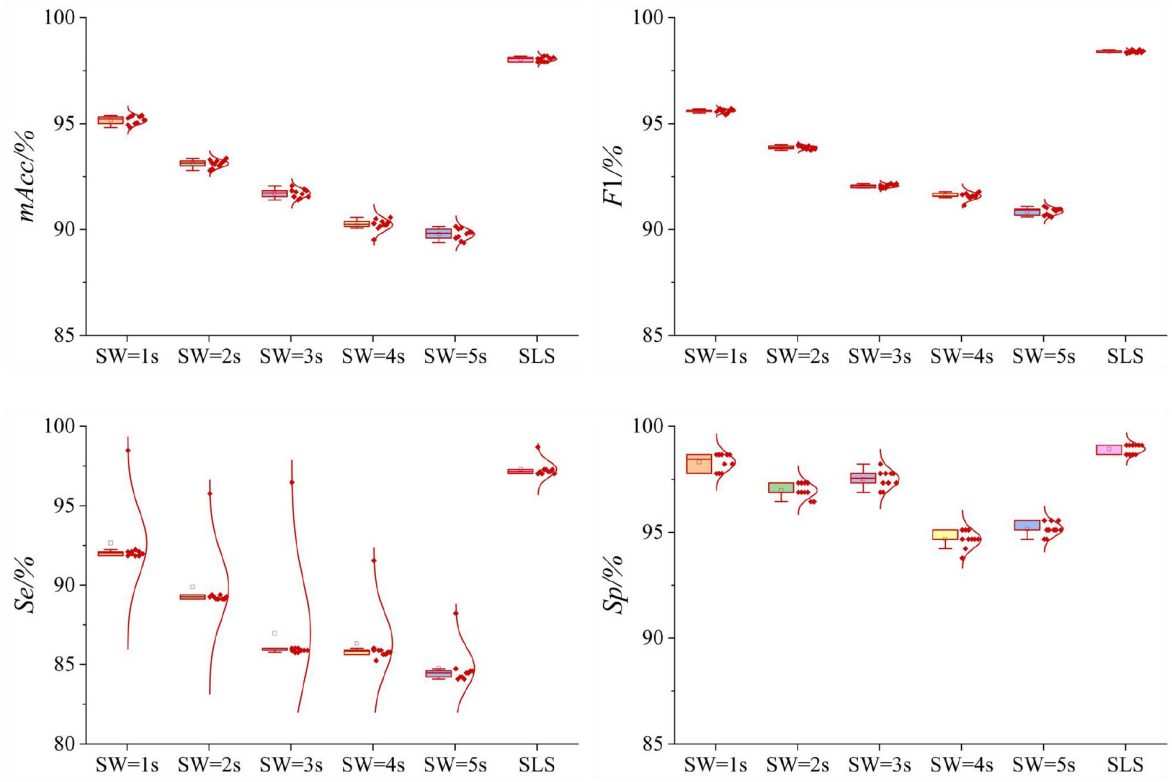

FIGURE 6
Boxplots of the normal distribution curves of the 10-fold cross-validation of VR and SLS filtration methods in 12-leads ECGs Dataset. For the VR method, when the length of sliding window increases gradually, the average value of *mAcc* decreases gradually. The 10-fold cross-validation results of *mAcc*, *F1*, *Se*, *Sp* are relatively concentrated. For the SLS method, the results of 10-fold cross-validation of *mAcc*, *F1*, *Se*, *Sp* are relatively scattered. But the average value of *mAcc* is higher than that of VR method.

the *mAcc* of the point cloud dataset with a sliding window length of 0.1 s is 98.55%, and the standard deviation is 0.13%. As the length of sliding windows increasing, the classifying performances decrease. The *mAcc* of the persistence diagram obtained by SLS filtration is 97.25%, and the standard deviation is 0.39%.

Discussion

This study proposed a new signals quality assessment method of wearable dynamic ECGs based on persistent homology method and GoogLeNet method. This method has strong robustness in quality assessing, which can be used for both 12-leads and single-lead ECG signals. VR and SLS two filtration methods were employed for persistent homology feature extraction. For the 12-leads ECGs Dataset, SLS filtration method has the best classification performance, *mAcc* = 98.04%, while for the single-lead ECGs Dataset, the classification result of VR filtration method with sliding window of 0.1 s is the highest, *mAcc* = 98.55%.

Comparison between VR filtation and SLS filtation

In this study, VR filtration method needs to reconstruct the time series of ECG signal, while sliding window method is used to construct the point cloud structure of ECG signal. For 12-leads ECGs Dataset, the sliding window lengths are 1, 2, 3, 4, and 5 s, respectively, and the dimensions are 120, 60, 36, 24, and 24, respectively. The results show that the sliding window is 1 s, and the classification result is the highest. For the single-lead ECGs Dataset, the sliding window lengths are 0.1, 0.2, 0.3, 0.4, and 0.5 s, respectively, and the dimensions are 100, 50, 33, 25, and 20, respectively. It can be seen that the classification

TABLE 2 Classification results of VR and SLS filtration methods in single-lead ECGs Dataset.

	SW = 0.1 s	SW = 0.2 s	SW = 0.3 s	SW = 0.4 s	SW = 0.5 s	SLS
mAcc (%)	**98.55 ± 0.13**	94.98 ± 0.55	94.06 ± 0.96	92.17 ± 0.76	89.76 ± 0.56	97.25 ± 0.39
F1 (%)	**98.62 ± 0.12**	95.32 ± 0.56	93.75 ± 1.73	92.51 ± 0.79	89.71 ± 1.11	97.39 ± 0.39
Se (%)	**98.37 ± 0.18**	95.81 ± 1.41	93.73 ± 3.13	91.93 ± 2.16	87.93 ± 2.63	97.77 ± 0.89
Sp (%)	**98.85 ± 0.20**	94.15 ± 1.14	94.24 ± 1.40	92.50 ± 1.87	91.59 ± 2.22	96.74 ± 1.13

Bold values represent the data with the best results.

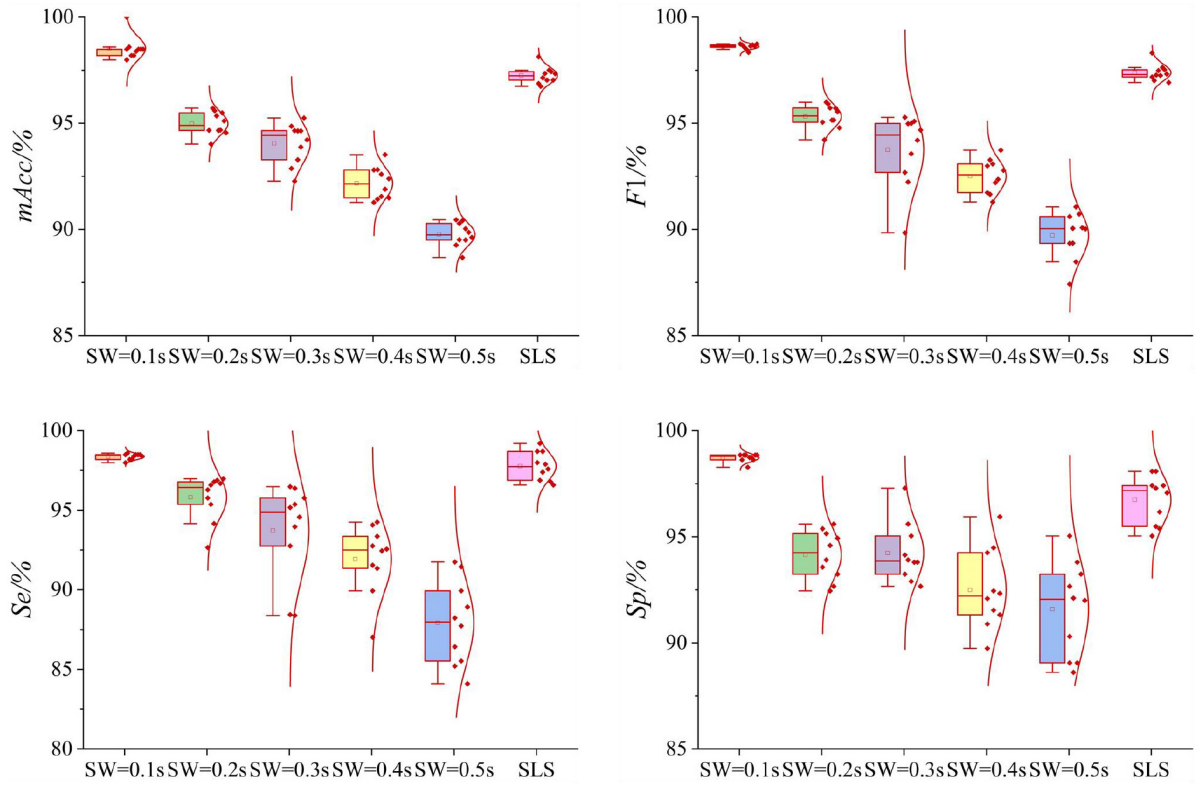

FIGURE 7
Boxplots of the normal distribution curves of the 10-fold cross-validation of VR and SLS filtration methods in single-lead ECGs Dataset. For the VR method, when the length of sliding window increases gradually, the average value of *mAcc* decreases gradually. The 10-fold cross-validation results of *mAcc* with different sliding windows are relatively concentrated, and the results of *F1*, *Se*, *Sp* are relatively scattered. For the SLS method, the 10-fold cross-validation results of *mAcc* is relatively concentrated, while the results of *F1*, *Se*, *Sp* are relatively scattered. But the average value of *mAcc* is slightly lower than that of VR method.

accuracy with a sliding window length of 0.1 s is the highest, the average *mAcc* of the 10-fold cross-validation is as high as 98.55%. We found that for the two datasets, the classification accuracy decreases with the increase of window length. In this study, the sliding window length will not continue to decrease in the two datasets. In the 12-leads ECGs Dataset, for 12 leads signals, the further decrease of sliding window will cause the data dimension to be too large, which will increase the calculation cost. In the single-lead ECGs Dataset, the sliding window length does not continue to shrink because the classification accuracy achieves good results when the window length is 0.1 s. Taking the single-lead ECGs Dataset as an example, the "acceptable" and "unacceptable" ECG signal waveforms and persistence barcode of the five sliding window lengths are shown in Figure 8. It can be seen from the figure that the persistent barcodes of ECG signals with different window sizes are obviously different. As the window increases, the persistent barcodes gradually become sparse. There are also differences between "acceptable" and "unacceptable" ECG signals corresponding to persistent barcode.

In this study, in the 12-leads ECGs Dataset, the classification accuracy using the SLS filtration method is higher than the highest accuracy using the VR filtration method; in the single-lead ECGs Dataset, the classification accuracy using the SLS filtration method is lower than the highest accuracy using the VR filtration method. SLS filtration method finds the birth and death points on the waveform of the ECG signal. The VR filtration method uses a simple complex to reconstruct geometry to analyze the spatial characteristics of the ECG signal time series. However, VR filtration method depends on the construction of point cloud. SLS filtration method is more stable. In the 12-leads ECGs Dataset, *mAcc* = 98.04% and in the single-lead ECGs Dataset, *mAcc* = 97.25%. From the classification results, we can see that the

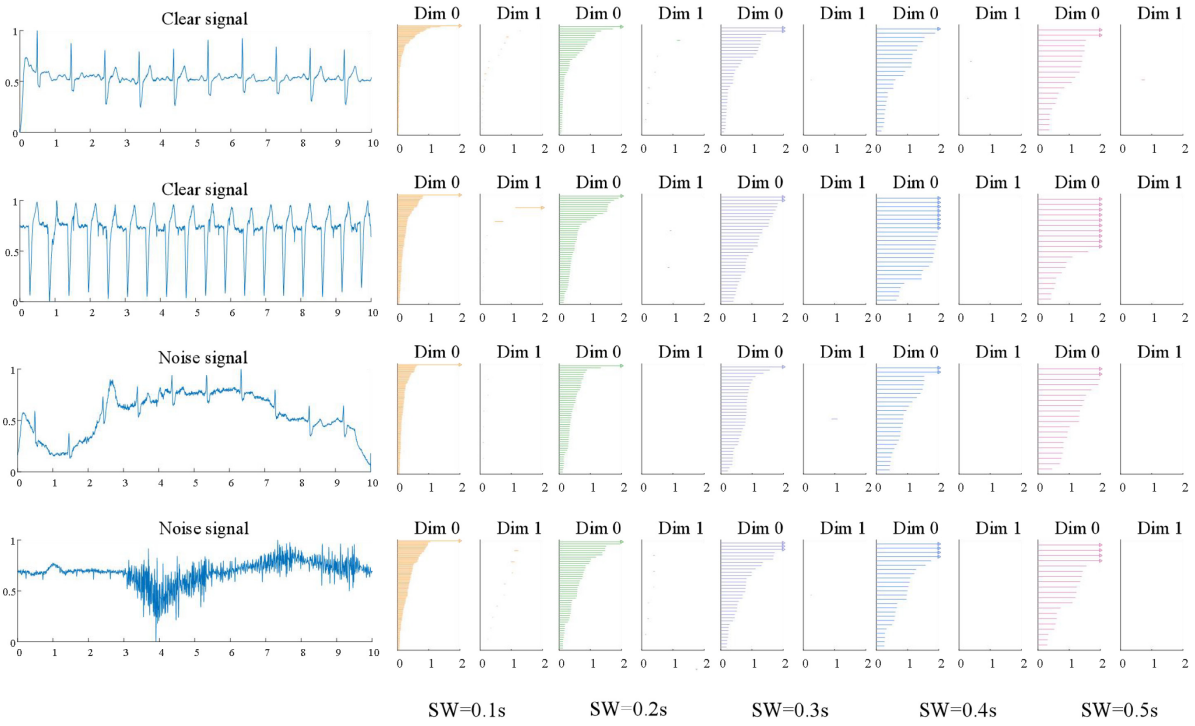

FIGURE 8
Persistence barcode pictures of "acceptable" and "unacceptable" ECG signals with five sliding window lengths of single-lead ECGs Dataset.

classification results of the two datasets based on this method are relatively good.

Comparison with other methods

In this study, SLS method is compared with some ECG signal quality evaluation methods in recent years, and the results are shown in **Table 3**. For example, Zhao and Zhang (2018) proposed a simple heuristic fusion and fuzzy comprehensive evaluation method based on SQI for ECG quality evaluation, with an accuracy rate of 94.67% on the test set. Jin et al. (2022) proposed a novel dual attention convolution long short-term memory neural network for ECG quality assessment, and the final classification accuracy was 94%. Shahriari et al. (2017) developed an image based ECG quality assessment technique with an accuracy of 82.50%; Zhang et al. (2019) conducted performance testing in ECG quality assessment by comparing seven feature schemes composed of random forest, SVM and its variants combined with nonlinear features, among which least squares SVM had the highest Acc of 92.20% in test data. Because the dataset is unbalanced, according to formula (8), we choose the *mAcc* to calculate the classification results. In order to unify the evaluation standard with other studies, we also calculate the *Acc* according to formula (7).

As can be seen from **Table 3**, the classification result of SLS filtration method is still the highest in the 12-leads ECGs Dataset. However, the labeling for "acceptable" or "unacceptable" for the whole 12 channels was not clear. In a 12-leads ECG signal, some single-lead signals are "acceptable" and some single-lead signals are "unacceptable." As shown in the **Figure 9**. We selected an "acceptable" and an unaccep2-leads ECG signal. From (A), we can see that there is also obvious noise in the "acceptable" 12-leads ECGs. From (B), We can see that in the "unacceptable" 12-leads ECG signal, the single-lead ECG signal may be bad, but part of the heart rate information could be calculate. Therefore, we considered the quality evaluation of single-lead ECG signals.

For single-lead ECGs Dataset, **Table 4** shows the comparison between VR filtration method and the other four methods. The references are as follows: reference (Liu et al., 2020) selected 26 signal quality indicators (SQI) to evaluate the quality of ECG signals, including time domain characteristics, frequency domain characteristics, and SQI based on QRS wave and nonlinear characteristics. Experiments were conducted to test the performance of a single classifier based on SQI features and multiple classifiers based on SQI features. The total classification

TABLE 3 Performance of the presented algorithm and methods participating in the PhysioNet/CinC Challenge.

	mAcc (%)	*Acc* (%)	*Se* (%)	*Sp* (%)
Kalkstein et al. (2011)	86.30	93.00	74.10	98.50
Xia et al. (2011)	89.11	85.90	95.11	83.10
Zhao and Zhang (2018)	91.67	94.67	90.33	93.00
Jin et al. (2022)	87.03	94.00	97.59	76.47
Shahriari et al. (2017)	80.80	82.50	83.90	77.70
Zhang et al. (2019)	88.02	92.20	77.94	98.09
Proposed SLS method	**98.04**	**97.70**	**97.15**	**98.93**

Se, *Sp*, *Acc* and *mAcc* for the 12-leads ECGs Dataset. Bold values represent the data with the best results.

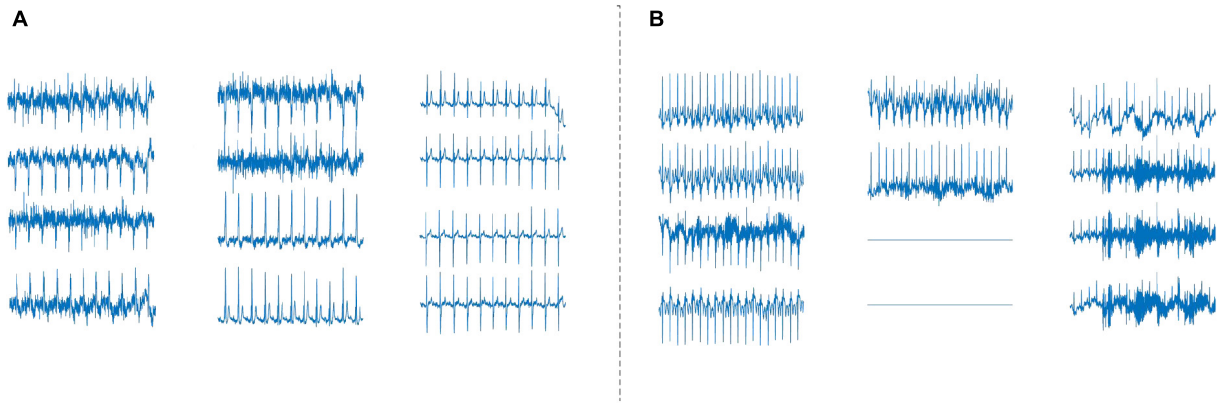

FIGURE 9
(A) The "acceptable" 12-leads ECG signal, **(B)** The "unacceptable" 12-leads ECG signal.

performance of a single classifier based on GbSQI features and the total classification performance of multiple classifiers based on GbSQI features are obtained. For the overall classification performance of a single GbSQI-based classifier, the QRS wave-based SQIs had the best performance; for example, the *mAcc* of bSQI_2 was (93.84 ± 1.47)% and bSQI_4 *mAcc* was (93.70 ± 1.49)%. For the overall classification performance of multiple classifiers based on GbSQI features, the effect of the classification model was best when 14 SQIs were selected, and the *mAcc* was 95.2%. Reference (Liu et al., 2018) redefined the bSQI with any two combined QRS detectors and then extended the redefined bSQI to the bSQI of multiple QRS detectors, represented by GbSQI. The experimental results showed that the mAcc of the classifier with the best combination of six QRS detectors and a single GbSQI feature was 94.03%. The best combination of four QRS detectors was the GbSQI feature, and the *mAcc* of multiple classifiers was 94.76%. Study (Falk and Maier, 2014) proposed a quality index of ECG signals based on modulation spectrum signal representation, and a quality index MS-QI based on modulation spectrum was proposed. The experimental results of the above comparison methods are based on the original challenge data. In order to compare the performance of the methods proposed in this study, we selected several commonly used indicators from the reference literature to test based on the single-lead ECG datasets built in this study. A comparison of the results is shown in Table 4. According to the table, the classification accuracy of the VR filtration method is still the highest.

TABLE 4 Comparison of classification accuracy results of single-lead ECGs Dataset four methods.

Methods	*mAcc* (%)	*F1* (%)	*Se* (%)	*Sp* (%)
MS-QI Falk and Maier (2014)	85.61 ± 1.05	85.58 ± 0.48	81.57 ± 0.73	89.66 ± 1.77
bSQI_2 Liu et al. (2018)	84.08 ± 0.75	84.85 ± 0.33	83.79 ± 0.71	84.37 ± 1.90
bSQI_4 Liu et al. (2018)	89.28 ± 0.55	89.33 ± 1.07	86.21 ± 1.49	92.36 ± 1.20
picaSQI Liu et al. (2020)	93.11 ± 0.73	93.03 ± 0.58	89.33 ± 1.11	96.90 ± 0.58
Proposed VR method	**98.55 ± 0.13**	**98.62 ± 0.12**	**98.37 ± 0.18**	**98.85 ± 0.20**

Bold values represent the data with the best results.

In this study, the wearable ECG signals were graded into two groups: "acceptable" vs. "unacceptable." However, part of wearable ECG signals only R wave could be detected, other waves like P or ST were drowned out by the noise, as shown in Figure 9. These signals cannot be used for some CVDs detection, but they also cannot be abandoned as heart rate information can be obtained. Therefore, it is not appropriate to simply divide ECG signals into acceptable and unacceptable. A more detailed quality evaluation grades need to be considered in the future.

Conclusion

Cardiovascular disease poses a threat to human health, with tens of millions of deaths worldwide every year. Its prevention and monitoring are urgent issues. This study proposed a new signals quality assessment method of wearable dynamic ECGs based on persistent homology method and GoogLeNet method. This method has strong robustness in quality assessing, which can be used for both 12-leads and single-lead ECG signals. VR and SLS two filtration methods were employed for persistent homology feature extraction. The VR filtation method selected persistence barcode to quantify the topological features, and the SLS filtation method selected persistence diagram to quantify the topological features. When using VR filtation method, it is necessary to reconstruct the time series. The focus of this method is to use the sliding window method to construct the point cloud dataset. For 12-leads ECGs Dataset, the sliding window sizes are 0, 1, 2, 3, 4, and 5 s, respectively, and 120, 60, 36, 24, and 24 dimensions are established, respectively. When use the SLS filtation method, the classification result of 12-leads ECGs Dataset is the highest, *mAcc* = 98.04%. For single-lead ECGs Dataset, the sliding window sizes are 0.1, 0.2, 0.3, 0.4, and 0.5 s, respectively, and 100, 50, 33, 25, and 20 dimensions are established, respectively. The classification results show that when the window length of VR filtration method is 0.1 s, the classification result is the highest, *mAcc* = 98.55%. The results show that persistence homology method performed well in the quality evaluation of wearable ambulatory ECG. This study verified the feasibility of applying the persistence homology method to wearable ECG signal quality assessment. In this study, the

persistent homology method is still insufficient. We need the sliding window method to find the optimal point cloud matrix. In the next experiment, we integrate the experiment and the method to find an optimal point cloud construction method. This study is to classify acceptable and unacceptable ECG signals. In the next work, we will continue to refine the classification criteria to make Wearable ECG instruments more widely used.

Data availability statement

Publicly available datasets were analyzed in this study. This data can be found here: https://physionet.org/content/challenge-2011/1.0.0/.

Author contributions

YR, FL, and SX designed the research. YR designed the algorithm, analyzed the data, and wrote the manuscript. FL contributed to the signal relabeling. SS, LC, and ZW contributed to the collecting and sorting data. FL and SX contributed to the revising it critically for the important intellectual content. All authors contributed to the article and approved the submitted version.

Funding

This work was supported by the National Natural Science Foundation of China (grant numbers: 61901114, 82072014, 81871444, and 62171123), Shandong Province Key Basic Research Program (grant number: ZR2020ZD25), the Development Plan of Youth Innovation Team of University in Shandong Province (grant number: 2021KJ067), the National Key R&D Program of China (grant number: 2019YFE0113800), and the Shandong Province Natural Science Foundation (grant number: ZR2020MF028).

Acknowledgments

The datasets of this work was from the 2011 PhysioNet/CinC challenge. Thank the PhysioNet website for providing us with Wearable ECG datasets. From the beginning to the completion of this study, each step was accomplished under the patient guidance of SX and FL. The authors would like to express my great respect and heartfelt thanks to my tutor.

Conflict of interest

The authors declare that the research was conducted in the absence of any commercial or financial relationships that could be construed as a potential conflict of interest.

Publisher's note

References

Al-Issa, Y., and Alqudah, A. M. (2022). A lightweight hybrid deep learning system for cardiac valvular disease classification. *Sci. Rep.* 12, 1–20. doi: 10.1038/s41598-022-18293-7

Alqudah, A. M., Qazan, S., Al-Ebbini, L., Alquran, H., and Qasmieh, I. A. (2022). ECG heartbeat arrhythmias classification: A comparison study between different types of spectrum representation and convolutional neural networks architectures. *J. Ambient Intell. Hum. Comput.* 13, 4877–4907.

Assari, Z., Mahloojifar, A., and Ahmadinejad, N. (2022). A bimodal BI-RADS-guided GoogLeNet-based CAD system for solid breast masses discrimination using transfer learning. *Comput. Biol. Med.* 142:105160. doi: 10.1016/j.compbiomed.2021.105160

Carlsson, G. (2009). Topology and data. *Bull. Am. Math. Soc.* 46, 255–308. doi: 10.1090/S0273-0979-09-01249-X

Carlsson, G., Zomorodian, A., Collins, A., and Guibas, L. J. (2005). Persistence barcodes for shapes. *Int. J. Shape Model.* 11, 149–187.

Celi, L. A., Sarmenta, L., Rotberg, J., Marcelo, A., and Clifford, G. (2009). Mobile care (Moca) for remote diagnosis and screening. *J. Health Inf. Dev. Countries* 3:17.

Chung, Y. M., Hu, C. S., Lo, Y. L., and Wu, H. T. (2021). A persistent homology approach to heart rate variability analysis with an application to sleep-wake classification. *Front. Physiol.* 12:637684. doi: 10.3389/fphys.2021.637684

Dindin, M., Umeda, Y., and Chazal, F. (2020). "Topological data analysis for arrhythmia detection through modular neural networks," in *Proceedings of the Canadian conference on artificial intelligence*, Ottawa, ON, 177–188. 17 doi: 10.1007/978-3-030-47358-7

Edelsbrunner, H., and Harer, J. (2010). Computational topology: An introduction. *Am. Math. Soc.* XII:241. doi: 10.1090/mbk/069xcv

Edelsbrunner, H., Letscher, D., and Zomorodian, A. (2000). "Topological persistence and simplification," in *Proceedings of the 41st annual symposium on foundations of computer science*, (Manhattan, NY: IEEE), 454–463. doi: 10.1007/s00454-002-2885-2Jo

Falk, T. H., and Maier, M. (2014). MS-QI: A modulation spectrum-based ECG quality index for telehealth applications. *IEEE Transactions Biomed. Eng.* 63, 1613–1622. doi: 10.1109/TBME.2014.2355135

Goldberger, A. L., Amaral, L. A., Glass, L., Hausdorff, J. M., and Ivanov, P. C. (2000). PhysioBank, PhysioToolkit, and PhysioNet: Components of a new research resource for complex physiologic signals. *Circulation* 101, e215–e220.

Graff, G., Graff, B., Pilarczyk, P., Jablonski, G., Gasecki, D., and Narkiewicz, K. (2021). Persistent homology as a new method of the assessment of heart rate variability. *PLoS One* 16:e0253851. doi: 10.1371/journal.pone.0253851

Ignacio, P. S., Dunstan, C., Escobar, E., Trujillo, L., and Uminsky, D. (2019). "Classification of single-lead electrocardiograms: TDA informed machine learning," in *Proceedings of the 2019 18th IEEE international conference on machine learning and applications (ICMLA)*, Boca Raton, FL, 1241–1246. ICMLA.2019.00204 doi: 10.1109/

Jin, Y., Li, Z., Qin, C., Liu, J., Liu, Y., Zhao, L., et al. (2022). A novel attentional deep neural network-based assessment method for ECG quality. *Biomed. Signal Process. Control* 79:104064. doi: 10.1088/1361-6501/abf176

Kalkstein, N., Kinar, Y., Na'aman, M., Neumark, N., and Akiva, P. (2011). Using machine learning to detect problems in ECG data collection. *Comput. Cardiol.* 38, 437–440.

Liu, F., Liu, C., Zhao, L., Jiang, X., Zhang, Z., Li, J., et al. (2018). Dynamic ECG signal quality evaluation based on the generalized bSQI index. *IEEE Access* 6, 41892–41902. doi: 10.1161/01.CIR.101.23.e215

Liu, F., Wei, S., Lin, F., Jiang, X., and Liu, C. (2020). "An overview of signal quality indices on dynamic ECG signal quality assessment," in *Feature engineering and computational intelligence in ECG monitoring*, eds C. Liu and J. Li (Singapore: Springer Singapore), 33–54.

Moody, G. B., Muldrow, W., and Mark, R. G. (1984). Noise stress test for arrhythmia detectors. *Comput. Cardiol.* 11, 381–384.

Obeidat, Y., and Alqudah, A. M. (2021). A hybrid lightweight 1D CNN-LSTM architecture for automated ECG beat-wise classification. *Trait. Signal* 38, 1281–1291.

Redmond, S. J., Xie, Y., Chang, D., Basilakis, J., and Lovell, N. H. (2012). Electrocardiogram signal quality measures for unsupervised telehealth environments. *Physiol. Meas.* 33:1517. doi: 10.1088/0967-3334/33/9/1517

Shahriari, Y., Fidler, R., Pelter, M. M., Bai, Y., Villaroman, A., and Hu, X. (2017). Electrocardiogram signal quality assessment based on structural image similarity metric. *IEEE Transactions Biomed. Eng.* 65, 745–753. doi: 10.1109/TBME.2017.2717876

Silva, I., Moody, G. B., and Celi, L. (2011). "Improving the quality of ECGs collected using mobile phones: The Physionet/computing in cardiology challenge 2011," in *Proceedings of the 2011 computing in cardiology*, (Manhattan, NY: IEEE), 273–276.

Viegas, A., Abreu, M. M., and Pedrosa, I. (2016). "State-of-the-art in wearable technology: Medical area applications," in *Proceedings of the 2016 11th Iberian conference on information systems and technologies (CISTI)*, (Manhattan, NY: IEEE). doi: 10.1109/cisti.2016.7521565

Xia, H., Garcia, G. A., McBride, J. C., Sullivan, A., De Bock, T., Bains, J., et al. (2011). "Computer algorithms for evaluating the quality of ECGs in real time," in *Proceedings of the 2011 computing in cardiology*, (Hangzhou: IEEE), 369–372.

Yan, Y., Ivanov, K., Cen, J., Liu, Q. H., and Wang, L. (2019). Persistence landscape based topological data analysis for personalized arrhythmia classification. *Preprints* 2019:2019080320. doi: 10.20944/preprints201908.0320.v1

Zaunseder, S., Huhle, R., and Malberg, H. (2011). "CinC challenge-assessing the usability of ECG by ensemble decision trees," in *Proceedings of the 38th computing in cardiology*, (Manhattan, NY: IEEE), 277–280.

Zhang, Y., Wei, S., Zhang, L., and Liu, C. (2019). Comparing the performance of random forest, SVM and their variants for ECG quality assessment combined with nonlinear features. *J. Med. Biol. Eng.* 39, 381–392. doi: 10.1007/S40846-018-0411-0

Zhao, Z., and Zhang, Y. (2018). SQI quality evaluation mechanism of single-lead ECG signal based on simple heuristic fusion and fuzzy comprehensive evaluation. *Front. Physiol.* 9:727. doi: 10.3389/fphys.2018.00727

Zomorodian, A., and Carlsson, G. (2005). Computing persistent homology. *Discrete Comput. Geom.* 33, 249–274. doi: 10.1007/s00454-004-1146-y

frontiers | Frontiers in Neuroscience

TYPE Original Research
PUBLISHED 12 April 2023
DOI 10.3389/fnins.2023.1113225

OPEN ACCESS

EDITED BY
Lei Zhang,
Nanjing Normal University,
China

REVIEWED BY
Lianke Yao,
Binzhou University,
China
Yori Gidron,
University of Haifa,
Israel

*CORRESPONDENCE
Bo Shi
✉ shibo@bbmc.edu.cn
Xiaochun Zhang
✉ ceiq@sina.com

SPECIALTY SECTION
This article was submitted to Neuroprosthetics, a section of the journal Frontiers in Neuroscience

RECEIVED 01 December 2022
ACCEPTED 14 March 2023
PUBLISHED 12 April 2023

CITATION
Wu S, Li G, Chen M, Zhang S, Zhou Y, Shi B and Zhang X (2023) Association of heartbeat complexity with survival in advanced non-small cell lung cancer patients.
Front. Neurosci. 17:1113225.
doi: 10.3389/fnins.2023.1113225

Association of heartbeat complexity with survival in advanced non-small cell lung cancer patients

Shuang Wu[1,2], Guangqiao Li[3,4], Man Chen[5], Sai Zhang[3,4], Yufu Zhou[2], Bo Shi[3,4]* and Xiaochun Zhang[1,5]*

[1]School of Medicine, Yangzhou University, Yangzhou, Jiangsu, China, [2]Department of Radiation Oncology, First Affiliated Hospital, Bengbu Medical College, Bengbu, Anhui, China, [3]School of Medical Imaging, Bengbu Medical College, Bengbu, Anhui, China, [4]Anhui Key Laboratory of Computational Medicine and Intelligent Health, Bengbu Medical College, Bengbu, Anhui, China, [5]Department of Oncology, Yangzhou Hospital of Traditional Chinese Medicine, Yangzhou, Jiangsu, China

Background: Previous studies have shown that the predictive value of traditional linear (time domain and frequency domain) heart rate variability (HRV) for the survival of patients with advanced non-small cell lung cancer (NSCLC) is controversial. Nonlinear methods, based on the concept of complexity, have been used to evaluate HRV, providing a new means to reveal the physiological and pathological changes in HRV. This study aimed to assess the association between heartbeat complexity and overall survival in patients with advanced NSCLC.

Methods: This study included 78 patients with advanced NSCLC (mean age: 62.0±9.3years). A 5-min resting electrocardiogram of advanced NSCLC patients was collected to analyze the following HRV parameters: time domain indicators, i.e., standard deviation of the normal-normal intervals (SDNN) and root mean square of successive interval differences (RMSSD); frequency domain indicators, i.e., total power (TP), low frequency power (LF), high frequency power (HF), and the ratio of LF to HF (LF/HF); nonlinear HRV indicators characterizing heartbeat complexity, i.e., approximate entropy (ApEn), sample entropy (SampEn), and recurrence quantification analysis (RQA) indexes: mean diagonal line length (Lmean), maximal diagonal line length (Lmax), recurrence rate (REC), determinism (DET), and shannon entropy (ShanEn).

Results: Univariate analysis revealed that the linear frequency domain parameter HF and nonlinear RQA parameters Lmax, REC, and DET were significantly correlated with the survival of advanced NSCLC patients (all $p<0.05$). After adjusting for confounders in the multivariate analysis, HF, REC, and DET were found to be independent prognostic factors for the survival of patients with advanced NSCLC (all $p<0.05$).

Conclusion: There was an independent association between heartbeat complexity and survival in advanced NSCLC patients. The nonlinear analysis method based on RQA may provide valuable additional information for the prognostic stratification of patients with advanced NSCLC and may supplement the traditional time domain and frequency domain analysis methods.

KEYWORDS

heart rate variability, nonlinear methods, heartbeat complexity, recurrence quantification analysis, advanced non-small cell lung cancer, prognosis

Introduction

Lung cancer (LC) is the second most common cancer and the leading cause of cancer deaths worldwide (Sung et al., 2021). The pathological types of LC are mainly divided into non-small cell lung cancer (NSCLC; including squamous cell carcinoma and adenocarcinoma) and small cell lung cancer, of which NSCLC accounts for 85% of cases (Zheng, 2016). Previous studies have confirmed that abnormal increases in sympathetic activity or abnormal decreases in vagal activity (an important part of the parasympathetic nervous system) are related to the occurrence and development of LC (Wang H. M. et al., 2013; Gidron et al., 2018; Ha et al., 2019). Sympathetic nerves can promote tumor progression by regulating the inflammatory response (Huan et al., 2017) and angiogenesis (Garg et al., 2017), while vagus nerve activation can inhibit the inflammatory response (Tracey, 2009) and sympathetic nerve activity (Saku et al., 2014).

Heart rate variability (HRV) refers to the variation in time intervals between adjacent heartbeats and is considered a reliable indicator for the quantitative evaluation of autonomic nervous system activity (Camm et al., 1996; Lombardi and Stein, 2011). Traditional linear (time domain or frequency domain) HRV analysis is the main method to clinically evaluate autonomic function (Camm et al., 1996; Lombardi and Stein, 2011). Growing research has demonstrated the essential role of inflammatory cytokines, such as tumor necrosis factor-alpha (TNF-α), interleukin 6 (IL-6), and C-reactive protein (CRP), in promoting tumor occurrence and growth (Balkwill, 2009; Taniguchi and Karin, 2014; Hart et al., 2020). In a recent study, vagally mediated HRV parameters were inversely associated with levels of inflammatory markers such as TNF-α, IL-6, and CRP, possibly because vagal nerve stimulation reduces inflammatory cytokines through the cholinergic anti-inflammatory pathway (Williams et al., 2019). Published studies have suggested that linear (time domain or frequency domain) HRV is associated with the prognosis of patients with malignant tumors, including LC with brain metastasis (Wu et al., 2022), brain metastasis (Wang et al., 2021), gastric cancer (Hu et al., 2018), colorectal cancer (Mouton et al., 2012), liver cancer (Chiang et al., 2010), pancreatic cancer (De Couck et al., 2016), breast cancer (Giese-Davis et al., 2015), and so on. Although accumulating evidence suggests that linear HRV may be a prognostic marker for patients with malignant tumors, its predictive value in the survival of NSCLC patients remains controversial. For example, Kim et al. (2015) performed a univariate analysis, which showed that there was a significant correlation between the standard deviation of all normal-to-normal intervals (SDNN) and the overall survival of advanced NSCLC patients, while their multivariate analysis indicated that SDNN was not an independent prognostic factor for the overall survival of patients with advanced NSCLC. De Couck et al. (2013) confirmed that SDNN and the root mean square of successive interval differences (RMSSD) could not significantly predict the overall survival of NSCLC patients, while further analysis showed that they could significantly predict the overall survival of NSCLC patients who were under 65 years of age (all $p < 0.05$). This may be because the true effect of linear HRV analysis is greatly affected by the heterogeneity in the tumor stage of NSCLC patients and the length of ECG data used in the study (De Couck et al., 2013; Kim et al., 2015).

The human body is characterized by nonstationarity and nonlinearity, and simple linear information may be insufficient to correctly describe the complex nonlinear behavior that dominates the human system. The nonlinear analysis method accords with the nonlinear and nonstationary characteristics of heartbeat interval time series, providing a new perspective for revealing the physiopathological changes in HRV. It can not only reflect more information about heart rate dynamics but also complement traditional time domain and frequency domain analysis. The unpredictability or complexity of signals is one of the main characteristics of nonlinear heart rate dynamics. A healthy human system exhibits spatial and temporal complexity, but disease may involve an increase or decrease in complexity (Vaillancourt and Newell, 2002). Previous studies have also shown that compared with healthy people, the heartbeat complexity of patients with atrial fibrillation (Mohebbi and Ghassemian, 2011), coronary artery disease (Acharya et al., 2014), or acute myocardial ischemia (Peng and Sun, 2011) is significantly lower. Recently, some studies have been conducted to preliminarily examine the prognostic value of nonlinear HRV parameters in cancer (Shi et al., 2019; Escutia-Reyes et al., 2021; Li et al., 2022). For example, Shi et al. (2019) found that decreased heartbeat complexity was associated with higher carcinoembryonic antigen levels in gastric cancer patients. Li et al. (2022) showed that lower heartbeat complexity was predictive of shorter survival of LC patients with brain metastasis. However, few studies have explored the role of heartbeat complexity in the prognosis of patients with advanced NSCLC.

At present, it is not clear whether there is a correlation between heartbeat complexity and prognosis in advanced NSCLC patients. Therefore, this study aimed to verify the relationship between heartbeat complexity and overall survival in patients with advanced NSCLC.

Methods

Subjects

This prospective study enrolled NSCLC patients who were treated in the hospital from October 2019 to February 2021, with the approval of the Medical Ethics Committee of the First Affiliated Hospital of Bengbu Medical College. The inclusion criteria were as follows: (1) NSCLC confirmed by pathological examination and (2) stage III and IV NSCLC. The exclusion criteria were as follows: (1) installation of a cardiac pacemaker, (2) use of antiarrhythmic drugs or β-blockers, (3) complications with other types of malignant tumors, (4) lack of clinical or pathological data, and (5) treatment with chemotherapy, radiotherapy, or surgery within 3 weeks before data collection. The research process was carried out in accordance with the Helsinki Declaration. All patients provided written informed consent before study enrolment.

Data collection

The medical staff informed patients about the study and used a single-lead Micro-ECG recorder (HeaLink-R211B; HeaLinkLtd., Bengbu, China) to collect 5 min of ECG data from NSCLC patients at a 400 Hz sampling rate and V6-lead in an undisturbed quiet room. The participants, fully relaxed and in the supine position, were asked to

breathe regularly and gently and could neither speak nor move their bodies during the measurement.

We collected the following clinical background information from advanced NSCLC patients: sex, age, body mass index (BMI), smoking history, Karnofsky performance status (KPS), pathological type, prior treatment history (radiotherapy, chemotherapy, targeted therapy, and surgery), TNM stage, and overall survival. Patient overall survival was defined from the date of HRV detection to the date of death or the last follow-up. The patients were followed up by telephone call backs or by consulting the case data, and the last follow-up date was on September 03, 2022.

HRV analysis

This research used the Pan-Tompkins algorithm to extract R-R interval time series on ECG and to calculate linear (time domain or frequency domain) and nonlinear HRV parameters (Pan and Tompkins, 1985). An automatic artifact correction algorithm in the Kubios software was used to correct technical and physiological artifacts within R-R intervals. The estimated values for respiratory rate (RR) were calculated using an ECG-derived respiratory method (Moody et al., 1985). The following common time domain and frequency domain parameters were used: SDNN, RMSSD, total power (TP, 0–0.4 Hz), high frequency power (HF, 0.15–0.4 Hz), low frequency power (LF, 0.04–0.15 Hz), and the ratio of LF to HF (LF/HF). The power spectrum signal was analyzed in the frequency domain, and the fast Fourier transform algorithm was used to calculate the power spectrum density (Camm et al., 1996; Vanderlei et al., 2009; Lombardi and Stein, 2011).

Through the analysis of HRV by nonlinear dynamics, the following indexes characterizing the complexity of heartbeat were obtained [i.e., approximate entropy (ApEn), sample entropy (SampEn), and recurrence quantification analysis (RQA): mean diagonal line length (Lmean), maximal diagonal line length (Lmax), recurrence rate (REC), determinism (DET), and shannon entropy (ShanEn)]. ApEn and SampEn are typical nonlinear dynamic methods for quantifying the complexity and regularity of time series. The greater the complexity and randomness of the time series, the greater their values (Voss et al., 2009; de Godoy, 2016). SampEn aims to provide better consistency than ApEn (Yentes et al., 2013). RQA is a quantitative description of the deterministic structure and complexity in recursive graphs that reveals the system dynamical behavior. The smaller the Lmean and Lmax are, the higher the complexity and instability of the system. The higher the REC value is, the stronger the similarity of system dynamics. DET is an index used to quantify the regularity and certainty of system dynamics, and the higher the DET value is, the stronger the certainty. ShanEn is a measure of signal complexity. The smaller the ShanEn value, the closer it is to a chaotic dynamic behavior (Marwan et al., 2002, 2007; Sun and Wang, 2008).

The parameters for ApEn and SampEn were set to the embedding dimension $m = 2$, delay time $\tau = 1$ and the tolerance value $r = 0.2$ SD (SD is the standard deviation; Burioka et al., 2005; Lee et al., 2013; Mohseni et al., 2022). The parameters of RQA were set to the embedding dimension $m = 10$, delay time $\tau = 1$ and distance threshold $r = \sqrt{\text{m}}$ SD (SD is the standard deviation of the R-R time series; Webber and Zbilut, 1994; Dabiré et al., 1998; Zimatore et al., 2017). Linear and nonlinear HRV indicators were analyzed by Kubios HRV Premium software (version 3.1.0, https://www.kubios.com Magi Kubios Oy, Kuopio, Finland; Niskanen et al., 2004).

Statistical analysis

The sample size was estimated based on a previously published study about the association between vagal neuroimmunomodulation and the NSCLC survival rate (Gidron et al., 2018), and no specific statistical method was used to determine sample size. We added approximately 10% ($n = 78$) based on the Gidron et al. (2018) sample size ($n = 71$) in NSCLC patients. The normal continuous data are described as $x \pm s$, the nonnormal continuous data are described as M [Q1 and Q3], and the counting data are described as the frequency and percentage. Univariate Cox regression analysis was performed to determine the significant prognostic factors between the included clinical factors and the additional factors affecting HRV [mean heart rate (mean HR), RR]. The optimal cut-off value for the HRV parameters for evaluating the overall survival of patients was obtained by X-Tile software (Camp et al., 2004). The event-survival curve was constructed by the Kaplan–Meier method to estimate the median overall survival. Finally, considering the correlation among HRV indices, we performed a multivariate Cox regression analysis for each HRV indicator individually with the prognostic confounding factors that were shown to be significant in the univariate analysis to evaluate the independent prognostic HRV parameters affecting NSCLC patients. All the data were analyzed by SPSS Statistics 25.0 (IBM Corp., Chicago, Illinois, United States). All analyses were two-tailed tests, and a p value of <0.05 was considered statistically significant.

Results

Table 1 shows the general characteristics and HRV parameters of the advanced NSCLC patients. A total of 78 patients diagnosed with advanced NSCLC were included in this study, including 21 females and 57 males. The mean age was 62.0 ± 9.3 years. Forty-seven patients (60.3%) died, and 31 patients (39.7%) survived. The range of follow-up time was 0.5–34.8 months, with a median follow-up time of 21.4 months.

Univariate analysis showed that KPS and surgical history were significantly correlated with the overall survival of advanced NSCLC patients [KPS: hazard ratio = 2.430, 95% confidence interval (CI): 1.275–4.631, $p = 0.007$; surgery: hazard ratio = 3.861, 95% CI: 1.383–10.778, $p = 0.010$]. In univariate analysis, the overall survival of patients with advanced NSCLC was not significantly associated with sex, age, BMI, mean HR, RR, smoking history, pathological type, radiotherapy history, chemotherapy history, targeted therapy history, or TNM stage (Table 2).

Univariate and multivariate analyses were performed to determine the correlation between heartbeat complexity and survival in patients with advanced NSCLC. Univariate analysis showed that there were significant correlations between the frequency domain parameter HF as well as the RQA indicators Lmax, REC, and DET and the overall survival of advanced NSCLC patients. Specifically, compared with the high-value HF group, the low-value HF group had a poorer prognosis (7.1 vs. 15.0 months, $p = 0.016$). Compared with those in the low-value Lmax, REC, and DET group, the NSCLC patients in the high-value Lmax, REC, and DET group had a poorer prognosis (Lmax: 17.1 vs.

10.3389/fnins.2023.1113225

TABLE 1 Basic characteristics of the non-small cell lung cancer patients enrolled.

Characteristics	Values (*N*=78)
Sex	
Female	21 (26.9%)
Male	57 (73.1%)
Age (year)	62.0 ± 9.3
BMI (kg/m^2)	23.8 ± 3.4
Mean HR (bpm)	81.5 ± 13.7
RR (Hz)	0.32 ± 0.08
Smoking	
No	60 (76.9%)
Yes	18 (23.1%)
KPS	
≤70	15 (19.2%)
>70	63 (80.8%)
Pathological types	
Squamous cell carcinoma	18 (23.1%)
Adenocarcinoma	56 (71.8%)
Others	4 (5.1%)
Radiotherapy	
Without	23 (29.5%)
With	55 (70.5%)
Chemotherapy	
Without	16 (20.5%)
With	62 (79.5%)
Targeted therapy	
Without	34 (43.6%)
With	44 (56.4%)
Surgery	
Without	62 (79.5%)
With	16 (20.5%)
TNM stage	
IIIA	10 (12.8%)
IIIB	8 (10.3%)
IIIC	4 (5.1%)
IVA	34 (43.6%)
IVB	22 (28.2%)
SDNN (ms)	18.9 [11.6, 25.2]
RMSSD (ms)	10.2 [5.8, 16.1]
TP (ms^2)	204 [112, 467]
LF (ms^2)	37 [19, 82]
HF (ms^2)	33 [8, 70]
LF/HF	1.360 [0.554, 3.645]
ApEn	1.101 [1.022, 1.171]
SampEn	1.339 ± 0.376
Lmean (beats)	15.93 [12.66, 23.58]
Lmax (beats)	325.0 [192.3, 401.0]
REC (%)	43.83 [34.05, 48.63]
DET (%)	99.24 [98.14, 99.56]
ShanEn	3.578 ± 0.461

Values are expressed as the number of patients (percentage) or mean ± SD or median [Q1, Q3].
BMI, body mass index; Mean HR, mean heart rate; bpm, beats per minute; RR, respiration rate; KPS, Karnofsky performance status; TNM, tumor-node-metastasis; SDNN, standard deviation of all normal-to-normal intervals; RMSSD, root mean square of successive differences; TP, total power; LF, low-frequency power; HF, high-frequency power; LF/HF, ratio of low-frequency power to high-frequency power; ApEn, approximate entropy; SampEn, sample entropy; Lmean, mean diagonal line length; Lmax, maximal diagonal line length; REC, recurrence rate; DET, determinism; ShanEn, Shannon entropy; SD, standard deviation; Q1, first quartile; and Q3, third quartile.

TABLE 2 Univariate Cox regression analysis of clinical characteristics and survival in non-small cell lung cancer patients.

	Univariate analysis	
	Hazard ratio (95% CI)	*p* value
Sex		0.238
Female	0.665 (0.338, 1.309)	
Male	Ref	
Age (year)	0.990 (0.959, 1.021)	0.509
BMI (kg/m^2)	0.939 (0.860, 1.027)	0.168
Mean HR (bpm)	1.003 (0.982, 1.025)	0.782
RR (Hz)	16.451 (0.318, 851.677)	0.164
Smoking		0.833
No	1.078 (0.535, 2.171)	
Yes	Ref	
KPS		**0.007**
≤ 70	2.430 (1.275, 4.631)	
> 70	Ref	
Pathological types		0.752
Squamous cell carcinoma	1.753 (0.388, 7.917)	
Adenocarcinoma	1.510 (0.363, 6.291)	
Others	Ref	
Radiotherapy		0.157
Without	0.622 (0.322, 1.201)	
With	Ref	
Chemotherapy		0.460
Without	1.291 (0.656, 2.537)	
With	Ref	
Targeted therapy		0.134
Without	0.629 (0.343, 1.154)	
With	Ref	
Surgery		**0.010**
Without	3.861 (1.383, 10.778)	
With	Ref	
TNM Stage		0.074
IIIA	0.404 (0.150, 1.087)	
IIIB	0.453 (0.153, 1.340)	
IIIC	0.654 (0.193, 2.216)	
IVA	0.399 (0.204, 0.781)	
IVB	Ref	

Bold *p* values indicate statistical significance (*p* value < 0.05).
CI, confidence interval; BMI, body mass index; Mean HR, mean heart rate; bpm, beats per minute; RR, respiration rate; KPS, Karnofsky performance status; and TNM, tumor-node-metastasis.

23.6 months, $p = 0.039$; REC: 17.3 vs. 23.9 months, $p = 0.048$; and DET: 17.2 vs. 24.1 months, $p = 0.041$; Table 3; Figure 1).

In multivariate analysis, the frequency domain parameter HF and RQA indexes REC and DET were still shown to be important prognostic factors for the overall survival of patients with advanced NSCLC (HF: $p = 0.040$, hazard ratio = 2.108, 95% CI: 1.035–4.291; REC: $p = 0.025$, hazard ratio = 0.415, 95% CI: 0.192–0.896; DET: $p = 0.033$, hazard ratio = 0.432, 95% CI: 0.200–0.935). There was no significant correlation between Lmax and the overall survival of advanced NSCLC patients ($p = 0.056$, hazard ratio = 0.490, 95% CI: 0.236–1.017; Table 3).

Discussion

This study verified the correlation between heartbeat complexity and overall survival in patients with advanced NSCLC. Our study

TABLE 3 Univariate and multivariate analyses of HRV variables as predictors of survival.

	Median survival (M)	Univariate analysis		Multivariate analysis	
		Hazard ratio (95% CI)	*p* value	Hazard ratio (95% CI)	*p* value
SDNN (ms)					
≤ 23.5	13.6	1.412 (0.718, 2.775)	0.317	1.343 (0.680, 2.654)	0.396
> 23.5	16.2	Ref		Ref	
RMSSD (ms)					
≤ 8.9	11.3	1.413 (0.797, 2.506)	0.237	1.664 (0.911, 3.041)	0.098
> 8.9	16.2	Ref		Ref	
TP (ms^2)					
≤ 67	13.3	1.502 (0.672, 3.360)	0.321	1.121 (0.485, 2.587)	0.790
> 67	14.3	Ref		Ref	
LF (ms^2)					
≤ 31	11.1	1.563 (0.880, 2.775)	0.127	1.495 (0.841, 2.657)	0.170
> 31	16.2	Ref		Ref	
HF (ms^2)					
≤ 5	7.1	2.382 (1.174, 4.830)	**0.016**	2.108 (1.035, 4.291)	**0.040**
> 5	15.0	Ref		Ref	
LF/HF					
≤ 4.950	14.7	0.553 (0.266, 1.146)	0.111	0.525 (0.252, 1.094)	0.085
> 4.950	9.6	Ref		Ref	
ApEn					
≤ 1.140	14.7	0.703 (0.394, 1.254)	0.232	0.711 (0.396, 1.278)	0.254
> 1.140	11.3	Ref		Ref	
SampEn					
≤ 1.620	17.7	2.114 (0.896, 4.989)	0.087	1.784 (0.750, 4.247)	0.191
> 1.620	24.1	Ref		Ref	
Lmean (beats)					
≤ 10.74	18.2	0.528 (0.236, 1.180)	0.120	0.571 (0.252, 1.294)	0.180
> 10.74	13.3	Ref		Ref	
Lmax (beats)					
≤ 195.0	23.6	0.464 (0.224, 0.961)	**0.039**	0.490 (0.236, 1.017)	0.056
> 195.0	17.1	Ref		Ref	
REC (%)					
≤ 33.30	23.9	0.463 (0.216, 0.993)	**0.048**	0.415 (0.192, 0.896)	**0.025**
> 33.30	17.3	Ref		Ref	
DET (%)					
≤ 97.93	24.1	0.450 (0.210, 0.967)	**0.041**	0.432 (0.200, 0.935)	**0.033**
> 97.93	17.2	Ref		Ref	
ShanEn					
≤ 3.121	18.2	0.528 (0.236, 1.180)	0.120	0.571 (0.252, 1.294)	0.180
> 3.121	13.3	Ref		Ref	

Bold *p* values indicate statistical significance (p value < 0.05).

CI, confidence interval; SDNN, standard deviation of all normal-to-normal intervals; RMSSD, root mean square of successive differences; TP, total power; LF, low-frequency power; HF, high-frequency power; LF/HF, ratio of low-frequency power to high-frequency power; ApEn, approximate entropy; SampEn, sample entropy; Lmean, mean diagonal line length; Lmax, maximal diagonal line length; REC, recurrence rate; DET, determinism; and ShanEn, Shannon entropy.

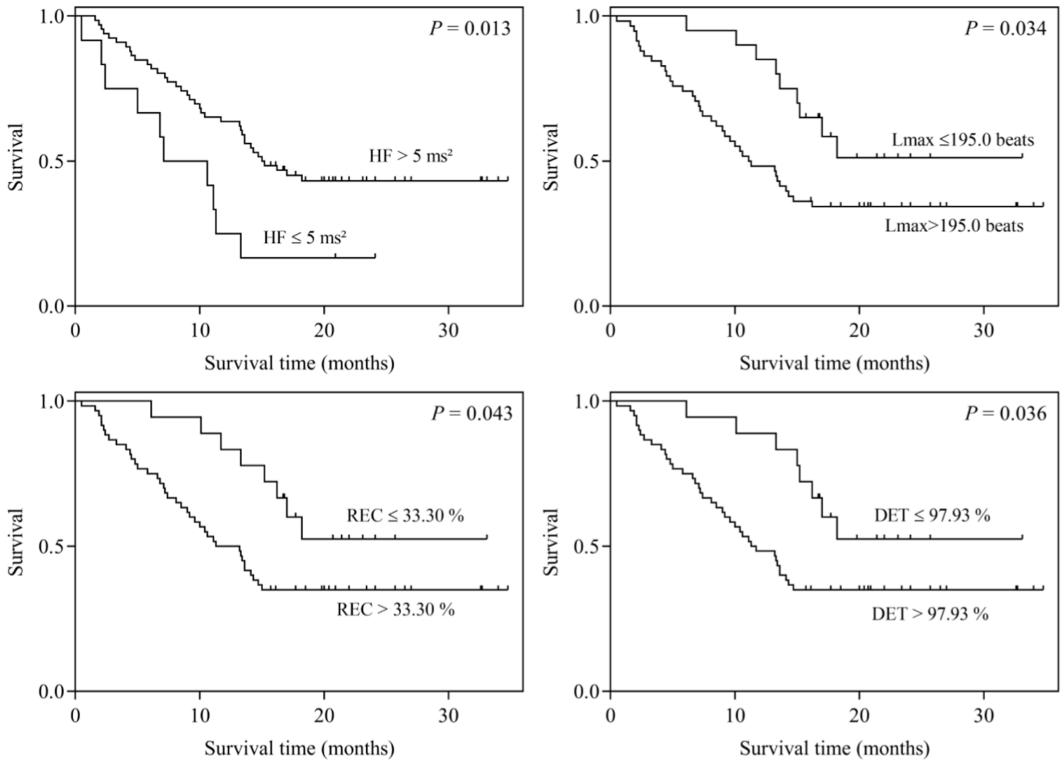

FIGURE 1
Kaplan–Meier survival curves for patients stratified by HF, Lmax, REC, and DET.

showed that the frequency domain parameter HF and RQA indexes Lmax, REC, and DET were significantly correlated with the overall survival of advanced NSCLC patients. In multivariate analysis, the frequency domain parameters HF and RQA indexes REC and DET were independently correlated with the overall survival of advanced NSCLC patients after adjusting for confounders.

The autonomic nervous system includes the sympathetic nervous system and the parasympathetic nervous system, which can antagonize or cooperate to maintain the normal physiological activities of the body (Schwartz and De Ferrari, 2011). The sympathetic nerve can regulate the pathological process of tumor growth (Coelho et al., 2017) and metastasis (Sloan et al., 2010), and the vagus nerve can affect tumor progression through systemic anti-inflammatory pathways (Hajiasgharzadeh et al., 2019) and the inhibition of sympathetic activity (Saku et al., 2014). At present, there are a variety of detection techniques to reflect autonomic function, among which HRV is a non-invasive and easily accessible detection method that has been used in clinical settings. It provides effective help for understanding the relationship between autonomic function and prognostic information in patients with malignant tumors (De Couck et al., 2018; Kloter et al., 2018). Previous studies revealed that there is a significant positive correlation between higher vagal activity and better prognosis in NSCLC patients (De Couck et al., 2013; Gidron et al., 2018). For example, Gidron et al. (2018) confirmed the relationship between neuroimmunomodulation (i.e., the ratio of RMSSD to CRP) and the NSCLC survival rate. The results showed that compared with those in the lower neuroimmunomodulation group, the NSCLC patients in the higher neuroimmunomodulation group had a better prognosis (475.2 vs. 285.1 days, $p < 0.05$). Therefore, Gidron et al. (2018) proposed that vagal regulation of inflammation may be a new biomarker for the prognosis of patients with NSCLC.

Time domain analysis is the simplest and easiest method to study HRV and can provide relatively clear physiological information, which is easily accepted by clinicians. The published literature suggests that SDNN and RMSSD are significantly associated with the overall survival of patients with advanced malignant tumors (Wang Y. M. et al., 2013; De Couck et al., 2016; Wu et al., 2022). For example, Wang Y. M. et al. (2013) showed that SDNN is an independent prognostic factor for the overall survival of patients with brain metastasis. De Couck et al. (2016) found that SDNN can significantly predict the overall survival in patients with advanced pancreatic cancer. In addition, our previous study showed that there is an independent association between RMSSD and overall survival in LC patients with brain metastasis (Wu et al., 2022). Although most previous studies showed that vagal activity based on linear HRV has a prognostic effect on cancer patients, a few studies found that the change in linear HRV is not an appropriate marker for predicting overall survival in advanced NSCLC patients. For instance, Kim et al. (2015) found that although there was a significant difference in the median survival between advanced NSCLC patients with SDNN ≥ 20.0 ms and those with SDNN < 20.0 ms (213 vs. 155 days, $p = 0.029$), SDNN was not an independent prognostic factor for overall survival in patients with advanced NSCLC. Similar to the study of Kim et al. (2015), our study found that compared with advanced NSCLC patients in the low-value SDNN or RMSSD group, patients in the high-value SDNN or RMSSD group had a better prognosis

(SDNN: 13.6 vs. 16.2 months; RMSSD: 11.3 vs. 16.2 months). However, SDNN and RMSSD were not independent prognostic factors for the overall survival of advanced NSCLC patients. This may be because the 22 patients with stage III NSCLC in this study received more active antitumor therapy (such as radiotherapy or surgery). While antitumor therapy successfully reduces the tumor load, it may mask the effect of autonomic function on patient prognosis to some extent, which might weaken the evaluation effect of the autonomic nervous system (investigated by linear HRV parameters; De Couck et al., 2018). Some studies have been conducted to preliminarily investigate the short-term effect of different antitumor treatments on linear HRV parameters (Hoca et al., 2012; Hansen et al., 2013; Stachowiak et al., 2018). It is not clear whether these treatments have short-term or long-term effects on nonlinear HRV parameters.

Frequency domain analysis is not only easy to implement but also a relatively accurate method to measure the regulatory state of the autonomic nervous system. Previous studies have indicated that the higher frequency domain parameter HF in patients with recurrent or metastatic breast cancer is closely related to their longer overall survival (Giese-Davis et al., 2015). Chiang et al. (2013) showed that there was a significant correlation between the frequency domain parameter HF of cancer patients without lung cancer and their 7-day survival rate. In addition, another study by Chiang et al. (2010) found that HF was significantly associated with prognosis in patients with advanced hepatocellular carcinoma. Similar to their results, the univariate analysis in our study revealed that there was a significant correlation between HF and the overall survival of advanced NSCLC patients ($p = 0.016$). In multivariate analysis, the correlation between overall survival and HF in patients with advanced NSCLC remained significant ($p = 0.040$, hazard ratio = 2.108, 95% CI: 1.035–4.291). HF reflects vagal activity (Vanderlei et al., 2009; Lombardi and Stein, 2011), indicating that vagal tone has a certain predictive value in the overall survival of patients with advanced NSCLC.

It is worth noting that most of the published studies use classical linear indexes (time domain or frequency domain) based on HRV analysis, reflecting the regulation of heart rate by sympathetic and parasympathetic nerves (De Couck et al., 2018; Kloter et al., 2018). Previous studies have also preliminarily explored the relationship between several nonlinear HRV parameters and the prognostic information of patients with malignant tumors (Bettermann et al., 2001; Shi et al., 2019; Escutia-Reyes et al., 2021; Wu et al., 2021). For example, Shi et al. (2019) found that the increase in irregularity and the decrease in complexity of heartbeat time series are significantly correlated with higher carcinoembryonic antigen levels in patients with gastric cancer. Bettermann et al. (2001) showed that compared with breast cancer patients without metastasis, the heartbeat complexity (reflected by ApEn) of breast cancer patients with metastasis was clearly lower. Escutia-Reyes et al. (2021) showed that nonlinear HRV parameters, such as the SampEn, were significantly different between a breast cancer survivor group and a cancer-free female control group. In our previous study exploring the correlation between short-term HRV and TNM staging in patients with breast cancer, the results showed that the nonlinear HRV parameters ApEn and SampEn, which characterize heartbeat complexity, were not significantly different between tumor stages (Wu et al., 2021). In this study, there was no significant correlation between ApEn or SampEn and the overall survival of advanced NSCLC patients ($p > 0.05$). Therefore, we strongly recommend that more background variables, such as type of cancer or severity of disease, and more entropy analysis parameters, such as distribution entropy, fuzzy entropy, permutation entropy, or multiscale entropy, can be included in future research to obtain more valuable prognostic information.

Because the RQA can be applied to short, nonstationary and high-noise signal sequences of the R-R interval, where there is not a strict requirement for the length of data, it has been used in many studies on heart rate dynamics (Mohebbi and Ghassemian, 2011; Acharya et al., 2014; Li et al., 2022). For example, Acharya et al. (2014) showed that Lmean, Lmax, REC, and DET in patients with coronary artery disease are significantly higher than those in healthy populations. Mohebbi and Ghassemian (2011) showed that compared with the ECG signals that are distant from paroxysmal atrial fibrillation, RQA indexes, such as Lmean, Lmax, REC, and ShanEn with the ECG signals that are before paroxysmal atrial fibrillation were significantly higher. Li et al. (2022) showed that higher Lmax is significantly associated with shorter overall survival in LC patients with brain metastasis. Similar to the above studies, our results showed that the RQA indexes REC and DET are independent prognostic factors for the overall survival of advanced NSCLC patients ($p < 0.05$), indicating that the increase in REC and DET, that is, the decrease in heartbeat complexity, is an independent risk factor for poor prognosis in patients with advanced NSCLC. In addition, in our study, compared with the low-value Lmax group, advanced NSCLC patients in the high-value Lmax group had a poorer prognosis (17.1 vs. 23.6 months). However, Lmax only tended to be significantly correlated with overall survival after adjusting for confounders ($p = 0.056$, hazard ratio = 0.490, 95% CI: 0.236–1.017), which may be related to the relatively small sample size in this study. Therefore, the results of the current research still needs to be confirmed with a long-term follow-up prospective study with further expansion of the sample size. The results of this study may provide new evidence for the role of heartbeat complexity in the prognosis of cancer patients. However, exact physiopathological mechanisms of nonlinear HRV parameters have yet to be fully elucidated in the prognosis of cancer patients. Vagally mediated linear HRV indicators were correlated with levels of inflammatory markers (Williams et al., 2019). We suggest to compare correlations between linear and nonlinear HRV parameters with inflammation markers in future studies, and this may provide some hints as to the better prognostic value of nonlinear HRV indicators in cancer patients.

Limitations

One major limitation of our study is the heterogeneity of antitumor therapy modalities. All patients with stage III or IV NSCLC were enrolled in this study, and they received different antitumor treatments (such as radiotherapy or surgery). It is not clear whether these treatments have short-term or long-term effects on heartbeat complexity. Second, our sample size was too small to allow sufficiently powered statistical analysis to be performed. With a small sample size, the performance of too many statistical tests without any correction of the *p*-level maybe causes risking a type-1 error. Could it be that other issues may have led to more prognostic power seen in the nonlinear HRV parameters such as type of cancer or severity of disease, etc. factors that may affect more the linear HRV parameters and possibly less the nonlinear HRV parameters? More studies are needed to prove this speculation. Therefore, we strongly recommend

expanding the sample size to conduct additional research on these differences.

Conclusion

This study reveals that the RQA parameters REC and DET, which characterize heartbeat complexity, are independently related to the overall survival of patients with advanced NSCLC. This finding indicates that heartbeat complexity based on RQA may be used as a new prognostic indicator for advanced NSCLC patients and may complement the traditional time domain and frequency domain indicators.

Data availability statement

The raw data supporting the conclusions of this article will be made available by the authors, without undue reservation.

Ethics statement

The studies involving human participants were reviewed and approved by the Medical Ethics Committee of the First Affiliated Hospital of Bengbu Medical College. The patients/participants provided their written informed consent to participate in this study.

Author contributions

BS: conceptualization, methodology, resources, and writing–review and editing. XZ and YZ: supervision and resources. SW: data collection, data analysis, and writing-original draft preparation. GL: data analysis and writing-original draft preparation. MC: data collection and writing-original draft preparation. SZ: writing-original draft preparation. All authors contributed to the article and approved the submitted version.

Funding

This research was funded by the "512" Outstanding Talents Fostering Project of Bengbu Medical College (grant number BY51201312), the Natural Science Research Project of Bengbu Medical College (grant number 2020byzd013), and the Scientific Research Innovation Project of Bengbu Medical College (grant number BYKC201905).

Conflict of interest

An immediate family member of BS owns stock in HeaLink Ltd., Bengbu, China.

The remaining authors declare that the research was conducted in the absence of any commercial or financial relationships that could be construed as a potential conflict of interest.

Publisher's note

References

Acharya, U. R., Faust, O., Sree, V., Swapna, G., Martis, R. J., Kadri, N. A., et al. (2014). Linear and nonlinear analysis of normal and CAD-affected heart rate signals. *Comput. Methods Prog. Biomed.* 113, 55–68. doi: 10.1016/j.cmpb.2013.08.017

Balkwill, F. (2009). Tumor necrosis factor and cancer. *Nat. Rev. Cancer* 9, 361–371. doi: 10.1038/nrc2628

Bettermann, H., Kröz, M., Girke, M., and Heckmann, C. (2001). Heart rate dynamics and cardiorespiratory coordination in diabetic and breast cancer patients. *Clin. Physiol.* 21, 411–420. doi: 10.1046/j.1365-2281.2001.00342.x

Burioka, N., Miyata, M., Cornélissen, G., Halberg, F., Takeshima, T., Kaplan, D. T., et al. (2005). Approximate entropy in the electroencephalogram during wake and sleep. *Clin. EEG Neurosci.* 36, 21–24. doi: 10.1177/155005940503600106

Camm, A. J., Malik, M., Bigger, J. T., Breithardt, G., Cerutti, S., Cohen, R. J., et al. (1996). Heart rate variability: standards of measurement, physiological interpretation and clinical use. Task force of the European society of cardiology and the north American society of pacing and electrophysiology. *Circulation* 93, 1043–1065. doi: 10.1161/01.CIR.93.5.1043

Camp, R. L., Dolled-Filhart, M., and Rimm, D. L. (2004). X-tile: a new bio-informatics tool for biomarker assessment and outcome-based cut-point optimization. *Clin. Cancer Res.* 10, 7252–7259. doi: 10.1158/1078-0432

Chiang, J. K., Koo, M., Kuo, T. B. J., and Fu, C. H. (2010). Association between cardiovascular autonomic functions and time to death in patients with terminal hepatocellular carcinoma. *J. Pain Symptom Manag.* 39, 673–679. doi: 10.1016/j.jpainsymman.2009.09.014

Chiang, J. K., Kuo, T. B. J., Fu, C. H., and Koo, M. (2013). Predicting 7-day survival using heart rate variability in hospice patients with non-lung cancers. *PLoS One* 8:e69482. doi: 10.1371/journal.pone.0069482

Coelho, M., Soares-Silva, C., Brandão, D., Marino, F., Cosentino, M., and Ribeiro, L. (2017). β-Adrenergic modulation of cancer cell proliferation: available evidence and clinical perspectives. *J. Cancer Res. Clin. Oncol.* 143, 275–291. doi: 10.1007/s00432-016-2278-1

Dabiré, H., Mestivier, D., Jarnet, J., Safar, M. E., and Chau, N. P. (1998). Quantification of sympathetic and parasympathetic tones by nonlinear indexes in normotensive rats. *Am. J. Phys.* 275, H1290–H1297. doi: 10.1152/ajpheart.1998.275.4.H1290

De Couck, M., Caers, R., Spiegel, D., and Gidron, Y. (2018). The role of the Vagus nerve in cancer prognosis: a systematic and a comprehensive review. *J. Oncol.* 2018, 1236787–1236711. doi: 10.1155/2018/1236787

De Couck, M., Maréchal, R., Moorthamers, S., Van Laethem, J. L., and Gidron, Y. (2016). Vagal nerve activity predicts overall survival in metastatic pancreatic cancer, mediated by inflammation. *Cancer Epidemiol.* 40, 47–51. doi: 10.1016/j.canep.2015.11.007

de Couck, M. A. R. I. J. K. E., van Brummelen, D., Schallier, D., de Grève, J. A. C. Q. U. E. S., and Gidron, Y. (2013). The relationship between vagal nerve activity and clinical outcomes in prostate and non-small cell lung cancer patients. *Oncol. Rep.* 30, 2435–2441. doi: 10.3892/or.2013.2725

de Godoy, M. F. (2016). Nonlinear analysis of heart rate variability: a comprehensive review. *J. Cardiol. Ther.* 3, 528–533. doi: 10.17554/j.issn.2309-6861.2016.03.101-4

Escutia-Reyes, D., de Jesús Garduño-García, J., Emilio-López-Chávez, G., Gómez-Villanueva, Á., Pliego-Carrillo, A. C., Soto-Piña, A. E., et al. (2021). Differences in heart rate variability and body composition in breast cancer survivors and women without cancer. *Sci. Rep.* 11:14460. doi: 10.1038/s41598-021-93713-8

Garg, J., Feng, Y. X., Jansen, S. R., Friedrich, J., Lezoualc'h, F., Schmidt, M., et al. (2017). Catecholamines facilitate VEGF-dependent angiogenesis via β2-adrenoceptor-induced Epac1 and PKA activation. *Oncotarget* 8, 44732–44748. doi: 10.18632/oncotarget.17267

Gidron, Y., De Couck, M., Schallier, D., De Greve, J., Van Laethem, J. L., and Maréchal, R. (2018). The relationship between a new biomarker of vagal

Neuroimmunomodulation and survival in two fatal cancers. *J Immunol Res* 2018, 1–5. doi: 10.1155/2018/4874193

Giese-Davis, J., Wilhelm, F. H., Tamagawa, R., Palesh, O., Neri, E., Taylor, C. B., et al. (2015). Higher vagal activity as related to survival in patients with advanced breast cancer: an analysis of autonomic dysregulation. *Psychosom. Med.* 77, 346–355. doi: 10.1097/PSY.0000000000000167

Ha, D., Malhotra, A., Ries, A. L., O'Neal, W. T., and Fuster, M. M. (2019). Heart rate variability and heart rate recovery in lung cancer survivors eligible for long-term cure. *Respir. Physiol. Neurobiol.* 269:103264. doi: 10.1016/j.resp.2019.103264

Hajiasgharzadeh, K., Sadigh-Eteghad, S., Mansoori, B., Mokhtarzadeh, A., Shanehbandi, D., Doustvandi, M. A., et al. (2019). Alpha7 nicotinic acetylcholine receptors in lung inflammation and carcinogenesis: friends or foes? *J. Cell. Physiol.* 234, 14666–14679. doi: 10.1002/jcp.28220

Hansen, M. V., Rosenberg, J., and Gögenur, I. (2013). Lack of circadian variation and reduction of heart rate variability in women with breast cancer undergoing lumpectomy: a descriptive study. *Breast Cancer Res. Treat.* 140, 317–322. doi: 10.1007/s10549-013-2631-x

Hart, P. C., Rajab, I. M., Alebraheem, M., and Potempa, L. A. (2020). C-reactive protein and cancer-diagnostic and therapeutic insights. *Front. Immunol.* 11:595835. doi: 10.3389/fimmu.2020.595835

Hoca, A., Yildiz, M., and Ozyigit, G. (2012). Evaluation of the effects of mediastinal radiation therapy on autonomic nervous system. *Med. Oncol.* 29, 3581–3586. doi: 10.1007/s12032-012-0237-5

Hu, S., Lou, J., Zhang, Y., and Chen, P. (2018). Low heart rate variability relates to the progression of gastric cancer. *World J. Surg. Oncol.* 16:49. doi: 10.1186/s12957-018-1348-z

Huan, H. B., Wen, X. D., Chen, X. J., Wu, L., Wu, L. L., Zhang, L., et al. (2017). Sympathetic nervous system promotes hepatocarcinogenesis by modulating inflammation through activation of alpha1-adrenergic receptors of Kupffer cells. *Brain Behav. Immun.* 59, 118–134. doi: 10.1016/j.bbi.2016.08.016

Kim, K., Chae, J., and Lee, S. (2015). The role of heart rate variability in advanced non-small-cell lung cancer patients. *J. Palliat. Care* 31, 103–108. doi: 10.1177/082585971503100206

Kloter, E., Barrueto, K., Klein, S. D., Scholkmann, F., and Wolf, U. (2018). Heart rate variability as a prognostic factor for cancer survival - a systematic review. *Front. Physiol.* 9:623. doi: 10.3389/fphys.2018.00623

Lee, G. M., Fattinger, S., Mouthon, A. L., Noirhomme, Q., and Huber, R. (2013). Electroencephalogram approximate entropy influenced by both age and sleep. *Front. Neuroinform.* 7:33. doi: 10.3389/fninf.2013.00033

Li, G., Wu, S., Zhao, H., Guan, W., Zhou, Y., and Shi, B. (2022). Non-invasive prognostic biomarker of lung cancer patients with brain metastases: recurrence quantification analysis of heart rate variability. *Front. Physiol.* 13:987835. doi: 10.3389/fphys.2022.987835

Lombardi, F., and Stein, P. K. (2011). Origin of heart rate variability and turbulence: an appraisal of autonomic modulation of cardiovascular function. *Front. Physiol.* 2:95. doi: 10.3389/fphys.2011.00095

Marwan, N., Carmenromano, M., Thiel, M., and Kurths, J. (2007). Recurrence plots for the analysis of complex systems. *Phys. Rep.* 438, 237–329. doi: 10.1016/j.physrep.2006.11.001

Marwan, N., Wessel, N., Meyerfeldt, U., Schirdewan, A., and Kurths, J. (2002). Recurrence-plot-based measures of complexity and their application to heart-ratevariability data. *Phys. Rev. E Stat. Nonlinear Soft Matter Phys.* 66:026702. doi: 10.1103/PhysRevE.66.026702

Mohebbi, M., and Ghassemian, H. (2011). Prediction of paroxysmal atrial fibrillation using recurrence plot-based features of the RR-interval signal. *Physiol. Meas.* 32, 1147–1162. doi: 10.1088/0967-3334/32/8/010

Mohseni, M., Redies, C., and Gast, V. (2022). Approximate entropy in canonical and non-canonical fiction. *Entropy* 24:278. doi: 10.3390/e24020278

Moody, G., Mark, R., Zoccola, A., and Mantero, S. (1985). Derivation of respiratory signals from multi-lead ECGs. *Comput. Cardiol.* 12, 113–116.

Mouton, C., Ronson, A., Razavi, D., Delhaye, F., Kupper, N., Paesmans, M., et al. (2012). The relationship between heart rate variability and time-course of carcinoembryonic antigen in colorectal cancer. *Auton. Neurosci.* 166, 96–99. doi: 10.1016/j.autneu.2011.10.002

Niskanen, J. P., Tarvainen, M. P., Ranta-Aho, P. O., and Karjalainen, P. A. (2004). Software for advanced HRV analysis. *Comput. Methods Prog. Biomed.* 76, 73–81. doi: 10.1016/j.cmpb.2004.03.004

Pan, J., and Tompkins, W. J. (1985). A real-time QRS detection algorithm. *IEEE Trans. Biomed. Eng.* 32, 230–236. doi: 10.1109/TBME.1985.325532

Peng, Y., and Sun, Z. (2011). Characterization of QT and RR interval series during acute myocardial ischemia by means of recurrence quantification analysis. *Med. Biol. Eng. Comput.* 49, 25–31. doi: 10.1007/s11517-010-0671-5

Saku, K., Kishi, T., Sakamoto, K., Hosokawa, K., Sakamoto, T., Murayama, Y., et al. (2014). Afferent vagal nerve stimulation resets baroreflex neural arc and inhibits sympathetic nerve activity. *Phys. Rep.* 2:e12136. doi: 10.14814/phy2.12136

Schwartz, P. J., and De Ferrari, G. M. (2011). Sympathetic-parasympathetic interaction in health and disease: abnormalities and relevance in heart failure. *Heart Fail. Rev.* 16, 101–107. doi: 10.1007/s10741-010-9179-1

Shi, B., Wang, L., Yan, C., Chen, D., Liu, M., and Li, P. (2019). Nonlinear heart rate variability biomarkers for gastric cancer severity: a pilot study. *Sci. Rep.* 9:13833. doi: 10.1038/s41598-019-50358-y

Sloan, E. K., Priceman, S. J., Cox, B. F., Yu, S., Pimentel, M. A., Tangkanangnukul, V., et al. (2010). The sympathetic nervous system induces a metastatic switch in primary breast cancer. *Cancer Res.* 70, 7042–7052. doi: 10.1158/0008-5472.CAN-10-0522

Stachowiak, P., Milchert-Leszczyńska, M., Falco, M., Wojtarowicz, A., Kaliszczak, R., Safranow, K., et al. (2018). Heart rate variability during and after chemotherapy with anthracycline in patients with breast cancer. *Kardiol. Pol.* 76, 914–916. doi: 10.5603/KP.2018.0098

Sun, R., and Wang, Y. (2008). Predicting termination of atrial fibrillation based on the structure and quantification of the recurrence plot. *Med. Eng. Phys.* 30, 1105–1111. doi: 10.1016/j.medengphy.2008.01.008

Sung, H., Ferlay, J., Siegel, R. L., Laversanne, M., Soerjomataram, I., Jemal, A., et al. (2021). Global cancer statistics 2020: GLOBOCAN estimates of incidence and mortality worldwide for 36 cancers in 185 countries. *CA Cancer J. Clin.* 71, 209–249. doi: 10.3322/caac.21660

Taniguchi, K., and Karin, M. (2014). IL-6 and related cytokines as the critical lynchpins between inflammation and cancer. *Semin. Immunol.* 26, 54–74. doi: 10.1016/j.smim.2014.01.001

Tracey, K. J. (2009). Reflex control of immunity. *Nat. Rev. Immunol.* 9, 418–428. doi: 10.1038/nri2566

Vaillancourt, D. E., and Newell, K. M. (2002). Changing complexity in human behavior and physiology through aging and disease. *Neurobiol. Aging* 23, 1–11. doi: 10.1016/s0197-4580(01)00247-0

Vanderlei, L. C., Pastre, C. M., Hoshi, R. A., Carvalho, T. D., and Godoy, M. F. (2009). Basic notions of heart rate variability and its clinical applicability. *Rev. Bras. Cir. Cardiovasc.* 24, 205–217. doi: 10.1590/s0102-76382009000200018

Voss, A., Schulz, S., Schroeder, R., Baumert, M., and Caminal, P. (2009). Methods derived from nonlinear dynamics for analysing heart rate variability. *Philos. Trans. A. Math. Phys. Eng. Sci.* 367, 277–296. doi: 10.1098/rsta.2008.0232

Wang, Y. M., Cheng, J. Y., Wang, C. J., Hseu, S. S., and Huang, E. Y. (2021). Outcomes and prognosis of non-elderly patients with brain metastases-a prospective cohort incorporating individualized assessment of heart rate variability. *J. Pers. Med.* 11:1049. doi: 10.3390/jpm11111049

Wang, H. M., Liao, Z. X., Komaki, R., Welsh, J. W., O'Reilly, M. S., Chang, J. Y., et al. (2013). Improved survival outcomes with the incidental use of beta-blockers among patients with non-small-cell lung cancer treated with definitive radiation therapy. *Ann. Oncol.* 24, 1312–1319. doi: 10.1093/annonc/mds616

Wang, Y. M., Wu, H. T., Huang, E. Y., Kou, Y. R., and Hseu, S. S. (2013). Heart rate variability is associated with survival in patients with brain metastasis: a preliminary report. *Biomed. Res. Int.* 2013:503421. doi: 10.1155/2013/503421

Webber, C. L. Jr., and Zbilut, J. P. (1994). Dynamical assessment of physiological systems and states using recurrence plot strategies. *J. Appl. Physiol.* 1985, 965–973. doi: 10.1152/jappl.1994.76.2.965

Williams, D. P., Koenig, J., Carnevali, L., Sgoifo, A., Jarczok, M. N., Sternberg, E. M., et al. (2019). Heart rate variability and inflammation: a meta-analysis of human studies. *Brain Behav. Immun.* 80, 219–226. doi: 10.1016/j.bbi.2019.03.009

Wu, S., Chen, M., Wang, J., Shi, B., and Zhou, Y. (2021). Association of Short-Term Heart Rate Variability with Breast Tumor Stage. *Front. Physiol.* 12:678428. doi: 10.3389/fphys.2021.678428

Wu, S., Li, G., Guan, W., Zhao, H., Wang, J., Zhou, Y., et al. (2022). Low heart rate variability predicts poor overall survival of lung cancer patients with brain metastases. *Front. Neurosci.* 16:839874. doi: 10.3389/fnins.2022.839874

Yentes, J. M., Hunt, N., Schmid, K. K., Kaipust, J. P., McGrath, D., and Stergiou, N. (2013). The appropriate use of approximate entropy and sample entropy with short data sets. *Ann. Biomed. Eng.* 41, 349–365. doi: 10.1007/s10439-012-0668-3

Zheng, M. (2016). Classification and pathology of lung cancer. *Surg. Oncol. Clin. N. Am.* 25, 447–468. doi: 10.1016/j.soc.2016.02.003

Zimatore, G., Garilli, G., Poscolieri, M., Rafanelli, C., Terenzio Gizzi, F., and Lazzari, M. (2017). The remarkable coherence between two Italian far away recording stations points to a role of acoustic emissions from crustal rocks for earthquake analysis. *Chaos* 27:043101. doi: 10.1063/1.4979351

frontiers | Frontiers in Neuroscience

TYPE Original Research
PUBLISHED 15 May 2023
DOI 10.3389/fnins.2023.1196750

OPEN ACCESS

EDITED BY
Lei Zhang,
Nanjing Normal University, China

REVIEWED BY
Qun Wei,
Keimyung University, Republic of Korea
Baoxian Yu,
South China Normal University, China

*CORRESPONDENCE
Chengyu Liu
✉ chengyu@seu.edu.cn
Jianqing Li
✉ ljq@seu.edu.cn

†These authors have contributed equally to this work and share first authorship

RECEIVED 30 March 2023
ACCEPTED 24 April 2023
PUBLISHED 15 May 2023

CITATION
Li J, Xing Y, Zhang Y, Cui C, Wang J, Li J and Liu C (2023) Evaluation of autonomic nervous system activity in intradialytic hypotension using entropy and skin sympathetic nerve activity.
Front. Neurosci. 17:1196750.
doi: 10.3389/fnins.2023.1196750

Evaluation of autonomic nervous system activity in intradialytic hypotension using entropy and skin sympathetic nerve activity

Jiayi Li[1†], Yantao Xing[1†], Yike Zhang[2], Chang Cui[2], Jing Wang[3], Jianqing Li[1*] and Chengyu Liu[1*]

[1]State Key Laboratory of Digital Medical Engineering, School of Instrument Science and Engineering, Southeast University, Nanjing, China, [2]Division of Cardiology, The First Affiliated Hospital of Nanjing Medical University, Nanjing, China, [3]Division of Nephrology, The First Affiliated Hospital of Nanjing Medical University, Nanjing, China

Introduction: The function of the autonomic nervous system (ANS) is crucial in the development of intradialytic hypotension (IDH). This study introduced the entropy of heart rate variability (HRV) and skin sympathetic nerve activity (SKNA) to provide a complementary nonlinear and dynamic perspective for evaluating ANS function concerning IDH.

Methods: 93 patients undergoing hemodialysis (HD) were enrolled, and the baseline data, electrocardiogram (ECG), and SKNA were collected. The patients were separated into the IDH and nonIDH groups based on the thresholds, which were characterized as reductions in systolic blood pressure (SBP) of at least 20 mm Hg or mean arterial pressure (MAP) of at least 10 mm Hg. We developed a logistic regression model for IDH after analyzing the changes in the time domain, frequency domain, the entropy of HRV, and SKNA indices during HD.

Results: After 4-h HD, the detected results for heart rate, the ratio of low frequency and high frequency (LF/HF), and average SKNA (aSKNA) all increased in both groups. Nine out of the ten HRV indices and aSKNA in the nonIDH group were higher than those in the IDH group at most moments. aSKNA was positively correlated with heart rate (p=0.0001) and LF/HF (p=0.0005) in the nonIDH group, while the correlation disappeared in the IDH group, which indicated a worse ANS response in IDH patients. The logistic regression model exhibited the results of initial SBP [odds ratio (OR) 1.076; p=0.001], and the difference between the last and first segments (DLF) of heart rate [OR 1.101; p=0.012] and LF/HF [OR 0.209; p=0.034], as well as the extreme value of the difference between other segments and the first segments (EOF) of aSKNA [OR 2.908; p=0.017], which were independent indicators for IDH.

Discussion: The new nonlinear and dynamic assessment perspectives provided by the entropy of HRV and SKNA help to distinguish differences in ANS patterns between IDH patients and nonIDH patients and have the potential to be used in clinical monitoring for HD patients.

KEYWORDS

ECG, skin sympathetic nerve activity, entropy, intradialytic hypotension, heart rate variability, autonomic nervous system, hemodialysis

1. Introduction

Intradialytic hypotension (IDH), as one of the main complications during hemodialysis (HD), is related to several adverse prognostic events, including inadequate dialysis dose (Ronco et al., 2000), end-organ ischemia (MacEwen et al., 2017; Seong et al., 2018), increased cardiovascular events (Stefánsson et al., 2014) and mortality (Shoji et al., 2004). It is crucial to have a throughout understanding of the physiological mechanism of IDH to effectively prevent and treat the condition.

During HD, as intravascular volume decreases, compensatory mechanisms are activated to counter the tendency to fall in blood pressure (BP) by increasing the plasma refill, cardiac output, and peripheral vascular resistance (Chou et al., 2017). IDH is the consequence of ultrafiltration exceeding plasma replacement (Davenport, 2022). The autonomic nervous system (ANS), comprising the sympathetic and parasympathetic nervous systems, is essential to this process. The sympathetic nervous activity (SNA), vascular resistance, and heart rate are found to increase in patients without IDH during HD, while decreasing during IDH episodes in IDH-prone patients, which indicates that insufficient sympathetic response contributes to IDH (Converse et al., 1992). Therefore, the accurate assessment of ANS patterns contributes to an in-depth understanding of IDH.

Heart rate variability (HRV) is a useful and noninvasive method for evaluating ANS function, which represents the changes in continuous heartbeats (Heart rate variability, 1996). Time and frequency domain analysis of HRV is widely utilized to assess IDH in patients with HD (Pelosi et al., 1999; Chang et al., 2016; Park et al., 2019). Nevertheless, the heart is a nonlinear dynamic system, and these linear statistical measures may mask the abnormal nonlinear information on heart rhythm (Denton et al., 1990). Entropy is used to evaluate the regularity between time intervals, where increased regularity tends to indicate a defect in the regulatory system (Mayer et al., 2014). Therefore, we introduced entropy methods to describe the relationship between regularity changes in heartbeats and ANS regulation.

Skin sympathetic nerve activity (SKNA) is a recent and high-frequency method for the noninvasive detection of SNA, which is proved to be well correlated with stellate ganglion activity and valid in related studies of diseases with abnormal SNA (Jiang et al., 2015; Doytchinova et al., 2017; He et al., 2020; Kusayama et al., 2020a). The cardiac sympathetic nerve alternates at the stellate ganglion, and its postganglionic fibers control cardiac activity. Thus stellate ganglion activity is indicative of sympathetic activity. SKNA provides a new perspective for evaluating SNA with the second-by-second temporal resolution. It can be applied to sinus node dysfunction scenarios, which are unavailable with HRV (Kusayama et al., 2020b). In an anesthesia injection study, SKNA was found to be superior to HRV in describing the inhibition of SNA (Xing et al., 2022). SKNA can be used as a more intuitive way to describe SNA, which complements the HRV's description of the ANS function.

To research the influence of the ANS on IDH, especially the SNA, we recruited patients to compare the ANS patterns between those who experienced IDH and those who did not during HD. A wearable device was applied to conveniently and noninvasively acquire physiological signals from HD patients. To the best of our knowledge, our study is the first to implement the methods for the entropy of HRV and SKNA to provide the nonlinear and dynamic perspective of the ANS function on IDH. Besides, we conducted correlations between SKNA and HRV indices to explore the mapping relationship. Moreover, the multivariate model was established by binary logistic regression based on baseline data, HRV, and SKNA indicators to determine the risk factors of IDH.

2. Methods

2.1. Participants

The study enrolled 93 patients who underwent maintenance HD at the First Affiliated Hospital of Nanjing Medical University between August and November 2020. All participants in this study were over the age of 18 and had been receiving HD treatment for at least 3 months, with each session lasting 4 h, three times a week. Patients who had a previous history of arrhythmia, cerebrovascular disease, heart valve disease, acute coronary syndrome, pacemaker installation, severe anemia, or severe infection were excluded. Written informed consent was obtained from all subjects before they participated in the study. To protect patients' privacy, all data were anonymized during the analysis procedure. The study was conducted after receiving approval from the Ethics Committee of the First Affiliated Hospital of Nanjing Medical University.

2.2. Baseline data

The baseline data were collected, including age, sex, body mass index, HD duration, ultrafiltration, the ratio of ultrafiltration and weight, systolic blood pressure (SBP) and diastolic blood pressure (DBP) before HD. The measurement of systolic blood pressure (SBP) and diastolic blood pressure (DBP) was conducted before HD, as the baseline, and every hour after the start of HD.

2.3. Blood pressure analysis

We used the four indicators of SBP, DBP, mean arterial pressure (MAP), and pulse pressure (PP) to comprehensively evaluate BP in HD. MAP was determined by adding 1/3 SBP and 2/3 DBP, while PP was determined as SBP minus DBP.

There is no widely accepted definition for the condition in previous studies on IDH. We defined IDH, referring to the K/DOQI Clinical Practice Guidelines (K/DOQI Clinical Practice Guidelines for Cardiovascular Disease in K/DOQI Workgroup, 2005), as a reduction in SBP of at least 20 mm Hg or a reduction in MAP of at least10 mm Hg. To be clear, we omitted the clinical symptoms in our study, compared to the definition in the guidelines. On one hand, it is possible that symptoms and treatments are unnecessarily linked to end-organ damage or hemodynamic instability, which could be deceptive (Assimon and Flythe, 2017). On the other hand, we intended to pay more attention to the changes in objective BP values to uncover the relevant physiological changes in patients with asymptomatic or latent IDH. The subjects with an SBP reduction of at least 20 mmHg or a MAP reduction of at least 10 mmHg were divided into the IDH group. Otherwise, they were divided into the nonIDH group.

2.4. Acquisition of ECG and SKNA

Our team developed a portable, noninvasive, and high-frequency electrophysiological signal acquisition device with a sampling

frequency of up to 16 kHZ, input noise as low as 0.1μV_{rms}, and size of 7 mm * 8 mm * 2 mm, which can simultaneously collect ECG and SKNA signals (Xing et al., 2022). Before this, SKNA had not been acquired by proprietary acquisition equipment. In comparison with the reference system, the acquired signal quality of the device was verified to be effective and reliable (Xing et al., 2020, 2022). In this study, we used this device to acquire physiological signals from HD patients. Subjects were required to remain in the supine position and avoid unnecessary movement during HD to improve signal quality, while ECG and SKNA signals were simultaneously measured by the devices for 4 h (Figure 1A). The sampling frequency was 4 kHz. Three wet electrodes were applied to the skin of each subject to monitor single lead signals.

2.5. Preprocessing of ECG and SKNA

ECG and SKNA signals were obtained through a 150 Hz low-pass filter and a 500 to 1,000 Hz band-pass filter, respectively (Figure 1B). We introduced the preprocessing processes of noise reduction (Pandit et al., 2017), R-peak detection (Wang et al., 2022), and signal quality assessment (Liu et al., 2019) to ensure the reliability of RR intervals. Furthermore, RR intervals that changed more than 20% from the previous interval or did not fall within the range of 0.375 s to 2 s were removed. Since SKNA signals were not rhythmic like ECG signals, the preprocessing of SKNA signals mainly considered the removal of outliers. The interquartile range and an absolute value threshold of 80 μV were used to identify outliers. All values that were not in the range of [Q1-1.5 * IQR, Q3 + 1.5 * IQR] were removed, where Q1 was the lower quantile and Q3 was the upper quantile. Values outside the absolute value threshold were eliminated. The average SKNA (aSKNA) index was determined by computing the mean of the rectified SKNA signals. ECG and SKNA signals were divided into 5 min and 30 min windows, respectively, with no overlap between windows.

2.6. HRV analysis

HRV analysis was performed from three perspectives: the time domain, frequency domain, and nonlinear analysis. The indices of the time domain analysis included the standard deviation of the RR intervals (SDNN), the square root of the mean squared differences of subsequent RR intervals (RMSSD), and the proportion obtained by dividing the number of interval differences of subsequent RR intervals greater than 50 ms by the overall number of the RR intervals (PNN50). The indices of the frequency domain analysis included low frequency (0.04 to 0.15 Hz, LF), high frequency (0.15 to 0.40 Hz, HF), the ratio of low frequency to high frequency (LF/HF), and the ratio of low frequency to the sum of low frequency and high frequency (LF/LF + HF). The nonlinear analysis mainly considered the complexity of RR intervals from the perspective of entropy. The indices of the nonlinear analysis included approximate entropy (ApEn) (Pincus, 1995), sample entropy (Richman and Moorman, 2000; Lake et al., 2002), and fuzzy measure entropy (FuzzyMEn) (Liu et al., 2013). The parameters of ApEn and SampEn were chosen as the dimension $m = 2$ and the tolerance $r = 0.2$. The parameters of FuzzyMEn were chosen as the dimension $m = 2$, the local threshold $r_l = 0.2$, the global threshold $r_g = 0.2$, the local weight of sequence segments' similarity $n_l = 3$, and the global weight of sequence segments' similarity $n_g = 2$.

2.7. Statistical analysis

All data statistics were performed based on SPSS and MATLAB. Shapiro–Wilk test and Kolmogorov–Smirnov test were applied to determine the normality of the data. Continuous data with normal distribution were given as mean ± standard deviation (SD). Otherwise, data were summarized by median (interquartile range [IQR]). Categorical data was given as frequency and percentage. The Levene test was conducted to test the homogeneity of variance. Independent-sample Student's t-test, Mann–Whitney U test, and Chi-square test were performed to describe the differences between

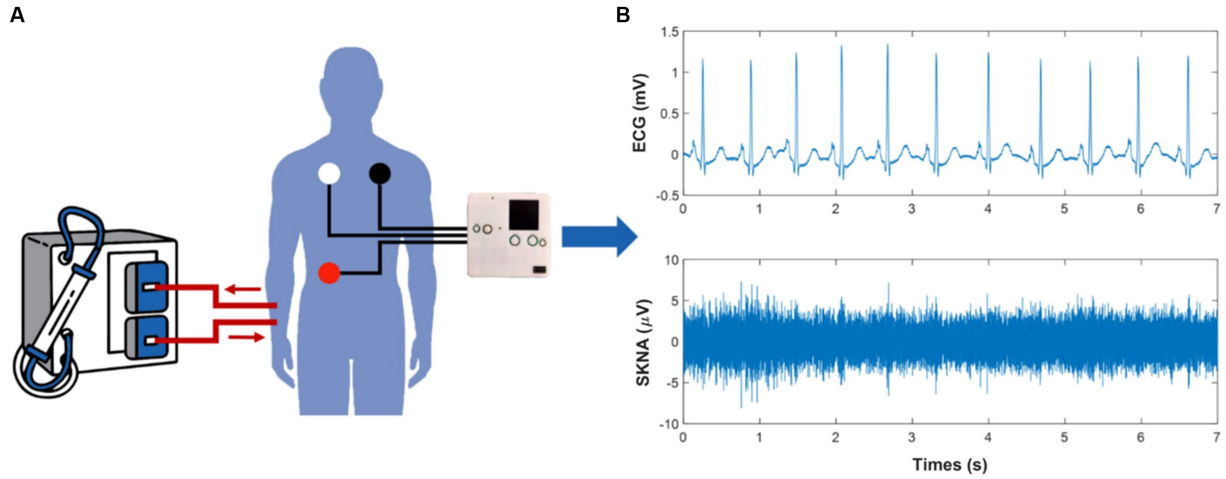

FIGURE 1
Schematic of the physiological signal acquisition process and data processing. **(A)** illustrates the scenario of signal acquisition during hemodialysis (HD). **(B)** shows the electrocardiogram (ECG) and skin sympathetic nerve activity (SKNA) signals separated from the raw signals, respectively.

the two subgroups. Student paired t-tests and Wilcoxon signed-rank test were utilized to explore the changes of physiological data in different periods within the group. Pearson correlation coefficient, Spearman correlation coefficient, and least square method were used to analyze the correlation. To investigate the correlation between aSKNA and other indicators, the mean values of segments 1 and 2, 12 and 13, 24 and 25, 35 and 36, 47, and 48 of each index were computed based on the 5 min results, corresponded with the five measurements of SBP and DBP. Two-sided $p < 0.05$ was regarded as significant.

Binary logistic regression was employed for univariate and multivariate analyses to explore the independent risk factors of IDH. In the multivariate analysis, the indicators with $p < 0.2$ in the univariate analysis were included. To more comprehensively explore the underlying association between the indicators of physiological signals and IDH, this study processed the indicators from three dimensions to build multivariate models. Using the 5 min results, we calculated the difference between the last and first segments (DLF), the extreme value of the difference between other segments and the first segments (EOF), and the extreme value of the difference between adjacent segments (EDA). It should be stated that after each calculation of EOF and EDA, the maximum and minimum values were obtained. In univariate analysis, we included the maximum and minimum values of EOF and EDA, respectively, and consider the corresponding extreme values with smaller p-values to be included in the multivariate model. To assess the model goodness of fit, the accuracy of the model, the Akaike Information Criterion (AIC), and Omnibus Tests of Model Coefficients were used.

3. Results

3.1. Participant information

In this study, among the total of 93 patients, 66 subjects had IDH, and 27 subjects did not have that, with an incidence rate of 71.0%. Table 1 displays the baseline data of the total and the two subgroups. The patients in the IDH group were older than those in the nonIDH group (65 [53.3, 69] vs. 54.15 ± 3.1, $p = 0.039$), with higher initial SBP (150.7 ± 2.1 vs. 133.6 ± 2.8, $p < 0.001$). Other characteristics were comparable between the two subgroups, and no significant differences were found. The mean initial SBP was above the 140 mm Hg threshold for hypertension in the IDH group, whereas the mean initial SBP was below this threshold in the nonIDH group.

TABLE 1 Baseline data of the total and the two subgroups.

	Total $N=93$	IDH $N=66$	nonIDH $N=27$	p value
Age (year)	62.0[50.0, 69.5]	65.0[52.5, 69.3]	54.2 ± 3.1	**0.039**
Male (n, %)	62 (66.7)	47 (71.2)	15 (55.6)	0.146
Body mass index (kg/m^2)	22.9 ± 0.4	22.8 ± 0.4	22.1[20.4, 24.4]	0.666
HD duration (year)	3.0[1.4, 6.0]	3.0[1.8, 5.0]	3.0[1.0, 7.0]	0.682
Ultrafiltration (kg)	2.6 ± 0.1	2.5 ± 0.1	2.8 ± 0.2	0.293
Ultrafiltration/ Weight (%)	4.1 ± 0.1	3.9 ± 0.2	4.4 ± 0.3	0.155
Pre-HD SBP (mm Hg)	145.7 ± 1.9	150.7 ± 2.1	133.6 ± 2.8	**<0.001**
Pre-HD DBP (mm Hg)	78.3 ± 1.2	79.1 ± 1.4	76.4 ± 2.4	0.331

HD, hemodialysis; IDH, intradialytic hypotension; SBP, systolic blood pressure; DBP, diastolic blood pressure. p values for variables with $p<0.05$ are bolded, indicating a significant difference between the two subgroups of indicators.

3.2. Changes in BP during HD

The changes in BP indicators during HD in the subgroups are shown in Figure 2. The initial SBP, DBP, MAP, and PP were higher in IDH patients than those in patients without nonIDH, and the differences between the other three indicators were significant except for DBP. On the contrary, the final SBP, DBP, and MAP in IDH patients were lower than those in patients without nonIDH, and the differences in the other three indices were significant except PP. In the IDH group, all four indicators showed a significant decrease during the first 3 hours of HD, but there were no significant changes observed during the last hour, with only slight fluctuations. In the nonIDH group, there was no obvious trend in the changes of BP-related indicators during HD, and the changes were relatively stable, except for the cases of significant rises in DBP and MAP during the first hour. From the perspective of slope changes, the indicators changed most sharply during the first hour, and the degree of change weakened gradually in each subsequent hour.

3.3. Changes in heart rate, HRV, and SKNA indices during HD

Figure 3 illustrates the comparison of HRV and SKNA indices, as well as heart rate, during HD between the two subgroups. The heart rate in IDH patients was significantly lower than that in patients without nonIDH at the beginning of HD, gradually increased during HD, and was comparable to that of the nonIDH group at the end of HD (Figure 3A). Among the 10 HRV indices in the IDH group, 7 indicators [SDNN, RMSSD, LF, HF, LF/HF, LF/(LF + HF), SampEn] were lower than those of the nonIDH group. At most moments, PNN50 and ApEn were also lower than those of the nonIDH group, while only FuzzyMEn was higher than those of the nonIDH group at most moments. The values of SDNN, RMSSD, and LF/HF increased, while FuzzyMEn decreased in both subgroups. PNN50, LF, HF, LF/(LF + HF), ApEn, and SampEn rose in the nonIDH group and reduced in the IDH group. LF, LF/HF, LF/(LF + HF), ApEn, and SampEn showed good discrimination effects between the two subgroups (Figures 3B-K). For SKNA, aSKNA in the IDH group was lower than that in the nonIDH group, but there was no statistical difference between the two subgroups at each segment. Besides, aSKNA was elevated at end-HD in both groups.

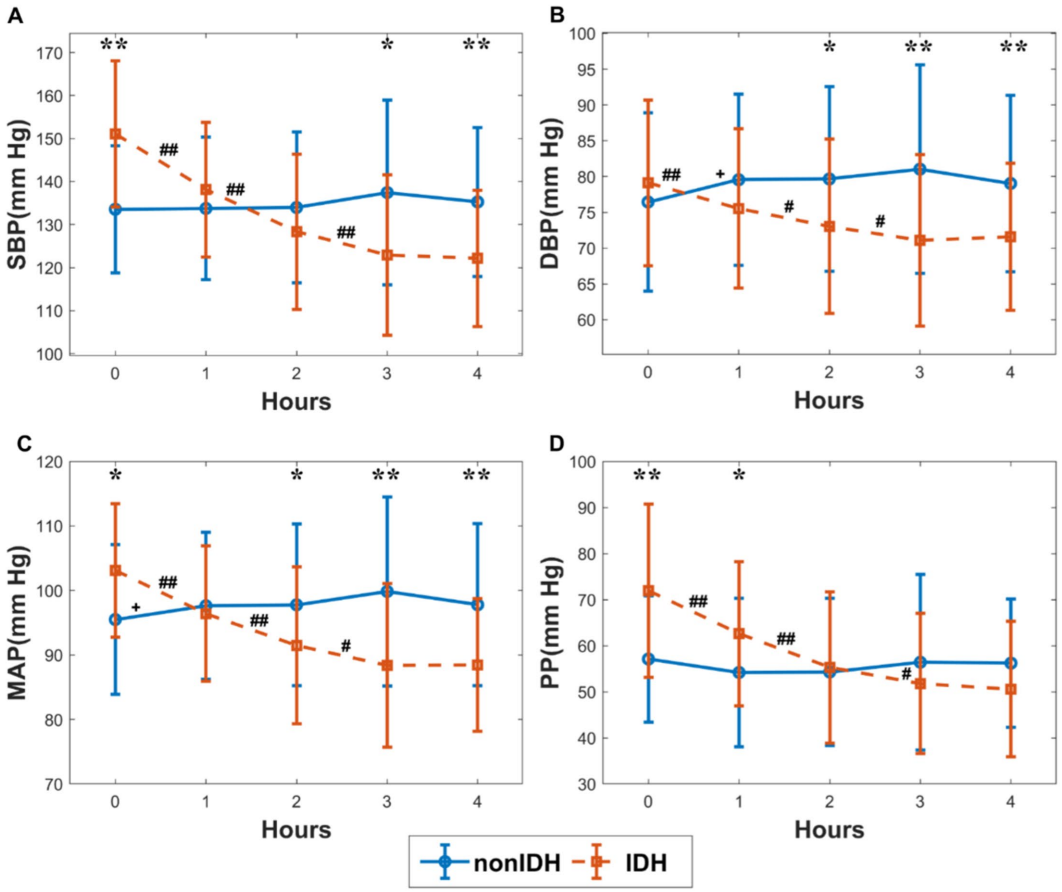

FIGURE 2
The changes in blood pressure (BP) indicators during hemodialysis (HD) in the subgroups. **(A)** systolic blood pressure (SBP), **(B)** diastolic blood pressure (DBP), **(C)** mean arterial pressure (MAP), **(D)** pulse pressure (PP). The red and blue lines stand for the IDH group and nonIDH group, respectively. '#' and '+' represent statistically significant changes per hour in the IDH group and nonIDH group, respectively. $^{\#\#}p<0.001$, $^{\#}p<0.05$, $^{+}p<0.05$. '*' shows statistically significant differences between two subgroups in the same period. $^{**}p<0.001$, $^{*}p<0.05$. Error bars represent the standard error of the mean (SEM).

3.4. Correlation analysis between aSKNA and other indices

We examined the correlation between aSKNA and the other physical indicators: SBP, heart rate, and HRV indices in the subgroups, respectively (Figure 4). As it can be seen, there was no correlation between SBP and aSKNA in the nonIDH group, but there was a negative correlation ($r=-0.1961$, $p=0.0155$) in the IDH group (Figures 4A,M). A moderate correlation was observed between aSKNA and heart rate in the nonIDH group ($r=0.3584$, $p=0.0001$), but no correlation in the IDH group (Figures 4B,N). Interestingly, the HRV indices of the time domain and entropy related to aSKNA in the two subgroups are completely complementary. SDNN ($r=0.1718$, $p=0.0362$), RMSSD ($r=0.1778$, $p=0.0350$), PNN50 ($r=0.2033$, $p=0.0176$), ApEn ($r=0.2301$, $p=0.0042$) and SampEn ($r=0.2086$, $p=0.0097$) were all positively correlated with aSKNA in the IDH group, while none of these parameters were correlated with aSKNA in the nonIDH group. FuzzyMEn ($r=-0.3947$, $p<0.0001$) was correlated with aSKNA in the nonIDH group and had no correlation in the IDH group. For parameters in the frequency domain, except LF/HF ($r=0.3307$, $p=0.0005$) and LF/(LF + HF) ($r=0.3085$, $p=0.0010$) in the nonIDH group, which were positively correlated with aSKNA, there was no correlation in other cases.

3.5. Establishment of IDH risk factor model

Binary logistic regression was utilized to establish models. Firstly, univariate analysis was used to analyze the influence of baseline data on IDH. The results of the univariate analysis using the baseline data are reported in Table 2. Among these characteristics, variables with $p<0.2$ in the univariate analysis, including age, sex, ultrafiltration/weight, and SBP before HD, were integrated into the multivariate analysis.

Then, to better evaluate the impact of HRV and SKNA indicators on IDH, we processed the indicators in three different ways and obtained the results of DLF, EOF, and EDA. The results of the univariate models and multivariate models using these calculated variables are listed in Table 3. For HRV indices, DLF showed that most HRV indicators were integrated into the multivariate analysis, and the multivariate model performed best, with the highest accuracy (77.4) and lowest AIC (274.268). By contrast, the minimal values of EOF and

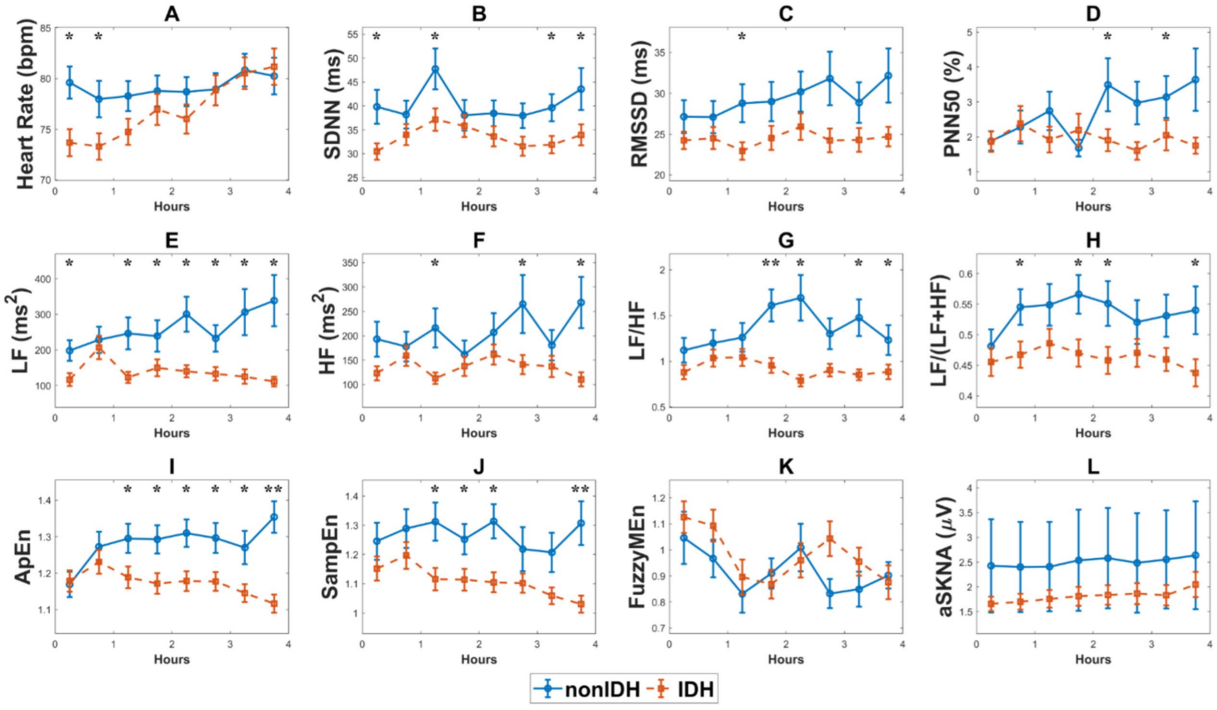

FIGURE 3
The comparison of heart rate variability (HRV) and skin sympathetic nerve activity (SKNA) indices, as well as heart rate, during hemodialysis (HD) between the two subgroups. **(A)** heart rate, **(B)** the standard deviation of the RR intervals (SDNN), **(C)** the square root of the mean squared differences of subsequent RR intervals (RMSSD), **(D)** the proportion derived by dividing the number of interval differences of subsequent RR intervals greater than 50ms by the overall number of the RR intervals (PNN50), **(E)** low frequency (LF), **(F)** high frequency (HF), **(G)** LF/HF ratio, **(H)** LF/(LF+HF) ratio, **(I)**. approximate entropy (ApEn), **(J)** sample entropy (SampEn), **(K)** fuzzy measure entropy (FuzzyMEn), **(L)** the average SKNA (aSKNA). The red and blue lines represent the IDH and nonIDH groups, respectively. '*' shows statistically significant differences between two subgroups in the same period. $^{**}p<0.001$, $^{*}p<0.05$. Error bars represent the standard error of the mean (SEM).

EDA for aSKNA were statistically significant in univariate analysis and were included in subsequent multivariate analysis.

Finally, the baseline data and SKNA indices with $p<0.2$ in the univariate analysis and HRV indices from the HRV multivariate Model 1 were integrated into the multivariate model for comprehensive analysis. Five models with different combinations of variables are reported in Table 4. Compared with model 1, models 2, 3, and 4 were optimized by adding HRV and SKNA parameters. Model 3 had the highest accuracy (84.9) and lowest AIC (250.356), which was also superior to the HRV multivariate Model 1 (Table 3). We found that higher SBP before HD [odds ratio (OR) 1.076; 95% confidence interval (CI) 1.031–1.124, $p=0.001$], heart rate-DLF [OR 1.101; 95% CI 1.022–1.187, $p=0.012$], and aSKNA-EOF [OR 2.908; 95% CI 1.210–6.989, $p=0.017$], and lower LF/HF-DLF [OR 0.209; 95% CI 0.049–0.885, $p=0.034$] were four independent indicators for IDH (Table 5).

4. Discussion

Time and frequency domain analysis of HRV was widely utilized in previous IDH-related studies. However, this traditional method ignores the nonlinear dynamical information on heart rate (Denton et al., 1990) and lacks a more intuitive description of SNA (Kusayama et al., 2020b). We implemented the methods for the entropy of HRV and SKNA to explore the physiological mechanism of IDH, which described the nonlinear and dynamic changes of the ANS in IDH. Two distinct response patterns of the ANS during HD were observed in the two subgroups, and the IDH group showed worse ANS activity and ability to cope with the stimulation. Higher initial SBP, the DLF of heart rate, and the EOF of aSKNA, as well as the lower DLF of LF/HF were found to be independent indicators for IDH.

4.1. ANS patterns revealed by HRV indices

The overall level of HRV indices, excluding FuzzyMEn, was lower in the IDH group than that in the nonIDH group. Reduced HRV is a remarkable predictor of symptoms and death of a wide broad spectrum of diseases, especially cardiovascular diseases (Sessa et al., 2018; Fang et al., 2020). LF/HF, which describes the balance of SNA and parasympathetic nervous activity (PNA), increased in both subgroups, consistent with the previous study (Chang et al., 2016; Park et al., 2019). However, the same outcomes indicate different ANS patterns, mainly due to increased LF in nonIDH patients and decreased HF in IDH patients. Lower HF and reduced HF show suppressed PNA in the IDH group, which also points to a poor cardiac prognosis (Algra et al., 1993).

Moreover, inconsistent interpretations of indices in previous studies affected the credibility of HRV. LF was initially interpreted to characterize SNA. Nonetheless, accumulating evidence demonstrates that LF represents a nonlinear interaction between SNA and PNA

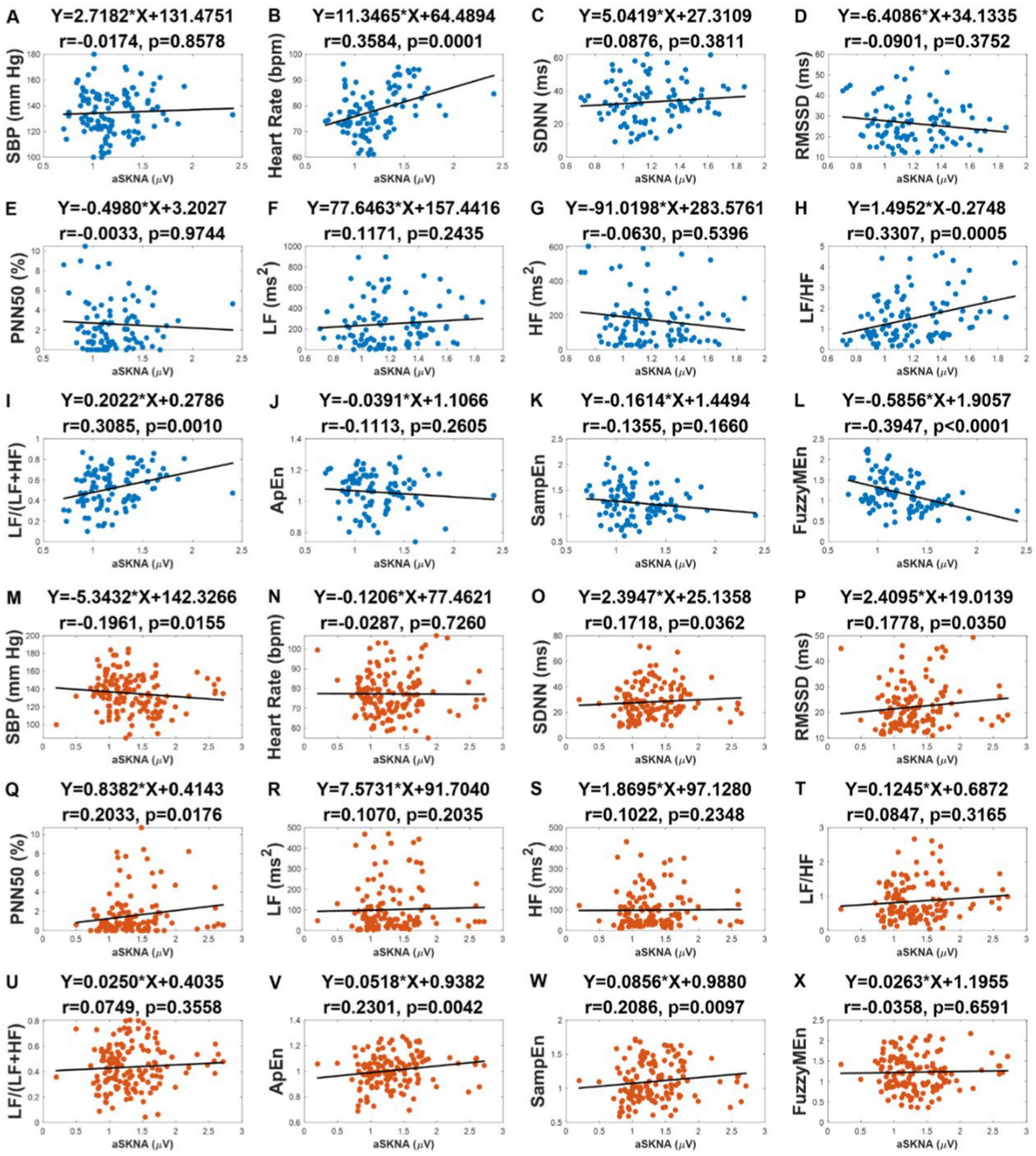

FIGURE 4
The correlation between the average of skin sympathetic nerve activity (aSKNA) and other physical indicators: systolic blood pressure (SBP), heart rate, heart rate variability (HRV) indices in the intradialytic hypotension (IDH) group and nonIDH group. **(C,O)** the standard deviation of the RR intervals (SDNN); **(D,P)** the square root of the mean squared differences of subsequent RR intervals (RMSSD); **(E,Q)** the proportion derived by dividing the number of interval differences of subsequent RR intervals greater than 50ms by the overall number of the RR intervals (PNN50); **(F)**, **(R)** low frequency (LF); **(G,S)** high frequency (HF); **(H,T)** LF/HF ratio; **(I,U)** LF/(LF+HF) ratio; **(J,V)** approximate entropy (ApEn); **(K,W)** sample entropy (SampEn); **(L,X)** fuzzy measure entropy (FuzzyMEn). **(A)** to **(L)** represent the results of the nonIDH group, and **(M)** to **(X)** represent the results of the IDH group. The first rows of the figures are titled regression equations obtained by the least squares method, and the second rows are titled correlation coefficients and *p* values.

(Billman, 2013; Chang et al., 2016). Although LF/HF indirectly represents the intensity of SNA through the balance of ANS, when the ANS function is weakened to a certain extent, LF/HF will lose its significance (Billman, 2013). This hypothesis is confirmed by the evidence that LF/HF and aSKNA were positively correlated in the nonIDH group, but this correlation disappeared in the IDH group with weaker ANS function. Consequently, in the assessment of patients with impaired ANS function, such as those with IDH, HRV may not provide an accurate evaluation of SNA, and the obtained results should be interpreted with caution.

4.2. Evaluation of entropy and SKNA during HD

ApEn and SampEn and FuzzyMEn describe the regularity of RR intervals. ApEn is used to address short-time noisy signals, with strong robustness (Pincus, 1991). SampEn solves the self-matching of the template in ApEn and is less dependent on data length (Richman and Moorman, 2000). FuzzyMEn introduces the fuzzy measure of variable similarity and considers both local and global similarity comprehensively to have better performance in short-time series processing (Liu et al., 2013). The lower values of ApEn and SampEn in the IDH group exhibit that patients who had higher regularity of heart rate may be prone to a higher risk of cardiovascular diseases (Fleisher et al., 1993; Mäkikallio et al., 1998; Rajendra Acharya et al., 2006; Shin et al., 2006). Besides, it was found that ApEn and SampEn showed better discrimination ability for IDH in comparing the differences in index values between the two subgroups (Figures 3I-K), indicating that ApEn and SampEn can better characterize the difference in ANS function. But only FuzzyMEn was included in model 3 of HRV when determining the risk factors ($p < 0.05$, Table 3). This illustrates that introducing a global perspective helps predict the tendency of IDH over time. FuzzyMEn showed better performance on the 5-min scale compared to the 30-min scale, confirming the superiority of FuzzyMEn in the processing of short-time sequences.

As an emerging tool for assessing SNA, SKNA overcomes the limitation that HRV needs to be based on sinus rhythm and elevates time resolution to the level of seconds. During HD, aSKNA increased in both subgroups, similar to LF/HF, suggesting sympathetic activation, consistent with the expected feedback of compensatory mechanism triggered by increased ultrafiltration, which was in line with previous studies (Park et al., 2019; Zhang et al., 2022). Lower aSKNA in the IDH group indicated that patients had insufficient sympathetic activation (Converse et al., 1992). Moreover, aSKNA was positively correlated with heart rate in the nonIDH group, but this relationship disappeared in the IDH group. The loss might imply worse neurologic recovery, which was also observed in individuals

TABLE 2 The results of the univariate analysis using the baseline data for evaluating intradialytic hypotension (IDH).

Variable	OR(95% CI)	*p* value
Age	1.042 (1.007, 1.078)	**0.018**
Sex	0.543 (0.216, 1.368)	**0.195**
Body mass index	0.994 (0.882, 1.121)	0.922
HD duration	0.974 (0.876, 1.082)	0.619
Ultrafiltration	0.772 (0.477, 1.248)	0.291
Ultrafiltration/Weight	0.000 (0.000, 13232.122)	**0.155**
Pre-HD SBP	1.071 (1.033, 1.110)	**<0.001**
Pre-HD DBP	1.019 (0.981, 1.060)	0.328

Pre-HD, before hemodialysis; SBP, systolic blood pressure; DBP, diastolic blood pressure; OR, odds ratio; CI, confidence interval. *p* values were obtained from logistic regression, and *p* values for variables with $p<0.2$ are bolded.

TABLE 3 The results of univariate analysis and multivariate analysis of heart rate variability (HRV) and skin sympathetic nerve activity (SKNA) indices for evaluating intradialytic hypotension (IDH).

			Univariate analysis			Multivariate analysis		
			DLF	EOF	EDA	Model 1	Model 2	Model 3
#*p* values	HRV	Heart Rate	**0.009**	**0.015**$^{-}$	0.662^{+}	**0.016**	**0.049**$^{-}$	–
		SDNN	0.373	0.315^{+}	0.558^{+}	–	–	–
		RMSSD	**0.141**	0.204^{+}	0.560^{-}	0.236	–	–
		PNN50	**0.141**	**0.132**$^{+}$	0.321^{+}	0.215	**0.147**$^{+}$	–
		LF	0.333	0.795^{+}	0.861^{+}	–	–	–
		HF	**0.151**	0.329^{+}	0.384^{+}	**0.060**	–	–
		LF/HF	**0.011**	**0.085**$^{+}$	**0.120**$^{-}$	**0.016**	0.386^{+}	**0.135**$^{-}$
		LF/(LF + HF)	**0.109**	0.208^{-}	0.365^{+}	**0.113**	–	–
		ApEn	0.460	0.297^{-}	0.303^{+}	–	–	–
		SampEn	**0.186**	0.775^{+}	0.578^{-}	0.480	–	–
		FuzzyMEn	0.505	**0.165**$^{-}$	**0.035**$^{+}$	–	0.694^{-}	**0.038**$^{+}$
	SKNA	aSKNA	0.768	**0.009**$^{-}$	**0.039**$^{-}$	–	–	–
Constant			–	–	–	**0.021**	**0.044**	0.968
Accuracy			–	–	–	77.4	73.1	69.9
AIC			–	–	–	274.268	286.839	290.921
**p* value			–	–	–	0.010	0.024	0.028

DLF, the difference between the last and first segments; EOF, the extreme value of the difference between other segments and the first segment; EDA, the extreme value of the difference between adjacent segments; SDNN, the standard deviation of the RR intervals; RMSSD, the square root of the mean squared differences of subsequent RR intervals; PNN50, the proportion derived by dividing the number of interval differences of subsequent RR intervals greater than 50 ms by the overall number of the RR intervals; LF, low frequency; HF, high frequency; LF/HF, LF/HF ratio; LF/(LF + HF), LF/(LF + HF) ratio; ApEn, approximate entropy; SampEn, sample entropy; FuzzyMEn, fuzzy measure entropy; aSKNA, the average SKNA; AIC, Akaike Information Criterion. In extreme value calculation, the maximum value and the minimum value are included, and '+' and '−' represent the maximum value and the minimum value, respectively. #*p* values were obtained from logistic regression, and *p* values for variables with $p < 0.2$ are bolded. **p* values in the last row were obtained from Omnibus Tests of Model Coefficients. $^{*}p < 0.05$ indicates that the model is overall significant.

TABLE 4 The results of the different multivariate models for predicting intradialytic hypotension (IDH).

		Model 1	Model 2	Model 3	Model 4	Model 5
#*p* value	Pre-HD SBP	**< 0.001**	**0.001**	**0.001**	**0.001**	–
	Age	0.085	0.577	0.874	0.706	–
	Ultrafiltration/Weight	0.297	0.133	0.087	0.110	–
	Sex	0.265	0.551	0.806	0.584	–
	Heart Rate-DLF	–	**0.021**	**0.012**	**0.024**	**0.015**
	LF/HF-DLF	–	**0.039**	**0.034**	**0.037**	**0.024**
	HF-DLF	–	0.147	0.169	0.158	**0.038**
	LF/(LF + HF)-DLF	–	0.214	0.186	0.210	0.131
	RMSSD-DLF	–	–	–	–	0.130
	PNN50-DLF	–	–	–	–	0.184
	SampEn-DLF	–	–	–	–	0.569
	aSKNA-EOF⁻	–	–	**0.017**	–	**0.010**
	aSKNA-EDA⁻	–	–	–	0.132	–
Constant		**0.001**	**0.013**	**0.030**	**0.019**	**0.002**
Accuracy		77.4	81.7	84.9	82.8	78.5
AIC		271.835	255.684	250.356	253.349	265.998
**p* value		<0.001	<0.001	<0.001	<0.001	<0.001

Pre-HD, before hemodialysis; SBP, systolic blood pressure; LF, low frequency; HF, high frequency; LF/HF, LF/HF ratio; LF/(LF+HF), LF/(LF+HF) ratio; RMSSD, the square root of the mean squared differences of subsequent RR intervals; PNN50, the proportion derived by dividing the number of interval differences of subsequent RR intervals greater than 50 ms by the overall number of the RR intervals; SampEn, sample entropy; aSKNA, the average of skin sympathetic nerve activity; AIC, Akaike Information Criterion. '-DLF' denotes the difference between the last and first segments of the calculated variable. '-EOF⁻' denotes the minimum value of the difference between other segments and the first segment of the calculated variable. '-EDA⁻' denotes the minimum value of the difference between adjacent segments of the calculated variable. #p values were obtained from logistic regression, and p values for variables with $p < 0.05$ are bolded. **p* values in the last row were obtained from Omnibus Tests of Model Coefficients. **p* < 0.05 indicates that the model is overall significant.

TABLE 5 The optimal model for predicting intradialytic hypotension (IDH) based on logistic regression.

	OR(95% CI)	*p* value
Pre-HD SBP	1.076 (1.031, 1.124)	**0.001**
Age (per 1 year)	1.004 (0.956, 1.054)	0.874
Ultrafiltration/Weight	0.000 (0.000, 1606.431)	0.087
Sex		
Male	1.000	–
Female	0.844 (0.218, 3.271)	0.806
Heart Rate-DLF	1.101 (1.022, 1.187)	**0.012**
LF/HF-DLF	0.209 (0.049, 0.885)	**0.034**
HF-DLF	1.001 (1.000, 1.002)	0.169
LF/(LF + HF) -DLF	247.191 (0.070, 869089.763)	0.186
SKNA-EOF-	2.908 (1.210, 6.989)	**0.017**
Constant	0.001	**0.030**

Pre-HD, before hemodialysis; SBP, systolic blood pressure; LF, low frequency; HF, high frequency; LF/HF, LF/HF ratio; LF/(LF+HF), LF/(LF+HF) ratio; aSKNA, average of skin sympathetic nerve activity; OR, odds ratio; CI, confidence interval. '-DLF' denotes the difference between the last and first segments of the calculated variable. 'EOF-' denotes the minimum value of the difference between other segments and the first segment of the calculated variable. *p* values for variables with $p < 0.05$ in the logistic regression are bolded.

receiving targeted temperature control (Kutkut et al., 2021). aSKNA was negatively correlated with SBP in the IDH group, but this relationship was lost in the IDH group, which revealed a worse systemic ability to resist the loss of volume in IDH patients. In the IDH group, not only the activation of SNA was insufficient, but also other physiological mechanisms failed to resist the reduction of BP.

4.3. Risk factors for IDH

DLF, EOF, and EDA methods were used to process HRV and SKNA indices in the establishment of the IDH multivariate model. DLF model of HRV performed best, indicating that the difference in HRV values before and after dialysis better described the

occurrence of IDH. In the final multivariate model comparison, the two iterations from model 1 to model 3 indicated that adding HRV indices and SKNA index based on clinical baseline information helped assess IDH, respectively. The comparison of models 3 and 4 showed that the maximum change in SKNA from the initial value could better distinguish IDH. That is, the changes in SNA during HD affect the development of IDH relative to the baseline. Model 5 was introduced to illustrate the importance of baseline data in the model.

In the final assessment model of IDH, higher initial SBP, the DLF of heart rate, and the EOF of aSKNA, as well as the lower DLF of LF/HF became the risk factors for IDH. Higher initial BP promotes IDH which is consistent with previous study (Chang et al., 2016). The mean initial SBP in IDH patients was above the diagnostic criteria of hypertension, which is 140 mmHg, whereas that in nonIDH patients were normal. On one hand, we speculate that hypertension may be related to greater weight gain when not receiving HD but with inadequate dialysis because of an unexpected weight gain. On the other hand, we think that IDH patients initially may have over-activated sympathetic nerves, which are more susceptible to hypertension (Masuo et al., 2010), resulting in vascular overload and pathological changes (Cachofeiro et al., 2009), but abnormal SNA gradually decreases with the increase of the HD duration (Masuo et al., 2010), even lower than other HD patients. Therefore, patients are unable to further raise peripheral vascular resistance in response to the increase in SNA, resulting in IDH (Dubin et al., 2011). In addition, LF is nonlinearly regulated by the SNA and PNA, as well as other factors, with the effect of PNA being approximately twice as strong as that of SNA (Randall et al., 1991). That is, LF/HF is more sensitive to PNA at lower SNA. Thus, we hypothesized that the lower DLF of LF/HF directed to the depressed PNA or other factors in IDH patients, which are different from the depressed SNA generally believed.

4.4. Limitation

It should be noted that this study still has several limitations. First of all, this research was conducted in a single center, and the sample size of patients was small, so the data may be biased. Secondly, the lack of clinical symptoms and interventions reduced the physiological differences between IDH and nonIDH patients, making it more difficult to identify IDH. What is more, physical data during HD were collected only once for each patient, and no long-term follow-up was formed, so there may be some contingency in the results. Finally, although the SKNA assessment achieved satisfactory results in this study, the specific physiological mechanism of SKNA is still unclear, and the underlying relationship between SKNA and HRV indicators needs to be further studied.

5. Conclusion

In this study, a portable, noninvasive, and high-frequency electrophysiological acquisition device was used to collect ECG and SKNA signals of patients during HD, which were combined with baseline data to evaluate ANS function during HD. Compared with previous studies, this study introduced the entropy of HRV and SKNA methods to provide a nonlinear and dynamic perspective of ANS function assessment and investigated the underlying physiological mechanism of IDH. We found different patterns in response to plasma loss between IDH patients and nonIDH patients, and the IDH group exhibited worse ANS function. In addition, we found that higher initial SBP, the DLF of heart rate and the EOF of aSKNA, and the lower DLF for LF/HF were independent factors of IDH. The SKNA showed good performance in both group comparison and model evaluation in this study. Although the entropy of HRV was not integrated into the final multivariate model, the nonlinear information it provided deserved further exploration.

Data availability statement

The original contributions presented in the study are included in the article/supplementary materials, further inquiries can be directed to the corresponding authors.

Ethics statement

The studies involving human participants were reviewed and approved by the Ethics Committee of the First Affiliated Hospital of Nanjing Medical University. The patients/participants provided their written informed consent to participate in this study.

Author contributions

JiayL, YX, CC, and CL contributed to the conception and design of the study. JiayL and JianL processed the signals, performed the statistical analysis, and wrote the manuscript. YX provided the devices and processed the signals. YZ, CC, and JW collected the data and organized the database. JianL and CL contributed to the guidance of the whole study. All authors contributed to the article and approved the submitted version.

Funding

This work was supported by the National Natural Science Foundation of China (62171123, 62071241, 62201144, and 62211530112), and the Natural Science Foundation of Jiangsu Province of China (BK20192004).

Acknowledgments

We thank Xingyao Wang for help in data processing, Zhijun Xiao for the valuable discussion on the structure of this paper, and Lukai Pang for polishing the paper.

Conflict of interest

The authors declare that the research was conducted in the absence of any commercial or financial relationships that could be construed as a potential conflict of interest.

Publisher's note

References

Algra, A., Tijssen, J. G., Roelandt, J. R., Pool, J., and Lubsen, J. (1993). Heart rate variability from 24-hour electrocardiography and the 2-year risk for sudden death. *Circulation* 88, 180–185. doi: 10.1161/01.CIR.88.1.180

Assimon, M. M., and Flythe, J. E. (2017). Definitions of intradialytic hypotension. *Semin. Dial.* 30, 464–472. doi: 10.1111/sdi.12626

Billman, G. E. (2013). The LF/HF ratio does not accurately measure cardiac sympatho-vagal balance. *Front. Physio.* 4:26. doi: 10.3389/fphys.2013.00026

Cachofeiro, V., Miana, M., Heras, N. D. L., Martín-Fernandez, B., Ballesteros, S., Balfagon, G., et al. (2009). Inflammation: a link between hypertension and atherosclerosis. *Curr. Hypertens. Rev.* 5, 40–48. doi: 10.2174/157340209787314333

Chang, Y.-M., Shiao, C.-C., Chang, K.-C., Chen, I.-L., Yang, C.-L., Leu, S.-C., et al. (2016). Heart rate variability is an indicator for intradialytic hypotension among chronic hemodialysis patients. *Clin. Exp. Nephrol.* 20, 650–659. doi: 10.1007/s10157-015-1189-9

Chou, J. A., Kalantar-Zadeh, K., and Mathew, A. T. (2017). A brief review of intradialytic hypotension with a focus on survival. *Semin. Dial.* 30, 473–480. doi: 10.1111/sdi.12627

Converse, R. L., Jacobsen, T. N., Jost, C. M., Toto, R. D., Grayburn, P. A., Obregon, T. M., et al. (1992). Paradoxical withdrawal of reflex vasoconstriction as a cause of hemodialysis-induced hypotension. *J. Clin. Invest.* 90, 1657–1665. doi: 10.1172/JCI116037

Davenport, A. (2022). Why is intradialytic hypotension the commonest complication of outpatient Dialysis treatments? *Kidney Int. Rep.* 8, 405–418. doi: 10.1016/j.ekir.2022.10.031

Denton, T. A., Diamond, G. A., Helfant, R. H., Khan, S., and Karagueuzian, H. (1990). Fascinating rhythm: a primer on chaos theory and its application to cardiology. *Am. Heart J.* 120, 1419–1440. doi: 10.1016/0002-8703(90)90258-Y

Doytchinova, A., Hassel, J. L., Yuan, Y., Lin, H., Yin, D., Adams, D., et al. (2017). Simultaneous noninvasive recording of skin sympathetic nerve activity and electrocardiogram. *Heart Rhythm.* 14, 25–33. doi: 10.1016/j.hrthm.2016.09.019

Dubin, R., Owens, C., Gasper, W., Ganz, P., and Johansen, K. (2011). Associations of endothelial dysfunction and arterial stiffness with intradialytic hypotension and hypertension: vascular dysfunction and hemodynamic instability. *Hemodial. Int.* 15, 350–358. doi: 10.1111/j.1542-4758.2011.00560.x

Fang, S.-C., Wu, Y.-L., and Tsai, P.-S. (2020). Heart rate variability and risk of all-cause death and cardiovascular events in patients with cardiovascular disease: a Meta-analysis of cohort studies. *Biol. Res. Nurs.* 22, 45–56. doi: 10.1177/1099800419877442

Fleisher, L. A., Pincus, S. M., and Rosenbaum, S. H. (1993). Approximate entropy of heart rate as a correlate of postoperative ventricular dysfunction. *Anesthesiology* 78, 683–692. doi: 10.1097/00000542-199304000-00011

He, W., Tang, Y., Meng, G., Wang, D., Wong, J., Mitscher, G. A., et al. (2020). Skin sympathetic nerve activity in patients with obstructive sleep apnea. *Heart Rhythm.* 17, 1936–1943. doi: 10.1016/j.hrthm.2020.06.018

Heart rate variability (1996). Heart rate variability. *Eur. Heart J.* 17, 28–29. doi: 10.1093/eurheartj/17.suppl_2.28

Jiang, Z., Zhao, Y., Doytchinova, A., Kamp, N. J., Tsai, W.-C., Yuan, Y., et al. (2015). Using skin sympathetic nerve activity to estimate stellate ganglion nerve activity in dogs. *Heart Rhythm.* 12, 1324–1332. doi: 10.1016/j.hrthm.2015.02.012

K/DOQI Workgroup (2005). K/DOQI Clinical Practice Guidelines for Cardiovascular Disease in Dialysis Patients. *Am. J. Kidney Dis.* 45, 16–153. doi: 10.1053/j.ajkd.2005.01.019

Kusayama, T., Douglas, A. II, Wan, J., Doytchinova, A., Wong, J., Mitscher, G., et al. (2020a). Skin sympathetic nerve activity and ventricular rate control during atrial fibrillation. *Heart Rhythm.* 17, 544–552. doi: 10.1016/j.hrthm.2019.11.017

Kusayama, T., Wong, J., Liu, X., He, W., Doytchinova, A., Robinson, E. A., et al. (2020b). Simultaneous noninvasive recording of electrocardiogram and skin sympathetic nerve activity (neuECG). *Nat. Protoc.* 15, 1853–1877. doi: 10.1038/s41596-020-0316-6

Kutkut, I., Uceda, D., Kumar, A., Wong, J., Li, X., Wright, K. C., et al. (2021). Skin sympathetic nerve activity as a biomarker for neurologic recovery during therapeutic hypothermia for cardiac arrest. *Heart Rhythm.* 18, 1162–1170. doi: 10.1016/j.hrthm.2021.03.011

Lake, D. E., Richman, J. S., Griffin, M. P., and Moorman, J. R. (2002). Sample entropy analysis of neonatal heart rate variability. *Am. J. Phys. Regul. Integr. Comp. Phys.* 283, R789–R797. doi: 10.1152/ajpregu.00069.2002

Liu, C., Li, K., Zhao, L., Liu, F., Zheng, D., Liu, C., et al. (2013). Analysis of heart rate variability using fuzzy measure entropy. *Comput. Biol. Med.* 43, 100–108. doi: 10.1016/j.compbiomed.2012.11.005

Liu, C., Zhang, X., Zhao, L., Liu, F., Chen, X., Yao, Y., et al. (2019). Signal quality assessment and lightweight QRS detection for wearable ECG SmartVest system. *IEEE Internet Things J.* 6, 1363–1374. doi: 10.1109/JIOT.2018.2844090

MacEwen, C., Sutherland, S., Daly, J., Pugh, C., and Tarassenko, L. (2017). Relationship between hypotension and cerebral ischemia during hemodialysis. *JASN* 28, 2511–2520. doi: 10.1681/ASN.2016060704

Mäkikallio, T. H., Ristimäe, T., Airaksinen, K. E. J., Peng, C.-K., Goldberger, A. L., and Huikuri, H. V. (1998). Heart rate dynamics in patients with stable angina pectoris and utility of fractal and complexity measures. *Am. J. Cardiol.* 81, 27–31. doi: 10.1016/S0002-9149(97)00799-6

Masuo, K., Lambert, G. W., Esler, M. D., Rakugi, H., Ogihara, T., and Schlaich, M. P. (2010). The role of sympathetic nervous activity in renal injury and end-stage renal disease. *Hypertens. Res.* 33, 521–528. doi: 10.1038/hr.2010.35

Mayer, C. C., Bachler, M., Hörtenhuber, M., Stocker, C., Holzinger, A., and Wassertheurer, S. (2014). Selection of entropy-measure parameters for knowledge discovery in heart rate variability data. *BMC Bioinformatics* 15:S2. doi: 10.1186/1471-2105-15-S6-S2

Pandit, D., Zhang, L., Liu, C., Aslam, N., Chattopadhyay, S., and Lim, C. P. (2017). "Noise reduction in ECG signals using wavelet transform and dynamic thresholding" in *Emerging Trends in Neuro Engineering and Neural Computation Series in Bio Engineering*. eds. A. Bhatti, K. H. Lee, H. Garmestani and C. P. Lim (Singapore: Springer), 193–206.

Park, S., Kim, W.-J., Cho, N.-J., Choi, C.-Y., Heo, N. H., Gil, H.-W., et al. (2019). Predicting intradialytic hypotension using heart rate variability. *Sci. Rep.* 9:2574. doi: 10.1038/s41598-019-39295-y

Pelosi, E., Emdin, M., Carpeggiani, C., Morales, M. A., Piacenti, M., Dattolo, P., et al. (1999). Impaired sympathetic response before intradialytic hypotension: a study based on spectral analysis of heart rate and pressure variability. *Clin. Sci.* 96, 23–31. doi: 10.1042/CS19980180

Pincus, S. M. (1991). Approximate entropy as a measure of system complexity. *Proc. Natl. Acad. Sci.* 88, 2297–2301. doi: 10.1073/pnas.88.6.2297

Pincus, S. (1995). Approximate entropy (ApEn) as a complexity measure. *Chaos* 5, 110–117. doi: 10.1063/1.166092

Rajendra Acharya, U., Paul Joseph, K., Kannathal, N., Lim, C. M., and Suri, J. S. (2006). Heart rate variability: a review. *Med. Bio. Eng. Comput.* 44, 1031–1051. doi: 10.1007/s11517-006-0119-0

Randall, D. C., Brown, D. R., Raisch, R. M., Yingling, J. D., and Randall, W. C. (1991). SA nodal parasympathectomy delineates autonomic control of heart rate power spectrum. *Am. J. Phys. Heart Circ. Phys.* 260, H985–H988. doi: 10.1152/ajpheart.1991.260.3.H985

Richman, J. S., and Moorman, J. R. (2000). Physiological time-series analysis using approximate entropy and sample entropy. *Am. J. Phys. Heart Circ. Phys.* 278, H2039–H2049. doi: 10.1152/ajpheart.2000.278.6.H2039

Ronco, C., Brendolan, A., Milan, M., Rodeghiero, M. P., Zanella, M., and La Greca, G. (2000). Impact of biofeedback-induced cardiovascular stability on hemodialysis tolerance and efficiency. *Kidney Int.* 58, 800–808. doi: 10.1046/j.1523-1755.2000.00229.x

Seong, E. Y., Zheng, Y., Winkelmayer, W. C., Montez-Rath, M. E., and Chang, T. I. (2018). The relationship between intradialytic hypotension and hospitalized mesenteric ischemia: a case-control study. *CJASN* 13, 1517–1525. doi: 10.2215/CJN.13891217

Sessa, F., Anna, V., Messina, G., Cibelli, G., Monda, V., Marsala, G., et al. (2018). Heart rate variability as predictive factor for sudden cardiac death. *Aging* 10, 166–177. doi: 10.18632/aging.101386

Shin, D.-G., Yoo, C.-S., Yi, S.-H., Bae, J.-H., Kim, Y.-J., Park, J.-S., et al. (2006). Prediction of paroxysmal atrial fibrillation using nonlinear analysis of the R-R interval dynamics before the spontaneous onset of atrial fibrillation. *Circ. J.* 70, 94–99. doi: 10.1253/circj.70.94

Shoji, T., Tsubakihara, Y., Fujii, M., and Imai, E. (2004). Hemodialysis-associated hypotension as an independent risk factor for two-year mortality in hemodialysis patients. *Kidney Int.* 66, 1212–1220. doi: 10.1111/j.1523-1755.2004.00812.x

Stefánsson, B. V., Brunelli, S. M., Cabrera, C., Rosenbaum, D., Anum, E., Ramakrishnan, K., et al. (2014). Intradialytic hypotension and risk of cardiovascular disease. *Clin. J. Am. Soc. Nephrol.* 9, 2124–2132. doi: 10.2215/CJN.02680314

Wang, X., Gao, H., Ma, C., Cui, C., Zhu, T., Cheng, X., et al. (2022). PN-QRS: An Uncertainty-Aware Qrs-Complex Detection Method for Wearable ECGS. *TechRxiv.* [preprint]. doi: 10.36227/techrxiv.21431673.v1

Xing, Y., Li, J., Hu, Z., Li, Y., Zhang, Y., Cui, C., et al. (2020). A portable neuECG monitoring system for cardiac sympathetic nerve activity assessment. in 2020 international conference on sensing, Measurement & Data Analytics in the era of artificial intelligence (ICSMD) (IEEE), 407–412.

Xing, Y., Zhang, Y., Yang, C., Li, J., Li, Y., Cui, C., et al. (2022). Design and evaluation of an autonomic nerve monitoring system based on skin sympathetic nerve activity. *Biomed. Signal Proc. Control* 76:103681. doi: 10.1016/j.bspc.2022.103681

Zhang, Y., Wang, J., Xing, Y., Cui, C., Cheng, H., Chen, Z., et al. (2022). Dynamics of cardiac autonomic responses during hemodialysis measured by heart rate variability and skin sympathetic nerve activity: the impact of Interdialytic weight gain. *Front. Physiol.* 13:890536. doi: 10.3389/fphys.2022.890536

frontiers | Frontiers in Neuroscience

TYPE Original Research
PUBLISHED 06 July 2023
DOI 10.3389/fnins.2023.1219553

OPEN ACCESS

EDITED BY
Lei Zhang,
Nanjing Normal University, China

REVIEWED BY
Yuanpeng Zhang,
Nantong University, China
Jing Xue,
Wuxi People's Hospital Affiliated to Nanjing Medical University, China
Mingming Zhang,
Southern University of Science and Technology, China

*CORRESPONDENCE
Baoguo Xu
✉ xubaoguo@seu.edu.cn

RECEIVED 09 May 2023
ACCEPTED 20 June 2023
PUBLISHED 06 July 2023

CITATION
Wang X, Xu B, Zhang W, Wang J, Deng L, Ping J, Hu C and Li H (2023) Recognizing emotions induced by wearable haptic vibration using noninvasive electroencephalogram. *Front. Neurosci.* 17:1219553. doi: 10.3389/fnins.2023.1219553

Recognizing emotions induced by wearable haptic vibration using noninvasive electroencephalogram

Xin Wang[1], Baoguo Xu[1]*, Wenbin Zhang[1], Jiajin Wang[1], Leying Deng[1], Jingyu Ping[1], Cong Hu[2] and Huijun Li[1]

[1]The State Key Laboratory of Digital Medical Engineering, Jiangsu Key Laboratory of Remote Measurement and Control, School of Instrument Science and Engineering, Southeast University, Nanjing, China, [2]Guangxi Key Laboratory of Automatic Detecting Technology and Instruments, Guilin University of Electronic Technology, Guilin, China

The integration of haptic technology into affective computing has led to a new field known as affective haptics. Nonetheless, the mechanism underlying the interaction between haptics and emotions remains unclear. In this paper, we proposed a novel haptic pattern with adaptive vibration intensity and rhythm according to the volume, and applied it into the emotional experiment paradigm. To verify its superiority, the proposed haptic pattern was compared with an existing haptic pattern by combining them with conventional visual–auditory stimuli to induce emotions (joy, sadness, fear, and neutral), and the subjects' EEG signals were collected simultaneously. The features of power spectral density (PSD), differential entropy (DE), differential asymmetry (DASM), and differential caudality (DCAU) were extracted, and the support vector machine (SVM) was utilized to recognize four target emotions. The results demonstrated that haptic stimuli enhanced the activity of the lateral temporal and prefrontal areas of the emotion-related brain regions. Moreover, the classification accuracy of the existing constant haptic pattern and the proposed adaptive haptic pattern increased by 7.71 and 8.60%, respectively. These findings indicate that flexible and varied haptic patterns can enhance immersion and fully stimulate target emotions, which are of great importance for wearable haptic interfaces and emotion communication through haptics.

KEYWORDS

affective haptics, wearable haptic vibration, electroencephalogram, affective computing, emotion recognition

1. Introduction

Emotions play a crucial role in human social communication and interaction (Keltner et al., 2019). With the development of computer technology and human-computer interaction, the field of affective computing (Picard, 1997) has emerged with the primary objective of studying and developing theories, methods, and systems to recognize, interpret, process, and simulate human emotions. Emotions normally change in response to external stimuli, and haptic stimuli can convey more intricate and subtle emotional experiences to the human body compared to visual and auditory stimuli (Hertenstein et al., 2006, 2009). Consequently, a new research trend has arisen in affective computing, which aims to explore the potential of incorporating haptic

technology into the processes of emotion recognition, interpretation, and simulation. This integration of haptic technology with affective computing has given rise to a new area called "Affective Haptics" (Eid and Al Osman, 2016).

Affective haptics focuses on the analysis, design, and evaluation of systems capable of inducing, processing, and simulating emotions through touch, which has been applied in many fields. For example, e-learning applications may benefit from affective haptics by reinvigorating learners' interest when they feel bored, frustrated, or angry (Huang et al., 2010). In healthcare applications, affective haptics can be used to treat depression and anxiety (Bonanni and Vaucelle, 2006), as well as assist in the design of enhanced communication systems for children with autism (Changeon et al., 2012). Other applications include entertainment and games (Hossain et al., 2011), social and interpersonal communication (Eid et al., 2008), and psychological testing (Fletcher et al., 2005).

Affective haptics consists of two subfields: emotion recognition and haptic interfaces. Emotion recognition is to identify emotional states through the user's behavior and physiological reactions (Kim et al., 2013). Haptic interfaces provide a communication medium between touch and the human subject (Culbertson et al., 2018). The current status of these two subfields will be discussed in the following paragraphs.

Emotion recognition can be broadly divided into two categories: recognition based on non-physiological signals and physiological signals (Fu et al., 2022). Non-physiological signals, such as speech signals (Zhang et al., 2022), facial expressions (Casaccia et al., 2021), and body posture (Dael et al., 2012), are easily influenced by personal volition and the environment, which makes it hard to accurately evaluate an individual's emotional state. Conversely, physiological signals, which include electroencephalogram (EEG) (Li et al., 2018), electrocardiogram (ECG) (Sarkar and Etemad, 2022), electromyogram (EMG) (Xu et al., 2023), and electrodermal activity (EDA) (Yin et al., 2022), vary according to emotional states, thus providing a more objective means of measuring emotions (Giannakakis et al., 2022). Among these signals, EEG is widely applied in various fields (Zhang et al., 2023; Zhong et al., 2023) and particularly closely associated with emotions (Zhang et al., 2020), so emotion recognition based on EEG has gained widespread usage.

The process of EEG-based emotion recognition involves emotion induction, EEG data preprocessing, feature extraction, and classification models. Koelstra created a publicly available emotion dataset, the DEAP dataset, which contains the EEG and peripheral physiological signals of subjects when watching music videos (Koelstra et al., 2012). Additionally, Zheng also published continuously three emotion datasets based on 62-channel EEG signals: SEED, SEED-IV, and SEED-V (Zheng et al., 2019a,b; Wu et al., 2022). Currently, the above datasets are commonly utilized to extract various features and boost the classification performance by deep learning algorithms (Craik et al., 2019). Liu proposed a three-dimension convolution attention neural network composed of spatio-temporal feature extraction module and EEG channel attention weight learning module (Liu et al., 2022). Zhong proposed a regularized graph neural network for EEG-based emotion recognition and validated its superiority on two public datasets, SEED, and SEED-IV (Zhong et al., 2022). The datasets mentioned above induced emotions in subjects using movie clips of specific emotions. Recently, a few researchers attempted to combine other senses to induce emotions. Wu developed a novel experimental paradigm that allowed odor stimuli to participate in video-induced emotions, and investigated the effects of the different stages of olfactory stimuli application on subjects' emotions (Wu et al., 2023). Raheel verified that enhancing more than two of the human senses from cold air, hot air, olfaction, and haptic effects could evoke significantly different emotions (Raheel et al., 2020). In general, emotion induction often relies on visual–auditory stimuli, whereas research on emotions induced by haptic stimuli remains quite limited. In other words, there are few studies on recognizing emotions using EEG signals in affective haptics, which to some extent hinders the development of this field.

The haptic interfaces in affective haptics are primarily used to transmit touch sensations to the user through haptic devices (Culbertson et al., 2018). Incorporating haptic devices into emotional induction can convey feelings that are difficult to express with visual–auditory stimuli. Nardelli developed a haptic device that mimicked the sensation of stroking by moving a fabric strip at varying speeds and pressures to examine how the speed and pressure of haptic stimuli elicit different emotional responses (Nardelli et al., 2020). Tsalamlal used a haptic stimulation method of spraying air on the participant's arm (Tsalamlal et al., 2018). Haynes developed a wearable electronic emotional trigger device that produced a sense of pleasure by stretching and compressing the skin surface of the wearer (Haynes et al., 2019). Wearable devices such as haptic jackets (Rahman et al., 2010) and haptic gloves (Mazzoni and Bryan-Kinns, 2015) are also commonly used in the field of affective haptics. Ceballos designed a haptic jacket and proposed a haptic vibration pattern that enhanced emotions in terms of valence and arousal (Ceballos et al., 2018). Subsequently, Li combined this vibration pattern with visual–auditory stimuli to form a visual–auditory-haptic fusion induction method, demonstrating that haptic vibration improved the accuracy of EEG-based emotion recognition tasks (Li et al., 2022). Whereas, the design of haptic patterns requires further exploration to better understand the mechanism between haptics and emotions.

In conclusion, significant progress has been made in the field of affective haptics. However, the mechanism between haptics and emotions has not yet been clearly revealed. This is primarily due to: (1) the limited application of objective emotion recognition methods in affective haptics; and (2) the lack of diverse haptic patterns. To address these issues, this study designed two haptic vibration patterns and combined them with conventional visual–auditory stimuli to induce emotions (joy, sadness, fear, and neutral). EEG signals were utilized to classify four target emotions and to explore the effects of haptic stimuli on emotions. The contributions of this work are summarized as follows,

- This paper proposed a novel haptic pattern with adaptive vibration intensity and rhythm according to the video volume, and applied it into the EEG emotional experiment paradigm.
- Compared to the existing haptic pattern with fixed vibration intensity and rhythm, the proposed haptic pattern significantly enhanced emotions.
- This paper analyzed the possible reasons for emotional enhancement due to haptic vibration from the perspective of neural patterns.

2. Materials and methods

In this work, we presented a novel framework for emotion recognition in combination with two haptic vibration patterns, as illustrated in Figure 1. It included visual–auditory-haptic fusion stimuli, EEG acquisition, EEG pre-processing, feature extraction, and emotion classification. Compared to the conventional EEG-based emotion recognition framework, the innovation of this study is to incorporate two haptic patterns with visual–auditory stimuli to explore the effects on emotions. The former is an existing haptic pattern, named Haptic 1. The latter is the proposed adaptive haptic pattern, named Haptic 2. Please see Section 2.3 for details of the two haptic patterns.

2.1. Subjects

Sixteen subjects (11 males and 5 females) aged between 20 and 30 years old, all right-handed and with no history of psychiatric illness, participated in the emotion experiment. Prior to the experiment, they were informed about the procedure and allowed to adapt to the experimental setting. The study was approved by the Ethics Committee of Southeast University, and all subjects received compensation for their involvement in the experiment.

2.2. Experimental setup

In this experiment, the subjects were exposed to visual–auditory-haptic fusion stimuli to induce emotion. The subjects wore a haptic vest and sat in a comfortable chair approximately 0.7 meters away from the monitor, as shown in Figure 2A. EEG signals were recorded by a 64-channel active electrode cap (Brain Products GmbH, Germany), following the international standard 10–20 system. All channels were referenced to the FCz channel, and the Fpz channel was chosen as the ground, as shown in Figure 2B, so a total of 63 channels of EEG data are available. During the recording, the impedance of all channels was kept below 10 kΩ. The EEG sampling frequency was set to 1,000 Hz, and a band-pass filter from 0.05 to 100 Hz was utilized to filter the EEG signals to attenuate high-frequency band components. Meanwhile, a notch filter at 50 Hz was applied to reduce power line interference.

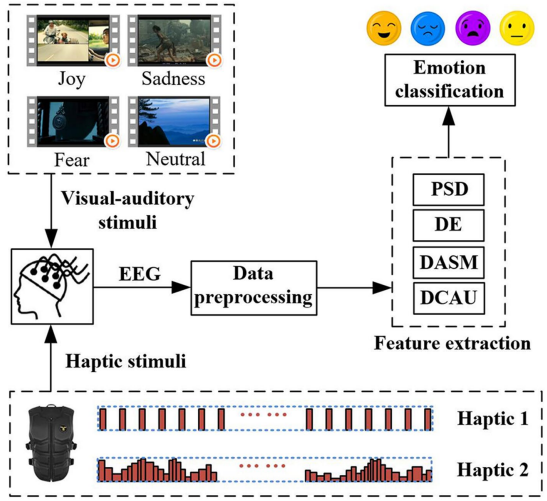

FIGURE 1
The framework for emotion recognition that incorporates two haptic patterns with traditional visual–auditory stimuli.

In order to elicit target emotions (joy, sadness, fear, and neutral) in the subjects, we employed a team of eight psychology graduate students to jointly select 16 movie clips that characterized the above four emotions. Each emotion corresponded to 4 movie clips, and all the movie clips were accompanied by Chinese subtitles. Further details can be found in Table 1.

The haptic stimuli implemented in the experiment were realized by using a haptic vest from bHaptics Inc., as illustrated in Figure 3A. As we can see from Figure 3B, this wearable and portable vest provides a double 5 × 4 matrix with motors positioned at both the front and back areas. Each motor provides two methods of vibration modulation: the first is to set the motor's vibration intensity and rhythm directly, while the second one adjusts the intensity and rhythm of the motor adaptively according to the intensity and frequency of the audio signals. Various haptic vibration patterns can be created by setting the individual parameters of each motor and the overall linkage to give users a specific feeling. The device is controlled through the Unity application via Bluetooth. By incorporating corresponding haptic vibration patterns with different movie clips, we generated emotional stimulation materials that combine visual, auditory, and haptic sensations. The detailed descriptions of the vibration patterns are provided in the next section Experimental protocol.

2.3. Experimental protocol

Two different haptic vibration patterns were designed to explore their differential effects on emotion. The detailed flow of the emotion experiment is depicted in Figure 4. In total, there were 16 sessions for each experiment. Firstly, each session had a 5-s cue to start. Next, the visual–auditory-haptic fusion stimuli were applied for approximately 4 min, where the visual–auditory stimuli used a previously selected film clip and the haptic stimuli were chosen from either of the two haptic patterns. Then, the subjects were required to conduct a 20-s self-assessment, followed by a 30-s rest. During the self-assessment, the subjects were requested to declare their emotional responses to each session, which would be used later as a reference for assessing the validity of the collected data.

The visual–auditory-haptic fusion stimuli scheme is shown in Figure 5. The visual–auditory stimuli were presented as movie clips throughout the experiment, while the haptic stimuli were applied only in the second half of each clip to explore whether haptic stimuli could enhance emotions. Importantly, we aimed to examine the differences between the two haptic patterns in inducing emotions. We randomly assigned Haptic 1 or Haptic 2 to the 16 movie clips. The first haptic vibration pattern employed a fixed vibration intensity and rhythm, where each emotion (joy, sadness, and fear) corresponded to a specific intensity and rhythm of vibration, as displayed in Table 2. This pattern has been demonstrated to be effective in previous studies (Ceballos et al., 2018; Li et al., 2022). The second haptic pattern adapted the vibration intensity and rhythm to the video volume. Specifically, the vibration intensity was positively correlated with volume, and the vibration rhythm was adjusted by setting a volume threshold below

which no vibration was generated. To maintain sample balance, both patterns were presented for eight sessions.

2.4. Data preprocessing

The EEG signals were decomposed using the EEGLAB toolbox. Initially, the sampling rate of the EEG signals was reduced from 1,000 to 200 Hz to expedite computation. Furthermore, a bandpass filter ranging from 1 to 50 Hz was applied to the signals. Then, the independent component analysis (ICA) was employed to remove EOG and EMG artifacts. Furthermore, the common average reference (CAR) was used to re-reference EEG signals to eliminate the global background activity. To correct for stimulus-unrelated variations in power over time, the EEG signal from the 5 s before each video was extracted as a baseline. Finally, the non-haptic and haptic signals were separately intercepted for subsequent analysis. In this study, the EEG signals were divided into five frequency bands: delta (1–4 Hz), theta (4–8 Hz), alpha (8–14 Hz), beta (14–31 Hz), and gamma (31–50 Hz).

2.5. Feature extraction and classification

After data preprocessing, we extracted the frequency domain features and their combinations in this study. Four features that proved to be efficient for EEG-based emotion recognition were compared (Zheng et al., 2019b), including PSD, DE, DASM, and DCAU.

The PSD feature is the average energy of EEG signals in five frequency bands for 63 channels, and can be computed directly using a 256-point short-time fourier transform (STFT) with a 1-s-long window and non-overlapped Hanning window. The DE feature is defined as follows,

$$h(X) = -\int_{-\infty}^{\infty} \frac{1}{\sqrt{2\pi\delta^2}} \exp\frac{(x-\mu)^2}{2\delta^2} \log\frac{1}{\sqrt{2\pi\delta^2}} \exp\frac{(x-\mu)^2}{2\delta^2} dx = \frac{1}{2}\log 2\pi e\delta^2 \quad (1)$$

where the time series X obeys the Gauss distribution $N(\mu, \delta^2)$, x is a variable, and π and e are constants. It has been proven that, in a certain band, DE corresponds to the logarithmic spectral energy of a fixed-length EEG series (Shi et al., 2013). Compared with the PSD, DE has a balanced ability to distinguish between low and high frequency energy in EEG patterns.

The DASM feature is calculated as the differences between DE features of 28 pairs of hemispheric asymmetry electrodes (Fp1-Fp2, F7-F8, F3-F4, FT7-FT8, FC3-FC4, T7-T8, P7-P8, C3-C4, TP7-TP8, CP3-CP4, P3-P4, O1-O2, AF3-AF4, F5-F6, FC5-FC6, FC1-FC2, C5-C6, C1-C2, CP5-CP6, CP1-CP2, AF7-AF8, P5-P6, P1-P2, PO7-PO8, PO3-PO4, FT9-FT10, TP9-TP10, and F1-F2), expressed as

$$DASM = h\left(X_i^{left}\right) - h\left(X_i^{right}\right) \quad (2)$$

The DCAU feature is defined as the differences between DE features of 22 pairs of frontal-posterior electrodes (FT7-TP7, FC5-CP5, FC3-CP3, FC1-CP1, FCZ-CPZ, FC2-CP2, FC4-CP4, FC6-CP6, FT8-TP8, F7-P7, F5-P5, F3-P3, F1-P1, FZ-PZ, F2-P2, F4-P4, F6-P6, F8-P8, Fp1-O1,Fp2-O2, AF3-CB1, and AF4-CB2). DCAU is defined as

$$DCAU = h\left(X_i^{frontal}\right) - h\left(X_i^{posterior}\right) \quad (3)$$

After feature extraction, we utilized linear-kernel SVM classifiers for the 4-class classification. For statistical analysis, a 4-fold cross-validation strategy was utilized to evaluate the classification performance.

TABLE 1 Details of selected film clips.

No.	Label	File clips sources	Film time
1	Joy	Lost in Thailand	1:03:41–1:08:30
2	Joy	Mr. Bean's Holiday	0:36:47–0:40:55
3	Joy	Kung Fu Hustle	0:31:58–0:36:49
4	Joy	Fight Back to School	0:39:52–0:43:34
5	Sadness	Aftershock	0:19:36–0:23:15
6	Sadness	Aftershock	1:47:49–1:51:47
7	Sadness	To live	1:12:55–1:17:45
8	Sadness	To live	1:59:49–2:03:32
9	Fear	The Conjuring	0:37:06–0:40:41
10	Fear	The Skeleton Key	1:23:43–1:27:29
11	Fear	Black Swan	1:21:48–1:25:20
12	Fear	Dead Silence	0:08:09–0:12:11
13	Neutral	Huangshan documentary	0:00:50–0:04:36
14	Neutral	Mount Tai documentary	0:00:38–0:04:36
15	Neutral	Aerial China: Xinjiang	0:2:29–0:6:33
16	Neutral	Aerial China: Shanxi	0:31:05–0:34:53

3. Results

3.1. Analysis of frequency band energy distribution

To investigate the continual progression of emotional states, we employed wavelet transform methods to conduct time-frequency analysis on EEG signals. A 5-s time window was used to slide the EEG data without overlapping for analysis. According to the two haptic patterns, we calculated the average value of all channels across all subjects in four emotion types, with the results presented in Figures 6, 7. We find that the energy distribution of all emotional states diminishes with an increase in frequency. In comparison to the corresponding non-haptic patterns, the energy distributions of the three emotions (joy, sadness, and fear) are obviously higher in the high-frequency band under the two haptic patterns. Joy and sadness show no obvious changes in the

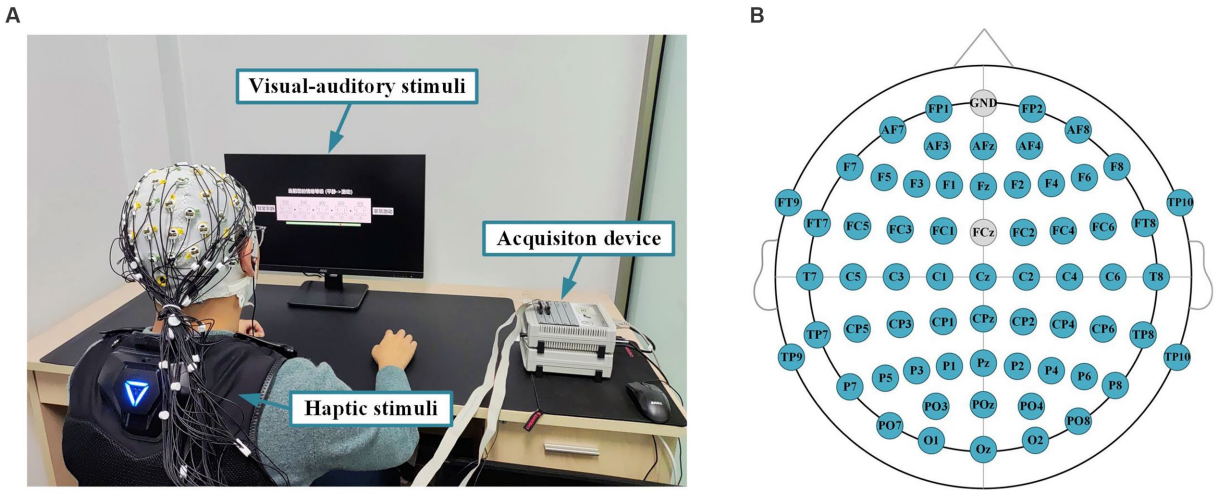

FIGURE 2
Experimental setup and paradigm for emotion recognition. **(A)** An experimental platform for evoking subjects' emotions through the visual–auditory-haptic fusion stimulation. **(B)** The EEG cap layout for 64 channels.

FIGURE 3
The haptic vest with a dual vibration motors matrix: **(A)** Vest. **(B)** Front view of the motors matrix.

TABLE 2 Parameters of Haptic 1.

Emotion type	Haptic parameters	
Joy	Frequency: 1.4 Hz Intensity: 90%	Direction: Inward Pattern: Discrete
Sadness	Frequency: 0.45 Hz Intensity: 50%	Direction: Outward Pattern: Discrete
Fear	Frequency: 0.5 Hz Intensity: 90%	Direction: Inward Pattern: Discrete

low-frequency band, whereas fear emotions reveal a decrease in energy. This suggests that haptic vibration patterns are capable of affecting various emotions. Moreover, it can be seen that Haptic 2 has more energy in the alpha, beta, and gamma bands than Haptic 1 when comparing Figure 6 with Figure 7. Since the average energy is based on all channels and all time segments, the next paragraph requires further analysis considering topographical maps.

3.2. Analysis of brain topographical maps

In order to analyze whether and how haptic stimuli affect emotional brain regions, we computed the mean DE features across all subjects in five frequency bands and then projected them onto the scalp. To highlight the changes more distinctly, the corresponding baseline features (collected during the 5-s preparation period) were subtracted from the projected DE features. Figures 8, 9 display the brain topographic maps for different emotional states in non-Haptic 1, Haptic 1, non-Haptic 2, and Haptic 2, respectively.

In Figure 8, the average neural patterns for different emotions in non-Haptic 1 and Haptic 1 are depicted. In the non-Haptic 1 state, the four types of emotions differ in the lateral temporal areas mainly in beta and gamma frequency bands. Specifically, the lateral temporal areas exhibit obvious activation for happy emotions in beta and gamma bands, while the corresponding areas for neutral emotions are inhibited. The prefrontal areas of sadness show more activation in beta and gamma bands compared to other emotions. The alpha band activation in the parietal areas is higher for happy and neutral emotions than for sadness and fear. The occipital regions in the theta and alpha bands for all emotions show low activation, with sadness and fear showing less activation. Afterward, with the application of Haptic 1, the energy distribution of different emotions across brain regions follows a similar trend as non-Haptic 1, but with more notable variations. The lateral temporal areas show more activation in beta and gamma bands for joy. The lateral temporal and parietal areas for sadness and fear concentrate more energy in both beta and gamma bands. Therefore, haptic vibration not only maintains the fundamental neural patterns for different emotions, but also increases the activation of the lateral temporal and prefrontal areas.

Figure 9 presents the average neural patterns of the four emotions for all subjects in non-Haptic 2 or Haptic 2. In non-Haptic 2, the brain topography maps for the four emotions are similar to those displayed in Figure 8, with only minor discrepancies. This phenomenon can be attributed to the fact that subjects are unlikely

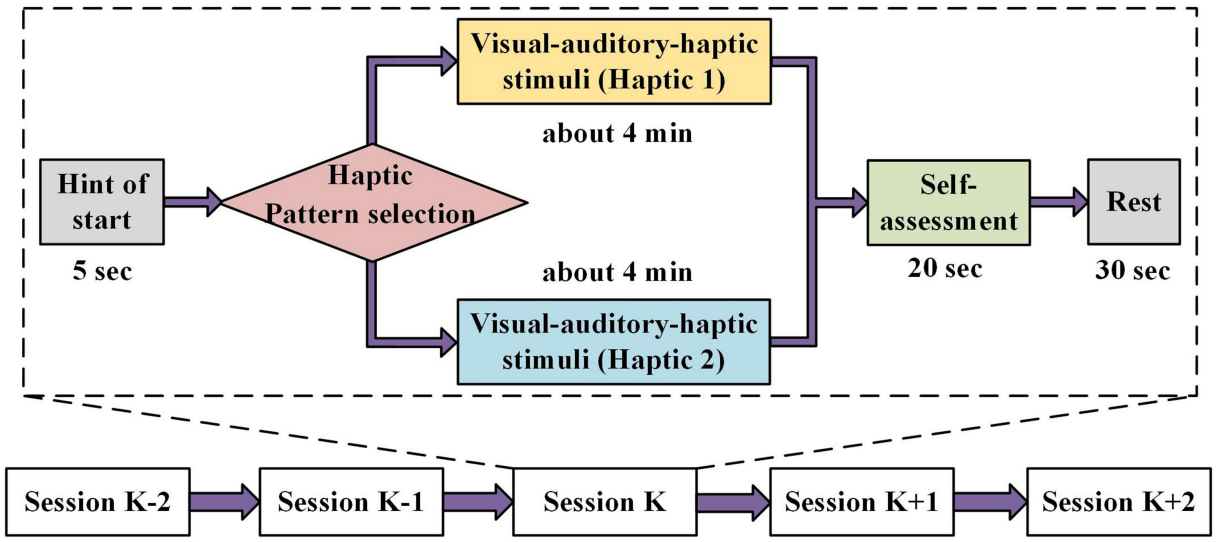

FIGURE 4
Emotion experimental paradigm based on the visual–auditory-haptic stimuli. The visual–auditory stimuli include a previously selected film clip and the haptic stimuli chosen from either of the two haptic patterns.

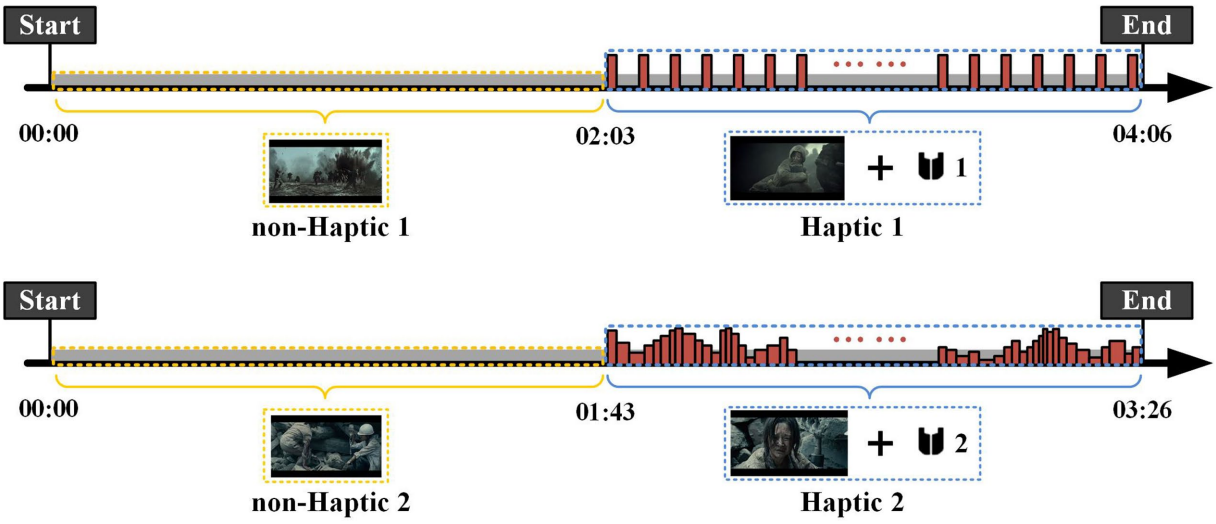

FIGURE 5
Procedure of two visual–auditory-haptic fusion stimuli. The visual–auditory stimuli were presented as movie clips throughout the experiment, while the haptic stimuli were applied only in the second half of each clip. The first haptic vibration pattern employed a fixed vibration intensity and rhythm, and the second haptic pattern adapted the vibration intensity and rhythm to the video volume.

to respond identically to various audiovisual materials conveying the same emotion. Subsequently, the neural patterns of the different emotions in Haptic 2 state showed some similarity to those of Haptic 1. However, there is a more concentrated distribution of energy in brain regions in Haptic 2 state, with greater activation in lateral temporal and prefrontal areas in beta and gamma bands, and more inhibition in occipital areas in alpha bands. Hence, the above two haptic patterns indeed have different effects on emotion-related regions.

3.3. Classification performance

We employed SVM to classify the DE features in all frequency bands. Figure 10 provides a visual representation of the emotional classification results for 16 subjects in non-Haptic 1, Haptic 1, non-Haptic 2, and Haptic 2, respectively. It can be observed that the classification accuracy of DE features in beta, gamma, and full band frequency ranges is significantly higher than in delta and theta bands. This indicates that the delta and theta bands have little impact on

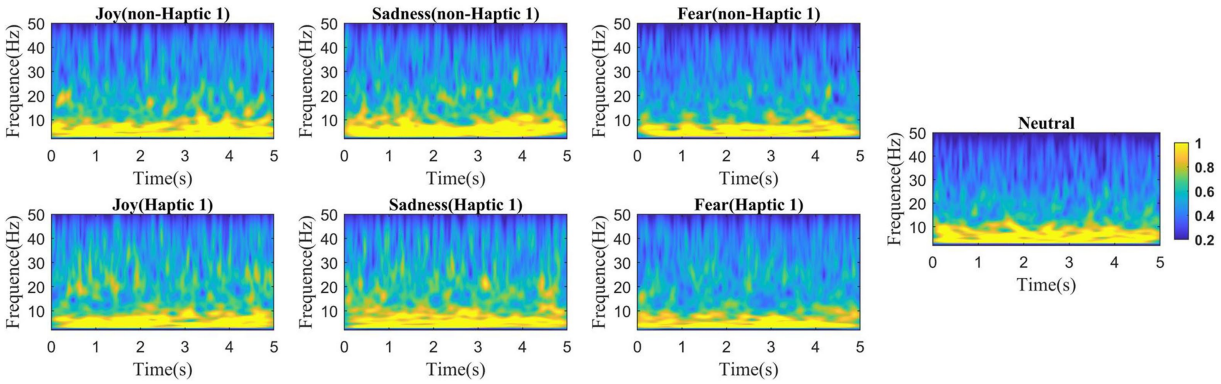

FIGURE 6
Mean time-frequency analysis based on 16 subjects with non-Haptic 1 or Haptic 1.

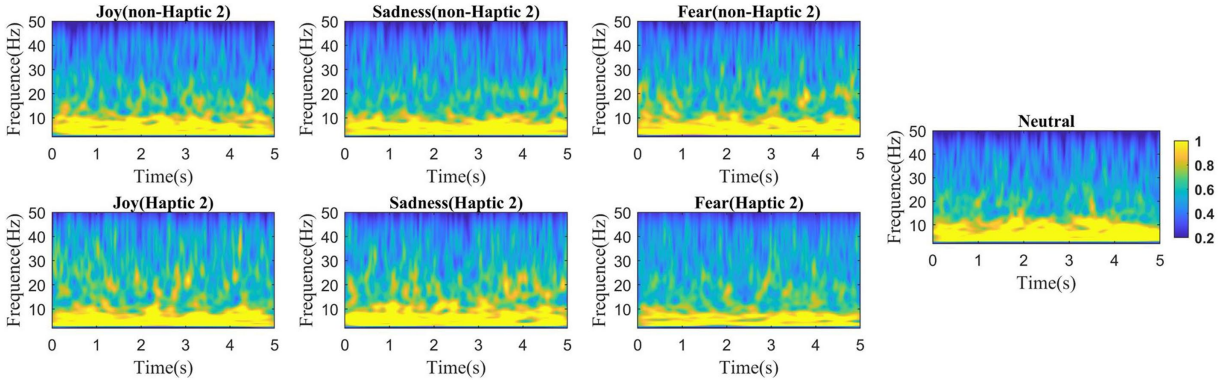

FIGURE 7
Mean time-frequency analysis based on 16 subjects with non-Haptic 2 or Haptic 2.

emotion recognition, similar to the difficulty of finding obvious differences between these two bands in different emotions in brain topographic maps. Moreover, the accuracy in haptic patterns is significantly higher than that in non-haptic patterns, especially in beta, gamma, and full band frequencies. The results demonstrate that combining traditional visual–auditory stimuli with haptic stimuli can effectively induce emotions.

Tables 3, 4 present the average SVM classification results of different features of the five frequency bands in Haptic 1 and Haptic 2, respectively. Meanwhile, the paired-sample *t*-test results on the accuracy of four features in different frequency bands for the two cases of non-Haptic 1 - Haptic 1, and non-Haptic 2 - Haptic 2 are shown in Table 5. The results indicate that the average accuracy of PSD, DE, DASM, and DCAU features in the two haptic patterns is significantly higher than that in non-haptic patterns, demonstrating that haptic stimuli can enhance subjects' emotions. In most cases, the average accuracy of DE features is higher than that of the other three features, indicating that DE features are superior in representing emotions. Additionally, the average accuracy of beta and gamma bands is significantly higher than that of other bands for four features. These findings suggest that beta and gamma bands play a crucial role in EEG-based emotion recognition and are highly correlated with emotional states. These quantitative results are consistent with the qualitative results obtained from the brain topographic maps.

To further compare the emotional enhancement effects of different haptic patterns, we calculated the average classification accuracy growth rates of four features across various frequency bands in Haptic 1 and Haptic 2, as presented in Table 6. It can be seen that the accuracy growth rates in Haptic 2 are higher than those in Haptic 1 for all features and all frequency bands, with a more significant increase observed in the alpha and beta frequency bands. Taking DE features as an example, the classification accuracy of Haptic 1 and Haptic 2 increased by 7.71 and 8.60%, respectively. In particular, as shown in Table 5, Haptic 2 presents a significant improvement in classification accuracy compared to not applying haptic stimuli in almost all bands, but the classification accuracy of Haptic 1 is not significantly improved in the lower bands. These results suggest that Haptic 2, with adaptive vibration intensity and rhythm, is more effective in eliciting emotions than Haptic 1, which has constant vibration intensity and rhythm.

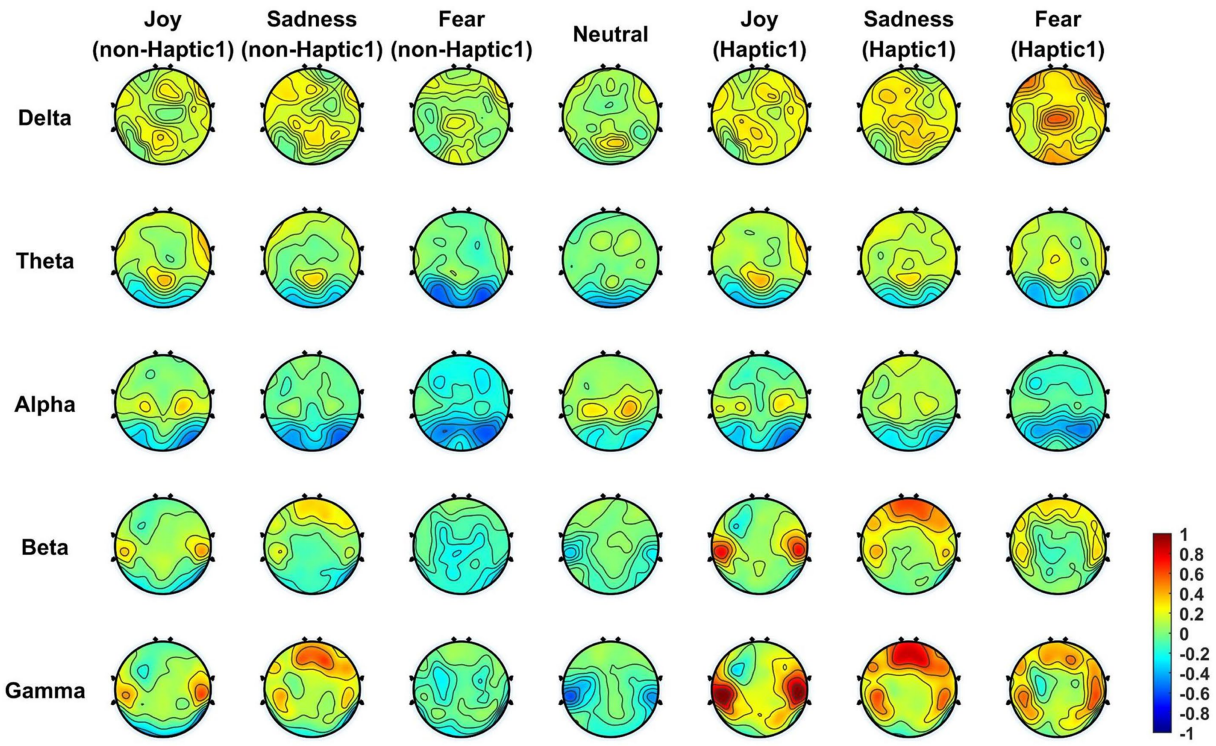

FIGURE 8
The average neural patterns in different emotional states for 16 subjects with non-Haptic 1 or Haptic 1.

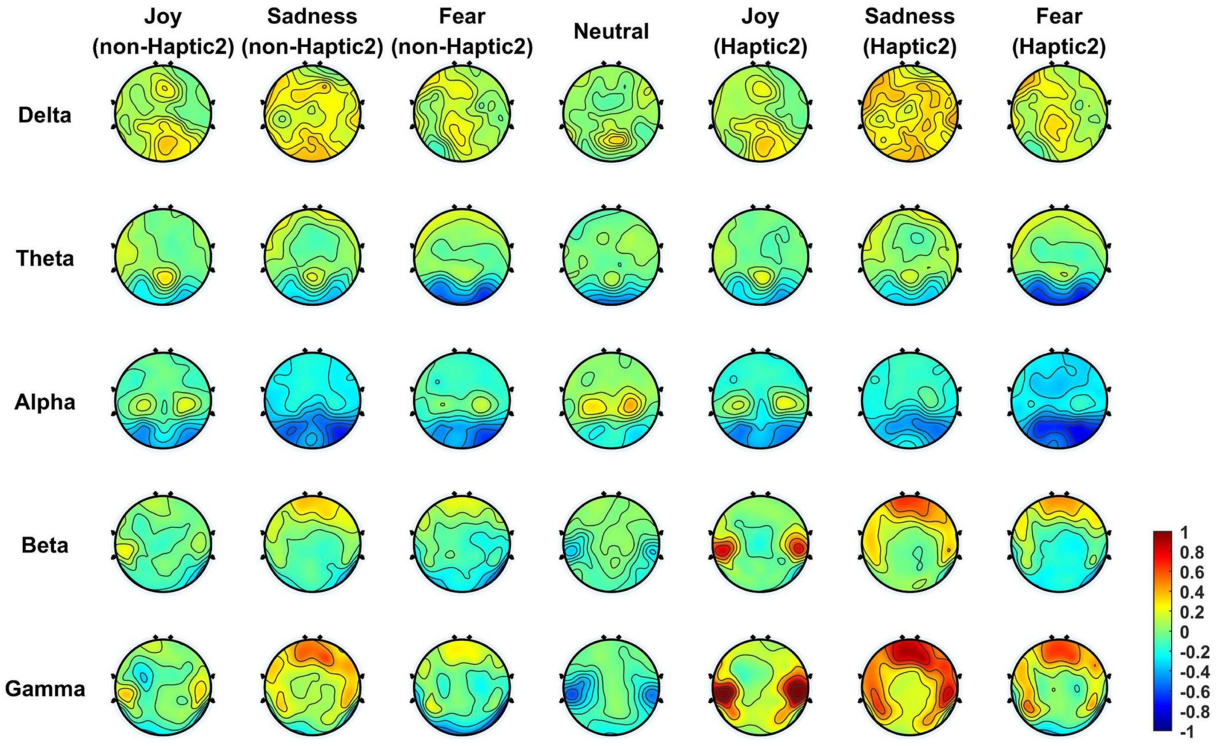

FIGURE 9
The average neural patterns in different emotional states for 16 subjects with non-Haptic 2 or Haptic 2.

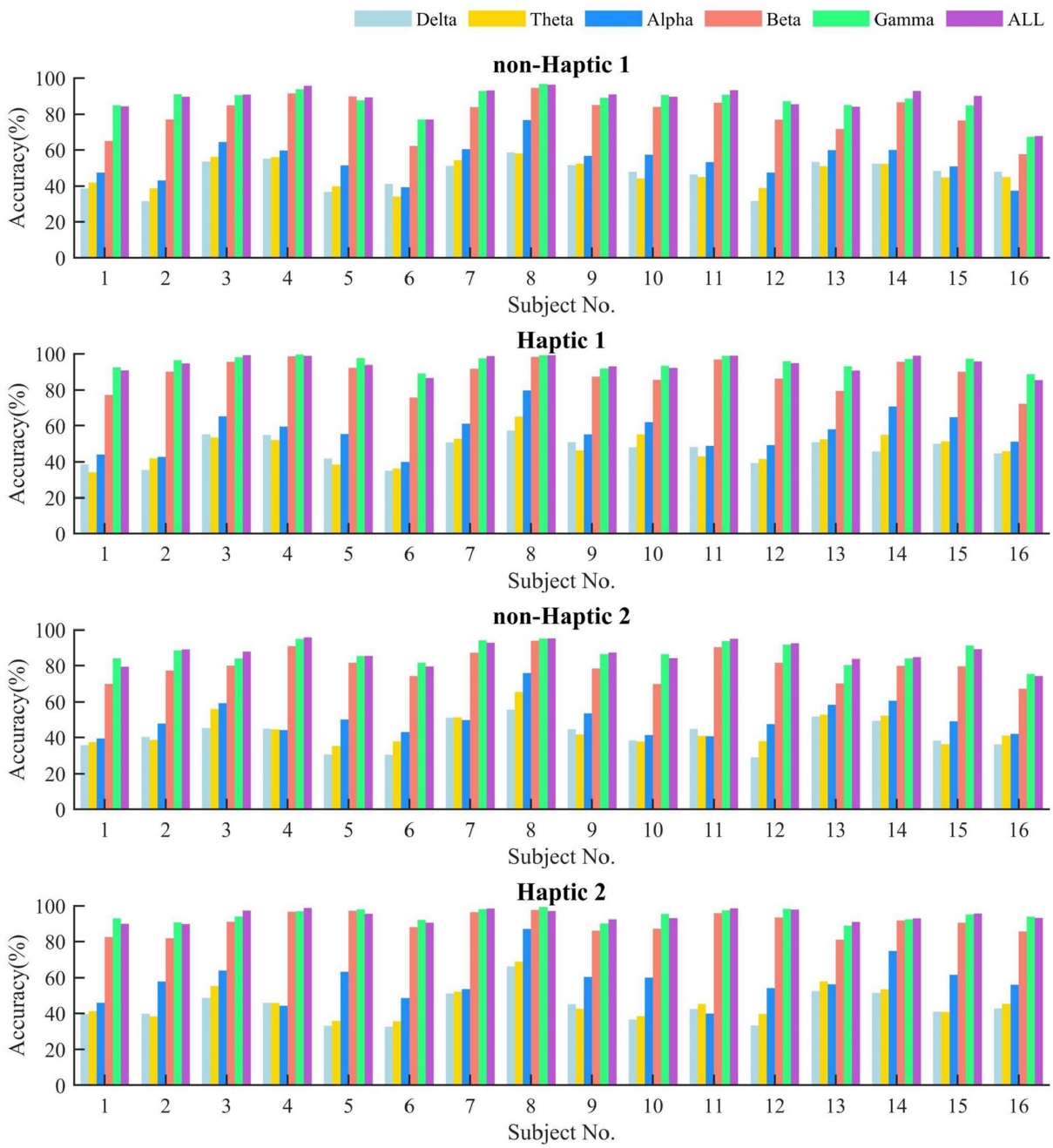

FIGURE 10
The average classification accuracy of DE feature by SVM in different frequency bands with non-haptic and haptic patterns.

4. Discussion

4.1. Important brain regions and frequency bands for emotion

This paper presented the average neural patterns associated with four emotional states evoked by visual–auditory stimuli, as depicted in Figures 8, 9. Notably, the activation of lateral temporal and prefrontal areas in beta and gamma bands varied obviously in different emotional states. It suggests that these brain regions are highly correlated with different emotions and are considered the key regions for generating emotions. Overall, these findings are consistent with the results of previous research (Zheng and Lu, 2015; Zheng et al., 2019b). Besides, the accuracy of emotion classification was obviously higher in beta and gamma bands compared to other single bands. Interestingly, in some cases, the accuracy in total bands was lower than that in gamma bands. This may be due to the low classification accuracy of lower frequency band signals, which disturb the overall emotion classification. In summary, collecting EEG signals in beta and gamma bands from lateral temporal and prefrontal regions is an effective approach for recognizing emotions induced by

TABLE 3 The average classification accuracy of four features in different frequency bands with non-Haptic 1 and Haptic 1.

	PSD		DE		DASM		DCAU	
	Non-Haptic 1	Haptic 1	Non-Haptic 1	Haptic 1	Non-Haptic 1	Haptic 1	Non-Haptic 1	Haptic 1
Delta	40.77%	40.96%	46.60%	46.73%	36.36%	36.40%	37.99%	38.27%
Theta	40.12%	40.92%	46.99%	47.87%	35.70%	35.85%	38.58%	38.75%
Alpha	45.37%	47.72%	54.05%	56.75%	39.81%	41.48%	40.89%	42.18%
Beta	72.47%	82.06%	79.60%	88.35%	65.37%	73.36%	60.59%	68.58%
Gamma	82.56%	91.16%	87.30%	95.42%	77.06%	84.11%	70.15%	79.37%
Total	82.82%	89.87%	88.09%	94.53%	78.99%	85.69%	75.34%	82.62%

TABLE 4 The average classification accuracy of four features in different frequency bands with non-Haptic 2 and Haptic 2.

	PSD		DE		DASM		DCAU	
	Non-Haptic 2	Haptic 2	Non-Haptic 2	Haptic 2	Non-Haptic 2	Haptic 2	Non-Haptic 2	Haptic 2
Delta	37.28%	38.16%	41.64%	43.90%	33.60%	34.59%	35.52%	35.81%
Theta	38.27%	39.39%	44.19%	46.01%	34.39%	35.24%	36.88%	38.07%
Alpha	42.59%	49.54%	50.19%	57.96%	38.77%	43.40%	39.09%	42.41%
Beta	72.05%	84.61%	79.52%	90.17%	66.06%	76.35%	57.09%	70.86%
Gamma	82.41%	91.79%	87.34%	94.60%	77.89%	86.32%	68.49%	79.56%
Total	80.81%	91.40%	87.31%	94.51%	78.32%	86.79%	71.59%	82.36%

TABLE 5 Paired-sample *t*-test results on the accuracy of four features in different frequency bands for two cases of non-Haptic 1 - Haptic 1, and non-Haptic 2 - Haptic 2 (α=0.05).

	(Non-Haptic 1) – (Haptic 1)				(Non-Haptic 2) - (Haptic 2)			
	PSD	DE	DASM	DCAU	PSD	DE	DASM	DCAU
Delta	0.7921	0.8896	0.9598	0.5535	0.3148	0.0138	0.0624	0.7836
Theta	0.8374	0.4872	0.0686	0.1751	0.0469	0.0045	0.2201	0.2252
Alpha	0.1325	0.0745	0.2065	0.4003	0.0001	0.0001	0.0001	0.0286
Beta	0.0001	0.0001	0.0001	0.0001	0.0001	0.0001	0.0001	0.0001
Gamma	0.0001	0.0001	0.0001	0.0001	0.0001	0.0001	0.0001	0.0001
Total	0.0001	0.0001	0.0001	0.0001	0.0001	0.0001	0.0001	0.0001

TABLE 6 The average classification accuracy growth rates of four features in different frequency bands with Haptic 1 and Haptic 2.

	PSD		DE		DASM		DCAU	
	Growth rate 1	Growth rate 2	Growth rate 1	Growth rate 2	Growth rate 1	Growth rate 2	Growth rate 1	Growth rate 2
Delta	0.85%	2.12%	1.23%	5.76%	0.63%	3.32%	0.33%	0.11%
Theta	0.24%	3.05%	2.09%	4.13%	0.52%	2.37%	0.93%	3.60%
Alpha	5.67%	17.36%	5.57%	15.87%	4.89%	12.94%	3.69%	9.70%
Beta	14.36%	18.22%	11.75%	13.93%	13.56%	16.04%	14.55%	25.23%
Gamma	11.35%	11.95%	7.79%	8.62%	9.93%	11.40%	14.36%	16.96%
Total	8.95%	13.66%	7.71%	8.60%	9.49%	11.46%	10.35%	15.56%

visual–auditory stimuli. This finding can be utilized as a reference to simplify the number of EEG acquisition electrodes and reduce the data scale.

4.2. Neural pattern for haptic-enhanced emotion

This paper demonstrated the superiority of the application of haptic patterns over non-haptic patterns in EEG-based emotion recognition. Certainly, previous studies have come to a similar conclusion that haptic stimuli improve the efficiency of emotion recognition tasks (Raheel et al., 2020; Li et al., 2022). However, few studies have analyzed and explained the phenomenon from the perspective of neural patterns. Notably, haptic stimuli not only maintain the fundamental neural patterns for different emotions, but also increase the activation of lateral temporal and prefrontal areas that closely associated with emotion, as illustrated in Figures 8, 9. We speculate that there are two reasons for this phenomenon: (1) Although haptic stimuli applied to the torso typically activate the somatosensory cortex in the parietal area directly, there was only a weak enhancement of the parietal area in the brain topographic maps. However, the brain is a complex interconnected structure, and it is possible that haptic stimuli affect lateral temporal and frontal regions through the somatosensory cortex. Meanwhile, a converging body of literature has shown that the somatosensory cortex plays an important role in each stage of emotional processing (Kropf et al., 2019; Sel et al., 2020). (2) The application of haptic stimuli increased the subjects' immersion. Rather than exclusively focusing on haptic stimuli, the subjects' senses may have been fully engaged in watching emotional movie clips.

4.3. Efficiency of the proposed haptic pattern

In this paper, a novel haptic pattern (Haptic 2) was designed and compared with the existing haptic pattern (Haptic 1) in EEG emotional paradigm. The experimental results demonstrate that different haptic patterns have varying levels of emotional enhancement. According to the *t*-test in Table 5, the classification accuracy of Haptic 2 was significantly increased over non-haptic pattern in almost all frequency bands. However, the classification accuracy of Haptic 1 was not significantly improved in the lower bands. Furthermore, as shown in Table 6, the classification accuracy growth rates in Haptic 2 were slightly higher than those in Haptic 1. As we can see from Figure 9, Haptic 2 resulted in a more concentrated energy distribution in subjects' brain regions. Specifically, lateral temporal and prefrontal regions increased activation in beta and gamma bands, while occipital regions exhibited greater inhibition in alpha bands. This amplified difference in energy distribution in emotion-related regions may account for higher classification accuracy growth rates of Haptic 2. Additionally, based on subjective feedback from subjects, most of them said that Haptic 2 was more suitable for the movie scene. We hypothesize that the adaptive adjustment of vibration intensity and rhythm with audio in Haptic 2 can enhance immersion and fully stimulate target emotions compared to Haptic 1. In general, these findings suggest that the proposed haptic pattern has superiority in evoking target emotions to some degree.

4.4. Limitations and future work

In our work, we combined two haptic vibration patterns with visual–auditory stimuli to induce emotions and classify four emotions based on EEG signals. However, our study still has certain limitations. Firstly, the number of subjects was not large enough, and the age range was limited to 20 to 30 years old. In the future, we will extend the proposed experiment paradigm to a larger number of subjects and a wider age range to investigate whether there are gender and age differences in the effects of haptic stimuli on emotion. In addition, this study only extracted features from single-channel EEG data, ignoring the functional connectivity between brain regions. Subsequently, we will utilize EEG-based functional connectivity patterns and more advanced deep learning algorithms considering brain topology in future studies. Moreover, our experimental results preliminarily showed the adaptive haptic vibration pattern is more advantageous to enhance emotion, while more detailed and reasonable designs of the haptic patterns require further exploration. In the design of the two haptic patterns, we only considered vibration intensity and rhythm, but neglected the impact of vibration location. Hence, we will create more comprehensive haptic vibration patterns to further investigate the mechanism of haptic stimuli on emotion enhancement.

5. Conclusion

The motivation of this study is to investigate the variations in emotional effects induced by different haptic patterns. This paper proposed a novel haptic pattern with adaptive vibration intensity and rhythm according to the video volume, and compared it to the existing haptic pattern in emotional experiment paradigm. Specifically, the above two haptic patterns were combined with traditional visual–auditory stimuli to induce emotions, and four target emotions were classified based on EEG signals. Compared with the visual–auditory stimuli, the visual–auditory-haptic fusion stimuli significantly improved the emotion classification accuracy. The possible reason is that haptic stimuli cause distinct activation in lateral temporal and prefrontal areas of the emotion-related regions. Moreover, different haptic patterns had varying effects on enhancing emotions. The classification accuracy of the existing and the proposed haptic patterns increased by 7.71 and 8.60%, respectively. In addition, the proposed haptic pattern showed a significant improvement in classification accuracy compared to non-haptic pattern in almost all bands. The results show that the haptic pattern with adaptive vibration intensity and rhythm is more effective in enhancing emotion. Therefore, flexible and varied haptic patterns have extensive potential in the field of affective haptics.

Data availability statement

The raw data supporting the conclusions of this article will be made available by the authors, without undue reservation.

Ethics statement

The studies involving human participants were reviewed and approved by Ethics Committee of Southeast University. The patients/participants provided their written informed consent to participate in this study.

Author contributions

XW and BX designed the study, analyzed the data, and wrote the manuscript. XW, WZ, and JW set up the experiment platform. LD and JP performed the experiment. JW, CH, and HL reviewed and edited the manuscript. All authors read and approved the final manuscript.

Funding

This work was supported by National Key Research and Development Program of China (2022YFC2405602), the Natural Science Foundation of Jiangsu Province (No. BK20221464), the Key Research and Development Program of Jiangsu Province (No. BE2022363), the Basic Research Project of Leading Technology of Jiangsu Province (No. BK20192004), the National Natural Science Foundation of China (Nos. 92148205, 62173088, and 62173089), and Guangxi Key Laboratory of Automatic Detecting Technology and Instruments (No. YQ22207).

Acknowledgments

We would like to thank Muhui Xue, Zelin Gao and numerous helpers for their suggestions in implementing experiment.

Conflict of interest

The authors declare that the research was conducted in the absence of any commercial or financial relationships that could be construed as a potential conflict of interest.

Publisher's note

References

Bonanni, L., and Vaucelle, C. (2006). "A framework for haptic psycho-therapy," in Proceedings of IEEE ICPS Pervasive Servives (ICPS), France.

Casaccia, S., Sirevaag, E. J., Frank, M. G., O'Sullivan, J. A., Scalise, L., and Rohrbaugh, J. W. (2021). Facial muscle activity: high-sensitivity noncontact measurement using laser doppler vibrometry. *IEEE Trans. Instrum. Meas.* 70, 1–10. doi: 10.1109/TIM.2021.3060564

Ceballos, R., Ionascu, B., Park, W., and Eid, M. (2018). Implicit emotion communication: EEG classification and haptic feedback. *ACM Trans. Multimed. Comput. Commun. Appl.* 14, 1–18. doi: 10.1145/3152128

Changeon, G., Graeff, D., Anastassova, M., and Lozada, J. (2012). "Tactile emotions: a vibrotactile tactile gamepad for transmitting emotional messages to children with autism" in *Haptics: Perception, devices, mobility, and communication, 2012* (Finland)

Craik, A., He, Y. T., and Contreras-Vidal, J. L. (2019). Deep learning for electroencephalogram (EEG) classification tasks: a review. *J. Neural Eng.* 16:031001. doi: 10.1088/1741-2552/ab0ab5

Culbertson, H., Schorr, S. B., and Okamura, A. M. (2018). Haptics: the present and future of artificial touch sensation. *Annu. Rev. Control Robot. Auton. Syst.* 1, 385–409. doi: 10.1146/annurev-control-060117-105043

Dael, N., Mortillaro, M., and Scherer, K. R. (2012). Emotion expression in body action and posture. *Emotion* 12, 1085–1101. doi: 10.1037/a0025737

Eid, M. A., and Al Osman, H. (2016). Affective haptics: current research and future directions. *IEEE Access.* 4, 26–40. doi: 10.1109/ACCESS.2015.2497316

Eid, M., Cha, J. E., and El Saddik, A. (2008). "HugMe: a haptic videoconferencing system for interpersonal communication," VECIMS 2008 – IEEE conference on virtual environments, human-computer interfaces and measurement systems proceedings. Turkey

Fletcher, D. C., Dreer, L. E., and Elliott, T. R. (2005). Tactile analogue scale instrument for investigation of low vision patient psychological characteristics. *Int. Congr. Ser.* 1282, 125–128. doi: 10.1016/j.ics.2005.05.173

Fu, Z. Z., Zhang, B. N., He, X. R., Li, Y. X., Wang, H. Y., and Huang, J. (2022). Emotion recognition based on multi-modal physiological signals and transfer learning. *Front. Neurosci.* 16:1000716. doi: 10.3389/fnins.2022.1000716

Giannakakis, G., Grigoriadis, D., Giannakaki, K., Simantiraki, O., Roniotis, A., and Tsiknakis, M. (2022). Review on psychological stress detection using biosignals. *IEEE Trans. Affect. Comput.* 13, 440–460. doi: 10.1109/TAFFC.2019.2927337

Haynes, A., Simons, M. F., Helps, T., Nakamura, Y., and Rossiter, J. (2019). A wearable skin-stretching tactile interface for human-robot and human-human communication. *IEEE Robot. Autom. Lett.* 4, 1641–1646. doi: 10.1109/LRA.2019.2896933

Hertenstein, M. J., Holmes, R., McCullough, M., and Keltner, D. (2009). The communication of emotion via touch. *Emotion* 9, 566–573. doi: 10.1037/a0016108

Hertenstein, M. J., Keltner, D., App, B., Bulleit, B. A., and Jaskolka, A. R. (2006). Touch communicates distinct motions. *Emotion* 6, 528–533. doi: 10.1037/1528-3542.6.3.528

Hossain, S. K. A., Rahman, A., and El Saddik, A. (2011). Measurements of multimodal approach to haptic interaction in second life interpersonal communication system. *IEEE Trans. Instrum. Meas.* 60, 3547–3558. doi: 10.1109/TIM.2011.2161148

Huang, K., Starner, T., Do, E., Weinberg, G., Kohlsdorf, D., Ahlrichs, C., et al. (2010). "Mobile music touch: mobile tactile stimulation for passive learning," Proceedings of the SIGCHI conference on Human factors in computing systems (CHI), 2010 Atlanta

Keltner, D., Sauter, D., Tracy, J., and Cowen, A. (2019). Emotional expression: advances in basic emotion theory. *J. Nonverbal Behav.* 43, 133–160. doi: 10.1007/s10919-019-00293-3

Kim, M. K., Kim, M., Oh, E., and Kim, S. P. (2013). A review on the computational methods for emotional state estimation from the human EEG. *Comput. Math. Method Med.* 2013:573734. doi: 10.1155/2013/573734

Koelstra, S., Muhl, C., Soleymani, M., Lee, J. S., Yazdani, A., Ebrahimi, T., et al. (2012). DEAP: a database for emotion analysis using physiological signals. *IEEE Trans. Affect. Comput.* 3, 18–31. doi: 10.1109/T-AFFC.2011.15

Kropf, E., Syan, S. K., Minuzzi, L., and Frey, B. N. (2019). From anatomy to function: the role of the somatosensory cortex in emotional regulation. *Braz. J. Psychiat.* 41, 261–269. doi: 10.1590/1516-4446-2018-0183

Li, X., Song, D. W., Zhang, P., Zhang, Y. Z., Hou, Y. X., and Hu, B. (2018). Exploring EEG features in cross-subject emotion recognition. *Front. Neurosci.* 12:162. doi: 10.3389/fnins.2018.00162

Li, D. H., Yang, Z. Y., Hou, F. H., Kang, Q. J., Liu, S., Song, Y., et al. (2022). EEG-based emotion recognition with haptic vibration by a feature fusion method. *IEEE Trans. Instrum. Meas.* 71, 1–11. doi: 10.1109/TIM.2022.3147882

Liu, S. Q., Wang, X., Zhao, L., Li, B., Hu, W. M., Yu, J., et al. (2022). 3DCANN: a spatio-temporal convolution attention neural network for EEG emotion recognition. *IEEE J. Biomed. Health Inform.* 26, 5321–5331. doi: 10.1109/JBHI.2021.3083525

Mazzoni, A., and Bryan-Kinns, N. (2015). "How does it feel like? An exploratory study of a prototype system to convey emotion through haptic wearable devices," International conference on intelligent technologies for interactive entertainment (INTETAIN), 2015. Torino

Nardelli, M., Greco, A., Bianchi, M., Scilingo, E. P., and Valenza, G. (2020). Classifying affective haptic stimuli through gender-specific heart rate variability nonlinear analysis. *IEEE Trans. Affect. Comput.* 11, 459–469. doi: 10.1109/TAFFC.2018.2808261

Picard, R. W. (1997). *Affective computing*. USA: MIT Press.

Raheel, A., Majid, M., and Anwar, S. M. (2020). DEAR-MULSEMEDIA: dataset for emotion analysis and recognition in response to multiple sensorial media. *Inf. Fusion.* 65, 37–49. doi: 10.1016/j.inffus.2020.08.007

Rahman, A., Hossain, S., and El-Saddik, A. (2010). "Bridging the gap between virtual and real world by bringing an interpersonal haptic communication system in second life," IEEE International Symposium on Multimedia, 2010 Taiwan

Sarkar, P., and Etemad, A. (2022). Self-supervised ECG representation learning for emotion recognition. *IEEE Trans. Affect. Comput.* 13, 1541–1554. doi: 10.1109/TAFFC.2020.3014842

Sel, A., Calvo-Merino, B., Tsakiris, M., and Forster, B. (2020). The somatotopy of observed emotions. *Cortex* 129, 11–22. doi: 10.1016/j.cortex.2020.04.002

Shi, L. C., Jiao, Y. Y., and Lu, B. L. (2013). "Differential entropy feature for EEG-based vigilance estimation," 35th Annual International Conference of the IEEE-Engineering-in-Medicine-and-Biology-Society (EMBC), 2013, Japan

Tsalamlal, M. Y., Rizer, W., Martin, J. C., Ammi, M., and Ziat, M. (2018). Affective communication through air jet stimulation: evidence from event-related potentials. *Int. J. Hum. Comput. Interact.* 34, 1157–1168. doi: 10.1080/10447318.2018.1424065

Wu, M. C., Teng, W., Fan, C. H., Pei, S. B., Li, P., and Lv, Z. (2023). An investigation of olfactory-enhanced video on EEG-based emotion recognition. *IEEE Trans. Neural Syst. Rehabil. Eng.* 31, 1602–1613. doi: 10.1109/TNSRE.2023.3253866

Wu, X., Zheng, W. L., Li, Z. Y., and Lu, B. L. (2022). Investigating EEG-based functional connectivity patterns for multimodal emotion recognition. *J. Neural Eng.* 19:016012. doi: 10.1088/1741-2552/ac49a7

Xu, M. H., Cheng, J., Li, C., Liu, Y., and Chen, X. (2023). Spatio-temporal deep forest for emotion recognition based on facial electromyography signals. *Comput. Biol. Med.* 156:106689. doi: 10.1016/j.compbiomed.2023.106689

Yin, G. H., Sun, S. Q., Yu, D. A., Li, D. J., and Zhang, K. J. (2022). A multimodal framework for large-scale emotion recognition by fusing music and electrodermal activity signals. *ACM Trans. Multimed. Comput. Commun. Appl.* 18, 1–23. doi: 10.1145/3490686

Zhang, M. M., Wu, J. D., Song, J. B., Fu, R. Q., Ma, R., Jiang, Y. C., et al. (2023). Decoding coordinated directions of bimanual movements from EEG signals. *IEEE Trans. Neural Syst. Rehabil. Eng.* 31, 248–259. doi: 10.1109/TNSRE.2022.3220884

Zhang, J. H., Yin, Z., Chen, P., and Nichele, S. (2020). Emotion recognition using multi-modal data and machine learning techniques: a tutorial and review. *Inf. Fusion.* 59, 103–126. doi: 10.1016/j.inffus.2020.01.011

Zhang, S. Q., Zhao, X. M., and Tian, Q. (2022). Spontaneous speech emotion recognition using multiscale deep convolutional LSTM. *IEEE Trans. Affect. Comput.* 13, 680–688. doi: 10.1109/TAFFC.2019.2947464

Zheng, W. L., Liu, W., Lu, Y. F., Lu, B. L., and Cichocki, A. (2019a). EmotionMeter: a multimodal framework for recognizing human emotions. *IEEE T. Cybern.* 49, 1110–1122. doi: 10.1109/TCYB.2018.2797176

Zheng, W. L., and Lu, B. L. (2015). Investigating critical frequency bands and channels for EEG-based emotion recognition with deep neural networks. *IEEE Trans. Auton. Ment. Dev.* 7, 162–175. doi: 10.1109/TAMD.2015.2431497

Zheng, W. L., Zhu, J. Y., and Lu, B. L. (2019b). Identifying stable patterns over time for emotion recognition from EEG. *IEEE Trans. Affect. Comput.* 10, 417–429. doi: 10.1109/TAFFC.2017.2712143

Zhong, B., Shen, M., Liu, H. W., Zhao, Y. J., Qian, Q. Y., Wang, W., et al. (2023). A cable-driven exoskeleton with personalized assistance improves the gait metrics of people in subacute stroke. *IEEE Trans. Neural Syst. Rehabil. Eng.* 31, 2560–2569. doi: 10.1109/TNSRE.2023.3281409

Zhong, P. X., Wang, D., and Miao, C. Y. (2022). EEG-based emotion recognition using regularized graph neural networks. *IEEE Trans. Affect. Comput.* 13, 1290–1301. doi: 10.1109/TAFFC.2020.2994159

frontiers | Frontiers in Neuroscience

TYPE Original Research
PUBLISHED 11 July 2023
DOI 10.3389/fnins.2023.1219556

OPEN ACCESS

EDITED BY
Lei Zhang,
Nanjing Normal University, China

REVIEWED BY
Xiaobin Xu,
Hohai University, China
Hongdan Li,
Shandong University, China

*CORRESPONDENCE
Jing Bai
✉ baijing@njit.edu.cn

RECEIVED 09 May 2023
ACCEPTED 20 June 2023
PUBLISHED 11 July 2023

CITATION
Bai J, Wang Z, Lu X and Wen X (2023) Improved spatial–temporal graph convolutional networks for upper limb rehabilitation assessment based on precise posture measurement.
Front. Neurosci. 17:1219556.
doi: 10.3389/fnins.2023.1219556

Improved spatial–temporal graph convolutional networks for upper limb rehabilitation assessment based on precise posture measurement

Jing Bai[1,2]*, Zhixian Wang[3], Xuanming Lu[1,2] and Xiulan Wen[3]

[1]Industrial Technology Research Institute of Intelligent Equipment, Nanjing Institute of Technology, Nanjing, China, [2]Jiangsu Provincial Engineering Laboratory of Intelligent Manufacturing Equipment, Nanjing, China, [3]School of Automation, Nanjing Institute of Technology, Nanjing, China

After regular rehabilitation training, paralysis sequelae can be significantly reduced in patients with limb movement disorders caused by stroke. Rehabilitation assessment is the basis for the formulation of rehabilitation training programs and the objective standard for evaluating the effectiveness of training. However, the quantitative rehabilitation assessment is still in the experimental stage and has not been put into clinical practice. In this work, we propose improved spatial-temporal graph convolutional networks based on precise posture measurement for upper limb rehabilitation assessment. Two Azure Kinect are used to enlarge the angle range of the visual field. The rigid body model of the upper limb with multiple degrees of freedom is established. And the inverse kinematics is optimized based on the hybrid particle swarm optimization algorithm. The self-attention mechanism map is calculated to analyze the role of each upper limb joint in rehabilitation assessment, to improve the spatial-temporal graph convolution neural network model. Long short-term memory is built to explore the sequence dependence in spatial-temporal feature vectors. An exercise protocol for detecting the distal reachable workspace and proximal self-care ability of the upper limb is designed, and a virtual environment is built. The experimental results indicate that the proposed posture measurement method can reduce position jumps caused by occlusion, improve measurement accuracy and stability, and increase Signal Noise Ratio. By comparing with other models, our rehabilitation assessment model achieved the lowest mean absolute deviation, root mean square error, and mean absolute percentage error. The proposed method can effectively quantitatively evaluate the upper limb motor function of stroke patients.

KEYWORDS

rehabilitation assessment, upper limb, posture measurement, graph convolutional networks, motion range

1. Introduction

Stroke is the second leading cause of death in the world, and its incidence rate is on the rise in recent years (Paul and Candelario-Jalil, 2021). The disability rate of this disease is high, and more than 50% of survivors will leave varying degrees of disability, which seriously affecting the daily life of patients, causing great pain to themselves, and adding a heavy economic burden to

families and society. The World Stroke Organization (WSO) estimates that the global cost of stroke is over $721 billion (Feigin et al., 2022). Therefore, there is a great demand for rehabilitation training and assessment in patients with motor dysfunction.

Rehabilitation assessment is not only the basis of making a rehabilitation treatment plan but also the objective standard to observe its treatment effect. It plays an important role in rehabilitation treatment, evaluation of treatment effect, and prediction of functional recovery (Liao et al., 2020). At present, the commonly used assessment method is carried out by experienced rehabilitation physicians using the evaluation scale. The popular clinical evaluation tools are the Brunnstrom evaluation method, Fugl-Meyer Assessment (FMA), Barthel index, and so on. However, these methods are subjective assessment methods of rehabilitation physicians, with inconsistent judgment standards and inability to distinguish between compensation and true recovery (Li et al., 2022; Rahman et al., 2023). The main defect of the subjective scale is that it has a 'ceiling effect' on patients with mild injury. In addition, completing assessment tests is time consuming, complex, and labor intensive.

Scholars have carried out related research on rehabilitation assessment to solve the problems above. It is proposed to use an inertial measurement unit, accelerometer, VICON, infrared camera, and so on to capture human posture data (Fang et al., 2019; Hussain et al., 2019; Ai et al., 2021). The manual features are extracted from human posture data to represent human motion (Cai et al., 2019; Hamaguchi et al., 2020). Mahalanobis distance, and dynamic time warping (DTW) algorithm is used to quantify the correctness of rehabilitation exercise, support vector machine, logistic regression, and neural network are also used to grade the rehabilitation assessment (Houmanfar et al., 2016; Fang et al., 2019; Li et al., 2021). These methods rely on the results of sub-problems such as preprocessing and feature extraction, but the optimal solution of the sub-problem is not necessarily the global optimal solution and lacks end-to-end learning intuition.

Because wearable measuring equipment is very cumbersome to use, the acceptance of patients is not high, markers may be moved due to soft tissue effects, and motion capture systems such as VICON are too expensive. As an unmarked tool, Kinect is increasingly being applied to human posture tracking (Zelai and Begonya, 2016; Bawa et al., 2021). Kinect-based joint data contains a variety of information, including spatial information between joint nodes and their adjacent nodes, as well as time-domain information between frames. It has been widely used in motion recognition (Wang et al., 2020), gesture recognition (Ma et al., 2021), somatosensory interaction (Qiao et al., 2022), and also has applications in rehabilitation assessment (Agami et al., 2022) proposed a method for generating accurate skeleton data based on the offline fusion of a Kinect 3D video sensor and an electronic goniometer. This method is difficult to measure the patient's joint angles with the electronic goniometer (Lee et al., 2018) used Kinect v2 and force sensing resistor sensors based on Fugl-Meyer assessment for evaluating upper extremity motor function (Bai and Song, 2019) conducted a preliminary rehabilitation assessment using the first-generation Kinect to measure the joint data of stroke patients, ignoring the drawbacks of a single camera.

However, there is an issue of inaccurate joint position recognition using a single Kinect. This type of erroneous recognition is prone to occur in situations of self-occlusion, when the subject is not facing the camera, or when moving at high speeds (Han et al., 2016; Wang et al., 2016). This is because although the connections of the bones obtained during recognition are biologically consistent, the length of the limbs and the limitations of the joints are not limited, resulting in unrealistic and distorted movements. Adding additional manual measurements or wearable sensors can be time-consuming and reduce patient comfort. The accuracy of tracking data for human motion posture seriously affects the correctness of rehabilitation assessment results, therefore, the accuracy of human motion tracking should be improved. How to improve the accuracy of patient pose recognition using only visual sensors is a complex problem.

An approach to improve the accuracy of human motion tracking is to combine a rigid body model with the depth camera (Matthew et al., 2019) used this approach in the sit-to-stand movement and the upper limb motion. Due to the lack of hand modeling and occlusion, the estimation of joint position is incorrect. In the Proximal Function test, the system error is introduced, and the accuracy of the overall pose estimate is reduced (Matthew et al., 2020). Using one Kinect for rehabilitation assessment (Liu et al., 2016), the body information is particularly prone to occlusion, in some specific evaluation movements such as touching the back of the head, touching the lumbar vertebrae, and so on. The occlusion problem should be solved in order to improve the accuracy of rehabilitation assessment. So, in our work, we have added an Azure Kinect and optimized the rigid body model.

Neural networks and deep learning have been used in quantitative rehabilitation assessment research (Kipf and Welling, 2017; Williams et al., 2019). Graph convolutional neural networks have been widely used in traffic prediction based on historical traffic speeds and route maps (Guo et al., 2019). It is also possible to realize action recognition and gesture recognition based on human skeleton data (Ahmad et al., 2021). According to current research, spatial–temporal graph convolutional networks (STGCN) have been used to achieve motion recognition based on dynamic bones (Yan et al., 2018). However, the application of STGCN in upper limb rehabilitation assessment is relatively limited. This study proposes to use an improved STGCN based on precise posture measurement to assess the motor function of hemiplegic upper limbs.

In this work, we proposed an innovative method as follows: two Azure Kinects is used combined with a comprehensive rigid body model to improve the biological feasibility of the skeleton. A hybrid particle swarm optimization algorithm is used to optimize inverse kinematics. A rich movement protocol is proposed to test the movement of the patient's upper limbs from the reachable workspace and proximal function. A modified STGCN model with LSTM is proposed to assess the upper limb motor function.

2. Methods

We proposed an upper limb rehabilitation assessment method based on posture measurement, as shown in Figure 1. The upper limb rigid body model is established to increase the constraints of biological behavior and improve the accuracy of human posture data collection. The motion protocol for upper limb motion assessment is proposed,

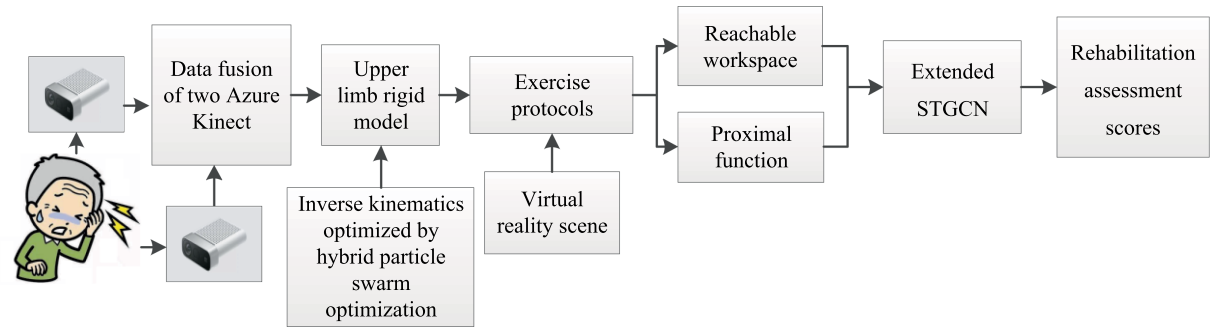

FIGURE 1
The upper limb rehabilitation assessment method based on posture measurement.

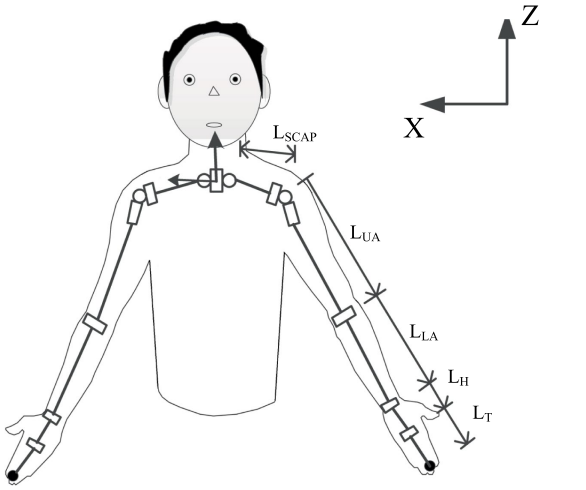

FIGURE 2
The rigid model of upper limb.

and the extended STGCN is adopted to achieve continuous upper limb rehabilitation assessment.

2.1. Two-camera synchronization

Azure Kinect can extract the position of 32 human bone skeletons, and there is occlusion when the upper limb moves to the back of the body. Using two Azure Kinect can effectively fill the occluded area and increase the spatial coverage of the camera. Therefore, we use two Azure Kinect to collect the motion of patients' limbs in this study. During the use of two Azure Kinect, synchronization is necessary to ensure that each frame of data captured by the two cameras is the scene at the same time. One camera is set as master and the other as subordinate. The two cameras are connected *via* a 3.5 mm synchronization port attached to the device. This study adopts a daisy chain configuration, with the master's synchronization port connected to the output synchronization port of the slave device through a cable. Then calibrate the two devices using the black and white checkerboard calibration method to obtain the internal and external parameters of the devices, and fuse joint data from different perspectives into the same perspective.

2.2. Models

Taking the torso as the base frame, the upper limbs can be modeled as two branches of the torso. The kinematic model of the right arm is as follows. The Kinect captured joints information, the Torso can be defined by the spine-chest and spine-naval markers. Anatomically, the shoulder is a complex composed of the glenohumeral joint, sternoclavicular joint, acromioclavicular joint and, the scapulothoracic joint. The glenohumeral joint can realize flexion/extension, adduction/abduction, and adduction/abduction. The sternoclavicular joint allows retraction/protraction, elevation/depression and backward of the glenohumeral joint. The elbow allows two movements for flexion/extension and pronation/supination. To simplify the human upper limb mechanism model, this paper singles out 2-DOF at the sternoclavicular joint, 3-DOF at the shoulder, 1-DOF at the elbow, 2-DOF at the wrist, and 1-DOF at the hand. Thus, the equivalent mechanism model of human upper limbs can be established as a 9-DOF series motion model, as shown in Figure 2. L_{SCAP} is the initial length of the upper limb girdle, L_{UA} is the length of the upper arm, L_{LA} is the length of the forearm, L_H is the length from palm to the wrist, L_T is the length of the hand tip. The position of the hand, wrist, elbow, shoulder, clavicle, neck, and spine chest can be obtained by Azure Kinect. The base frame is fixed at the neck and the hand position is the palm position. Both left and right hands are modeled, and the right hand is taken as an example to illustrate the modeling process.

2.2.1. Rigid model

The upper limb rigid model consists of 10 segments connected by 11 joint markers. The human torso is modeled as the base of the rigid body, the neck joint of the torso is set as the origin, and the two scapulae rotate at the origin. The rigid body model is divided into two continuous chains of the left arm and the right arm. The motion of the torso (T) in the world coordinate system (W) is modeled as a system with associated homogeneous transformations:

$$T_{W,To} = \begin{bmatrix} R_X R_Y R_Z & t \\ 0 & 1 \end{bmatrix} \quad (1)$$

Where R represents rotation, each rotation is determined by the angle θ, and t represents translation. Then model the scapula (SC),

upper arm (UA), forearm (FA), hand (HA) and fingertip (TIP) as two branches of the trunk. The right arm is modeled as:

$$T_{TO,RSC} = \begin{bmatrix} R_Z R_Y & 0 \\ 0 & 1 \end{bmatrix} \tag{2}$$

$$T_{RSC,RUA} = \begin{bmatrix} R_X R_Y R_Z & q_{RSJC} \\ 0 & 1 \end{bmatrix} \tag{3}$$

$$T_{RUA,RFA} = \begin{bmatrix} R_X & q_{REJC} \\ 0 & 1 \end{bmatrix} \tag{4}$$

$$T_{RFA,RHA} = \begin{bmatrix} R_X R_Z & q_{RHJC} \\ 0 & 1 \end{bmatrix} \tag{5}$$

$$T_{RHA,RTIP} = \begin{bmatrix} R_X & q_{RTJC} \\ 0 & 1 \end{bmatrix} \tag{6}$$

The left arm is modeled in a similar way, but the direction of rotation is opposite. The forward kinematics model of the rigid body can be obtained by multiplying the coordinate changes of each segment in turn. The positions of each joint can be written as:

$$\begin{aligned} p_{tor} &= T_{W,TO}(t,\theta) q_{tor} \\ p_{RSHO} &= T_{W,RSC}(t,\theta) q_{RSHO} \\ p_{RELB} &= T_{W,RUA}(t,\theta) q_{RELB} \\ p_{RWRI} &= T_{W,RFA}(t,\theta) q_{RWRI} \\ p_{RHAN} &= T_{W,RHA}(t,\theta) q_{RHAN} \\ p_{RTIP} &= T_{W,RTIP}(t,\theta) q_{RTIP} \end{aligned} \tag{7}$$

Where q is the local position of each joint. The position of each joint p is solved according to the forward kinematics, and the mapping relationship is established. The forward kinematic map is:

$$F(x_i) = \begin{bmatrix} p_{tor}, p_{RSHO}, p_{RELB}, p_{RWRI}, p_{RHAN}, p_{RTIP}, \\ p_{LSHO}, p_{LELB}, p_{LWRI}, p_{LHAN}, p_{LTIP} \end{bmatrix} \tag{8}$$

Scapulohumeral rhythm is present during arm abduction (Klopčar and Lenarčič, 2006) calculated the scapulohumeral rhythm of the generalized shoulder joint movement of the upper limb on four lifting planes with angles of 0°, 45°, 90° and 135° through experiments. The functional relationship between the lift angle β and the forward/backward extension angle θ_{fb} and the upward/downward angle θ_{ud} of the SC joint is as follows.

$$\theta_{fb} = \begin{cases} -0.35\beta & \beta < 0° \\ 0° & 0° \le \beta \le 70° \\ -0.22\beta + 15.4° & \beta > 70° \end{cases} \tag{9}$$

$$\theta_{ud} = \begin{cases} -0.3\beta & \beta < 0° \\ 0° & 0° \le \beta \le 30° \\ 0.36\beta - 10.8° & \beta > 30° \end{cases} \tag{10}$$

2.2.2. Inverse kinematics optimized by crossbreed particle swarm optimization

The inverse kinematics of the rigid body model is a nonlinear problem. Solving the joint posture through the upper limb end posture is a one-to-many mapping relationship. The inverse kinematics is optimized based on a hybrid particle swarm optimization algorithm. The classical particle swarm optimization (PSO) algorithm belongs to a global random optimization algorithm with the advantages of few parameters required, simple algorithm structure, fast operation speed, etc. (Zhou et al., 2011). Suppose a D dimension search space has N particles, the position, and velocity of a particle in a group is,

$$\begin{aligned} X_i &= [x_{i1}, x_{i2}, \cdots, x_{iD}]^T \\ V_i &= [v_{i1}, v_{i2}, \cdots v_{iD}]^T \end{aligned} \tag{11}$$

The evolution of particles at each iteration consists of three parts: inheritance of the previous velocity, self-memory, and information exchange of the population. Therefore, the kth iteration process can be expressed as:

$$\begin{aligned} v_{ij}(k+1) = \omega v_{ij}(k) + c_1 r_1 \left[p_{best}(k) - x_{ij}(k) \right] \\ + c_2 r_2 \left[g_{best}(k) - x_{ij}(k) \right] \end{aligned} \tag{12}$$

$$x_{ij}(k+1) = x_{ij}(k) + v_{ij}(k+1) \tag{13}$$

Where ω is inertia weight coefficient, c_1 and c_2 are two different learning factors, r_1 and r_2 are two randomly generated numbers in [0,1], p_{best} represents the personal best solution of the particle, g_{best} represents the global best solution of the swarm.

Due to the drawbacks of premature convergence and poor local optimization ability in PSO. Crossbreed Particle Swarm Optimization (CBPSO) is used to increase the fitness of the offspring population through the natural evolution of the population, thus jumping out of the local extreme value in the search process and converging to the global optimal solution. During the iteration process, the formula for updating the position and velocity of the offspring particles is as follows:

$$\begin{cases} child(x) = P_c \times parent_1(x) + (1 - P_c) \times parent_2(x) \\ child(v) = \dfrac{parent_1(v) + parent_2(v)}{\left| parent_1(v) + parent_2(v) \right|} \left| parent_1(v) \right| \end{cases} \tag{14}$$

where $child(x)$ and $child(v)$ represent the position and velocity of the child particle respectively, $parent(x)$ and $parent(v)$ represent position and the velocity of the parent particle, respectively. When two particles trapped in different local optimums are hybridized, they can often escape from the local optimality, and the introduction of a hybrid algorithm can enhance the global optimization ability of the population.

Our goal is to make the "distance" between the current end effector position $F(x_i)$ and y_k the shortest. So inverse kinematics is transformed into an optimization problem.y_k is the joint point collected by Azure Kinect. The fitness function is as follows:

$$fitness(X^*) = \min \left\| y_k - F(x_i) \right\|^2 \tag{15}$$

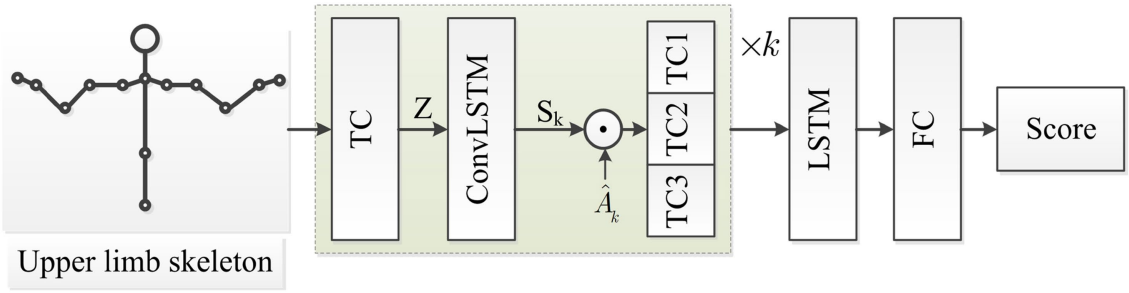

FIGURE 3
The extended STGCN for rehabilitation exercise assessment.

The specific steps of the algorithm are: First initialize the particle swarm and parameter settings, and then iterate the algorithm to calculate the fitness function value of each particle, compare the current fitness of each particle with the size of the individual extreme value, update the individual extreme value, and judge whether the hybridization condition is met. If not, return to the continuous update. Finally, select the particles corresponding to the global extremum as the optimal solution for the population.

2.3. Extended STGCN

Human skeleton motion is a string of time series, with spatial features at each time point and time features between frames. In the process of evaluating the motor function of the upper limb, different joints play different roles. For example, in the movement of touching the nose with the right upper limb, the joints on the left side of the body participate less and show less importance, and the degree of participation of the joints on the right side is different. Self-attention mechanisms can select more critical information from a lot of information. The self-attention mechanism is adopted to extract the spatial relationship of each joint and distinguish their important degree, in order to guide patients to strengthen the rehabilitation training of important joints and obtain higher evaluation scores. The extended graph network structure is shown in Figure 3.

ConvLSTM can extract the characteristics of spatial and temporal features on time series data simultaneously (Deb et al., 2022). The STGCN is improved by the self-attention mechanism graph S_k calculating form ConvLSTM. The skeleton sequence is initially processed by temporal convolution with kernel Γ^{μ}.

$$Z = X \oplus \left(\Gamma^{u} \otimes V\right) \tag{16}$$

Where, V is the skeleton sequence, let $Q_k = ZW_k$

$$\begin{aligned} i_k^t &= \sigma\left(W_i * Q_k^t + U_i * h_k^{t-1} + b_i\right) \\ f_k^t &= \sigma\left(W_f * Q_k^t + U_f * h_k^{t-1} + b_f\right) \\ o_k^t &= \sigma\left(W_o * Q_k^t + U_o * h_k^{t-1} + b_o\right) \\ g_k^t &= \tanh\left(W_c * Q_k^t + U_c * h_k^{t-1} + b_c\right) \\ c_k^t &= f_k^t \odot c_k^{t-1} + i_k^t \odot g_k^t \\ h_k^t &= o_k^t \odot \tanh\left(c_k^t\right) \end{aligned} \tag{17}$$

Where $*$ is convolution, σ is the sigmoid function, W is weight, b is bias, $S_k = h_k$. The GCN improved with the self-attention map is as follows,

$$G_k = \sigma\left(\phi\left(\hat{A}_k \odot S_k\right) Z W_k\right) \tag{18}$$

$$\hat{A}_k = A_k + I \tag{19}$$

Where, $A + I = \sum_k A_k$, $A \in R^{N \times N}$ is the adjacency matrix, $A_0 = I$ and $A_1 = A$, $\mathrm{D}^{\%}$ is the degree matrix, W_k is the weight matrix. ϕ is normalization, σ is an activation function.

Then three Temporal convolutional (TC) layers with different kernels Γ_1^l, Γ_2^l and Γ_3^l is adopted to extract time features and concatenate them. Multiple STGCN layers are stacked to obtain more complex features of different lengths, and LSTM is used to extract the time dependence of the series. Finally, continuous rehabilitation assessment scores are obtained by the full connection layer.

2.4. Exercise protocols base on VR

The exercise protocols were designed according to the anatomical position, clinical evaluation methods such as the Fugl-Meyer scale, Barthel index, range of motion, and some related articles. The measurement of upper limb motor function mainly includes distal reachable workspace measurement and proximal function measurement, the specific movement methods are shown in Table 1. The reachable workspace measurement was used to evaluate the motion range of the upper limb, and the proximal functional measurement was used to evaluate the subjects' ability to self-care in daily life, such as eating, combing hair, and so on.

Vivid virtual reality (VR) scene modeling can improve the enthusiasm and initiative of patients to participate in rehabilitation assessment. In this manuscript, a virtual scene of motion assessment was built, in which the therapist demonstrates the action, and the subjects follow the therapist to carry out the same action. The subject's avatar was designed and the visual feedback is applied to facilitate the subjects to observe whether their movements are completed or not. Auditory feedback was used to guide related movements with a variety of sensory stimuli, to increase the feasibility of the virtual environment demonstration. The rehabilitation training game is shown in Figure 4,

when the position of the subject's hand coincides with the minion, the animation of the minion jumping with the sound effect is played. The patient's participation increased, and the patient's tension and anxiety were relieved.

3. Experimental validation

The experimental setup is as follows, two Azure Kinect depth cameras were placed on the tripod with a spacing of 2 m and an angle of 90°, and adjusted horizontally using a spirit level, as shown in Figure 5. During the experiment, the subjects were asked to perform the designed movements in front of the camera and could not rotate their bodies. To reduce the impact of accidental factors, explanations and related training were provided to the subjects before the experiment. The participants simulated the coach's actions by watching pre-recorded videos on the display screen, enabling them to proficiently apply the assessment method before conducting relevant experiments.

This experiment recruited a total of 20 subjects, including 10 healthy individuals and 10 stroke patients. Among them, two rehabilitation physicians from the rehabilitation department of Nanjing Tongren Hospital voluntarily participated in the experiment. The exclusion criteria for participants in the experiment are cognitive impairment or inability to cooperate in the experiment. This work is approved by the local science and ethics committee.

4. Results

The data collected by Azure Kinect needs to be preprocessed to reduce individual differences, and eliminate migration and expansion during the experimental process. Median filtering can effectively eliminate isolated noise points. First, median filtering is performed on the data, and then the 6th-order low-pass Butterworth filter with a cut-off frequency of 30 Hz is used to filter again.

4.1. Model optimization result

According to the reachable workspace and proximal measurement in the exercise protocols, the validity of the optimized rigid body model is verified through the data of 10 healthy people. Taking the right upper limb as an example, the reachable workspace and its area of the upper limb was calculated by reference (Bai and Song, 2019). The brief description is as follows: the center of the upper limb workspace is at the shoulder joint, the motion trajectory is fitted using the least squares method, coordinate transformation is performed, Alpha Shape algorithm is used to locate the maximum boundary of the trajectory, Catmull-Rom spline interpolation is used to smooth the boundary, coordinate transformation is performed again, surface blocks are selected, the surface area is calculated, and normalization is performed. The reachable workspace is divided into four quadrants, with the first quadrant (blue) located on the inner side above the shoulder, quadrant 2 (pink) located on the inner side below the

TABLE 1 The exercise protocols.

IDX	Protocol					
Reachable workspace (straighten the arm)	Vertical direction	Azimuth angle (°)	0	45	90	135
		Elevation angle (°)	0 ~ 180			
	Horizontal direction	Azimuth angle (°)	0 ~ 135			
		Elevation angle (°)	45	90	135	0 ~ 180
Proximal function	①Side, ②Lumber spine, ③Stomach, ④Contralateral shoulder, ⑤Ipsilateral shoulder, ⑥Nose, ⑦Ear, ⑧Head top					

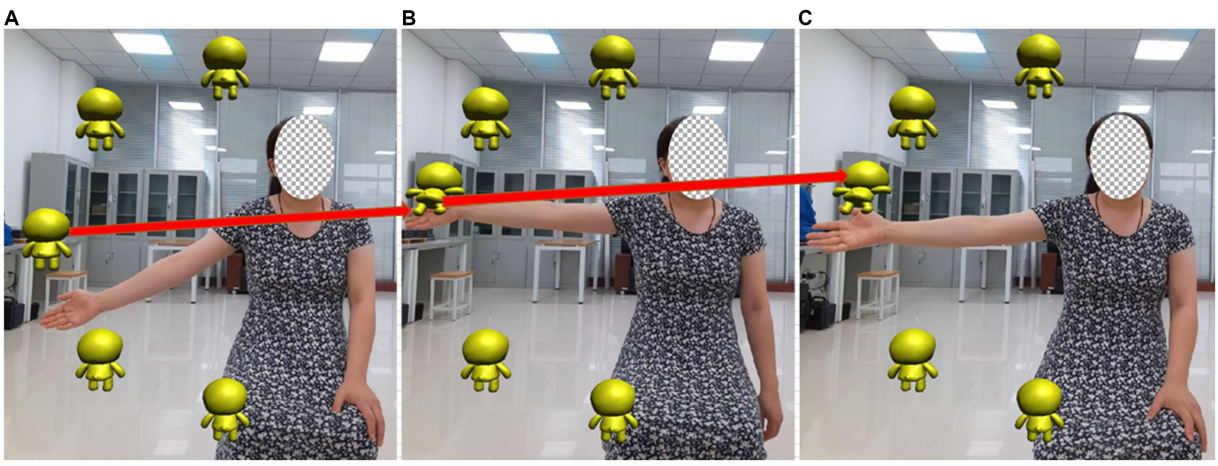

FIGURE 4
Virtual scene of motion assessment. In the rehabilitation training game, when the position of the subject's hand coincides with the minion, the animation of the minion jumping with the sound effect is played. **(A)** The hand has not move to the minion position **(B)** Hand and minion position coincide **(C)** After the position of the hand and the minion overlap, the minion jumps and accompanies the sound effect.

FIGURE 5
The experimental setup.

shoulder, quadrant 3 (red) located on the outer side above the shoulder, and quadrant 4 (green) located on the outer side below the shoulder. Figure 6 shows the reachable workspace results, A is the result measured by Azure Kinect, and B is the result optimized using the method we proposed.

In the Figure 6A the solid lines represent the original trajectory information, the dashed lines represent the preprocessed results. The red ellipse marks show some points away from the track, or even skipping points. These points are not consistent with the biological characteristics of human movement. These spots can be caused by the arms facing the camera, moving too fast, or being blocked by the torso when extended backwards.

Due to the fan-shaped measurement range of the camera, occlusion can easily occur when the arm moves between the body and the camera, or the arm extends to the back of the body. At this point, a single camera cannot detect the position information of the occluded joint. Error signals will be detected at these occlusion positions, as shown in the ellipse inside Figure 6. Occlusion positions are points with obvious jumps and abrupt changes, which can easily lead to the phenomenon of unclosed fitting boundaries in the reachable workspace.

In this study, a part of the occlusion problems can be solved by using two cameras. The other part of the occlusion problem can be optimized by adding a rigid body model. After model optimization, the number of singularities was significantly reduced, the occurrence of non-biological motion was reduced and the accuracy and stability of hand joint motion measurement was improved.

Figure 7 shows the proximal function results, A is the result measured by Azure Kinect, and B is the result optimized using the method we proposed. From the comparison of Figures 7A,B, without the addition of a rigid body model, during the process of the upper limb touching the ear and the hand touching the lumbar spine, the trajectory did not reach the position of the ear/lumbar spine. After adding the rigid body model, the measurement results were improved, and the hand motion trajectory could reach the corresponding position.

Table 2 shows the Signal Noise Ratio (SNR) of the motion trajectory of raw Kinect, two Azure Kinect, and two Azure Kinect with the rigid model. The raw Kinect trajectory exhibit low SNRs, especially in the Y and Z directions of the chest joint and the Z direction of the ipsilateral shoulder joint, the signal-to-noise ratio is below 10. The SNR of the final motion trajectory measured by two Kinects has increased, but there is still an SNR of less than 10. This study applied two Azure Kinect combined with a rigid body model, the measurement results show that all directions of each joint are greater than 10, and the SNRs are greater than 20 in the elbow joint, wrist joint, and hand joint. This table indicates that the method used in this study can improve the SNR of collected signals from each joint and increase the accuracy of upper limb posture recognition.

4.2. Assessment result

In rehabilitation assessment experiments, each subject underwent 5 exercises, with 30 groups tested each time and 10 groups resting for 10 min. A total of 3,000 sets of data were collected. Each action data in the dataset consists of a series of skeletal action frames. Each frame contains up to two skeletons, each with 11 skeletal nodes of the upper limbs. The data includes distal and proximal actions, with a total of 16 action categories, and each bone node has corresponding three-dimensional spatial coordinate data.

Three STGCN blocks are used. The optimization strategy of the model is the Adam optimizer, with a learning rate of 0.1, a batch size of 4, and an output space dimension of 80,40,40,80 for the LSTM layer. The model shares four LSTM layers with a dropout of 0.25.

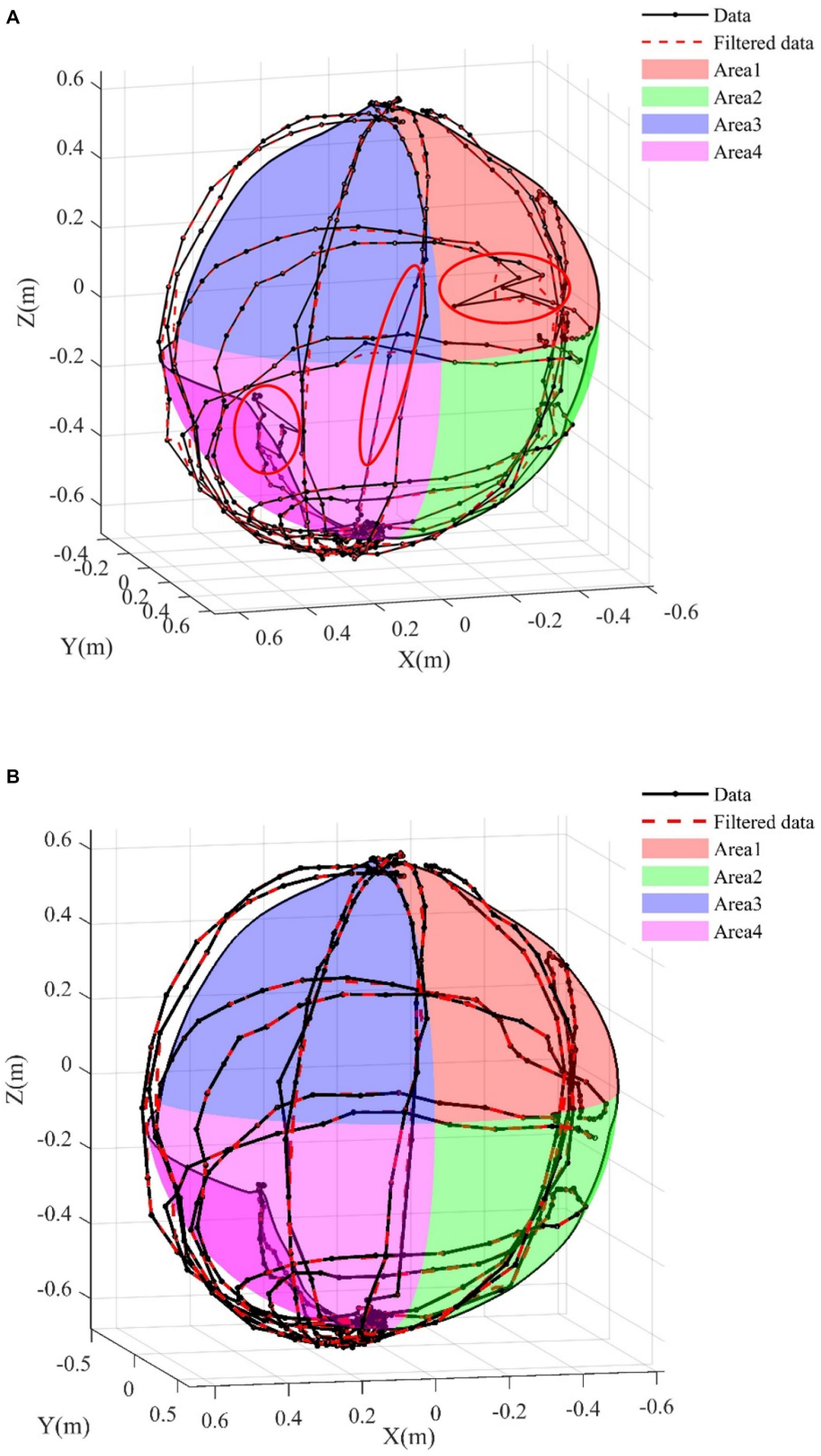

FIGURE 6
Reachable workspace results. **(A)** Raw data. **(B)** Data after rigid model.

The accuracy of the assessment model is measured using Mean Absolute Deviation (MAD), Root Mean Square Error (RMSE), and Mean Absolute Percentage Error (MAPE). The lower the error, the higher the accuracy of the model. The model was trained and predicted 10 times, and the obtained MAD, RMSE, and MAPE are recorded simultaneously. Finally, the

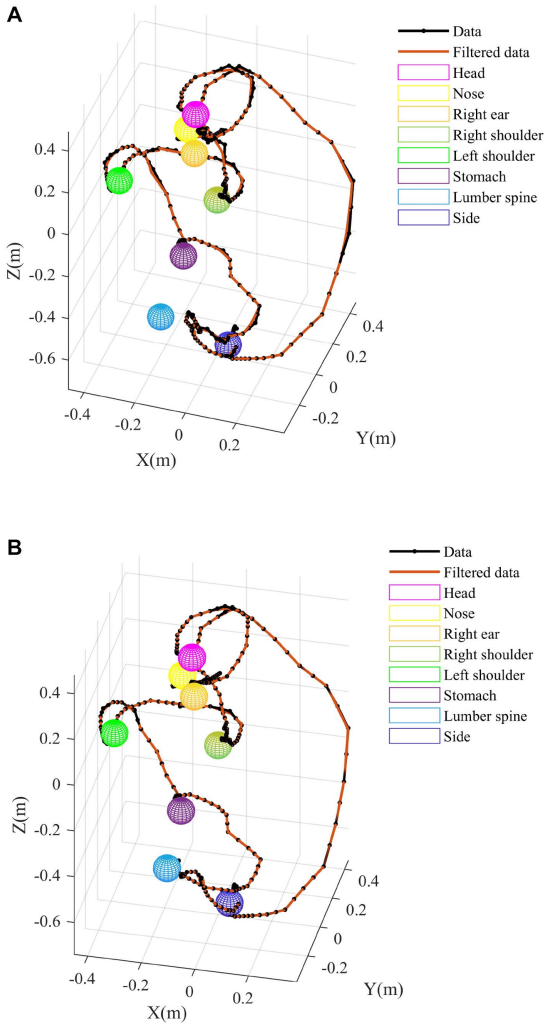

FIGURE 7
Proximal function results. **(A)** Raw data. **(B)** Data after rigid model.

average of the 10 results is taken to ensure the reliability of the results.

Each joint plays a different role in limb movement. Attention-guided graph convolution is used to extract spatial information, and each joint is processed differently based on the spatiotemporal frames, increasing the impact of different joints on the evaluation results. STGCN based on an attention mechanism makes the evaluation results more accurate, and can also provide guidance for rehabilitation and strengthen the training of important joints.

Figure 8 shows the impact of each joint on different assessed movements. As can be seen from the figure, in the movement of touching the nose with the right upper limb, the left joints of the body participate less in the movement and show lower importance. The degree of participation of the right joints varies, such as higher participation of the elbow joint and hand joint, and lower participation of the sternoclavicular joint. The wrist joint plays a crucial role in measuring the entire reachable workspace. The importance of different joints in different movements varies.

Table 3 compares the performance of our proposed model, a single Azure Kinect and two Azure Kinect algorithms combined with

TABLE 2 Signal to Noise ratio.

Segment	Axis	RW			PF		
		TKM	TK	RK	TKM	TK	RK
Spine chest	X	18	18	18	18	20	20
	Y	20	9	7	20	12	11
	Z	12	9	5	15	11	6
Ipsilateral neck	X	19	21	21	22	24	23
	Y	16	16	14	19	19	16
	Z	12	12	10	14	15	13
Ipsilateral clavicle	X	20	18	19	22	20	20
	Y	18	18	16	15	16	15
	Z	15	12	9	17	14	14
Ipsilateral Shoulder	X	27	20	18	20	20	18
	Y	18	11	11	19	14	15
	Z	14	9	7	16	10	7
Ipsilateral Elbow	X	26	14	14	20	14	14
	Y	25	12	11	25	15	14
	Z	28	14	14	21	13	15
Ipsilateral Wrist	X	28	17	16	29	16	15
	Y	29	14	14	27	12	11
	Z	27	17	16	28	18	17
Ipsilateral Hand	X	26	16	16	27	16	15
	Y	28	14	12	24	13	10
	Z	26	17	15	25	15	11

Two Azure Kinect optimization model (TKM), Two Azure Kinect (TK), Kinect (RK).

STGCN. MAD, RMS, and MAPE are analyzed. It is obvious from the table that our proposed model finally gets the lowest evaluation error.

5. Discussion

(1) Improve posture recognition accuracy

Accurate recognition of posture is key to the rehabilitation assessment of upper limb motor function using posture. However, human posture recognition is very complex and the accuracy is difficult to be guaranteed. Occlusion is easy to occur when using a single Kinect (Han et al., 2016) only used a one-generation Kinect to collect the reachable workspace of the upper limb in Duchenne muscular dystrophy, without proposing a method to solve the occlusion problem, resulting in low accuracy in human pose recognition (Matthew et al., 2020) also used only one-generation Kinect, with an improvement of adding a model. The model had fewer degrees of freedom and does not include the degrees of freedom of the wrist and hand. The accuracy of human body recognition measurement was not high, and there was a significant error in proximal upper limb movement.

Therefore, this study proposes to use two Azure Kinects and increase the constraint of the rigid body model at the same time, in order to reduce the inconsistency of human bone connection in biology, and then improve the accuracy of posture recognition. In the experimental results, Figure.6 contains the action of touching the

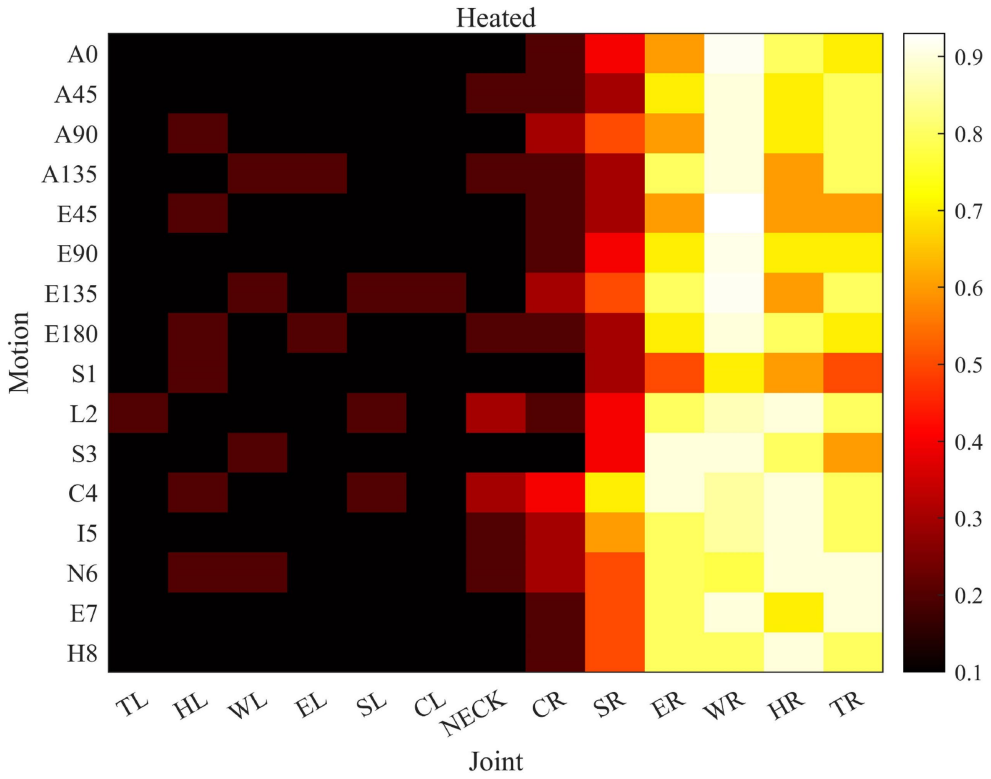

FIGURE 8
The role of joints in different movements. (The importance increases sequentially from 0 to 1. The vertical axis represents 16 evaluation actions, A * and E * represent the reachable workspace actions respectively, S1-H8 represents the proximal actions. The horizontal axis is an abbreviation for the names of each joint, from left hand to neck and then to the fingertip of the right hand).

TABLE 3 Assessment results.

Metric	Our Methods	STGCN with two Azure Kinect	STGCN with one Azure Kinect
MAD	1.021	2.757	5.378
RMSE	1.180	3.259	8.671
MAPE	3.973	5.875	25.092

lumbar vertebrae by hand. It can be clearly seen that the occlusion phenomenon is very obvious in the absence of a rigid body model, especially when the upper limb moves to coincide with other joints, the trajectory of the occluded part is messy and irregular, and the joint motion trajectory does not comply with human biology. The results of different test methods in the figure can obviously show the effectiveness of the proposed posture recognition method. Due to the inability of the camera to test the rotational motion of the arm, a more abundant human rigid body model is proposed to measure human posture from both attitude and position, achieving accurate posture recognition.

(2) Improve the accuracy of the assessment model

The effective and accurate assessment of upper limb motor function can provide the scientific basis for rehabilitation training, but the existing rehabilitation assessment methods lack universality, robustness, and practical relevance. Convolutional neural networks can be used to design scientifically reasonable quantitative assessment methods, but the accuracy of the assessment results still needs further verification. On the basis of improving the accuracy of human body recognition, this study conducts rehabilitation assessment tasks to increase the accuracy of assessment model recognition. Due to the varying degrees of participation of each joint in different movements, the importance of each joint is increased based on attention mechanisms. When the right hand is active, the participation of the left joint is lower, while when the left hand is active, the participation of the right joint is lower. At the same time, the importance of each joint is calculated for both the expert therapist and the patient. The difference in joint function between the patient and the therapist is significant. By comparing the difference in joint function with the average expert therapist, it can be determined which joints can be trained more effectively to improve the patient's rehabilitation assessment score based on the size of the difference. The difference in joint function can provide a reasonable direction for rehabilitation training for patients. Adding joint participation to a rehabilitation assessment model can achieve continuous assessment and improve the accuracy of rehabilitation evaluation.

6. Conclusion

This study addresses the issue of non-quantification in rehabilitation assessment, and proposes an improved STGCN

based on precise upper limb posture recognition to achieve continuous quantitative rehabilitation assessment. Two Azure Kinects were used to expand the field of view, a multi-degree of freedom upper limb motion rigid body model was proposed, making the upper limb posture measurement in line with normal human biological movement. The accuracy of upper limb posture recognition is increased, and the signal-to-noise ratio of measurement is improved. By identifying the participation degree of each joint in different movements based on the self-attention mechanism, the STGCN algorithm was improved to achieve continuous quantitative rehabilitation assessment. The experimental comparison results show that the upper limb posture recognition algorithm proposed in this study can effectively reduce incorrect joint coordinates, and the rehabilitation assessment model based on improved STGCN can effectively reduce the assessed MAD and RMS and MAPE. This study provides a new approach for the quantitative rehabilitation assessment of stroke patients. In the future work, we will continue to optimize the rigid body model and improve the rehabilitation assessment method.

Data availability statement

The raw data supporting the conclusions of this article will be made available by the authors, without undue reservation.

Ethics statement

The studies involving human participants were reviewed and approved by Nanjing Tongren Hospital science and ethics committee. The patients/participants provided their written informed consent to participate in this study.

Author contributions

JB was responsible for the study scheme design, data analysis, and manuscript writing. ZW was responsible for the data acquisition. XL was responsible for the experiment. XW was responsible for the revision of the manuscript. All authors contributed to the article and approved the submitted version.

Funding

This work was supported by the Natural Science Foundation of Jiangsu Province (Grant no. BK20210930), Natural Science Research of Jiangsu higher education institutions of China (Grant no. 21KJB510039), and the Scientific Research Foundation of Nanjing Institute of Technology (Grant no. YKJ2019113).

Conflict of interest

The authors declare that the research was conducted in the absence of any commercial or financial relationships that could be construed as a potential conflict of interest.

Publisher's note

All claims expressed in this article are solely those of the authors and do not necessarily represent those of their affiliated organizations, or those of the publisher, the editors and the reviewers. Any product that may be evaluated in this article, or claim that may be made by its manufacturer, is not guaranteed or endorsed by the publisher.

References

Agami, S., Riemer, R., and Berman, S. (2022). Enhancing motion tracking accuracy of a low-cost 3D video sensor using a biomechanical model, sensor fusion, and deep learning. *Front. Rehabil. Sci.* 3:956381. doi: 10.3389/fresc.2022.956381

Ahmad, T., Jin, L., Zhang, X., Lin, L., and Tang, G. (2021). Graph convolutional neural network for human action recognition: a comprehensive survey. *IEEE Trans. Artificial Intell.* 2, 128–145. doi: 10.1109/TAI.2021.3076974

Ai, Q. S., Liu, Z., Meng, W., Liu, Q., and Xie, S. Q. (2021). Machine learning in robot assisted upper limb rehabilitation: a focused review. *IEEE Trans. Cog. Dev. Syst.*:1. doi: 10.1109/TCDS.2021.3098350

Bai, J., and Song, A. G. (2019). Development of a novel home based multi-scene upper limb rehabilitation training and evaluation system for post-stroke patients. *IEEE Access.* 7, 9667–9677. doi: 10.1109/ACCESS.2019.2891606

Bawa, A., Banitsas, K., and Abbod, M. (2021). A review on the use of Microsoft Kinect for gait abnormality and postural disorder assessment. *Hindawi Limited* 2021:60122. doi: 10.1155/2021/4360122

Cai, S., Li, G., Zhang, X., Huang, S., and Xie, L. (2019). Detecting compensatory movements of stroke survivors using pressure distribution data and machine learning algorithms. *J. Neuroeng. Rehabil.* 16, 131–111. doi: 10.1186/s12984-019-0609-6

Deb, S., Islam, M. F., Rahman, S., and Rahman, S. (2022). Graph convolutional networks for assessment of physical rehabilitation exercises. *IEEE Trans. Neural Syst. Rehabil. Eng.* 30, 410–419. doi: 10.1109/TNSRE.2022.3150392

Fang, Q., Mahmoud, S. S., Gu, X., and Fu, J. (2019). A novel multi-standard compliant hand function assessment method using an infrared imaging device. *IEEE J. Biomed. Health Inform.* 23, 758–765. doi: 10.1109/JBHI.2018.2837380

Feigin, V. L., Brainin, M., Norrving, B., Martins, S., Sacco, R. L., Hacke, W., et al. (2022). World stroke organization (WSO): global stroke fact sheet 2022. *Int. J. Stroke* 17, 18–29. doi: 10.1177/17474930211065917

Guo, S., Lin, Y., Feng, N., Song, C., and Wan, H. (2019). Attention based spatial-temporal graph convolutional networks for traffic flow forecasting. *Proc. AAAI Con. Artificial Intell.* 33, 922–929. doi: 10.1609/aaai. v33i01.3301922

Hamaguchi, T., Saito, T., Suzuki, M., Ishioka, T., Tomisawa, Y., Nakaya, N., et al. (2020). Support vector machine-based classifier for the assessment of finger movement of stroke patients undergoing rehabilitation. *J. Med. Biol. Eng.* 40, 91–100. doi: 10.1007/s40846-019-00491-w

Han, J. J., Bie, E. D., Nicorici, A., Abresch, R. T., Anthonisen, C., Bajcsy, R., et al. (2016). Reachable workspace and performance of upper limb (PUL) in Duchenne muscular dystrophy. *Muscle Nerve* 53, 545–554. doi: 10.1002/mus.24894

Houmanfar, R., Karg, M., and Kulic, D. (2016). Movement analysis of rehabilitation exercises: distance metrics for measuring patient progress. *IEEE Syst. J.* 10, 1014–1025. doi: 10.1109/JSYST.2014.2327792

Hussain, T., Maqbool, H. F., Iqbal, N., Khan, M., and Sanij, A. A. D. (2019). Computational model for the recognition of lower limb movement using wearable gyroscope sensor. *Int. J. Sensor Networks.* 30, 35–45. doi: 10.1504/IJSNET.2019.10020697

Kipf, T. N., and Welling, M. (2017). Semi-supervised classification with graph convolutional networks. *ICLR*. doi: 10.48550/arXiv.1609.02907

Klopčar, N., and Lenarčič, J. (2006). Bilateral and unilateral shoulder girdle kinematics during humeral elevation. *Clin. Biomech.* 21, s20–s26. doi: 10.1016/j.clinbiomech.2005.09.009

Lee, S., Lee, Y. S., and Kim, J. (2018). Automated evaluation of upper-limb motor function impairment using Fugl-Meyer assessment. *IEEE Trans. Neural Syst. Rehabil. Eng.* 26, 125–134. doi: 10.1109/TNSRE.2017.2755667

Li, C., Cheng, L., Yang, H., Zou, Y., and Huang, F. (2021). An automatic rehabilitation assessment system for hand function based on leap motion and ensemble learning. *Cybern. Syst.* 52, 3–25. doi: 10.1080/01969722.2020.1827798

Li, C., Yang, H., Cheng, L., Huang, F., Zhao, S., Li, D., et al. (2022). Quantitative assessment of hand motor function for post-stroke rehabilitation based on HAGCN and multimodality fusion. *IEEE Trans. Neural Syst. Rehabil. Eng.* 30, 2032–2041. doi: 10.1109/TNSRE.2022.3192479

Liao, Y., Vakanski, A., and Xian, M. (2020). A deep learning framework for assessing physical rehabilitation exercises. *IEEE Trans. Neural Syst. Rehabil. Eng.* 28, 468–477. doi: 10.1109/TNSRE.2020.2966249

Liu, Z., Zhou, L., Leung, H., and Shum, H. P. H. (2016). Kinect posture reconstruction based on a local mixture of Gaussian process models. *IEEE Trans. Vis. Comput. Graph.* 22, 2437–2450. doi: 10.1109/TVCG.2015.2510000

Ma, C., Liu, Q., and Dang, Y. (2021). Multimodal art pose recognition and interaction with human intelligence enhancement. *Front. Psychol.* 12:769509. doi: 10.3389/fpsyg.2021.769509

Matthew, R. P., Seko, S., Bajcsy, R., and Lotz, J. (2019). Kinematic and kinetic validation of an improved depth camera motion assessment system using rigid bodies. *IEEE J. Biomed. Health Inform.* 23, 1784–1793. doi: 10.1109/JBHI.2018.2872834

Matthew, R. P., Seko, S., Kurillo, G., Bajcsy, R., Cheng, L., Han, J. J., et al. (2020). Reachable workspace and proximal function measures for quantifying upper limb motion. *IEEE J. Biomed. Health Inform.* 24, 3285–3294. doi: 10.1109/JBHI.2020.2989722

Paul, S., and Candelario-Jalil, E. (2021). Emerging neuroprotective strategies for the treatment of ischemic stroke: an overview of clinical and preclinical studies. *Exp. Neurol.* 335:113518. doi: 10.1016/j.expneurol.2020.113518

Qiao, C., Shen, B., Zhang, N., Jia, J., and Meng, L. (2022). Research on human-computer interaction following motion based on Kinect somatosensory sensor. In 2022 IEEE 6th Information Technology and Mechatronics Engineering Conference (ITOEC), 273–279,

Rahman, S., Sarker, S., Haque, A. K. M. N., Uttsha, M. M., Islam, M. F., and Deb, S. (2023). AI-driven stroke rehabilitation systems and assessment: a systematic review. *IEEE Trans. Neural Syst. Rehabil. Eng.* 31, 192–207. doi: 10.1109/TNSRE.2022.3219085

Wang, L., Huynh, D. Q., and Koniusz, P. (2020). A comparative review of recent Kinect-based action recognition algorithms. *IEEE Trans. Image Process.* 29, 15–28. doi: 10.1109/TIP.2019.2925285

Wang, Y., Zhang, J., Liu, Z., Wu, Q., Chou, P. A., Zhang, Z., et al. (2016). Handling occlusion and large displacement through improved RGB-D scene flow estimation. *IEEE Trans. Circuits Syst. Video Technol.* 26, 1265–1278. doi: 10.1109/TCSVT.2015.2462011

Williams, C., Vakanski, A., Lee, S., and Paul, D. (2019). Assessment of physical rehabilitation movements through dimensionality reduction and statistical modeling. *Med. Eng. Phys.* 74, 13–22. doi: 10.1016/j.medengphy.2019.10.003

Yan, S., Xi ong, Y., and Lin, D. (2018). Spatial temporal graph convolutional networks for skeleton-based action recognition. In Proceedings of the AAAI Conference on Artificial Intelligence .

Zelai, S., and Begonya, G. (2016). Kinect-based virtual game for the elderly that detects incorrect body postures in real time. *Sensors* 16:704. doi: 10.3390/s16050704

Zhou, D., Xiang, G., Liu, G., Mei, C., Dong, J., and Ying, L. (2011). Randomization in particle swarm optimization for global search ability. *Expert Syst. Appl.* 38, 15356–15364. doi: 10.1016/j.eswa.2011.06.029

frontiers | Frontiers in Neuroscience

TYPE Original Research
PUBLISHED 21 July 2023
DOI 10.3389/fnins.2023.1222715

OPEN ACCESS

EDITED BY
Chang Yan,
Southeast University, China

REVIEWED BY
Liting Zhang,
Shandong Provincial Hospital, China
L. C. Yang,
Shandong University, China

*CORRESPONDENCE
Feifei Liu
✉ feifeiliu1987@gmail.com

RECEIVED 15 May 2023
ACCEPTED 28 June 2023
PUBLISHED 21 July 2023

CITATION
Jiang X, Ren Y, Wu H, Li Y and Liu F (2023) Convolutional neural network based on photoplethysmography signals for sleep apnea syndrome detection.
Front. Neurosci. 17:1222715.
doi: 10.3389/fnins.2023.1222715

Convolutional neural network based on photoplethysmography signals for sleep apnea syndrome detection

Xinge Jiang[1], YongLian Ren[2], Hua Wu[1], Yanxiu Li[1] and Feifei Liu[2]*

[1]School of Information Science and Electrical Engineering, Shandong Jiaotong University, Jinan, China, [2]School of Science, Shandong Jianzhu University, Jinan, China

Introduction: The current method of monitoring sleep disorders is complex, time-consuming, and uncomfortable, although it can provide scientifc guidance to ensure worldwide sleep quality. This study aims to seek a comfortable and convenient method for identifying sleep apnea syndrome.

Methods: In this work, a one-dimensional convolutional neural network model was established. To classify this condition, the model was trained with the photoplethysmographic (PPG) signals of 20 healthy people and 39 sleep apnea syndrome (SAS) patients, and the influence of noise on the model was tested by anti-interference experiments.

Results and Discussion: The results showed that the accuracy of the model for SAS classifcation exceeds 90%, and it has some antiinterference ability. This paper provides a SAS detection method based on PPG signals, which is helpful for portable wearable detection.

KEYWORDS

sleep apnea syndrome (SAS), convolutional neural networks (CNN), photoplethysmographic (PPG) signals, sleep apnea syndrome (SAS) recognition, cross entropy

1. Introduction

According to the statistics of the World Health Organization, more than one-third of the world's population suffers from sleep disorders, which seriously affect people's health. SAS is a common sleep disorder, and its standard recognized method of diagnosis is polysomnography. However, this method requires multiple sensors, resulting in discomfort during the detection process. It can also seriously affect the patient's natural sleep mode, with high costs (Phan and Mikkelsen, 2022). Thus, it is an urgent problem to find a simple and comfortable diagnostic method for the detection of SAS. To improve the comfort of the diagnostic process, thermal infrared imaging, radio frequency (RF) architecture, and sound detection have been introduced for non-contact detection (Murthy et al., 2009; Norman et al., 2014; Penzel, 2017; Tran et al., 2019), since body position, limb movement, and noise can easily interfere with the monitoring results. In recent years, some scholars have been committed to researching SAS detection based on wearable devices, which are used to collect chest bioimpedance, electrocardiogram (ECG), or PPG. At the same time, machine learning or deep learning are used to detect SAS, with accuracy generally around 70–85% (Baty et al., 2020; Hsu et al., 2020; Papini et al., 2020; van Steenkiste et al., 2020).

At present, many scholars have conducted research on convenient SAS detection based on neural networks. Convolutional neural networks have been gradually applied to analyze sleep quality. Song and other researchers constructed convolutional neural networks to classify sleep stages using single-channel electrocardiogram signals (Song et al., 2016; Sors et al., 2018; Wang

et al., 2019; Eldele et al., 2021; Haghayegh et al., 2023). Guo et al. (2022) proposed a pseudo-3D convolutional neural network method to detect people's nocturnal sleep behavior, with an accuracy of 90.67% on the test set. du-Yan et al. (2022) used convolutional neural networks to analyze sleep stages using heart rate variability. Casal et al. (2022) constructed a time convolutional network and transformer using pulse oximeter signals to classify sleep stages. The above research methods mostly extract classification features from ECG signals. However, ECG signals are easily affected by low-frequency and large-amplitude P and T waves, and the above studies are mostly used for sleep stages but not for SAS detection.

Pulse signals contain all kinds of human information and can be easily obtained, and monitoring it is of great significance in assessing the risk of various diseases (Allen and Hedley, 2019). Pulse wave amplitude and pulse rate variability have been used for SAS diagnosis and detection (Haba-Rubio et al., 2005; Liu, 2017). However, when the signal is disturbed or weak, it is very difficult to extract local features of the waveform using these methods. As fitting functions, the Gaussian function and lognormal function use the global information of the signal to extract the characteristics of pulse waves for SAS research (Jiang et al., 2021), but this method requires normalizing the data, resulting in a long processing period. Shen et al. established a convolutional network using PPG signals collected from wearable smart bracelet devices to detect sleep apnea syndrome, but the accuracy of fragment detection is approximately 80% (Shen et al., 2022).

In this study, a one-dimensional convolutional neural network (1D-CNN) was established by using PPG signals for the recognition of SAS, with a classification accuracy of over 90%. The results indicate that the convolutional model based on PPG has satisfactory recognition performance for SAS. This means that SAS can be identified using PPG signals by a one-dimensional convolutional model, which can make the detection process of SAS convenient and comfortable.

2. Methods

2.1. Subjects and data

In this study, signals were collected from 59 subjects, which included 20 healthy people and 39 SAS patients. The data used for analysis were the PPG signals of the subject's fingers obtained from the Alice 5 detection system of the polysomnography monitor in the Sleep Center of Shandong Provincial Hospital. It was approved by the committee of our research institute as a retrospective study with the subjects' informed consent. The PPG signals (sampling frequency is 100 Hz) of each subject are segmented by 1,500 points. Table 1 shows the clinical information of 59 subjects and the summary of the PPG datasets.

As shown in Table 1, this study used 35,741 data segments, all of which were randomly divided into training, validation, and test sets, with a ratio of 6:2:2. To avoid the contingency of the experimental results, five cross-validations were used for training.

2.2. One-dimensional convolutional neural network

The convolutional neural network (CNN) is a common deep learning model, whose convolutional kernel can extract intrinsic features from different dimensions. It has the characteristics of local perception and weight, allowing the merging of local features from different fields of view. This greatly enhances learning efficiency and accuracy. In addition, its network structure mainly adopts local connections and weight-sharing methods, which reduce the number of weights, facilitate network optimization, and minimize model complexity and the occurrence of overfitting. Considering that pulse wave data is a one-dimensional time series signal, this study proposes a 1D-CNN model for SAS classification and detection that includes eight convolutional layers, four maximum pooling layers, two LSTMs, and two fully connected layers. Figure 1 shows the structure of the 1D-CNN model.

2.2.1. Convolutional layers

Convolutional layers are mainly used for feature extraction and can automatically extract features for learning. Different convolutional kernels can extract different local features, and the amount of feature learning can be increased by setting different convolutional kernels. As the number of layers in a neural network increases, convolutional neural networks typically have stronger feature extraction capabilities and yield better results. However, increasing the number of convolutional kernels significantly raises computational complexity and the difficulty of network training. At the same time, with the increase in network depth, it is easy to cause gradient vanishing and overfitting. To prevent these phenomena and obtain accurate results, this paper designs a progressive convolutional kernel scheme layer by layer. As shown in Figure 1, the model consists of eight convolutional layers, divided into four groups, each with two convolutional layers. A pooling layer and the ELU activation function are added between the convolution layer groups. The k-value of each convolutional kernel is 3, and the number of neurons in the four groups is 32, 64, 128, and 256, respectively.

2.2.2. Pooling layers

Pooling is a process of data processing that reduces the dimensionality of feature maps and the number of parameters in the network. The pooling layer can gradually reduce the feature map output of the network and improve learning efficiency. In this study, four maximum pooling layers were designed. This design achieves rapid dimensionality reduction of information by mapping distributed features to the sample label space while ensuring its comprehensiveness and translation invariance.

2.2.3. LSTM

The Long Short-Term Memory (LSTM) neural network is an improved network based on recurrent neural networks. Due to the fact that traditional RNN structures are prone to associated gradient problems during training, they are not suitable for processing time dependence. The LSTM network can solve the dependency problem of RNN networks through the gate structure, thereby establishing a larger deep network. Its structural diagram is shown in Figure 2. Input gates can facilitate the flow of information and update the state of cells. The output gate can not only achieve information outflow but also be used to determine the value of the next hidden state. The Forgotten Gate can update the previous state and choose whether to discard or retain the information. The sigmoid function categorizes the data between 0 and 1, filters the updated data, and then transfers the output data of the previously hidden layer and the current state data together to the *Tanh* function to determine a new candidate value. Finally, the outputs of these two functions are multiplied.

TABLE 1 Summary of PPG datasets.

Category	Number	Gender Male subjects / female subjects	Age (years) Mean [range]	Record duration (min) Mean [range]	Data segments
Healthy	20	11/9	29 [21–56]	473 [348–563]	15,343
SAS patient	39	29/10	48 [22–76]	494 [318–557]	20,398
Total	59	40/19	42 [21–76]	486 [318–563]	35,741

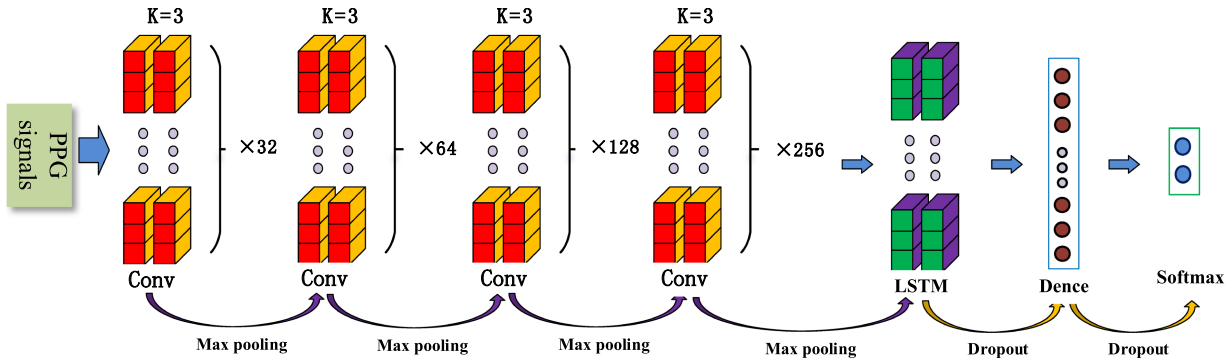

FIGURE 1
The structure of the 1D-CNN model.

$$I_t = Sigmoid\left(W_i \cdot \left[h_{t-1}, X_t\right]\right)$$

$$F_t = Sigmoid\left(W_f \cdot \left[h_{t-1}, X_t\right]\right)$$

$$\widetilde{h_t} = Tanh\left(W \cdot \left[I_t * h_{t-1}, X_t\right]\right)$$

$$h_t = \left(1 - F_t\right) * h_{t-1} + F_t * \widetilde{h_t}$$

where I_t represents input gates; F_t represents forgetting gates; h_t represents the hidden layer of the output gate; X_t is the external input at the current time; and h_{t-1} is the output of the network at the previous time.

The pulse wave is a temporal signal, and this article uses two LSTMs to extract temporal features from the data.

2.2.4. Cross-entropy loss function

The loss function is the key factor that guides the optimization direction of neural network parameters. The parameters of the network model are updated according to the backpropagation of the loss function to optimize the model. The cross-entropy loss function uses the logic function to obtain probabilities and adopts an inter-class competition mechanism to effectively learn inter-class information. This scientific question in this paper is a binary problem; therefore, the binary cross-entropy loss function is utilized, which is defined in Formula 1 as:

$$L = -\frac{1}{N}\sum_{i=1}^{N}\left[y_i \cdot \log\left(p_i\right) + \left(1 - y_i\right) \cdot \log\left(1 - p_i\right)\right] \quad (1)$$

where N represents the total number of samples, y_i represents the label of sample i, with positive classes being 1 and negative classes being 0; p_i represents the probability that sample i is predicted to be positive.

3. Results

3.1. Evaluation indicators

To validate the performance of the model, four indicators were used to evaluate the classification performance of the model: accuracy (ACC), precision (PRE), sensitivity (SE), and specificity (SP). The calculation formula for each indicator is as follows:

$$ACC = \frac{TP + TN}{TP + TN + FP + FN}$$

$$PRE = \frac{TP}{TP + FP}$$

$$SE = \frac{TP}{TP + FN}$$

$$SP = \frac{TN}{TN + FP}$$

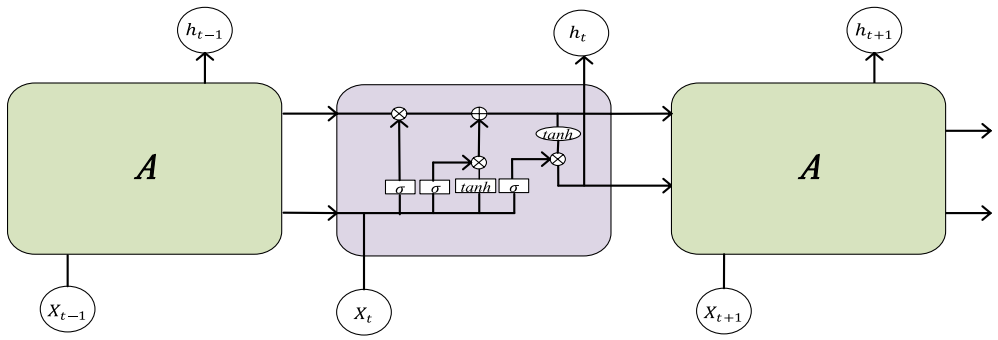

FIGURE 2
The structural diagram of LSTM.

3.2. Result comparison

In order to verify the performance of the 1D-CNN model, SVM, LSTM, and KNN models were also constructed using the same data. The comparison between the confusion matrix results of the four models is shown in Figure 3. The evaluation index values of each model are shown in Table 2.

Compared to the other three models, it is obvious from Table 2 that the 1D-CNN model established in this paper exhibited good performance. Except for the PRE indicator, the 1D-CNN model achieved the highest values for the other three performance indicators, ACC, SE, and SP Their values are 91.40, 98.36, and 87.63%, respectively, in the validation set; and 90.75, 98.24, and 86.74%, respectively, in the test set.

3.3. Anti-interference experiment

To test the influence of noise on the performance of 1D-SCNN, an anti-interference experiment was designed by adding Gaussian white noise to the original signal with a signal-to-noise ratio (SNR) of 5, 10, 15, 20, 25, and 30 dB, respectively. The data segments were also randomly divided into training, validation, and test sets in a ratio of 6:2:2. The anti-interference test results of the model's test set are shown in Table 3. The experimental results indicated that noise has little effect on the performance indicators of 1D-SCNN, and the model has a certain anti-interference ability.

3.4. Ablation experiment

To verify the role of the LSTM layer in the model, we designed an ablation experiment by removing the LSTM layer from the 1D-CNN model, and then used the original data and followed the same method to train the model without the LSTM layer. The performance indicators ACC, *PRE*, SE, and SP of the test set without the LSTM layer had values of 89.94, 78.57, 97.71, and 85.81%, respectively, which reduced its accuracy by 0.81% compared to the 1D-CNN model. The results showed that the LSTM layer can improve system performance, although the accuracy improvement is not very significant.

4. Discussion

In this study, we constructed a 1D-CNN model for SAS detection and compared its performance with SVM, LSTM, and KNN models. The results showed that the accuracy of the 1D-CNN model on the test set was 90.75%, which was 11.2% higher than the results for the SVM model, with a recorded accuracy of 79.55% on the test set. The results indicate that the constrained 1D-CNN model in this study has better performance in the classification of SAS. At the same time, we designed anti-interference and ablation experiments to test the anti-noise performance of the model and the role of LSTM layers, respectively. The experimental results indicated that the model has a certain level of anti-interference ability, and the LSTM layer helps to improve the performance of the model.

Shen et al. (2022) proposed a Multitask Residual Shrinkage Convolutional Neural Network that utilizes PPG signals to detect SAS with a fragment detection accuracy of 81.82%. Lazazzera et al. (2021) also proposed a method to detect and classify sleep apnea and hypopnea using light plethysmography (PPG) and peripheral oxygen saturation [$SpO_{(2)}$] signals. However, there is significant room for improvement in the accuracy of their models. In our previous work (Jiang et al., 2021), Gaussian and lognormal functions were used to build SVM models based on PPG signals to classify SAS. The correct rate of the SVM model with a lognormal function in the awake period reached 95.00%, and the correct rate of the SVM model with a Gaussian function in the rapid eye movement periods reached 93%. However, in this study, only 10 cycles of pulse signals were captured from each subject, and the difference between the number of healthy individuals and the number of patients was too large, while the SVM machine learning method did not separate more subtypes. All these factors make the generalization ability of SVM models weak.

This study has several limitations. First, the sample size is small, involving only 59 subjects for a total of 35,741 data segments, which may have affected the performance of the model. Second, compared to SAS patients, healthy subjects are younger. Previous studies have shown that age affects PPG signals (Millasseau et al., 2002; Liu et al., 2015), and differences in PPG signals caused by different age groups may also affect the classification performance of the model. However, the above factors have a small impact on the performance of the model, which has not changed much overall.

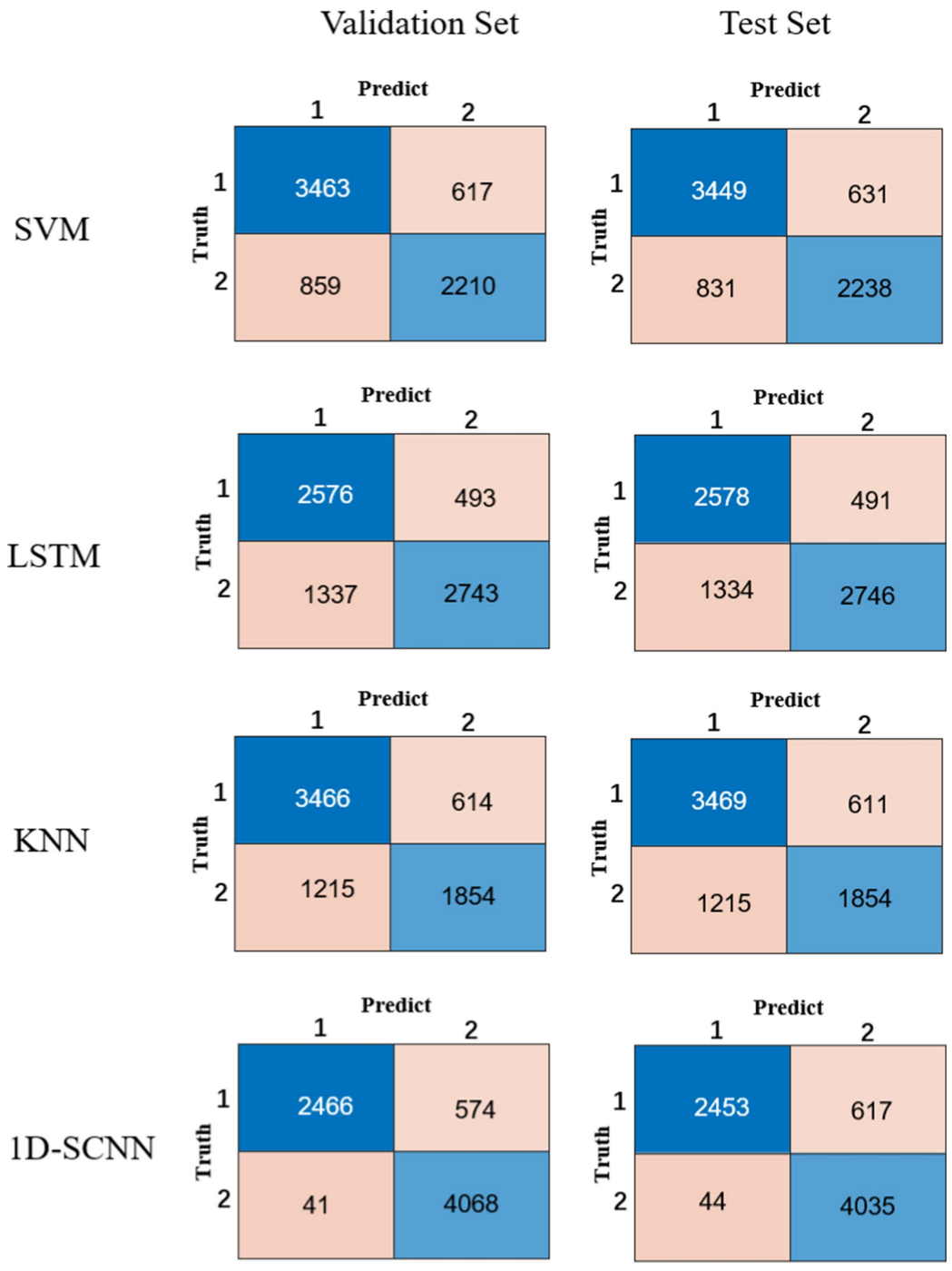

FIGURE 3
Confusion matrix results of the four models.

TABLE 2 Evaluation index values for each model.

Method	Validation set	Test set						
	ACC (%)	PRE (%)	SE (%)	SP (%)	ACC (%)	PRE (%)	SE (%)	SP (%)
SVM	79.35	84.88	80.12	78.17	79.55	84.53	80.58	78.01
LSTM	74.40	83.94	65.83	84.77	74.47	84.00	65.90	84.83
KNN	74.42	84.95	74.04	75.12	74.46	85.02	74.06	75.21
1D-CNN	**91.40**	**81.12**	**98.36**	**87.63**	**90.75**	**79.90**	**98.24**	**86.74**

TABLE 3 Anti-interference test results of the 1D-SCNN model.

SNR	ACC (%)	PRE (%)	SE (%)	SP (%)
5 dB	90.74	79.92	98.16	86.76
10 dB	90.80	80.01	98.20	86.82
15 dB	90.28	79.12	98.08	86.09
20 dB	91.22	80.86	98.21	87.44
25 dB	90.05	78.68	97.91	85.87
30 dB	89.91	78.56	97.63	85.81

5. Conclusion

In this study, a 1D-CNN model based on PPG signals for SAS classification was established. The results showed that this had the best performance, with a test set accuracy of over 90%, compared to other types of models. Our research results indicate that using only PPG signals for SAS classification is feasible, which can provide a foundation for seeking convenient and comfortable SAS detection methods. Furthermore, this can be helpful for portable wearable detection.

Data availability statement

The raw data supporting the conclusions of this article will be made available by the authors, without undue reservation.

Ethics statement

Written informed consent was obtained from the individual(s) for the publication of any potentially identifiable images or data included in this article.

Author contributions

XJ was mainly responsible for data analysis and writing of the manuscript. YR was mainly responsible for data collection and analysis of the manuscript. HW was mainly responsible for algorithms. YL was mainly responsible for organizing data. FL was mainly responsible for the structural design and revision of the manuscript. All authors contributed to the article and approved the submitted version.

Funding

This work was supported by the National Natural Science Foundation of China (Grant nos. 82072014 and 61901114), the National Key R&D Program of China (Grant no. 2019YFE010670), the Natural Science Foundation of Shandong Province (Grant no. ZR2020MF028), and the Key R&D Program of Shandong Province (Grant no.2020CXGC010110).

Acknowledgments

The authors acknowledge the support of the Southeast-Lenovo Wearable Heart-Sleep-Emotion Intelligent Monitoring Lab.

Conflict of interest

The authors declare that the research was conducted in the absence of any commercial or financial relationships that could be construed as a potential conflict of interest.

Publisher's note

References

Allen, J., and Hedley, S. (2019). Simple photoplethysmography pulse encoding technique for communicating the detection of peripheral arterial disease-a proof of concept study. *Physiol. Meas.* 40:08NT01. doi: 10.1088/1361-6579/ab3545

Baty, F., Boesch, M., Widmer, S., Annaheim, S., Fontana, P., Camenzind, M., et al. (2020). Classification of sleep apnea severity by electrocardiogram monitoring using a novel wearable device. *Sensors* 20, 286–298. doi: 10.3390/s20010286

Casal, R., Di Persia, L. E., and Schlotthauer, G. (2022). Temporal convolutional networks and transformers for classifying the sleep stage in awake or asleep using pulse oximetry signals. *J. Comput. Sci.* 59:101544. doi: 10.1016/j.jocs.2021.101544

du-Yan, G., Jia-Xing, W., Yan, W., and Xuan-Yu, L. (2022). Convolutional neural network is a good technique for sleep staging based on HRV: a comparative analysis. *Neurosci. Lett.* 779:136550. doi: 10.1016/j.neulet.2022.136550

Eldele, E., Chen, Z., Liu, C., Wu, M., Kwoh, C. K., Li, X., et al. (2021). An attention-based deep learning approach for sleep stage classification with single-channel EEG. *IEEE Trans. Neural Syst. Rehabil. Eng.* 29, 809–818. doi: 10.1109/TNSRE.2021.3076234

Guo, R., Zhai, C., Zheng, L., and Zhang, L. (2022). Sleep behavior detection based on pseudo-3d convolutional neural network and attention mechanism. *IEEE Access* 10, 90101–90110. doi: 10.1109/ACCESS.2022.3201496

Haba-Rubio, J., Darbellay, G., Herrmann, F. R., Frey, J. G., Fernandes, A., Vesin, J. M., et al. (2005). Obstructive sleep apnea syndrome: effect of respiratory events and arousal on pulse wave amplitude measured by photoplethysmography in NREM sleep. *Sleep Breath.* 9, 73–81. doi: 10.1007/s11325-005-0017-y

Haghayegh, S., Hu, K., Stone, K., Redline, S., and Schernhammer, E. (2023). Automated sleep stages classification using convolutional neural network from raw and time-frequency electroencephalogram signals: systematic evaluation study. *J. Med. Internet Res.* 25:e40211. doi: 10.2196/40211

Hsu, Y.-S., Chen, T. Y., Wu, D., Lin, C. M., Juang, J. N., and Liu, W. T. (2020). Screening of obstructive sleep apnea in patients who snore using a patch-type device with electrocardiogram and 3-axis accelerometer. *J. Clin. Sleep Med.* 16, 1149–1160. doi: 10.5664/jcsm.8462

Jiang, X., Wei, S., Zhao, L., Liu, F., and Liu, C. (2021). Analysis of photoplethysmographic morphology in sleep apnea syndrome patients using curve fitting and support vector machine. *J. Mech. Med. Biol.* 21:2140019. doi: 10.1142/S0219519421400194

Lazazzera, R., Deviaene, M., Varon, C., Buyse, B., Testelmans, D., Laguna, P., et al. (2021). Detection and classification of sleep apnea and hypopnea using PPG and SpO_2 signals. *IEEE Trans. Biomed. Eng.* 68, 1496–1506. doi: 10.1109/TBME.2020.3028041

Liu, S. (2017). Comparison between heart rate variability and pulse rate variability during different sleep stages for sleep apnea patients. *Technol. Health Care* 25, 435–445. doi: 10.3233/THC-161283

Liu, C., Zheng, D., and Murray, A. (2015). Arteries stiffen with age, but can retain an ability to become more elastic with applied external cuff pressure. *Medicine* 94:e1831. doi: 10.1097/MD.0000000000001831

Millasseau, S. C., Kelly, R. P., Ritter, J. M., and Chowienczyk, P. J. (2002). Determination of age-related increases in large artery stiffness by digital pulse contour analysis. *Clin. Sci.* 103, 371–377. doi: 10.1042/cs1030371

Murthy, J. N., van Jaarsveld, J., Fei, J., Pavlidis, I., Harrykissoon, R. I., Lucke, J. F., et al. (2009). Thermal infrared imaging: a novel method to monitor airflow during polysomnography. *Sleep* 32, 1521–1527. doi: 10.1093/sleep/32.11.1521

Norman, M. B., Middleton, S., Erskine, O., Middleton, P. G., Wheatley, J. R., and Sullivan, C. E. (2014). Validation of the sonomat: a contactless monitoring system used for the diagnosis of sleep disordered breathing. *Sleep* 37, 1477–1487. doi: 10.5665/sleep.3996

Papini, G. B., Fonseca, P., van Gilst, M. M., Bergmans, J. W. M., Vullings, R., and Overeem, S. (2020). Wearable monitoring of sleep-disordered breathing: estimation of the apnea–hypopnea index using wrist-worn reflective photoplethysmography. *Sci. Rep.* 10:13512. doi: 10.1038/s41598-020-69935-7

Penzel, T. (2017). "Home sleep testing – science direct" in *Principles and practice of sleep medicine*. eds. M. Kryger, T. Roth and C. William. 6th ed, (Elsevier), 1610–1614.

Phan, H., and Mikkelsen, K. (2022). Automatic sleep staging of EEG signals: recent development, challenges, and future directions. *Physiol. Meas.* 43:04TR01. doi: 10.1088/1361-6579/ac6049

Shen, Q., Yang, X., Zou, L., Wei, K., Wang, C., and Liu, G. (2022). Multitask residual shrinkage convolutional neural network for sleep apnea detection based on wearable bracelet photoplethysmography. *IEEE Internet Things J.* 9, 25207–25222. doi: 10.1109/JIOT.2022.3195777

Song, C., Liu, K., Zhang, X., Chen, L., and Xian, X. (2016). An obstructive sleep apnea detection approach using a discriminative hidden Markov model from ECG signals. *IEEE Trans. Biomed. Eng.* 63, 1532–1542. doi: 10.1109/TBME.2015.2498199

Sors, A., Bonnet, S., Mirek, S., Vercueil, L., and Payen, J. F. (2018). A convolutional neural network for sleep stage scoring from raw single-channel EEG. *Biomed. Signal Proces. Control* 42, 107–114. doi: 10.1016/j.bspc.2017.12.001

Tran, T. H., Nguyen, T. T., Yuldashev, Z. M., Sadykova, E. V., and Nguyen, M. T. (2019). The method of smart monitoring and detection of sleep apnea of the patient out of the medical institution. *Proc. Comput. Sci.* 150, 397–402. doi: 10.1016/j.procs.2019.02.069

van Steenkiste, T., Groenendaal, W., Dreesen, P., Lee, S., Klerkx, S., de Francisco, R., et al. (2020). Portable detection of apnea and hypopnea events using bio-impedance of the chest and deep learning. *IEEE J. Biomed. Health Inform.* 24, 2589–2598. doi: 10.1109/JBHI.2020.2967872

Wang, T., Lu, C., and Shen, G. (2019). Detection of sleep apnea from single-lead ecg signal using a time window artificial neural network. *Biomed. Res. Int.* 2019, 1–9. doi: 10.1155/2019/9768072

frontiers | Frontiers in Neuroscience

TYPE Methods
PUBLISHED 23 August 2023
DOI 10.3389/fnins.2023.1236128

OPEN ACCESS

EDITED BY
Chang Yan,
Southeast University, China

REVIEWED BY
Sishen Yuan,
The Chinese University of Hong Kong, China
Hongsheng Gui,
Henry Ford Health System, United States

*CORRESPONDENCE
Shengxiang Xia
✉ 11072@sdjzu.edu.cn

RECEIVED 07 June 2023
ACCEPTED 02 August 2023
PUBLISHED 23 August 2023

CITATION
Zhang W, Xia S, Tang X, Zhang X, Liang D and Wang Y (2023) Topological analysis of functional connectivity in Parkinson's disease. *Front. Neurosci.* 17:1236128. doi: 10.3389/fnins.2023.1236128

Topological analysis of functional connectivity in Parkinson's disease

Weiwei Zhang[1], Shengxiang Xia[1]*, Xinhua Tang[2], Xianfu Zhang[3], Di Liang[1] and Yinuo Wang[4]

[1]School of Science, Shandong Jianzhu University, Jinan, China, [2]School of Cyberspace Security, Shandong University of Political Science and Law, Jinan, China, [3]School of Control Science and Engineering, Shandong University, Jinan, China, [4]School of Nursing and Rehabilitation, Cheeloo College of Medicine, Shandong University, Jinan, China

Parkinson's disease (PD) is a clinically heterogeneous disorder, which mainly affects patients' motor and non-motor function. Functional connectivity was preliminary explored and studied through resting state functional magnetic resonance imaging (rsfMRI). Through the topological analysis of 54 PD scans and 31 age-matched normal controls (NC) in the Neurocon dataset, leveraging on rsfMRI data, the brain functional connection and the Vietoris-Rips (VR) complex were constructed. The barcodes of the complex were calculated to reflect the changes of functional connectivity neural circuits (FCNC) in brain network. The 0-dimensional Betti number β_0 means the number of connected branches in VR complex. The average number of connected branches in PD group was greater than that in NC group when the threshold $\delta \leq 0.7$. Two-sample Mann–Whitney U test and false discovery rate (FDR) correction were used for statistical analysis to investigate the FCNC changes between PD and NC groups. In PD group, under threshold of 0.7, the number of FCNC involved was significantly differences and these brain regions include the Cuneus_R, Lingual_R, Fusiform_R and Heschl_R. There are also significant differences in brain regions in the Frontal_Inf_Orb_R and Pallidum_R, when the threshold increased to 0.8 and 0.9 ($p < 0.05$). In addition, when the length of FCNC was medium, there was a significant statistical difference between the PD group and the NC group in the Neurocon dataset and the Parkinson's Progression Markers Initiative (PPMI) dataset. Topological analysis based on rsfMRI data may provide comprehensive information about the changes of FCNC and may provide an alternative for clinical differential diagnosis.

KEYWORDS

resting-state fMRI, Parkinson's disease, persistent homology, functional connectivity neural circuits, VR complex

1. Introduction

Parkinson's disease (PD) is a clinically degenerative disorder disease of the nervous system with motor and non-motor symptoms. The disease mainly affects people's motor function, such as bradykinesia, tremor, muscle stiffness or rigidity, abnormal walking gait, etc. In addition, it will also affect non-motor function, such as cognitive impairment, insomnia, depression, autonomic nerve dysfunction, and so on. The cause of PD is unclear. In the early premotor stages, the diagnosis of this disease is still difficult (Aarsland et al., 2017). Anatomical magnetic resonance imaging could not detect the loss of dopamine neurons. With the development of molecular biology, neural structure, and functional imaging technology, more and more biomarkers of PD can be discovered, providing the possibility for early diagnosis, disease monitoring, and differential diagnosis, thus achieving accurate early intervention and efficacy

evaluation of the disease. Dopamine transporter single photon emission computed tomography (DAT-SPECT) and resting state functional magnetic resonance imaging (rsfMRI) are potential techniques for detecting the survival status of neurons in PD (Wang et al., 2012). Among them, DAT-SPECT can provide quantitative information about dopamine neurons, which is very useful for assessing disease severity and monitoring treatment effectiveness. However, it is expensive and carries the risk of radioactive tracer. On the other hand, rsfMRI is a non-invasive imaging technique that is relatively inexpensive and can avoid ionizing radiation. It can provide information about brain activity, which is very useful for studying the neural mechanisms of PD and evaluating treatment effectiveness.

Therefore, the study of functional connectivity (FC) based on rsfMRI is a promising method. Based on the correlation of time series, FC was preliminary explored and studied through rsfMRI (Aarsland et al., 2017). With rsfMRI, FC can be used to detect a variety of diseases such as Alzheimer's disease, PD, schizophrenia, and so on (Lee et al., 2013). Some studies have shown that motor and cognitive impairment in PD are related to abnormal functional connections (Putcha et al., 2015; Zhang et al., 2015). Graph theory-based approaches used in PD research have shown that topological properties of brain networks are disrupted, which can help identify this type of disease (Luo et al., 2015). Specifically, abnormal local and global network efficiency changes suggest clinical phenomena in PD. The above methods assume that the functional network is stable and does not change over time. A dynamic FC based method was used in recent research. For example, previous studies used rsfMRI and sliding windows to assess differences in dynamic connectivity between normal control (NC) and PD (Kim et al., 2017). Huang et al. (2020) proposed a regression method to model the dynamic correlation matrices as a linear combination of symmetric positive definite matrix to smooth the image acquisition and physiological noise. Pang et al. (2021) distinguished different motor subtypes of PD based on multilevel indices of rsfMRI and Support Vector Machine (SVM).

However, the graph theory analysis method can not describe the characteristics of higher-level complex brain networks. To study the topological characteristics of complex brain networks on a larger scale, researchers began to study Vietoris-Rips (VR) complex filtration based on persistent homology in brain networks. In topological data analysis (TDA), persistent homology is an effective tool to explore the nonlinear structure of the data. Compared with the common methods such as principal component analysis (PCA), cluster analysis, and graph theory (Li et al., 2009), TDA can effectively capture the topological information of high-dimensional data space. This kind of algorithm adopts a free threshold and solves the problem of threshold selection. It measures the topological characteristics of brain network under all possible thresholds (Choi et al., 2014; Chung et al., 2015; Lee et al., 2017). These approaches mainly associate the 0-dimensional Betti numbers β_0 with current varying thresholds. A connected component-based aggregation cost model called Integrated Persistence Features (IPF) was proposed in previous research (Kuang et al., 2019). Different from the above persistent homology feature which based on 0-dimensional Betti numbers, this paper proposes a persistent homology feature based on the 1-dimensional Betti number β_1. To our knowledge, there is little literature investigating the 1-dimensional Betti number β_1 in PD. Our main contributions of this paper are as follows: (1) The VR complex filtering model was established based on the relationship matrix of the human brain network. The persistent homology method was used to calculate VR filtered barcodes. And then the functional connectivity neural circuits (FCNC) at different thresholds are calculated from the barcodes. (2) Two-sample Mann–Whitney *U* test and FDR correction are used for statistical analysis to investigate the FCNC changes between PD and NC groups. (3) Through the statistical tests on the number of FCNC in PD and NC groups, our results show that there is a significant statistical difference between the PD group and the NC group.

2. Method

2.1. Basic concepts about persistent homology

The common method to reduce the dimension of data is PCA, but this method will lose some potentially valuable data more or less. Persistent homology provides us a method to find a complete data ship without dimensional reduction.

Persistent homology is an effective tool to analyze high-dimensional data and explore the nonlinear structure of data. It can calculate topological features at different spatial resolutions. By identifying persistent topological features over changing scales, persistent homology provides clues for effective analysis of multi-scale networks. Its core idea is to analyze the birth and death of holes in various dimensions in a multi-scale range. To extract persistent homology features, we first need to construct VR complex. Let $d(\cdot, \cdot)$ denote the distance between two points in the metric space Z. The value of δ denotes the threshold. When we change the threshold, we obtain a sequence of complexes. The VR(Z, δ) complex is defined as follows (Silva and Carlsson, 2004):

1. For vertices a and b, edge $[ab]$ is included in VR(Z, δ) if $d(a,b) \leq \delta$.
2. A higher dimensional simplex is included in VR(Z, δ) if all of its edges are included in it.

Note that $VR(Z, \delta_0) \subseteq VR(Z, \delta_1) \subseteq \cdots \subseteq VR(Z, \delta_n)$, for $\delta_0 \leq \delta_1 \leq \cdots \leq \delta n$. Therefore, the VR complex VR(X, δ_i) ($i = 0, 1, \cdots, n$) is a filtered simplicial complex.

Betti intervals help describe how the homology of VR(Z, δ) changes with δ. A k-dimensional Betti interval, with endpoints (δ_{start}, δ_{end}), corresponds roughly to a k-dimensional hole that appears at the threshold δ_{start}, remains open for $\delta_{start} \leq \delta < \delta_{end}$, and closes at δ_{end}.

The rank of the homology group is called Betti number (Woo et al., 2014), which is a set of important topological invariants. It uses the connectivity based on k-dimensional simplex complex to distinguish the topological space, which can well reflect the topological structure of an object. The k-dimensional Betti number is the rank of the k-th homology group and represents the number of "holes" in the k-th dimension. For example, the 0-dimensional Betti number β_0 refers to the number of connected branches (Lee et al., 2012). Similarly, the one-dimensional Betti number β_1 intuitively represents the number of one-dimensional "holes."

2.2. An example of persistent homology

Figure 1 gives an example of Betti number changes with $\delta = 1.4$, 5.2, 6.3, and 8.5, respectively. Take 10 points randomly and draw a

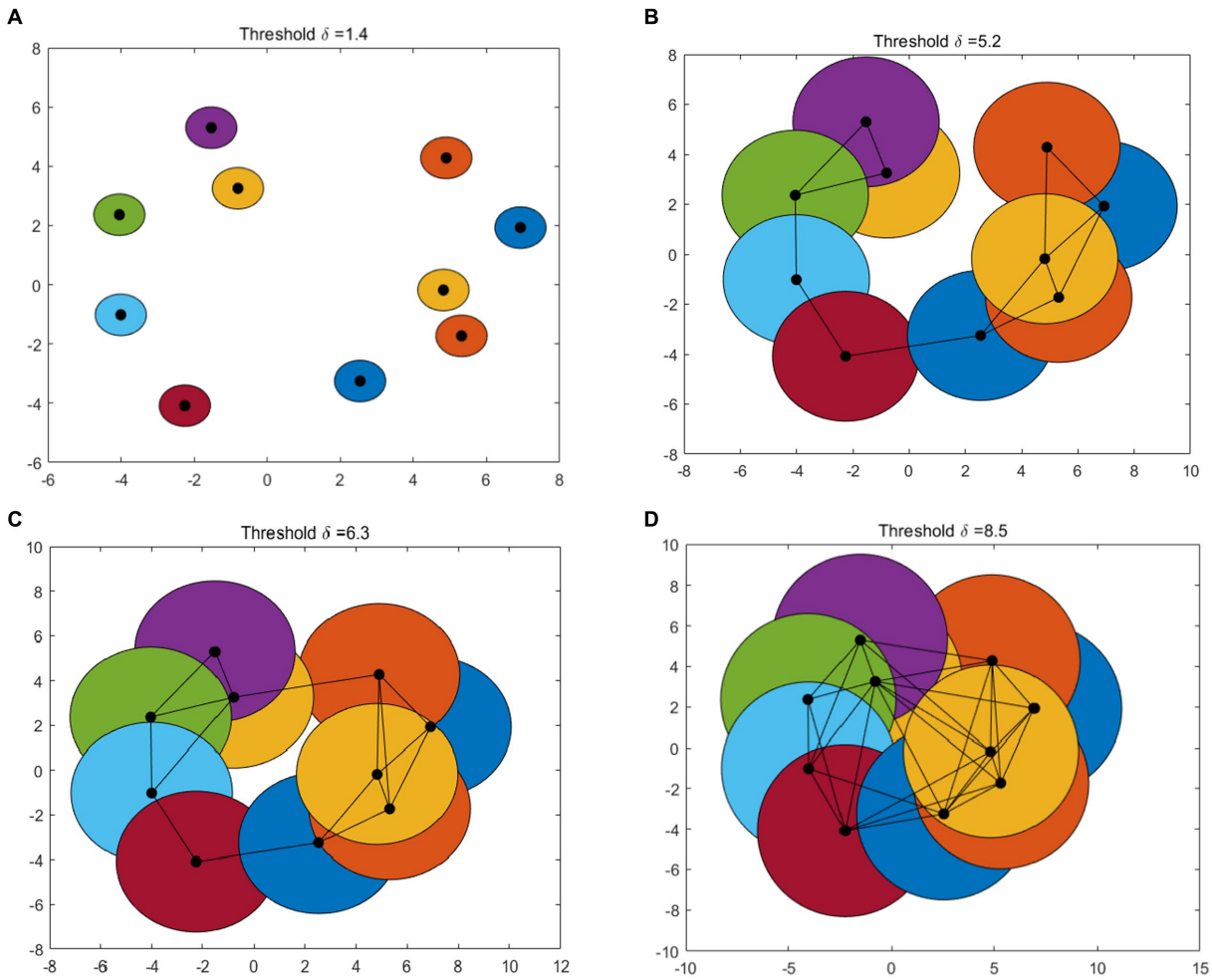

FIGURE 1
An example of VR complex. Betti number changes with **(A–D)**: $\delta = 1.4$, 5.2, 6.3, and 8.5, respectively.

circle centered on these points and radius of the threshold δ/2. In the process of increasing the threshold δ from 0 to the maximum, the 0-dimensional and 1-dimensional Betti numbers change constantly. When $\delta = 1.4$, the number of connected branches is 10, that means $\beta_0 = 10$ and the number of 1-dimensional "holes" $\beta_1 = 0$ (Figure 1A). In Figure 1B, when $\delta = 5.2$, $\beta_0 = 1$ and $\beta_1 = 0$. As the threshold δ increase, when $\delta = 6.3$ (Figure 1C), $\beta_0 = 1$ and $\beta_1 = 1$. When $\delta = 8.5$, some holes are "filled." At this time, there is only one connected branches ($\beta_0 = 1$) and one 1-dimensional "holes" ($\beta_1 = 0$) (Figure 1D).

With the change of the threshold δ, the topological characteristics of VR complex change. This process can be represented by a barcode and a persistence diagram (Figure 2). As shown in Figure 2A, a barcode is a set of finite intervals. Each interval represents the birth and death of holes in the corresponding dimension, and these intervals are parallel to each other. K-dimensional barcodes ($k = 0$, 1 in Figure 2A) show us the duration of k-dimensional topological features. Generally, we regard the features with very short duration as noise, and the features with long duration as real signal features. In Figure 2B, the persistence diagram provides a multi-scale feature description. The abscissa of each point in the diagram represents the birth of the topological feature, while the ordinate represents its demise. Points away from the diagonal represent features with a long life cycle, while points close to the diagonal represent features with a short life cycle. Among them, the feature that can be maintained for a longer time is a useful persistence feature with stronger robustness. The feature with short life is more likely to be noise or detail. The red vertical line on the ordinate axis is regarded as a point at infinity, representing a topological feature that will never die.

3. Results

3.1. Dataset and preprocessing

The datasets used in this article are the Neurocon dataset (Badea et al., 2017) and Parkinson's Progression Markers Initiative (PPMI) dataset (Marek et al., 2011). The Neurocon dataset includes rsfMRI data from 27 PD patients and 16 age matched NC patients, with each subject undergoing 2 repeated scans. One NC scan was subsequently excluded owing to data corruption. Finally, 54 PD scans and 31 NC scans were included in the final analyses. The Neurocon study has been approved by the Ethics Committee of the Emergency Hospital of

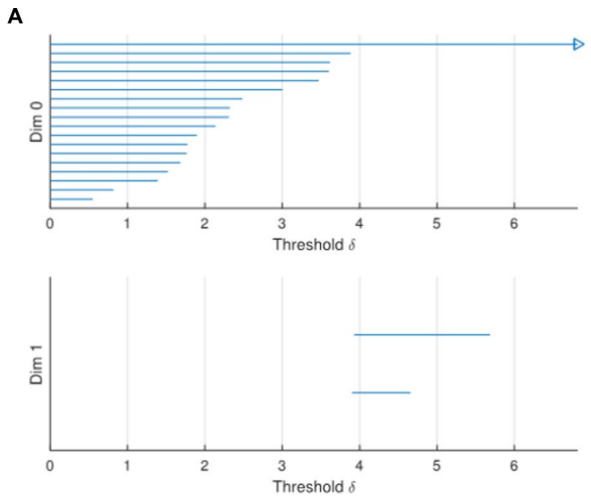

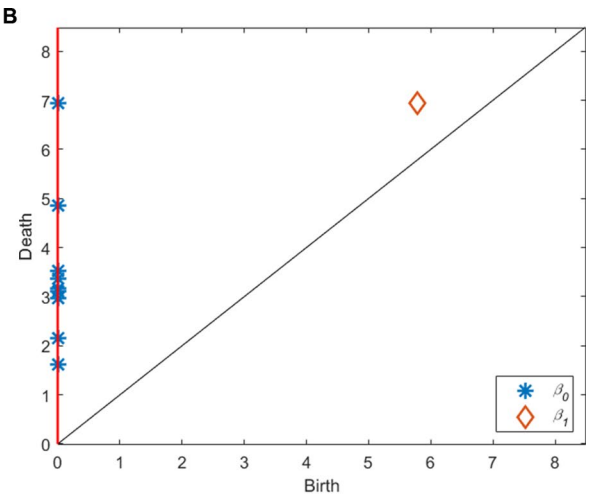

FIGURE 2
Barcodes and persistence graph. **(A)** Barcodes. **(B)** Persistence diagram.

TABLE 1 The details of the Neurocon dataset.

Dataset	PD subjects	NC subjects	PD scans	NC scans	Age PD (mean ± SD)	Age NC (mean ± SD)	P (age NC-PD)	H&Y (mean ± SD)	Disease duration (mean ± SD)
Neurocon	27 (16 M)	16 (5 M)	54	31	68.7 ± 10.6	67.6 ± 11.9	0.76	1.92 ± 0.33	4.6 ± 6.5

SD, standard deviation; H&Y, Hoehn and Yahr; PD, Parkinson's disease; NC, normal controls.

the University of Bucharest and is in line with the Helsinki Declaration 1964 and its later revised ethical standards (Badea et al., 2017). The scanner is Siemens AVanto 1.5 T, Scan time = 8.05 min, TR = 3.48 s, Voxel = 3.8 × 3.8 × 5 mm^3, volume = 137. Each rsfMRI consists of 2 mm isotropic voxels and 1,200 time points over a 14 min, 33 s scanning session. The details of the Neurocon dataset are shown in Table 1. Retrieve rsfMRI data from the PPMI dataset for 154 PD patients and 24 age matched NC patients. Each study in the PPMI dataset was approved by the Human Experimental Ethics Standards Committee before registration, and each subject signed a written informed consent form. This study obtained the right to use the PPMI database data.

The Neurocon dataset is preprocessed using DPABI (DPABI Software Library v5.1) (Yan et al., 2016) as follows:

1. Removing the first 10 time points of rsfMRI data to obtain a stable signal;
2. Time correction is performed on each slice to ensure that the data on each slice corresponds to the same time;
3. Realign: eliminate the data with the maximum value of translation greater than 3 mm and the maximum value of rotation greater than 3°;
4. Registration of structural image to functional image space. Use anatomical T1 images to register to the standard Montreal Institute of Neurology MNI152 template;
5. Check the coverage of function image by Automask;
6. Bandpass filtering with a frequency of 0.01 ~ 0.1 Hz is set;
7. Normalize using EPI templates;
8. Extract region of interest (ROI) time courses using Anatomical Automatic Labeling (AAL) atlas.

The brain parcellation used in this paper is the AAL brain template (Tzourio-Mazoyer et al., 2002). There are 116 regions in the AAL template, 90 belonging to the brain, and the remaining 26 belong to the cerebellar structure. There are few studies on the cerebellum. In this paper, the classical AAL template of 90 brain regions is used to construct VR complex.

3.2. Constructing VR complex

Firstly, we preprocess the rsfMRI image as described above, and then calculate the FC between the 90 brain regions in the AAL template. Pearson correlation is probably the most commonly used scheme for calculating functional connections (Valdes-Sosa et al., 2011). We also use the Pearson correlation coefficient between vertices to construct the FC matrix in this work. FC is defined as the temporal correlation of brain region. For convenience, we defined $P(j) = \{P_1(j), P_2(j), \cdots, P_n(j)\}$ $(j = 1, 2, \cdots, 90)$ as the average time signal sequence of the j-th brain regions, and n is the total number of time series. The FC matrix $M = (m_{ij})$ $(i, j = 1, 2, \cdots, 90)$ is calculated using equation (1):

$$m_{ij} = corr(P^i, P^j) = \frac{\sum_{k=1}^{n}(P_k^{(i)} - \overline{P}^{(i)})(P_k^{(j)} - \overline{P}^{(j)})}{\sqrt{\sum_{k=1}^{n}(P_k^{(i)} - \overline{P}^{(i)})^2}\sqrt{\sum_{k=1}^{n}(P_k^{(j)} - \overline{P}^{(j)})^2}} \quad (1)$$

To construct VR complex, we defined the distance between each two vertices using equation (2):

$$d\left(P^i,P^j\right)=\sqrt{1-corr\left(P^i,P^j\right)}\ \ (i,j=1,2,\cdots,90) \qquad (2)$$

For each value, the nested complex $VR\left(Z,\delta_0\right)\subseteq VR\left(Z,\delta_1\right)\subseteq\cdots\subseteq VR\left(Z,\delta_n\right)$ is constructed. Thus, a VR complex was further established for each subject. The VR complex take three inputs: the maximum dimension d_{max} of any included simplex, the maximum filtration value t_{max}, and the number of divisions. In our experiments, the maximum dimension $d_{max}=2$, which means we construct 0-dimensional simplex and 1-dimensional simplex. The maximum filtration value $t_{max}=0.9$ and the number of division is set to 450.

4. Discussion

The VR complex is established under multiple scales. The 0-dimensional Betti number β_0 and the 1-dimensional Betti number β_1 under each scale are calculated using Javaplex software. Figure 3 plots show the 0-dimensional and 1-dimensional Betti number curves between PD and NC. As depicted from the 0-dimensional Betti number diagram (Figure 3A), with the increase of threshold δ, the number of connected branches of PD and NC gradually decrease from the initial 90. Until the threshold $\delta=0.7$, they tend to be consistent and gradually decreased to 1. But β_0 in PD is always greater than that in NC when $\delta\leq0.7$. In the 1-dimensional Betti number curves (Figure 3B), the topological features was significantly different between the PD brain network and the NC brain network under different thresholds.

In Table 2, two sample Kolmogorov Smirnov (K-S) tests were also conducted from Figures 3A,B to compare whether there is a significant difference in distribution between the PD group and the NC group. From Table 2, it can be seen that the maximum absolute differences in the cumulative probability of Betti numbers in 0-dimension and 1-dimension are 0.049 and 0.082, respectively. Assuming a significance level of 0.05, as the probability *p*-values (both 0.000) are less than the significance level, it can be concluded that there is a significant difference in the Betti number curve between the PD group and the NC group, regardless of whether it is 0-dimensional or 1-dimensional. Therefore, by comparing the Betti numbers at all scales, the differences between these two groups can be detected.

To more intuitively show the difference between PD and NC groups, comparison of the 1-dimention FCNC in the PD group and the NC group with $\delta=0.4$ in the Neurocon dataset are shown in Figure 4. Among them, the coronal and sagittal views are shown in Figure 4A and Figure 4B respectively, and their corresponding relationship matrices are given in Figure 4C. Note that, the different colors in Figure 4 only represent different FCNC.

The number of FCNC in 90 brain regions was analyzed and a histogram was drawn in Figure 5. It can be seen intuitively, the average

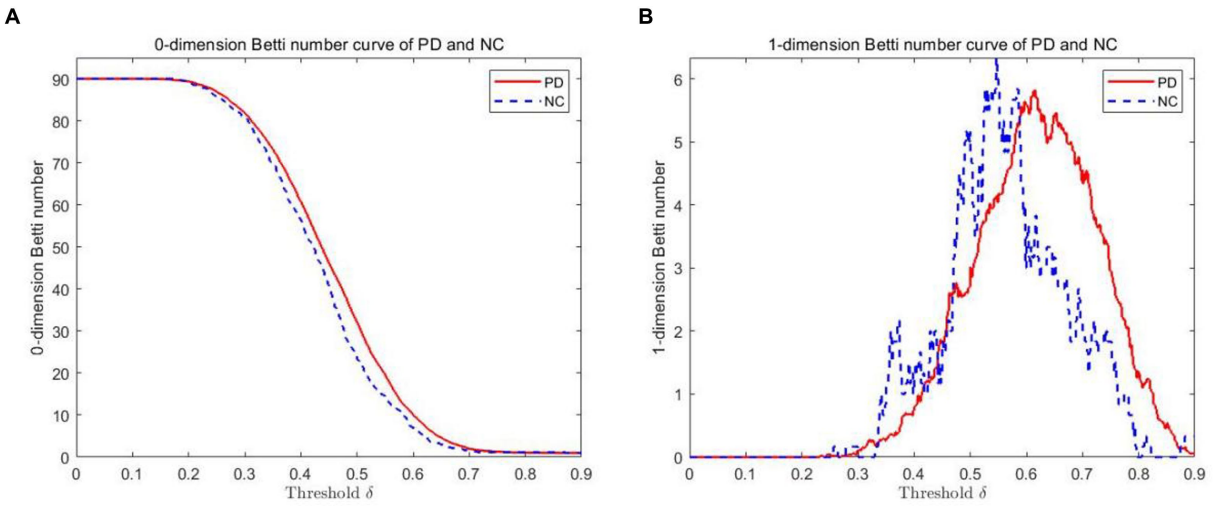

FIGURE 3
Betti number curves of PD and NC groups in 0 and 1 dimensions. **(A)** The 0-dimensional Betti number diagram. **(B)** The 1-dimensional Betti number diagram.

TABLE 2 Two-sample K-S tests.

		0-dimension	1-dimension
Extreme difference	Absolute	0.049	0.082
	Positive	0.049	0.082
	Negative	−0.038	−0.058
Kolmogorov Sminov Z		3.451	5.819
Asymptotic significance (double tailed)		0.000	0.000

0-dimension and 1-dimension represents PD and NC samples of different dimensions separately.

10.3389/fnins.2023.1236128

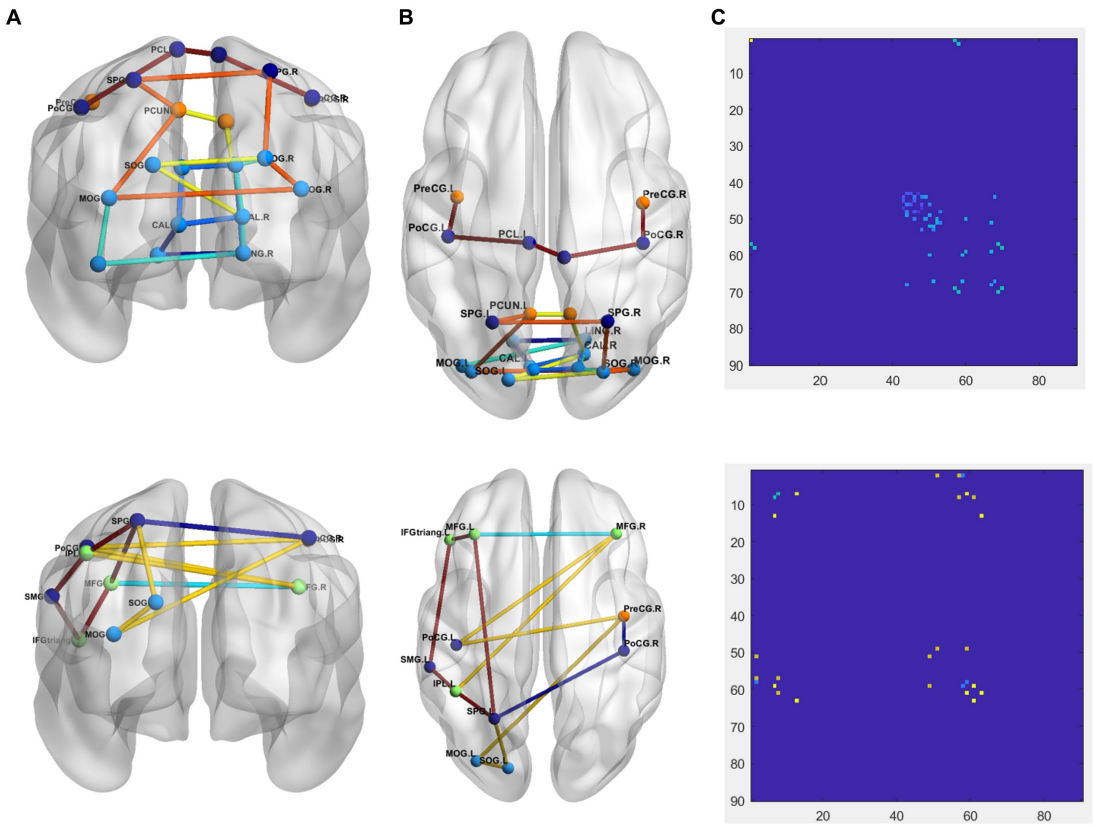

FIGURE 4
Comparison of the FCNC in the PD group and the NC group with $\delta = 0.4$ in the Neurocon dataset. **(A)** Coronal view. **(B)** Sagittal view. **(C)** The relation matrix. The first row: the FCNC in the PD group. The second row: the FCNC in the NC group. Different colors are just for the purpose of easy observation.

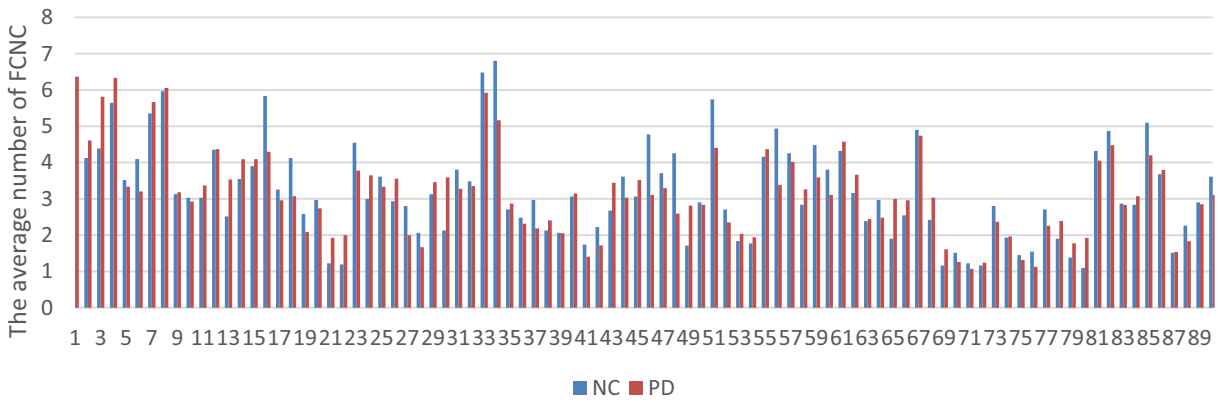

FIGURE 5
Comparison of the average number of FCNC between PD and NC groups in AAL 90 brain regions.

number of FCNC in PD and NC groups is significantly different in some brain regions. To further analyze these differences, the mean and standard deviation of the number of FCNC in each brain region were calculated for the PD and NC groups under thresholds of 0.7, 0.8, and 0.9 in Neurocon dataset, respectively. Then, two sample Mann Whitney *U* test and false discovery rate (FDR) correction were performed to detect differences between the two groups. The brain regions with statistical differences are shown in Table 3. In PD group, under threshold of 0.7, the number of FCNC involved was significantly differences and these brain regions include the Cuneus_R, Lingual_R, Fusiform_R and Heschl_R. In addition to the aforementioned brain regions, there are also significant differences in brain regions in the Frontal_Inf_Orb_R and Pallidum_R, when the threshold increases to 0.8 and 0.9 ($p < 0.05$ and FDR correction).

TABLE 3 Statistically significant differences in the numbers of FCNC in the involved brain regions.

Brain regions	Threshold	PD ($n = 54$) mean ± SD	NC ($n = 31$) mean ± SD	P-value	q-value (FDR-corrected)
Precentral_L	0.7	4.43 ± 3.611	3.03 ± 3.125	0.046*↓	0.0520
	0.8	6.07 ± 4.138	4.45 ± 3.075	0.039*↓	0.0520
	0.9	6.07 ± 4.138	4.52 ± 3.086	0.052	0.0520
Frontal_Inf_Orb_R	0.7	2.96 ± 2.747	3.97 ± 3.516	0.192	0.1920
	0.8	4.07 ± 3.392	5.74 ± 3.235	0.014*↓	0.0210*↓
	0.9	4.09 ± 3.388	5.81 ± 3.301	0.013*↓	0.0210*↓
Olfactory_R	0.7	0.63 ± 0.938	0.74 ± 0.999	0.672	0.6720
	0.8	1.81 ± 1.802	1.06 ± 1.181	0.059	0.0885
	0.9	1.91 ± 1.896	1.06 ± 1.181	0.043*↓	0.0885
Cuneus_R	0.7	2.15 ± 2.184	3.68 ± 2.774	0.008*↓	0.0210*↓
	0.8	2.91 ± 2.742	4.65 ± 3.431	0.018*↓	0.0210*↓
	0.9	2.93 ± 2.739	4.65 ± 3.431	0.021*↓	0.0210*↓
Lingual_R	0.7	1.81 ± 2.019	3.35 ± 3.251	0.035*↓	0.0350*↓
	0.8	2.33 ± 2.181	4.06 ± 3.255	0.010*↓	0.0150*↓
	0.9	2.35 ± 2.173	4.13 ± 3.274	0.008*↓	0.0150*↓
Occipital_Inf_R	0.7	0.98 ± 1.173	1.42 ± 1.205	0.041*↓	0.1230
	0.8	1.56 ± 1.690	1.77 ± 1.499	0.293	0.2930
	0.9	1.56 ± 1.690	1.77 ± 1.499	0.293	0.2930
Fusiform_R	0.7	2.35 ± 2.147	3.90 ± 2.508	0.003*↓	0.006*↓
	0.8	2.85 ± 2.227	4.68 ± 3.113	0.006*↓	0.006*↓
	0.9	2.85 ± 2.227	4.71 ± 3.090	0.005*↓	0.006*↓
Pallidum_R	0.7	0.43 ± 0.792	0.84 ± 1.293	0.085	0.0850
	0.8	0.81 ± 1.065	1.52 ± 1.480	0.007*↓	0.0150*↓
	0.9	0.83 ± 1.077	1.52 ± 1.480	0.010*↓	0.0150*↓
Heschl_R	0.7	1.19 ± 1.543	0.45 ± 0.675	0.013*↓	0.027*↓
	0.8	1.72 ± 1.857	1.06 ± 1.825	0.027*↓	0.027*↓
	0.9	1.72 ± 1.857	1.06 ± 1.825	0.027*↓	0.027*↓

SD, standard deviation; FDR, false discovery rate; ∗↓ denotes ($p < 0.05$).

TABLE 4 Statistically significant difference between the two groups in the number of medium length of FCNCs.

Datasets	Threshold value	PD (mean ± SD)	NC (mean ± SD)	P-value	q-value (FDR-corrected)
Neurocon	0.7	1.69 ± 1.286	1.30 ± 1.317	0.091	0.091
	0.8	2.33 ± 1.454	1.63 ± 1.377	0.017	0.043*↓
	0.9	2.330 ± 1.454	1.63 ± 1.377	0.029	0.043*↓
PPMI	0.7	1.14 ± 1.105	0.54 ± 0.977	0.004	0.008*↓
	0.8	1.36 ± 1.159	0.75 ± 1.113	0.008	0.008*↓
	0.9	1.38 ± 1.161	0.75 ± 1.113	0.007	0.008*↓

SD, standard deviation; FDR, false discovery rate; ∗↓ denotes ($p < 0.05$).

We also analyzed the statistical differences in the number of FCNC with medium lengths in the Neurocon and PPMI datasets (Table 4). From Table 4, it can be seen that there is a significant difference between the PD group and the NC group for medium length of FCNC. Specifically, at thresholds of 0.8 and 0.9, there was a significant difference between the two groups in the Neurocon dataset (length = 8). When the thresholds are 0.7, 0.8, and 0.9, there was a significant difference between the two groups in the PPMI dataset (length = 9). All results were corrected through FDR correction. In these two datasets, at different thresholds, the mean of the PD group is always greater than that of the NC group.

At different thresholds, we can also visually see the significant differences between the two groups through the box-plot in the Neurocon dataset. From the box-plot Figure 6, it can be seen that

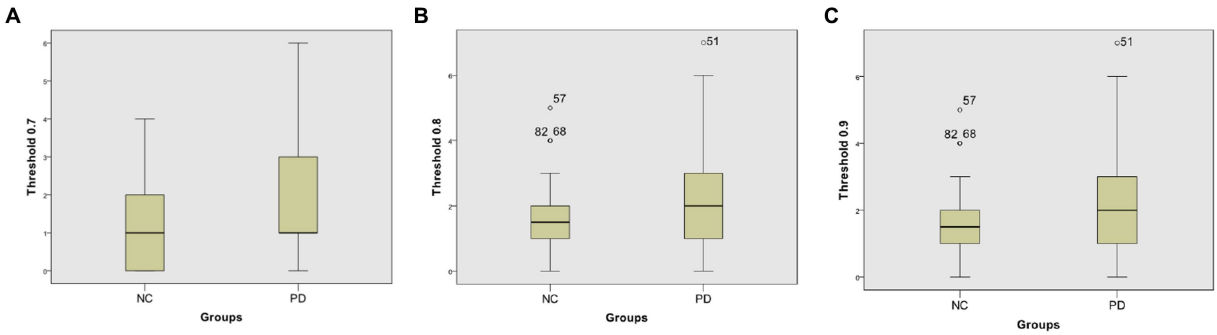

FIGURE 6
Box-plot comparison of the numbers of FCNC with length = 8. The numbers of FCNC with length = 8 when threshold = 0.7 **(A)**, 0.8 **(B)**, and 0.9 **(C)**, respectively.

when the threshold is 0.7, there is no significant difference in the median between the two groups. However, when the thresholds are increased to 0.8 and 0.9, the median of the PD group are significantly higher than that of the NC group. The above results show that there are significant differences in the characteristics of FCNC in some brain regions, and the medium length of FCNC in PD patients show significant changes.

According to the functional classification of the brain, Woo et al. (2014) divided the AAL brain regions into 7 sub networks. That is dorsal attention network (DAN), default mode network (DMN), the visual network (VSN), ventral attention network (VAN), limbic network (LBN), fronto parietal network (FPN) and somatomotor network (SMN) (Esposito et al., 2013; Baum et al., 2017).

By analyzing the FCNC, we found significant statistical difference in the Frontal_Inf_Orb, Cuneus, Lingual gyrus, Fusiform, Pallidum and Heschl areas. A similar result was obtained in previous studies regarding the function connectivity strength of the SMN and VAN (Caspers et al., 2021; Tsuboi et al., 2021) and our findings provide guidance for further studies on the pathogenesis of early PD. Interestingly, increases in FC within SMN (Pang et al., 2021) have been observed upon a dopaminergic challenge in PD patients. Both anterior central gyrus and transverse Nie gyrus belong to SMN. Caspers et al. (2021) pointed out that PD is accompanied by the loss of functional connection of SMN, whether within the network or in the interaction with other networks. The lesions of globus pallidus can have symptoms such as increased muscle tension, decreased movement and static tremor (such as Parkinson's syndrome). Globus pallidus plays an important role in the regulation of motor function. It is not only the relay nucleus between the caudate putamen (CPU) and subthalamic nucleus (STN), but also integrates the inhibitory afferent from CPU and the excitatory afferent from STN, neocortex and thalamus, thus affecting the efferent signal of basal ganglia (Esposito et al., 2013). Globus pallidus stimulation can be used to improve the brain connectivity in order to treat advanced PD (Tsuboi et al., 2021).

5. Conclusion

This study applies persistent homology to the brain functional networks of PD. This work provides some new insights into the evolution of functional network in the progression of PD and may provide evidence for the study of preclinical biomarkers of PD. We observed that there are significant differences in the characteristics of FCNC in some brain regions, and the medium length of FCNC in PD patients show significant changes. Topological analysis based on rsfMRI data may provide comprehensive information about the changes of FCNC and may provide an alternative for clinical differential diagnosis.

Data availability statement

Publicly available datasets were analyzed in this study. The Neurocon dataset can be found at: http://fcon_1000.projects.nitrc.org/indi/retro/parkinsons.html. The PPMI dataset can be found at: https://www.ppmi-info.org/.

Author contributions

WZ, SX, and XZ designed the research study. DL performed the research. XT and YW wrote the manuscript. All authors contributed to editorial changes in the manuscript, read, and approved the final manuscript.

Funding

This work was supported by the Natural Science Foundation of Shandong Province of China (ZR2020ZD25) and the Autonomous Innovation Team Foundation for "20 Items of the New University" of Jinan City (No. 202228087).

Acknowledgments

The authors would also like to thank the authors who provided the dataset used for experiments.

Conflict of interest

The authors declare that the research was conducted in the absence of any commercial or financial relationships that could be construed as a potential conflict of interest.

Publisher's note

References

Aarsland, D., Creese, B., Politis, M., Chaudhuri, K. R., Ffytche, D. H., Weintraub, D., et al. (2017). Cognitive decline in Parkinson disease. *Nat. Rev. Neurol.* 13, 217–231. doi: 10.1038/nrneurol.2017.27

Badea, L., Onu, M., Wu, T., Roceanu, A., Bajenaru, O., and Hayasaka, S. (2017). Exploring the reproducibility of functional connectivity alterations in Parkinson's disease. *PLoS One* 12:e0188196. doi: 10.1371/journal.pone.0188196

Baum, G. L., Ciric, R., Roalf, D. R., Betzel, R. F., Moore, T. M., Shinohara, R. T., et al. (2017). Modular segregation of structural brain networks supports the development of executive function in youth. *Curr. Biol.* 27, 1561–1572.e8. doi: 10.1016/j.cub.2017.04.051

Caspers, J., Rubbert, C., Eickhoff, S. B., Hoffstaedter, F., Südmeyer, M., Hartmann, C. J., et al. (2021). Within-and across-network alterations of the sensorimotor network in Parkinson's disease. *Neuroradiology* 63, 2073–2085. doi: 10.1007/s00234-021-02731-w

Choi, H., Kim, Y. K., Kang, H., Lee, H., Im, H. J., Hwang, D. W., et al. (2014). Abnormal metabolic connectivity in the pilocarpine-induced epilepsy rat model. A multiscale network analysis based on persistent homology. *Neuroimage* 99, 226–236. doi: 10.1016/j.neuroimage.2014.05.039

Chung, M. K., Hanson, J. L., Ye, J., Davidson, R. J., and Pollak, S. D. (2015). Persistent homology in sparse regression and its application to brain morphometry. *IEEE Trans. Med. Imaging* 34, 1928–1939. doi: 10.1109/TMI.2015.2416271

Esposito, F., Tessitore, A., Giordano, A., DeMicco, R., Paccone, A., Conforti, R., et al. (2013). Rhythm-specific modulation of the sensorimotor network in drug-naive patients with Parkinson's disease by levodopa. *Brain J. Neurol.* 136, 710–725. doi: 10.1093/brain/awt007

Huang, S. G., Samdin, S. B., Ting, C. M., Ombao, H., and Chung, M. K. (2020). Statistical model for dynamically-changing correlation matrices with application to brain connectivity. *J. Neurosci. Methods* 331:108480. doi: 10.1016/j.jneumeth.2019.108480

Kim, J., Criaud, M., Cho, S. S., Díez-Cirarda, M., Mihaescu, A., Coakeley, S., et al. (2017). Abnormal intrinsic brain functional network dynamics in parkinson's disease. *Brain* 140, 2955–2967. doi: 10.1093/brain/awx233

Kuang, L., Han, X., Chen, K., Caselli, R. J., Reiman, E. M., Wang, Y., et al. (2019). A concise and persistent feature to study brain resting-state network dynamics: findings from the Alzheimer's disease neuroimaging initiative. *Hum. Brain Map.* 40, 1062–1081. doi: 10.1002/hbm.24383

Lee, H., Kang, H., Chung, M. K., Kim, B. N., and Lee, D. S. (2012). Persistent brain network homology from the perspective of dendrogram. *IEEE Trans. Med. Imaging* 31, 2267–2277. doi: 10.1109/TMI.2012.2219590

Lee, H., Kang, H., Chung, M. K., Lim, S., Kim, B. N., and Dong, S. L. (2017). Integrated Multimodal network approach to PET and MRI based on multidimensional persistent homology. *Hum. Brain Map.* 38, 1387–1402. doi: 10.1002/hbm.23461

Lee, M. H., Smyser, C. D., and Shimony, J. S. (2013). Resting-state fMRI: a review of methods and clinical applications. *Am. J. Neuroradiol.* 34, 1866–1872. doi: 10.3174/ajnr.A3263

Li, K., Guo, L., Nie, J., Li, G., and Liu, T. (2009). Review of methods for functional brain connectivity detection using fMRI. *Comput. Radiol.* 33, 131–139. doi: 10.1016/j.compmedimag.2008.10.011

Luo, C. Y., Guo, X. Y., Song, W., Chen, Q., Cao, B., Yang, J., et al. (2015). Functional connectome assessed using graph theory in drug-naive Parkinson's disease. *J. Neurol.* 262, 1557–1567. doi: 10.1007/s00415-015-7750-3

Marek, K., Jennings, D., Lasch, S., Siderowf, A., Tanner, C., Simuni, T., et al. (2011). The Parkinson progression marker initiative (PPMI). *Prog. Neurobiol.* 95, 629–635. doi: 10.1016/j.pneurobio.2011.09.005

Pang, H. Z., Yu, Z. Y., Yu, H. M., Cao, J. B., Li, Y. M., Guo, M. R., et al. (2021). Use of machine learning method on automatic classification of motor subtype of Parkinson's disease based on multilevel indices of rs-fMRI. *Parkinsonism Relat. Disord.* 90, 65–72. doi: 10.1016/j.parkreldis.2021.08.003

Putcha, D., Ross, R. S., Cronin-Golomb, A., Janes, A. C., and Stern, C. E. (2015). Altered intrinsic functional coupling between core neurocognitive networks in Parkinson's disease. *Neuroimage* 7, 449–455. doi: 10.1016/j.nicl.2015.01.012

Silva, V. D., and Carlsson, G. (2004). Topological estimation using witness complexes. *Proceedings of the First Eurographics conference on Point-Based Graphics*. 157–166. doi: 10.2312/SPBG/SPBG04/157-166

Tsuboi, T., Charbel, M., Peterside, D. T., Rana, M., Elkouzi, A., Deeb, W., et al. (2021). Pallidal connectivity profiling of stimulation-induced dyskinesia in Parkinson's disease. *Mov. Disord.* 36, 380–388. doi: 10.1002/mds.28324

Tzourio-Mazoyer, N., Landeau, B., Papathanassiou, D., Crivello, F., Etard, O., Delcroix, N., et al. (2002). Automated anatomical labeling of activations in SPM using a macroscopic anatomical parcellation of the MNI MRI single-subject brain. *Neuroimage* 15, 273–289. doi: 10.1006/nimg.2001.0978

Valdes-Sosa, P. A., Roebroeck, A., Daunizeau, J., and Friston, K. J. (2011). Effective connectivity: influence, causality and biophysical modeling. *Neuroimage* 58, 339–361. doi: 10.1016/j.neuroimage.2011.03.058

Wang, L., Zhang, Q., Li, H., and Zhang, H. (2012). SPECT molecular imaging in Parkinson's disease. *J. Biomed. Biotechnol.* 2012, 1–11. doi: 10.1155/2012/412486

Woo, C. W., Krishnan, A., and Wager, T. D. (2014). Cluster-extent based thresholding in fMRI analyses: pitfalls and recommendations. *Neuroimage* 91, 412–419. doi: 10.1016/j.neuroimage.2013.12.058

Yan, C. G., Wang, X. D., Zuo, X. N., and Zang, Y. F. (2016). DPABI: data processing & analysis for (resting-state) brain imaging. *Neuroinformatics* 14, 339–351. doi: 10.1007/s12021-016-9299-4

Zhang, D., Liu, X., Chen, J., Liu, B., and Wang, J. (2015). Widespread increase of functional connectivity in Parkinson's disease with tremor: a resting-state fMRI study. *Front. Aging Neurosci.* 7:6. doi: 10.3389/fnagi.2015.00006

frontiers | Frontiers in Neuroscience

TYPE Original Research
PUBLISHED 13 September 2023
DOI 10.3389/fnins.2023.1220581

OPEN ACCESS

EDITED BY
Hong Zeng,
Southeast University, China

REVIEWED BY
Liliana Teixeira,
Polytechnic Institute of Leiria, Portugal
Zhuoying Qiu,
China Rehabilitation Research Center/WHO Collaborating Center for Family International Classifications, China

*CORRESPONDENCE
Akhila Veerubhotla
✉ Akhila.veerubhotla@nyulangone.org

RECEIVED 10 May 2023
ACCEPTED 23 August 2023
PUBLISHED 13 September 2023

CITATION
Mazzeo M, Hernan G and Veerubhotla A (2023) Usability and ease of use of long-term remote monitoring of physical activity for individuals with acquired brain injury in community: a qualitative analysis.
Front. Neurosci. 17:1220581.
doi: 10.3389/fnins.2023.1220581

Usability and ease of use of long-term remote monitoring of physical activity for individuals with acquired brain injury in community: a qualitative analysis

Marie Mazzeo, Gabriel Hernan and Akhila Veerubhotla*

Department of Rehabilitation Medicine, New York University - Grossman School of Medicine, New York, NY, United States

Introduction: Objective and continuous monitoring of physical activity over the long-term in the community is perhaps the most important step in the paradigm shift toward evidence-based practice and personalized therapy for successful community integration. With the advancement in technology, physical activity monitors have become the go-to tools for objective and continuous monitoring of everyday physical activity in the community. While these devices are widely used in many patient populations, their use in individuals with acquired brain injury is slowly gaining traction. The first step before using activity monitors in this population is to understand the patient perspective on usability and ease of use of physical activity monitors at different wear locations. However, there are no studies that have looked at the feasibility and patient perspectives on long-term utilization of activity monitors in individuals with acquired brain injury.

Methods: This pilot study aims to fill this gap and understand patient-reported aspects of the feasibility of using physical activity monitors for long-term use in community-dwelling individuals with acquired brain injury.

Results: This pilot study found that patients with acquired brain injury faced challenges specific to their functional limitations and that the activity monitors worn on the waist or wrist may be better suited in this population.

Discussion: The unique wear location-specific challenges faced by individuals with ABI need to be taken into account when selecting wearable activity monitors for long term use in this population.

KEYWORDS

stroke, traumatic brain injury, fitness trackers, community integration, usability, ease-of-use, remote patient monitoring

1. Introduction

Acquired brain injury (ABI) is an umbrella term that describes damage to the brain that occurs after birth; mechanisms of injury may be traumatic [e.g., traumatic brain injury (TBI)] or non-traumatic (e.g., stroke). ABI is a significant cause of morbidity and mortality worldwide, the recovery course is extremely varied, and residual disability is highly prevalent (Törnbom et al., 2017; Grabljevec et al., 2018). Potential sequelae include impaired functioning in physical, cognitive, neurological, behavioral, and lifestyle domains and most of these limitations persist even into the

chronic phase (>6 months) post-ABI. Compared to individuals with similar durations of hospitalization for different etiologies, individuals who have experienced a head injury have an increased risk of death for at least 13 years after hospital admission (Hillman et al., 2008).

Rehabilitation is an important part of the recovery process post-ABI and typically continues during the acute phase and the chronic phase. An essential aspect of rehabilitation during the chronic phase is physical activity (PA). Rehabilitation specialists are recommended to prescribe PA programs, especially in the chronic phase after ABI (Grabljevec et al., 2018). Increased physical activity has been associated with distinct anatomical and physiological changes and may improve physical and mental health; aerobic activity has demonstrable benefits on overall brain health (Hillman et al., 2008; Crosson et al., 2017; O'Carroll et al., 2020; Mercier et al., 2021; Sheng et al., 2021). PA is believed to facilitate neuronal plasticity and affect the brain's recovery following ABI, and engagement in PA has been shown to impact an individual's health-related quality of life (Hillman et al., 2008; Crosson et al., 2017; O'Carroll et al., 2020; Mercier et al., 2021; Sheng et al., 2021). Additionally, engagement in physical activity may improve sleep quality; sleep disturbances are highly prevalent in individuals with ABI and have a well-established impact on the efficacy of rehabilitation efforts (Bruijel et al., 2021; Dey et al., 2021). The significant role of PA in recovery is especially significant when considering that recent studies have demonstrated that individuals who have experienced ABI participate in less PA compared to healthy individuals, and are more sedentary than their age-matched peers (Törnbom et al., 2017).

Traditionally, questionnaires and surveys are used to measure PA; however, wearable physical activity monitors (PAMs) have emerged as an alternative objective method to measure PA (Brickwood et al., 2019; Cho et al., 2021; Veerubhotla et al., 2021). PAMs are designed to be small, lightweight, and low-cost devices (Brickwood et al., 2019; Veerubhotla et al., 2021). Wearable devices are beneficial because they can monitor PA over days to months in free-living conditions with minimal interference to the user's everyday life (Brickwood et al., 2019; Veerubhotla et al., 2021). The data derived from PAMs can be described as person-generated health data (PGHD)—a potentially valuable resource for researchers and care providers alike (Cho et al., 2021; Veerubhotla et al., 2021). For example, accelerometer counts have been used to measure walking intensity in individuals who have experienced a minor stroke and are significantly associated with physical capacity, a measure of functional status related to overall health and well-being (Braakhuis et al., 2022).

Usability and wearability are important considerations for the use of PAMs. As described by Eng et al., usability refers to the ease of use, which encompasses user interface, set-up, and errors (Louie et al., 2020). Wearability refers to donning, doffing, aesthetics, and the comfort of a device (Louie et al., 2020). A recent systematic review identified user-related factors (e.g., device non-wear) and device/technical-related factors (e.g., issues with hardware, software, etc.) as major categories that impact the quality of PGHD (Cho et al., 2021). It is essential that PAMs are specifically studied in individuals who have experienced ABI, because the unique sequelae which impact the usability and accuracy of these devices in this patient population may not be represented in studies of the general population (Campos et al., 2018; Veerubhotla et al., 2021). Additionally, to the best of our knowledge, the transition from laboratory to community-based studies of PAMs has not yet occurred for individuals who have experienced TBI (Veerubhotla et al., 2021). Further, there is a need for usability studies and community-based research in both individuals with TBI and stroke that have a duration of greater than 1 week (Hardy et al., 2018; Veerubhotla et al., 2021). There is a lack of information regarding the long-term utilization of PAMs, nor is there a consensus on the best wear location for PAMs, as studies have used different wear locations (e.g., wrist, waist, ankle) (Giggins et al., 2017).

To effectively undertake community-based research in individuals with ABI using wearable devices, it is important to first understand their usability and ease of use from the patient/user perspective. The goal of this pilot investigation was to determine the usability and feasibility of wearable PAM in individuals with ABI, specifically, in individuals who have experienced a stroke or TBI. This study assessed patient-reported challenges with PAMs at three popular wear locations (wrist, waist and ankle), patient reported wear location preferences, and the use of a remote data transfer hub for remote monitoring, for a duration of 4 weeks in community dwelling individuals with ABI. By doing so, this study seeks to provide a framework for important considerations for the use of PAMs in community-dwelling individuals who have experienced ABI.

2. Materials and methods

2.1. Participants

To be included in this study, participants had to (1) be between the ages of 45 and 75; (2) have been diagnosed with a stroke or a non-penetrating TBI by a physician and be at least 6 months post-injury; (3) have been medically stable for 3 months at the time of study participation; (4) no plans to make any drastic changes to medications for at least 4 weeks; (5) have sufficient endurance and motor ability to ambulate 10 m continuously with minimal assistance; (6) willing and able to give informed consent, and (7) be able and willing to comply with study procedures and verbal instructions.

Individuals were excluded from participation in this study if they had (1) existing severe cardiac conditions such as myocardial infarction or congestive heart failure; (2) fluctuating blood pressure; (3) a history of uncontrolled seizure disorder; (4) additional orthopedic, neuromuscular, or neurological conditions that would interfere with the ability to perform the assessments; (5) difficulty following or responding to commands that would limit the study participation, and (6) enrollment in another research study or therapy at the time of starting this study.

Individuals were recruited via telephone using a convenience sample from Kessler Foundation and the Kessler Institute for Rehabilitation (KIR) System. Of the 12 participants who attended the initial visit, two participants declined to participate, citing the 4-week time commitment.

All participants were paid $25 for the initial visit to Kessler Foundation and $50 for each week they completed study procedures in the community.

2.2. Design and procedure

The ActiGraph GT9X Link (ActiGraph LLC, FL, United States) was the physical activity monitor chosen for this study. The ActiGraph GT9X Link is an FDA-approved class II medical device that weighs 14 grams, has dimensions of 3.5 × 3.5 × 1 cm, and saves movement data without any identifiable information related to participants (User Guide ActiGraph GT9X Link + ActiLife, 2020). The ActiGraph PAM

is widely used in physical activity research across patient populations and is considered a gold standard for physical activity outcomes.

Following informed consent, participants were provided with three ActiGraph Link physical activity monitors and associated accessories, which included the dock and charger, CentrePoint Data Hub, sensor pouch, wrist band, ankle strap, and waist belt (Figure 1). All participants were trained to wear, charge, and dock the physical activity monitors for automatic remote data transfer to the research ActiGraph server using the dock and Data Hub. Participants were sent home with a detailed instruction sheet with instructions and graphical representation of instructions covered during the training. Participants were asked to go about their everyday routine in the community as usual and were not asked to engage in any physical activity specifically for the study in the community. Participants were instructed to wear all three ActiGraph activity monitors (one each on their non-affected or dominant wrist, ankle and waist) simultaneously for 4-weeks in the community and try to wear the activity monitors simultaneously for at least 10 hours during their wake time each day. Participants were instructed to charge each activity monitor once each week for a minimum of 2 hours.

This study follows the consolidated criteria for reporting qualitative research (COREQ) checklist. The questionnaires and semi-structured interviews, organized by wear location, were administered by AV (Ph.D., post-doctoral fellow, female) and OI (BS, research assistant, male). Neither AV nor OI had any relationship with the participants before the study commencement. During the initial visit, participants were introduced to the interviewers and their credentials. Study procedures, aims, and goals were discussed during informed consent. At the end of each week, AV or OI contacted the participant via telephone. Individuals were not specifically asked about the presence of non-participants (e.g., family members at home) during these phone calls.

Each week, participants were asked to complete a System Usability Scale (SUS) and an After-Scenario Questionnaire (ASQ). The SUS was used to collect feedback regarding wear locations; it is a 10-item questionnaire with a five-response option Likert scale; it is well-validated and commonly utilized in usability research (Bangor et al., 2009; Klug, 2017). The ASQ was used to quantify the perceived usability of remote data transfer; it is a 3-item questionnaire with a seven-response option Likert scale, it is popular in usability studies due to its simplicity (Lewis, 1991).

Semi-structured interview questions were not provided to participants in advance; however, repeat interviews with the same questions were carried out weekly for 4 weeks. The interview duration was approximately 5–10 min. Field notes were made during the interview, and transcripts were not returned to participants for comment or correction. Data saturation was not discussed with participants.

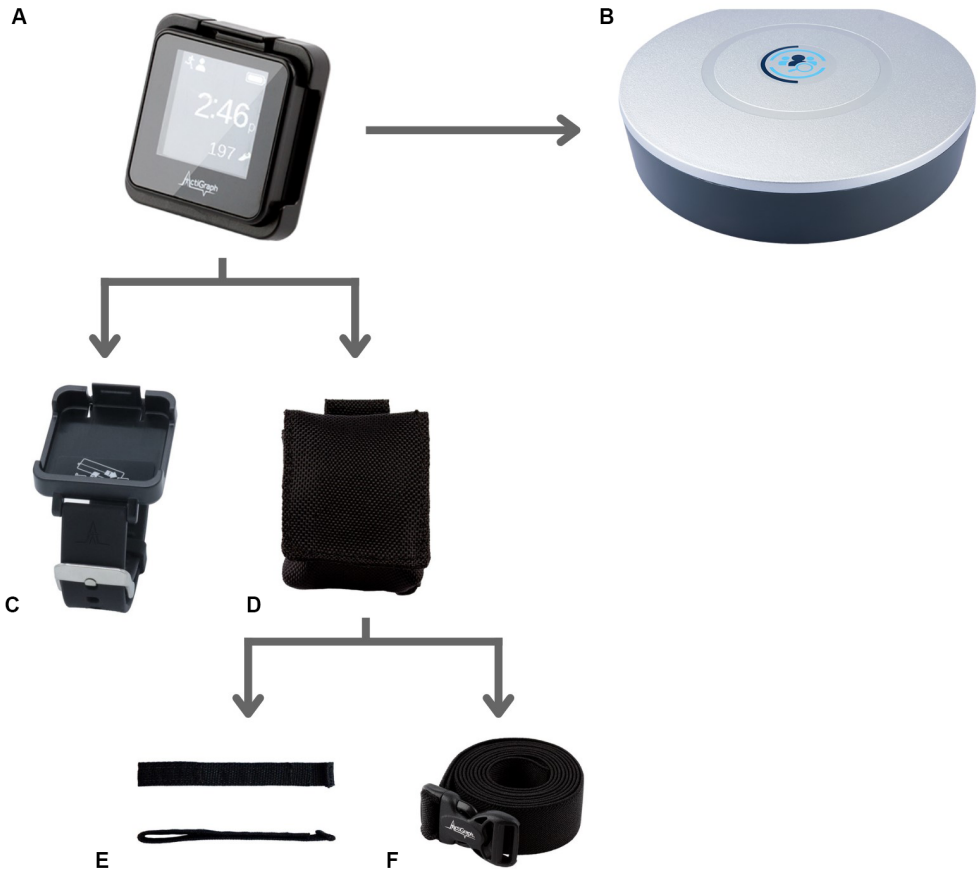

FIGURE 1
PAM and related study accessories. **(A)** ActiGraph GT9X Link PAM worn simultaneously by all study participants on the wrist, waist and ankle. **(B)** CentrePoint Data Hub used by all study participants for remotely transferring the daily PA data to the research server. **(C)** Wrist watch accessory for ActiGraph GT9X Link PAM used to wear the PAM on the wrist. **(D–F)** Pouch accessory, **(D)** used along with the ankle Velcro strap, **(E)** accessory and waist belt, **(F)** accessory to wear the PAM on the ankle and waist, respectively.

At the end of the 4-week study period, participants were asked to rank preferred wear locations and return the study equipment. Participants were not asked to provide feedback on the findings.

2.3. Research ethics

Written informed consent was obtained from all participants before enrollment. All study procedures involving human subjects were approved by the Institutional Review Board at Kessler Foundation, Protocol Number: R-1141-21.

3. Analysis

3.1. System usability scale

The SUS is composed of 10 alternating positive and negative statements (Bangor et al., 2009; Klug, 2017). Odd-numbered questions are scored 0–4, and even-numbered questions are scored 4–0 (Bangor et al., 2009; Klug, 2017). The sum of the scores yields a value between 0 and 40, this is subsequently multiplied by 2.5 to generate a SUS score out of 100. The numerical value can then be converted into a letter grade (Bangor et al., 2009; Klug, 2017). The 4 weeks of SUS scores for each participant were averaged for incorporation into the final analysis. Calculations were performed using Microsoft Excel.

3.2. After scenario questionnaire

The ASQ is calculated by using the average of the response to the three questions; if missing values were present, they were discarded. Higher scores reflect better usability, lower scores represent that the participants felt unsatisfied with either the ease of completing the tasks, the amount of time it took, and the support information, or a combination of these three (Lewis, 1991). The 4 weeks of ASQ scores for each participant were averaged for incorporation into the final analysis. Calculations were performed using Microsoft Excel.

3.3. Semi-structured interviews

Semi-structured interviews were analyzed using the Framework Method of Content Analysis, which consists of well-defined steps; this makes it a popular method in qualitative analysis, especially in health research (Goldsmith, 2021). There are five key steps: (1) data familiarization, (2) identifying a thematic framework; (3) indexing all study data against the framework; (4) charting to summarize the indexed data; (5) mapping and interpretation of patterns found within the charts (Bryman and Burgess, 1994; Goldsmith, 2021).

Deidentified transcript data were compiled and organized by a Participant ID. Researchers MM (4th-year medical student, research assistant, female) and GH (undergraduate, research assistant, male) familiarized themselves with the documents by reading the full transcriptions. Initial themes were derived directly from the semi-structured interview questions. Additional information provided which did not fit into the initial categories was added to a "Miscellaneous/Other Group." After initial coding, themes were refined by MM and GH, and agreed upon by AV; data categorization was discussed to ensure each final code represented participant responses. This process was done by hand.

Additionally, MM and GH assessed each transcript to determine whether the participants' opinions leaned positive, negative, or neutral/ambivalent. MM and GH discussed and agreed upon each participant's emotional valence (Table 1).

4. Results

The final pilot included 10 participants: 5 who had experienced a stroke, and 5 who had experienced a TBI (Table 2). The average age of the participants was about 60 years. None of the study participants used a wearable "activity monitor" or "fitness tracker" or "smart watch" before participating in this study. All of the participants who attended and completed the initial visit and started wearing PAM in the community completed the full 4-week duration of the study. Of note, two individuals in the TBI group lost a sensor (one wrist and one ankle). The study team replaced lost sensors by new sensors and the participants were asked to continue the study. Three of the five individuals with stroke wore the activity monitor on their right wrist and ankle (non-affected side or dominant side) while two of the five individuals with TBI wore the activity monitor on their right wrist and ankle (non-affected or dominant side). All other participants wore the activity monitor on their left wrist and ankle.

4.1. Usability questionnaire

Average pooled SUS Score for PAM placement was 97.63 for the wrist (Standard Deviation, SD: 3.68), 97.50 for the waist (SD: 3.37), and 96 for the ankle (SD: 6.01) (Figure 2). The average pooled ASQ Score for remote data transfer was 1.033 (SD 0.11).

4.2. Qualitative analysis

The major themes were "no challenges," location-specific usability and wearability, and location-independent general impressions are shown in Table 3.

TABLE 1 Emotional valence and PAM ranking.

	Wrist	Ankle	Waist
S1	Positive**(1)**	Ambivalent**(3)**	Positive**(2)**
S2	Positive**(1)**	Negative**(2)**	Negative**(3)**
S3	Negative**(3)**	Negative**(2)**	Positive**(1)**
S4	Ambivalent**(1)**	Ambivalent**(2)**	Negative**(3)**
S5	Negative**(3)**	Ambivalent**(2)**	Positive**(1)**
TBI 1	Ambivalent**(1)**	Negative**(3)**	Ambivalent**(2)**
TBI 2	Ambivalent**(1)**	Ambivalent**(2)**	Ambivalent**(3)**
TBI 3	Ambivalent**(1)**	Ambivalent**(2)**	Ambivalent**(3)**
TBI 4	Ambivalent**(1)**	Ambivalent**(3)**	Ambivalent**(2)**
TBI 5	Ambivalent**(3)**	Ambivalent**(1)**	Ambivalent**(2)**

4.2.1. Wrist usability and wearability

4.2.1.1. "No challenges"

Three participants in the stroke group reported "no challenges" with donning and doffing the wrist monitor. One participant reported difficulty with both actions; the other participant reported difficulty donning the device but could doff without assistance. Both of the individuals reported receiving help from family members to address these challenges. All participants in the TBI group reported "no challenges" in donning or doffing the device; however, one participant added that it was easier to "put on" than "take off" the PAM. All participants reported "no challenges" when asked about difficulty going about their daily routine.

4.2.1.2. Functional limitations impact use

Two participants in the stroke group reported functional limitations in one of their hands that impacted the use of the wrist monitor. One of these individuals reported difficulty with the wrist monitor all 4-weeks, stating, "It's slightly challenging to take it off given the functionality in my hands… I need two functional hands to take off the sensor from the wrist strap." On week two, the other participant reported occasional difficulty donning the wrist monitor, and stated that they "sometimes have limited function in one hand." This participant was able to doff the monitor without assistance.

TABLE 2 Study participant demographics.

	Stroke	TBI
Participants	$n = 5$	$n = 5$
Female	$n = 1$	$n = 2$
Male	$n = 4$	$n = 3$
Mean age	64.2	56.4
Age range	62–65	49–64

4.2.1.3. Intuitive use

Of the participants who made additional comments regarding the wrist monitor, "intuitive use" emerged as a minor usability theme. Participants often compared these devices to wearing a watch. As one participant in the stroke group stated, "[The wrist monitor] is easy to wear, like a wristwatch, I wear one every day, I cannot function without a watch; it's the most memorable routine."

4.2.1.4. Task-specific challenges

One participant in the stroke group and one participant in the TBI group described task-specific challenges. The participant in the stroke group stated, "Yes, [there is some difficulty] while doing some mechanical work, if I need to get my hand somewhere, it pops off and gets in the way. I'm trying to be more careful." The participant in the TBI group described, "[There is some difficulty] when at work, I'm handling babies. The wrist sensor is bulky, and I'm afraid it might get in my way of work. I'm used to wearing my watch on my left wrist and not my right. I'm being extra cautious at work and tucking the sensor under my sleeve."

4.2.1.5. Comfort

Two participants in the TBI group made additional comments regarding the comfort of this device; one stated, "It's snug, I really do not feel it," and the other described it as "comfortable."

4.2.2. Ankle usability and wearability

4.2.2.1. "No challenges"

Three participants in the stroke group reported "no challenges" with donning and doffing the ankle monitor. These challenges were addressed by utilizing the assistance of a family member. All of the participants in the TBI group reported "no challenges" with donning and doffing the ankle monitor. Three participants in the stroke group, and all of the participants in the TBI group, reported "no challenges" going about their daily routine while wearing the ankle monitor.

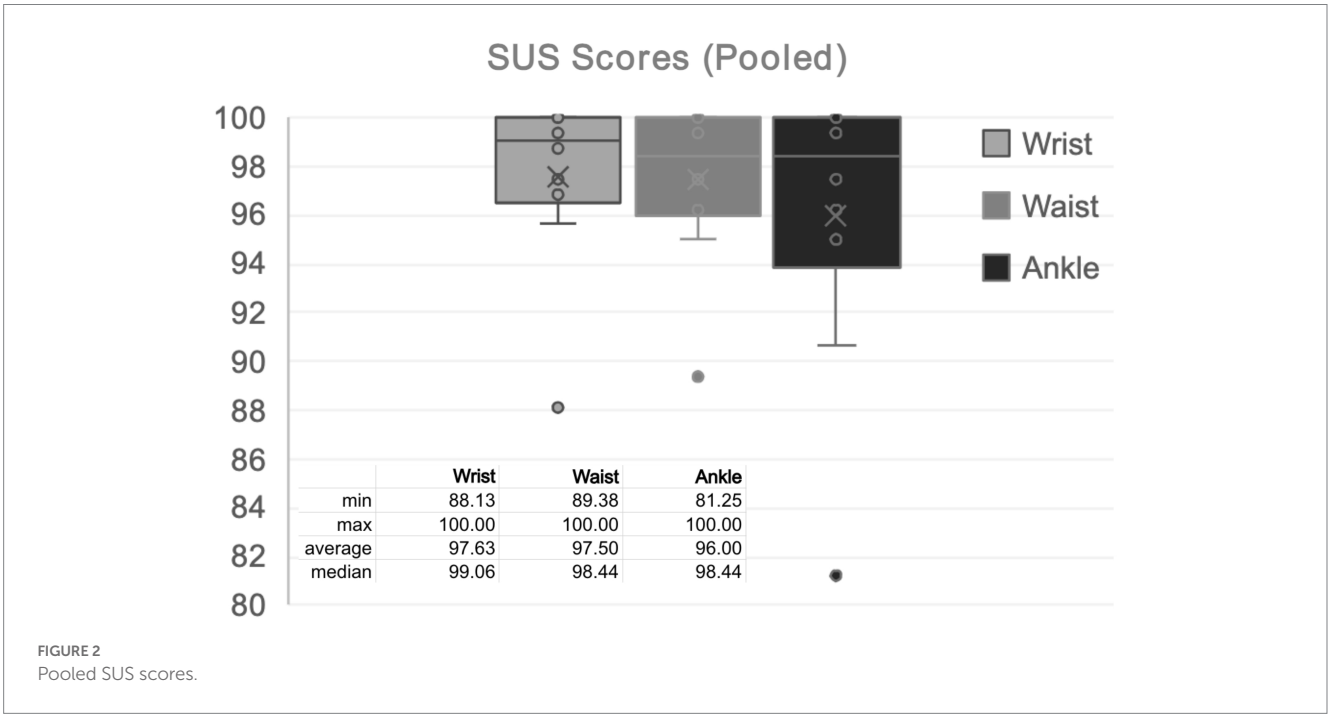

FIGURE 2
Pooled SUS scores.

TABLE 3 Qualitative analysis: major and minor themes.

	Major themes	Minor themes
Wrist	"No challenges"	*Donning/Doffing*
		Daily routine
	Usability	*Functional limitations impact use*
		Intuitive
		Task-specific challenges
	Wearability	*Comfort*
Ankle	"No challenges"	*Donning/Doffing*
		Daily routine
	Usability	*Functional limitations impact use*
		Requires effort/ Assistance
	Wearability	*Discomfort*
		Public perception
Waist	"No challenges"	*Donning/Doffing*
		Daily routine
	Usability	*Functional limitations impact use*
		Easy
	Wearability	*Adjust for comfort*
General impressions	Accessory impressions/ Suggestions	*Strap material*
		Sensor/Pouch preferences
	User interface	*Question utility*
		Technical challenges

4.2.2.2. Functional limitations impact use

Of the two participants in the stroke group that reported a functional limitation in their hands, both reported difficulty with the ankle monitor. One participant utilized the assistance of a family member, and the other replaced the velcro strap with an elastic pull-on band. One participant in the stroke group stated, "Yes, I had a lot of difficulties [with the ankle monitor]. It is almost impossible to put on with one hand."

4.2.2.3. Requires effort/Assistance

Of the participants who made additional comments regarding the ankle monitor, "Requires Effort/Assistance" emerged as a minor usability theme, this included requiring assistance with donning/doffing the device, finding the device when it fell out of the pouch, and keeping conscious tabs on device. One participant in the stroke group stated, "The Velcro does not hold for too long. I had to take it off at the golf course; I did not realize I had lost the activity monitor until another group of people playing behind us came and asked if it belonged to any one of us." A similar sentiment was described by a participant in the TBI group, "…it did fall off when I was at work… I looked around and asked people, and someone found the sensor for me. Now I keep a conscious tab on the sensor."

4.2.2.4. Discomfort

Of the participants who made additional comments regarding the ankle monitor, "Discomfort" emerged as a minor wearability theme. For example, one participant in the stroke group noted, "Sometimes it gets in the way when crossing my legs, but it's alright." Two participants in the TBI group described it was necessary to wear socks with this device to improve comfort.

4.2.2.5. Public perception

One participant in the stroke group made a comment regarding public perception of the device, stating, "I just need to hide it, people ask if I'm not allowed to be outside the home because it looks like a tracker, and people ask me if I'm on house arrest. I wear long pants to hide it. When people cannot see, it's okay, does not bother me."

4.2.3. Waist usability and wearability

4.2.3.1. "No challenges"

Four participants in the stroke group reported "no challenges" with donning and doffing the waist monitor. One participant reported difficulty and addressed this challenge through the assistance of a family member. All of the participants in the TBI group reported "no challenges" with donning and doffing the waist monitor. Four participants in the stroke group, and all participants in the TBI group, reported "no challenges" going about their daily routine while wearing the waist monitor.

4.2.3.2. Functional limitations impact use

Of the two participants in the stroke group that reported a functional limitation in their hands, only one reported difficulty with the waist monitor, difficulty was reported on all 4 weeks. This participant addressed this challenge through assistance from a family member.

4.2.3.3. Easy

Of the participants who made additional comments regarding the waist monitor, "easy" emerged as a minor wearability theme. For example, one participant in the stroke group noted, "This is the easiest and most convenient to use." Another participant said it was "just like wearing clothes," and another stated, "all sensors should be like this."

4.2.3.4. Adjust for comfort

Of the participants who made additional comments regarding the waist monitor, "Adjust for Comfort" emerged as another minor wearability theme. One participant in the stroke group found that the waist monitor was "quite stable, just like wearing a waist belt," but added that they "just need to pull it up or down" to make it comfortable. Another participant in the stroke group reported, "if [the waist monitor is] on a shirt, it feels great, but if it touches the skin, it itches slightly." Additionally, a participant in the TBI group said that "every now and then, it has to be re-adjusted to make sure it's hanging at the side."

4.2.4. General impressions: accessory impressions/suggestions

4.2.4.1. Strap material preference

Although many of the comments regarding "Strap Material Preference" emerged in the context of specific wear locations, this was categorized as a separate theme because PAM accessories vary widely

depending on the manufacturer. Comments regarding the wrist monitor are not included in this section because this accessory had a different mechanism to secure the monitor (Figure 1). One participant in the stroke group mentioned that they replaced the Velcro strap with an elastic band to "slip it on with one hand." Two participants in the TBI group described that it would be helpful if the pouch were securely attached to the strap; as one of these participants explained, "The strap stuck and was clinging to my sock but the sensor fell off, so having a pouch such that the sensor does not fall off unless the strap also falls off from the ankle would be helpful."

4.2.4.2. Sensor/Pouch preference

Of the participants that made impressions and suggestions regarding the accessories, "sensor/pouch preference" emerged as a minor theme. One participant in the TBI group mentioned that "[the sensor] is a little bulky, but it's ok." Two other participants in the TBI groups spoke about the requirement for water resistance. One of these participants explained that "it would be nice if the pouch were water resistant because when it rains, and [they] step into a puddle, the pouch gets wet." The other participant in the TBI group spoke about needing "to remember to take it off during showering and put it back on."

4.2.5. General impressions: user interface

Some participants made general impressions that were not location specific; one major theme that emerged was the user interface.

4.2.5.1. Question utility

Of the participants that made impressions and suggestions regarding the user interface, "question utility" emerged as a minor theme. One participant in the stroke group explained that they "use activity monitor phone-based apps" and were not sure why they "need the activity monitors in general."

4.2.5.2. Technical challenges

Of the participants that made impressions and suggestions regarding the user interface, "technical challenges" emerged as another minor theme. One participant in the TBI group remarked that "the last 2 days it did not show the circle for sending data." Another stated that "the sensor could not transfer data remotely" but added that once this sensor was replaced with a new sensor, it "work[ed] well."

4.3. Preferred wear location

The final ranking for each of the participants demonstrates that a majority of participants (7/10) preferred the wrist sensor. Two individuals ranked the waist sensor in first place, and one individual ranked the ankle sensor in first place. Utilizing ranked-choice voting may help visualize the overall ratings. A ranking of first place received one point, second place received two points, and third place received three points. Rankings for each location were calculated: wrist rank = 16, ankle rank = 22, and waist rank = 22. Based on these results, the wrist location was the preferred location, and the waist and ankle were tied.

5. Discussion

This study explored the use of PAMs in community-dwelling adults who had experienced an acquired brain injury, for 4 weeks, at three wear locations: the wrist, ankle, and waist. To the best of our knowledge, this is the first study to assess the perception of PAMs for a duration greater than 1 week in two key subsets of individuals with ABI, participants who had experienced TBI ($n = 5$) and stroke ($n = 5$).

The quantitative analysis portion of this study utilized two questionnaires which are popularly used in usability research, the SUS to assess each wear location and the ASQ to evaluate the data hub for remote data transfer. Average pooled SUS Scores for each wear location received a score of an A/A+, well within the acceptability range. The average pooled ASQ was 1.033, representing that participants "strongly agree" that the data hub was easy to use. Of note, 9/10 participants provided all three ASQ categories with a score of 1, or "strongly agree," for all 4 weeks. The remaining participant, a member of the TBI group, provided a score of 3 for Question 2: Overall, I am satisfied with the amount of time it took to complete this task for weeks one and two; however, they provided a score of 1 for the remaining 2 weeks. This improvement in rating likely represents an increase in satisfaction with the duration of time required to remotely transfer data or a learning curve on how to use the remote data hub to transfer the data. Taken together, these data support the assertion that the use of PAMs at each wear location, and remote data transfer, were user-friendly. This is a notable finding as "poor usability experience" has been identified as a factor contributing to user non-wear (Cho et al., 2021).

The major and minor themes revealed by qualitative analysis provide a deeper picture of the participants' perspectives on these devices. Based on our investigation, the participants interviewed described the wrist sensor as one that was easy and intuitive to use and was considered comfortable; however, it interfered with specific tasks due to its bulk, such as working with machinery or holding babies. "User's lifestyle or not wearing for certain activities" is a factor that impacts the quality of PGHD, and having a small, lightweight, and inconspicuous device has been identified as an important wearability factor (Louie et al., 2020; Cho et al., 2021). Some participants found that the ankle monitor required effort/assistance; this sensor was often dropped, and some participants checked on it throughout the day. Effort expenditure was reflected in the wearability of the ankle monitor; some participants found this device uncomfortable, either physically or psychologically (due to concerns regarding public perception). Being "unsatisfied with the appearance of the device" and "discomfort" are both factors that may contribute to user non-wear; having a "cosmetically pleasing" device has been identified as an important wearability factor (Louie et al., 2020; Cho et al., 2021). The participants' notable comments regarding the waist monitor demonstrate that some individuals favored this sensor, and found it the most comfortable, though it did require adjustment for some individuals.

Two participants described functional limitations in their hands and had difficulty donning and doffing the PAMs. Although these comments emerged regarding all three placement locations, it is notable many of these comments were regarding the wrist sensor. As demonstrated in Figure 1, the wrist sensor has a watch-buckle design. Fewer comments were made regarding the waist and ankle sensors, which do not have this buckle design. The requirement for accessible design features, especially in this patient population, is supported by the literature. "User's health condition prevents device use" has been identified as a factor that affects the quality of PGHD (Cho et al., 2021). Additionally, a focus group comprised of individuals with stroke and physical therapists identified the ability to don and doff a PAM with one hand as an important feature of wearable technology (Louie et al., 2020).

Many of the participants had negative perceptions of the ActiGraph GT9X Link strap accessories. Some participants believed that having a Velcro scrap would improve usability and wearability for the wrist worn PAM. A commonly cited difficulty was that the sensor pouch was not securely attached to the ankle strap (Figure 1); of note, this was not a problem for the wrist sensor, though this device had distinct difficulties. Notable comments for improvement regarding the sensor itself included addressing its bulk and the desire for this device to be waterproof. A waterproof sensor would allow individuals to participate in daily activities without having to consider removing the device and having to remember it afterward. "Forget to wear" has been identified as a component of user non-wear (Cho et al., 2021). Of note, the ActiGraph GT9X Link is water-resistant (IP27) for up to 1 meter and up to 30 min (User Guide ActiGraph GT9X Link + ActiLife, 2020). However, as raised by one of the participants, the pouch provided with the ankle monitor was not water resistant.

Device and technical-related factors have also been identified as factors that affect PGHD (Cho et al., 2021). A few participants noted some technical difficulty with the device, though these issues were infrequent and did not affect the perceived usability based on the results of the SUS and ASQ questionnaires. Another consideration raised by a participant is the utility of these devices compared to smart phone-based apps. The requirement for a wearable PAM vs. a smartphone app has been raised in the literature; a study of 21 chronically ill people found that some participants preferred using a cell phone app over a GPS tracking watch; however, further research is required to evaluate the efficacy of phone-based devices in individuals who experienced ABI (Hardy et al., 2018). Regardless, this raises an important consideration regarding the significance of user preferences when considering the incorporation of PAMs in clinical practice.

The emotional valence determination (ambivalent, lean positive, or lean negative) derived from the transcripts by MM and GH further highlights the significance of personal preferences in PAM location selection. The first-place ranking by two individuals, positive emotional valence for two individuals, and waist usability theme of "easy" supports the assertion that some individuals may prefer a waist sensor to a wrist or ankle sensor. This is an important consideration for health care professionals considering integrating PAMs into their rehabilitation practice.

This study has some limitations. Primarily, the sample size of this pilot study was small ($n = 10$). Additional limitations include a lack of demographic data, the presence of any lasting deficits (other than those elicited during the semi-structured interview), employment information, functional assessments and information on injury sequelae. An additional limitation of this study is that the semi-structured interview was of short duration, which resulted in limited transcripts.

6. Conclusion

This pilot investigation contributes to the literature regarding considerations for PAM wear location, patient preferences, and challenges specific to this population. Following an ABI, individuals report difficulty participating in, and sustaining, physical activity (Törnbom et al., 2017). PAMs may be a motivating factor for engaging in physical activity (McClure, 2002; Lynch et al., 2018). Additionally, as this technology continues to improve and access to PAMs becomes easier and affordable, these devices have a variety of benefits that may be helpful in this patient population. For example, in addition to the objective data collection on gait and fitness, the Apple Watch may detect falls and alert emergency contacts, and service providers, that help is required; this research is currently ongoing (Strauss et al., 2021). The incorporation of wearable PAM in the chronic phases of rehabilitation following ABI has the potential to provide valuable benefits for patients, caretakers, researchers, and rehabilitation professionals. However, to improve the usability and increasing the incorporation of PAM in longitudinal studies in individuals with ABI the challenges specific to this population need to be taken into account when choosing PAM and wear location.

Data availability statement

The de-identified data supporting the conclusions of this article will be made available by the authors, upon reasonable request.

Ethics statement

The studies involving humans were approved by the Institutional Review Board at Kessler Foundation. The studies were conducted in accordance with the local legislation and institutional requirements. The participants provided their written informed consent to participate in this study.

Author contributions

MM was a medical student mentored by AV and was involved with data analysis and drafting the manuscript. GH was an undergraduate student volunteer mentored by AV and was involved in data analysis and drafting the manuscript. AV was the principal investigator of this study and designed the study, collected data and was involved in data analysis and editing the manuscript. All authors contributed to the article and approved the submitted version.

Funding

This study was funded by the New Jersey Health Foundation (Grant # PC 10–21).

Acknowledgments

The authors would like to thank Olwaseun Ibironke (OI), research assistant at Kessler Foundation—Center for mobility and rehabilitation engineering, for his help with conducting patient interviews during the study. The authors would also like to thank Kessler Foundation for providing resources that enabled data collection for this study.

Conflict of interest

The authors declare that the research was conducted in the absence of any commercial or financial relationships that could be construed as a potential conflict of interest.

Publisher's note

References

Bangor, A., Kortum, P., and Miller, J. (2009). Determining what individual SUS scores mean: adding an adjective rating scale. *J. Usability Stud.* 4, 114–123. doi: 10.5555/2835587.2835589

Braakhuis, H. E. M., Roelofs, J. M. B., Berger, M. A. M., Ribbers, G. M., Weerdesteyn, V., and Bussmann, J. B. J. (2022). Intensity of daily physical activity - a key component for improving physical capacity after minor stroke? *Disabil. Rehabil.* 44, 3048–3053. doi: 10.1080/09638288.2020.1851781

Brickwood, K. J., Watson, G., O'Brien, J., and Williams, A. D. (2019). Consumer-based wearable activity trackers increase physical activity participation: systematic review and meta-analysis. *JMIR Mhealth Uhealth* 7:e11819. doi: 10.2196/11819

Bruijel, J., van Heugten, C. M., Murray, J., Grima, N., Ymer, L., Walters, E. M., et al. (2021). The bidirectional relationship between sleep and physical activity following traumatic brain injury. *J. Sleep Res.* 30:e13334. doi: 10.1111/jsr.13334

Bryman, A., and Burgess, B. (1994). *Analyzing qualitative data. 1st edn.* London: Routledge.

Campos, C., DePaul, V. G., Knorr, S., Wong, J. S., Mansfield, A., and Patterson, K. K. (2018). Validity of the ActiGraph activity monitor for individuals who walk slowly post-stroke. *Top. Stroke Rehabil.* 25, 295–304. doi: 10.1080/10749357.2018.1446487

Cho, S., Ensari, I., Weng, C., Kahn, M. G., and Natarajan, K. (2021). Factors affecting the quality of person-generated wearable device data and associated challenges: rapid systematic review. *JMIR Mhealth Uhealth* 9:e20738. doi: 10.2196/20738

Crosson, B., Hampstead, B. M., Krishnamurthy, L. C., Krishnamurthy, V., McGregor, K. M., Nocera, J. R., et al. (2017). Advances in neurocognitive rehabilitation research from 1992 to 2017: the Ascension of neural plasticity. *Neuropsychology* 31, 900–920. doi: 10.1037/neu0000396

Dey, A., Kam, A., Tam, A., Bayley, M., and Guo, M. (2021). Sleep disturbance and length of stay in the setting of acquired brain injury rehabilitation. *Brain Inj.* 35, 1022–1027. doi: 10.1080/02699052.2021.1945144

Giggins, O. M., Clay, I., and Walsh, L. (2017). Physical activity monitoring in patients with neurological disorders: a review of novel body-worn devices. *Digit. Biomark* 1, 14–42. doi: 10.1159/000477384

Goldsmith, L. (2021). Using framework analysis in applied qualitative research. *Qual. Rep.* 26, 2061–2076. doi: 10.46743/2160-3715/2021.5011

Grabljevec, K., Singh, R., Denes, Z., Angerova, Y., Nunes, R., Boldrini, P., et al. (2018). Evidence-based position paper on physical and rehabilitation medicine professional practice for adults with acquired brain injury. The European PRM position (UEMS PRM section). *Eur. J. Phys. Rehabil. Med.* 54, 971–979. doi: 10.23736/S1973-9087.18.05502-8

Hardy, J., Veinot, T. C., Yan, X., Berrocal, V. J., Clarke, P., Goodspeed, R., et al. (2018). User acceptance of location-tracking technologies in health research: implications for study design and data quality. *J. Biomed. Inform.* 79, 7–19. doi: 10.1016/j.jbi.2018.01.003

Hillman, C. H., Erickson, K. I., and Kramer, A. F. (2008). Be smart, exercise your heart: exercise effects on brain and cognition. *Nat. Rev. Neurosci.* 9, 58–65. doi: 10.1038/nrn2298

Klug, B. (2017). An overview of the system usability scale in library website and system usability testing. *Weave J. Lib. User Exp.* 1. doi: 10.3998/weave.12535642.0001.602

Lewis, J. (1991). Psychometric evaluation of an after-scenario questionnaire for computer usability studies. *ACM SIGCHI Bull.* 23, 78–81. doi: 10.1145/122672.122692

Louie, D. R., Bird, M. L., Menon, C., and Eng, J. J. (2020). Perspectives on the prospective development of stroke-specific lower extremity wearable monitoring technology: a qualitative focus group study with physical therapists and individuals with stroke. *J. Neuroeng. Rehabil.* 17:31. doi: 10.1186/s12984-020-00666-6

Lynch, E. A., Jones, T. M., Simpson, D. B., Fini, N. A., Kuys, S. S., Borschmann, K., et al. (2018). Activity monitors for increasing physical activity in adult stroke survivors. *Cochrane Database Syst. Rev.* 7:CD012543. doi: 10.1002/14651858.CD012543.p

McClure, J. B. (2002). Are biomarkers useful treatment aids for promoting health behavior change? An empirical review. *Am. J. Prev. Med.* 22, 200–207. doi: 10.1016/s0749-3797(01)00425-1

Mercier, L. J., Kowalski, K., Fung, T. S., Joyce, J. M., Yeates, K. O., and Debert, C. T. (2021). Characterizing physical activity and sedentary behavior in adults with persistent postconcussive symptoms after mild traumatic brain injury. *Arch. Phys. Med. Rehabil.* 102, 1918–1925.e1. doi: 10.1016/j.apmr.2021.05.002

O'Carroll, G. C., King, S. L., Carroll, S., Perry, J. L., and Vanicek, N. (2020). The effects of exercise to promote quality of life in individuals with traumatic brain injuries: a systematic review. *Brain Inj.* 34, 1701–1713. doi: 10.1080/02699052.2020.1812117

Sheng, S., Chen, L., Chen, Z., Zeng, J., Zheng, J., and Bei, Z. (2021). Study on the correlation between physical activity level and quality of life 1 year after stroke. *Ann. Palliat. Med.* 10, 5627–5632. doi: 10.21037/apm-21-962

Strauss, D. H., Davoodi, N. M., Healy, M., Metts, C. L., Merchant, R. C., Banskota, S., et al. (2021). The geriatric acute and post-acute fall prevention intervention (GAPcare) II to assess the use of the apple watch in older emergency department patients with falls: protocol for a mixed methods study. *JMIR Res. Protoc.* 10:e24455. doi: 10.2196/24455

Törnbom, K., Sunnerhagen, K. S., and Danielsson, A. (2017). Perceptions of physical activity and walking in an early stage after stroke or acquired brain injury. *PLoS One* 12:e0173463. doi: 10.1371/journal.pone.0173463

User Guide ActiGraph GT9X Link + ActiLife. (2020). *ActiGraph*. Available at: https://s3.amazonaws.com/actigraphcorp.com/wp-content/uploads/2020/03/05155628/ActiGraph_Link_UserGuide_E.200.6001_Revision6_FINAL.pdf (Accessed September 26, 2022).

Veerubhotla, A., Krantz, A., Ibironke, O., and Pilkar, R. (2021). Wearable devices for tracking physical activity in the community after an acquired brain injury: a systematic review. *PM R* 14, 1207–1218. doi: 10.1002/pmrj.12725

frontiers | Frontiers in Neuroscience

TYPE Original Research
PUBLISHED 14 September 2023
DOI 10.3389/fnins.2023.1238176

OPEN ACCESS

EDITED BY
Lei Zhang,
Nanjing Normal University, China

REVIEWED BY
Junyi Yin,
University of California, Los Angeles, United States
Erkan Kaplanoglu,
University of Tennessee at Chattanooga, United States

*CORRESPONDENCE
Guodong Zhang
✉ 32129060@qq.com
Xiaofeng Shen
✉ 29240818@qq.com

†These authors have contributed equally to this work

RECEIVED 11 June 2023
ACCEPTED 07 August 2023
PUBLISHED 14 September 2023

CITATION
Zha Q, Xu Z, Cai X, Zhang G and Shen X (2023) Wearable rehabilitation wristband for distal radius fractures.
Front. Neurosci. 17:1238176.
doi: 10.3389/fnins.2023.1238176

Wearable rehabilitation wristband for distal radius fractures

Qing Zha[1,2†], Zeou Xu[1,2†], Xuefeng Cai[3], Guodong Zhang[3*] and Xiaofeng Shen[3*]

[1]School of Biomedical Engineering (Suzhou), Division of Life Sciences and Medicine, University of Science and Technology of China, Hefei, China, [2]Suzhou Institute of Biomedical Engineering and Technology, Chinese Academy of Science, Suzhou, China, [3]Suzhou TCM Hospital Affiliated to Nanjing University of Chinese Medicine, Suzhou, China

Background: Distal radius fractures are a common type of fracture. For patients treated with closed reduction with splinting, a period of rehabilitation is still required after the removal of the splint. However, there is a general lack of attention and low compliance to rehabilitation training during this period, so it is necessary to build a rehabilitation training monitoring system to improve the efficiency of patients' rehabilitation.

Methods: A wearable rehabilitation training wristband was proposed, which could be used in the patient's daily rehabilitation training scenario and could recognize four common wrist rehabilitation actions in real-time by using three thin film pressure sensors to detect the pressure change curve at three points on the wrist. An algorithmic framework for classifying rehabilitation training actions was proposed. In our framework, an action pre-detection strategy was designed to exclude false detections caused by switching initial gestures during rehabilitation training and wait for the arrival of the complete signal. To classify the action signals into four categories, firstly an autoencoder was used to downscale the original signal. Six SVMs were then used for evaluation and voting, and the final action with the highest number of votes would be used as the prediction result.

Results: Experimental results showed that the proposed algorithmic framework achieved an average recognition accuracy of 89.62%, an average recognition recall of 88.93%, and an f1 score of 89.27% on the four rehabilitation training actions.

Conclusion: The developed device has the advantages of being small size and easy to wear, which can quickly and accurately identify and classify four common rehabilitation training actions. It can easily be combined with peripheral devices and technologies (e.g., cell phones, computers, Internet) to build different rehabilitation training scenarios, making it worthwhile to use and promote in clinical settings.

KEYWORDS

distal radius fracture, thin film pressure sensor, rehabilitation training action recognition, autoencoder, SVM

1. Introduction

Distal radius fractures are a common type of fracture in adults, accounting for approximately 17.5% of all fracture types (Ochen et al., 2020). Fracture treatment is divided into surgical and non-surgical treatment (He et al., 2020). There is a significant difference in the recovery of physical skeletal indicators between the two different treatments, but there is no significant difference in the functional recovery of the wrist joint, so patients mostly consider non-surgical treatment modalities first (He et al., 2020). A period of rehabilitation after the removal of the cast or splint plays a major role in the recovery of joint function (Badwaik et al., 2021). However, there is a common phenomenon that patients do not pay attention to rehabilitation training, have poor compliance, and have irregular training movements (Bhan et al., 2021). Therefore, it is important to build a rehabilitation training assistance monitoring system so that the physician can supervise the patient promptly and increase the patient's self-motivation for rehabilitation training.

Rehabilitation training assistance monitoring system for the patient's terminal equipment puts forward the requirements of physiological signal acquisition, rehabilitation training action recognition and evaluation, of which rehabilitation training action recognition is the main research direction, because this technology is the key to build a bridge of joint supervision between doctor and patient for distal radius fracture, and a large number of researches have existed for this task. The means of rehabilitation training action recognition fall into two broad categories, namely computer vision (CV) based and sensor based approaches (Zhu et al., 2019). The computer vision-based approach acquires raw image information through a vision-based sensor, then performs extraction of low-level features such as human joint positions, and after encoding and representing the feature data, it performs a number of tasks such as kinematic parameter comparisons, postural recognition, and clinical scoring (Debnath et al., 2022). Many image processing and machine learning techniques have been applied to these studies (Keskin et al., 2012; Tang et al., 2014; Sinha et al., 2016; Wan et al., 2019; Francisco and Rodrigues, 2022; Shen and Lu, 2022; Sun et al., 2022), which typically use single or multiple RGB or depth cameras as image acquisition units and analyze the images or videos to identify static gestures or motion flows within them (Hellsten et al., 2021). Although CV-based systems have the advantages of simple equipment and low cost, vision algorithms are inevitably accompanied by the shortcomings of being highly influenced by occlusions and light. More critically, CV-based systems have a single source of data (only image pixel information) and therefore lack the means to robustly monitor the patient's physiological parameters (e.g., pressure on the affected area), yet the tightness of the splints used for immobilization is an important influence on the outcome of fracture rehabilitation (Li et al., 2021). Therefore, the lack of capability of CV-based systems in this area is the greatest drawback compared to sensor-based rehabilitation training systems.

Sensor-based rehabilitation training devices have unique advantages due to their ability to detect multimodal physiological parameters directly or indirectly. These systems place multiple types of sensors on different carriers, and the data is collected and analyzed by a central processor (Nascimento et al., 2020; Yadav et al., 2021). Common sensors used in wrist rehabilitation systems include pressure sensors (Zhang et al., 2019; Atitallah et al., 2020; Guo et al., 2021; Pierre Claver and Zhao, 2021; Xu et al., 2021), surface electromyographic(sEMG) sensors (Prakash et al., 2019; Cheng et al., 2021; Dong et al., 2021; Moin et al., 2021; Copaci et al., 2022; Jeong et al., 2022), inertial sensors (Kim et al., 2019; Weygers et al., 2020; Bilius et al., 2023), and specialized sensors (e.g., acoustic sensors (Xiao et al., 2022), strain sensors (Gao et al., 2023). Currently, the main researched rehabilitation training devices usually include multiple sensors to achieve multimodal and more accurate training movement analysis, and the main presentation of wrist movement recognition devices is the rehabilitation glove. For example, Copaci et al. proposed a gesture classification algorithm for rehabilitation training gloves based on surface EMG signals, which is based on Bayesian neural networks, pattern recognition networks, and hierarchical recurrent networks, and allows users to retrain the algorithm at any time with their own surface EMG gesture data, with a recognition accuracy of up to 98.7% for six types of gestures (Copaci et al., 2022). Li et al. (2023) developed a set of multimodal sensor gloves for hand kinematics learning in Parkinson's patients, which used flexible bending sensors to detect finger curvature information, thin-film pressure sensors to measure changes in hand muscle strength, and an inertial navigation system to detect acceleration signals, and carried out a number of evaluations of finger dexterity, muscle strength, and other assessments based on multiple signal processing algorithm. Meng et al. developed a personalized and safe soft glove for rehabilitation training, which uses a pneumatic actuator module to provide active rehabilitation training for patients and acquires finger bending information based on bending sensor and air-pressure sensor. The system they developed included three modes of rehabilitation training to meet the rehabilitation requirements of patients with multiple hand dysfunctions (Meng et al., 2023). Since the rehabilitation glove provides a stable platform for sensor placement, it is particularly suitable for multimodal hand movement analysis (and, of course, wrist rehabilitation). Moreover, due to the large number of sensors it can deploy, accurate acquisition of finger bending information and hand posture information can be easily realized, and thus hand movement recognition based on such information can be easily achieved with good results. Compared to vision-based approaches, sensor-based rehabilitation assistance devices have some significant advantages, such as the accuracy of physiological information acquisition and the minuteness to environmental interference. In addition to rehabilitation training gloves, some special and novel rehabilitation assistance devices were also presented. For example, Han et al. (2022) proposed a cylindrical device based on a passive sensing layer called smart skin, which estimates the grip force by the change in the shape of the colored liquid in the subtle channels during gripping. Wong et al. (2021) developed a finger-worn capacitive sensor system that utilizes capacitance changes due to different hand movements for gesture classification tasks.

However, the main applications of these studies on hand rehabilitation assistance systems are for stroke and Parkinson's patients, and these application scenarios do not limit the pressure at the radius. In addition to proper rehabilitation, patients with distal radius fractures should also ensure that the pressure on the affected area of the radius is within the appropriate range, otherwise excessive splint pressure will likely bring about various syndromes as a result of vascular compression of the affected area, while too little pressure on the splint may result in secondary dislocation of the fracture. Therefore, rehabilitation equipment for patients with distal radius

10.3389/fnins.2023.1238176

fractures should have the ability to monitor skin pressure on the affected area in addition to supervised rehabilitation. At the same time, the variety and number of sensors deployed in rehabilitation training gloves [e.g., the data glove developed by Bin Fang et al. carries 36 inertial measurement units (Fang et al., 2019)] inevitably brings about an increase in cost, which no doubt increases the burden of treatment for patients. To address these issues, we designed a wearable rehabilitation wristband that used only three thin-film pressure sensors as the components for skin pressure signal acquisition. The thin-film pressure sensors are inexpensive to produce and can be mounted non-invasively between the patient's skin and the splint. The conversion of pressure data and the recognition of rehabilitation training actions are realized through the topmost control box, and the relevant information will be sent to the matching cell phone APP for display and storage. Compared to rehabilitation gloves, our devices are extremely low-cost and allow effective monitoring of splint tightness. The main contributions of this paper are as follows:

1. We proposed a wearable rehabilitation training wristband for distal radius fractures, which provided rehabilitation training actions recognition and detection functions, and opened up a Bluetooth interface that allowed simple connection to computers, cell phones, and other upper computers and the development of a variety of rehabilitation training software.
2. A rehabilitation training action classification algorithm based on an autoencoder and SVM classifier was designed, which could run on a microcontroller and classified action signals quickly and accurately.
3. An action signal pre-detection strategy was proposed to determine whether the window signal was a complete action signal, which reduced the false detection rate of the algorithm.

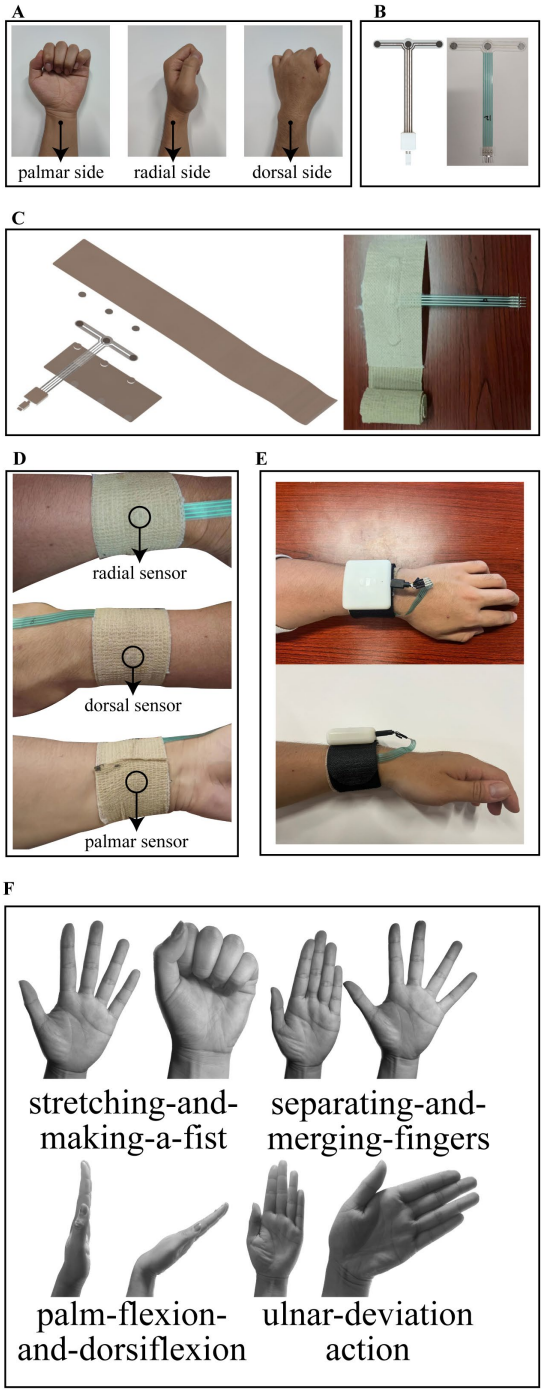

FIGURE 1
(A) Location of the collection points. **(B)** Design structure and object diagram of the thin film pressure sensor. **(C)** Structural schematic and object diagram of the inner bandage core. **(D)** Schematic of the bandage core after completion of wear. **(E)** Schematic of the entire system after wearing. **(F)** Rehabilitation training standardized actions including stretching-and-making-a-fist, separating-and-merging-fingers, palm-flexion-and-dorsiflexion, and ulnar-deviation action.

2. Materials and methods

2.1. Materials

2.1.1. Thin film pressure sensor

Thin-film pressure sensors are used to detect three channels of pressure on the palmar, radial and dorsal sides of the wrist. Hua et al. (2018) performed a biomechanical finite element analysis of the stress distribution on the arm for three common types of splints, and their stress analysis results showed that all three types of splints produced the greatest stresses in the vicinity of the radial stem eminence at a one-week location, but the absolute values of the stresses were different. Therefore, we followed the wrist force characteristics of splinting and chose the location of the radial collection point to be 1–2 cm from the malleolus on the lateral side of the radius, which is located near the distal radius fracture point and the maximal stress of the splint, so as to monitor the lateral force on the fracture point in an effective and obvious way. The dorsal and palmar collection points are centrally located on the dorsum and palm of the hand, respectively, and are on the same circumference as the radial collection point. The location of the collection points is shown schematically in Figure 1A.

A three-channel thin-film pressure sensor designed by our own structure is used as the detection element of the wristband, and presents a T-shaped structure. On the crossbeam of the T, three pressure-sensitive zones are distributed from left to right for the above-mentioned palmar, radial, and dorsal pressure detection. On the arm of the T, there are four copper wires leading out and connected to the control box through the MicroUSB interface, one of which is

connected to one of the pins of the three pressure-sensitive zones to form a common terminal. The T-shaped structure design avoids the problem of cable stacking when wearing the wristband. The design structure and object diagram of the thin film pressure sensor are shown in Figure 1B.

2.1.2. Rehabilitation wristband

The rehabilitation wristband is composed of an inner bandage core and an outer magic stick layer. The inner bandage core consists of two layers of medical bandages and film sensors pressed together, with the upper layer of bandages for the elastic self-adhesive bandages, longer length, for wearing around the fixed, and the lower layer of bandages for inelastic bandages. Both sides of the thin-film sensor are in contact with the upper and lower bandages by circular silicone pads with a thickness of 1 mm. The structural schematic of the inner bandage core is shown in Figure 1C along with its object diagram. The outer layer of the magic stick has rigid fibers on one side to provide a stable force platform for the pressure sensor and a magic stick on the other side to hold the entire structure in place. Our circuit board is enclosed in a control box, which is fixed above the outer magic stick and connected to the thin film sensors through an electrical interface. When worn, the radial sensor in the inner bandage core is first positioned at the location of the radial collection point described above, followed by stroking the wristband both palmarly and dorsally so that the wristband is wrinkle-free and fits completely around this part of the wrist, and finally the self-adhesive bandage of the wristband is wrapped around the wrist for 1 week and compacted to hold it in place. The schematic of the bandage core after completion of wear is shown in Figure 1D. Subsequently, the rigid side of the Velcro was attached to the inner bandage core, wrapped around for a week and then secured by a carabiner, and finally, the sensor interface was plugged into the control box. The schematic of the entire system after wearing is shown in Figure 1E. As you can see, the system we designed is simple in structure and compact in size. It should be noted that the remaining portion of the outer magic stick layer can be easily embedded in various splint systems (e.g., plaster splints, small splints, thermoplastic splints, etc.) as a splint pressure status monitoring terminal during the splint fixation period, which is an important use of this system beyond the description herein.

2.1.3. Control box circuit

The control box circuit is composed of four parts: a power supply circuit, STM32 microcontroller minimum system, pressure acquisition system, and BLE Bluetooth transmission circuit. The power supply circuit is used to charge the lithium battery and to regulate the input voltage of the lithium battery to the voltage required by other chips. It uses the PW5410A charge pump chip to regulate the input voltage of the lithium battery to 5 V, which is then stepped down to 3.3 V by the PW6566 LDO chip. 5 V is supplied to the operational amplifier in the system, and 3.3 V is supplied to the STM32 microcontroller, BLE Bluetooth transceiver module, and other chips. The STM32 microcontroller minimal system is used to detect the analog signal output from the pressure acquisition system, detect the transceiver signal of the Bluetooth module and run the classification algorithm of the rehabilitation action signal, which uses its own ADC peripheral to convert the analog voltage to digital, and uses the BLE Bluetooth module to send the detected action signal or receive the control signal from the upper computer. The pressure acquisition system consists of three Wheatstone bridges cascaded with differential amplification circuits, each of which is used to detect the pressure sensor information of one channel, and the output voltage of the pressure acquisition system is 0–3.3 V, which is received by the STM32 microcontroller. The BLE Bluetooth transmission module serves as a wireless communication medium between the control box and the upper computer, automatically converting serial signals and Bluetooth RF signals to each other, which simplifies the system development difficulty. The circuit system structure and module circuits are shown in Supplementary Figure S1.

2.1.4. Rehabilitation training action specification

Although it is now clinically recognized that appropriate functional exercises have a positive effect on the rehabilitation of distal radius fractures, there is no uniform standard for the details of the actions of rehabilitation training (Østergaard et al., 2021). Often hospitals in different areas will prescribe different rehabilitation exercises to patients. For example, in a clinical study of functional exercises based on cast immobilized patients conducted by Reid et al. (2020), patients were asked to perform palmar flexion and dorsiflexion and fist clenching for the wrist joint. Arora and Naqvi (2022) in a clinical validation trial of a leap motion tracking device had patients perform five movements: fingers flexion and extension, flexion and extension of the thumb, wrist radial and ulnar deviation, forearm pronation and supination and wrist flexion and extension. The results of the experiment verified the effectiveness of these rehabilitation exercises. Some other forms of rehabilitation training methods such as wrist rotation (Huang et al., 2019) and grip training (Quadlbauer et al., 2020) were also used by some organizations. We considered the available literature and selected the following four typical rehabilitation exercises by the chief physician of the author's hospital unit (Li et al., 2020), namely, stretching-and-making-a-fist, separating-and-merging-fingers, palm-flexion-and-dorsiflexion, and ulnar-deviation action. For rehabilitation, place the elbow on a flat table and hold the forearm upright in a neutral position. When stretching and making a fist, the palm of the hand is relaxed as the initial state, then the fingers are stretched, followed by a fist clenching as hard as possible, and finally returning to the initial state, which is considered a complete action. When separating and merging fingers, the palm of the hand is initially held with the five fingers together and straightened, then the fingers are separated as far as possible and finally returned to the initial state, which is considered a complete action. When performing palm flexion and dorsiflexion, the palm first maintains the same initial state of separating and merging fingers movement, then the palm tilts forward as far as possible to the side of the palm, followed by the palm tilting backward as far as possible to the dorsal direction, and finally returns to the initial state, which is considered a complete action. When performing the ulnar deviation movement, the palm is first maintained in the same initial state as the separating and merging fingers movement and then tilted towards the ulna as far as possible, and finally returned to the initial state, which is regarded as a complete action. The rehabilitation training standardized action is shown in Figure 1F.

2.2. Methods

2.2.1. Thin film pressure sensor calibration

The thin-film pressure sensors we used are resistance-strain sensors, whose resistance decreases gradually as the applied

10.3389/fnins.2023.1238176

pressure increases. After conversion by the sensor data acquisition circuit, the change in applied pressure will be reflected as a change in the output analog voltage of the circuit, which is converted into a digital quantity by the analog-to-digital conversion module of the microcontroller (hereinafter referred to as the AD value). Since it is not possible to calculate the applied pressure directly from the AD value, we conducted pressure calibration experiments of the sensor with the aim of finding the mapping between the pressure applied to the sensor and the corresponding output AD value.

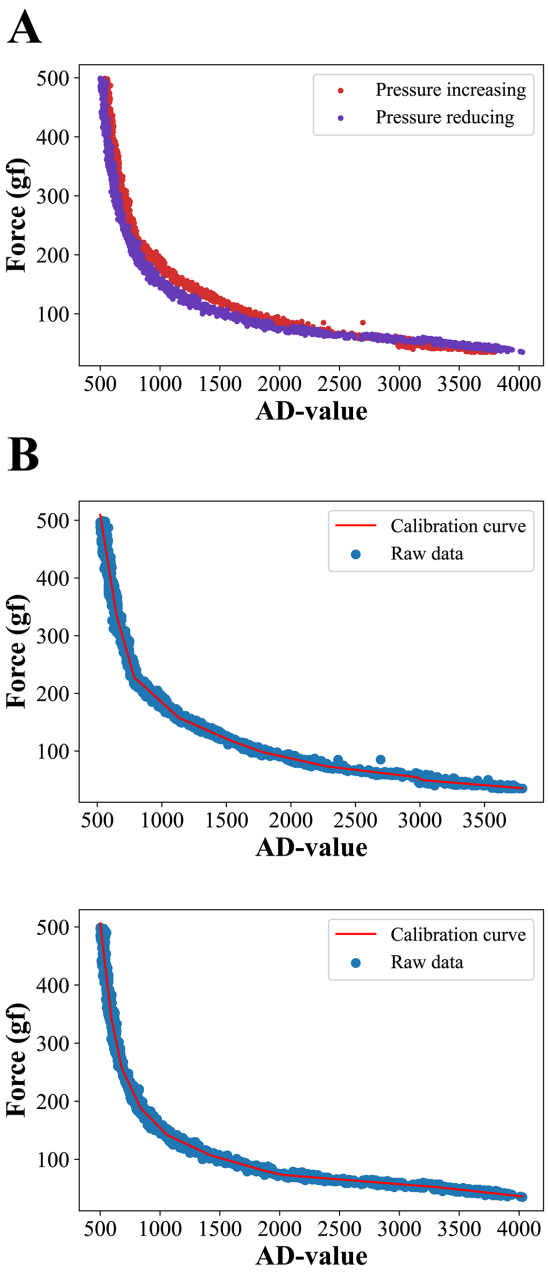

FIGURE 2
(A) Raw data from pressure collection. Due to hysteresis errors, the curves do not coincide exactly during forward and reverse pressure applying. **(B)** Results of fitting forward and backward curves using a 9-segmented linear function.

We first placed the pressure sensor on the pressure calibration platform, which consisted of a push-pull force gauge with a 3 kg range and 1 g resolution and a hand-cranked fixture. The push-pull gauge was fixed on a stationary frame and different pressures were applied to the pressure sensors by turning the rocker, and the AD values of the corresponding channels of the pressure sensor and the pressure measurements of the push-pull gauge were simultaneously collected by our computer. A total of 10 rounds of raw data were collected, with each round collecting 300 sets of data at a frequency of 3 Hz, in which the applied pressure was gradually increased to 500 gf during the first five rounds of collection, and gradually decreased to 30 gf during the last five rounds of collection (not reduced to 0 because the push-pull gauge had a 30 gf pressure dead zone). The acquisition results are shown in Figure 2A, where the red scatter plot represents gradually increasing pressure data and the blue scatter plot represents gradually decreasing pressure data. It can be seen that the thin-film pressure sensor has a significant hysteresis error, which makes the two pressure data not exactly coincide. We used clusters of segmented linear functions to fit the raw data for pressure increase and decrease separately, a process based on the python library pwlf. Both the final curves were divided into 9 folded segments and the fitted curves are shown in Figure 2B. The top and bottom graphs show the fitted curves for the pressure increase and decrease processes, respectively, and the final pressure prediction deployed to the microcontroller was given by the average of the two fitted curves.

2.2.2. Dataset acquisition

We use our own QT-based software platform for rehabilitation action acquisition. Five subjects were recruited for training set data collection, with two rounds per subject, and 50 reps of each of the four rehabilitation training actions were collected in turn. The type of raw data collected is the AD value. The sampling frequency of the software platform is 15 Hz, and since the rehabilitation training action is basically completed within 2 s, the number of sample collections is set to 30 times for each group. Thus the data structure of each action sample is $ch_i(j)$, where $i = 1, 2, 3$, $j = 1, 2, 3,..., 30$, and $ch_i(j)$ denotes the j th AD value of the i th channel of the sample. An example of one of the samples we collected is shown in Figure 3.

The initial state pressure varied slightly from subject to subject because the tightness of the rehabilitation wristband was not exactly the same each time the subject was strapped in. We bind an initial reference AD value $\mathrm{Re}\, f_i$ for the same batch of rehabilitation training for each subject. Firstly, the subject sits at the front of the experimental table and maintains the initial state of stretching and making a fist as required by the rehabilitation training, and then maintains this resting relaxed state and collects a sample, which is called the subject's resting sample. The resting sample has the same data structure as the action sample, and to distinguish it from the action sample representation, we use $CH_i(j)$ to denote its AD value of it. $\mathrm{Re}\, f_i$ is precisely calculated by $CH_i(j)$ with the following equation

$$\mathrm{Re}\, f_i = \sum_{j=1}^{30} CH_i(j) / 30 \quad (i = 1,2,3)$$

Subsequently, each action sample data collected by the subject will be transformed into a normalized value $u_i(j)$, where $i = 1, 2, 3$ and

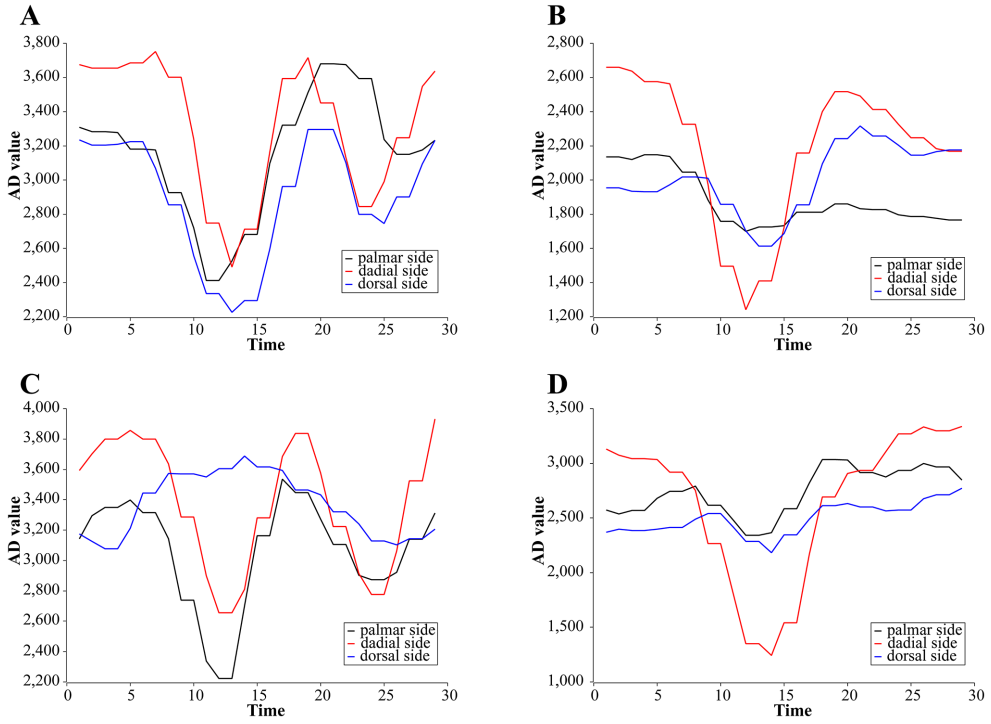

FIGURE 3
Examples of primary AD change curves for four rehabilitation training actions. **(A)** Stretching-and-making-a-fist. **(B)** Separating-and-merging-fingers. **(C)** Palm-flexion-and-dorsiflexion. **(D)** Ulnar-deviation action.

$j = 1, 2, 3,..., 30$, which maintains the same data structure as the action sample and is calculated by the following equation

$$u_i(j) = \frac{ch_i(j)}{\mathrm{Re}\, f_i}$$

As we can see, $u_i(j)$ is the ratio of the original three-channel AD value of this action sample to its bound initial reference AD value for each channel, which can reduce the impact of data variability caused by wearing rehabilitation wristbands with different tightness to a certain extent and improve the robustness and generalization ability of the system. These data are subsequently arranged in one dimension to form the final input data $x(k)$ of our designed classification algorithm, which is represented by the following equation

$$x(k) = u_\alpha(\beta)$$

Where $\alpha \equiv k(\mathrm{mod}\, 3,\ \alpha = 1, 2, 3),\ \beta = \left[\frac{k}{3}\right],\ k = 1, 2, 3,\ldots, 90.$

2.2.3. Rehabilitation training movement classification algorithm

Since the input data is a 90-dimensional $x(k)$, this is too many features for an action sample. We first perform dimensionality reduction and feature extraction on it using an autoencoder, which is a mature and effective algorithm for automatically finding features by training an adaptive encoder and decoder to match the original data, where the output of the encoder is the sample feature data we need. Then we classify the encoded data using six SVMs, which, as a binary classification algorithm with linearly divisible samples, improves model generalization by optimizing the hyperplane parameters so that the support vector has the maximum distance from it. Our six SVMs are denoted as $S_{ij}(i = 1, 2, 3, 4; j = i,\ldots, 4)$, which denotes the SVM that classifies action i with action j (the four rehabilitation training action mentioned above are denoted as actions 1–4). The 6 SVMs are given their predicted categories for a sample, and the corresponding category votes are increased by one vote, and finally, the predicted action with the highest number of votes is identified as the final prediction given by the classification algorithm. The structure of the classification algorithm is shown in Supplementary Figure S2.

2.2.4. Action pre-detection strategy

The classification algorithm will be deployed to the STM32 microcontroller to run after the training is completed. According to the input data requirements of the classification algorithm, after the user finishes installing the wristband and prepares the posture for rehabilitation training, the user first keeps the hand relaxed and the upper computer sends initialization instructions to the microcontroller, which continuously acquires 30 sets of three-channel AD values at a frequency of 15 Hz and automatically calculates three average AD values as the initial reference AD value $\mathrm{Re}\, f_i$ for this round of rehabilitation training. A sliding detection window of size 30 and step 1 is used for real-time detection of rehabilitation training actions. The window divides the current three-channel AD value with

Re f_i at each slide and places it at the end of the window queue, and removes the data at the head of the window queue. If the classification algorithm is propagated forward without discriminating the window data, the action data will be incorrectly classified as another action before it fully enters the window. In addition, the different initial hand postures for different rehabilitation training actions lead to different initial pressures for different actions, which can lead to an upward or downward slope in the data in the window when switching rehabilitation training actions, and if such window data is forward propagated by the classification algorithm, it may also lead to its being judged as one action and thus misclassified. Considering that all rehabilitation movements start and end with similar pressures (this is because all training actions end in the initial posture) and that the three-channel AD values remain essentially constant when the patient is not performing rehabilitation actions, we designed an action data detection strategy that is only window data that meet the following two conditions will be considered as a rehabilitation training action and input to the classification algorithm for recognition. (1) The maximum peak value of the first 10 data of the three channels of the window is greater than the thresholdT_1, i.e., $\max_i\left\{\max_j\left\{ch_i(j)\right\}-\min_j\left\{ch_i(j)\right\}\right\}>T_1$. (2) the minimum head-to-tail AD distance of the three channels of the window is less than the threshold T_2, i.e., $\min_i\left\{\left\|ch_i(1)-ch_i(30)\right\|\right\}<T_2$. Where the threshold values T_1 and T_2 are empirical values. The first rule ensures that window data is not classified when there is no action, and only window data with sufficiently forward action start points (which ensures that action data is not classified until it enters the window completely) will be classified. The second rule ensures that the window data with a strong change is indeed action data. The schematic of the action pre-detection strategy is shown in Figure 4.

3. Results

3.1. Pressure calibration results

We carried out two rounds of pressure calibration test experiments, each round of the first gradually increasing pressure on the sensor to reach the full range and then gradually reduce the pressure, the computer to store the process of pressure prediction of the microcontroller and the real readings of the push-pull gauge. The pressure error is calculated by $f_{error} = f_{predict} - f_{true}$, where $f_{predict}$ and f_{true} represent the predicted and true values of the pressure at the same moment in time, respectively, and the results of the two rounds of experiments are spliced together and shown in Figure 5A. The results show that overall the calibration curve seems to work well. The absolute value of f_{error} becomes progressively larger as the pressure increases. This is due to the fact that the pressure calibration curve has a large absolute value of the derivative of the pressure value to the AD value at higher pressures, resulting in a slight disturbance of the AD at higher pressures causing a large change in the pressure prediction. At one point the absolute value of f_{error} even exceeded 60gf at pressure values of 400gf or more, but under the range where our equipment is most often used (around 300gf), the absolute value of f_{error} basically stayed within 20gf. Figure 5B shows the value of f_{error} divided by f_{true} at each moment in time. The results show that the pressure calibration error is basically between ±20% throughout the test, except for a very few spikes that reach more than 50%, and these singularities occur at low pressures, which may be due to minor voltage disturbances in the interval between the microcontroller and the push-pull meter data transmission during the data acquisition.

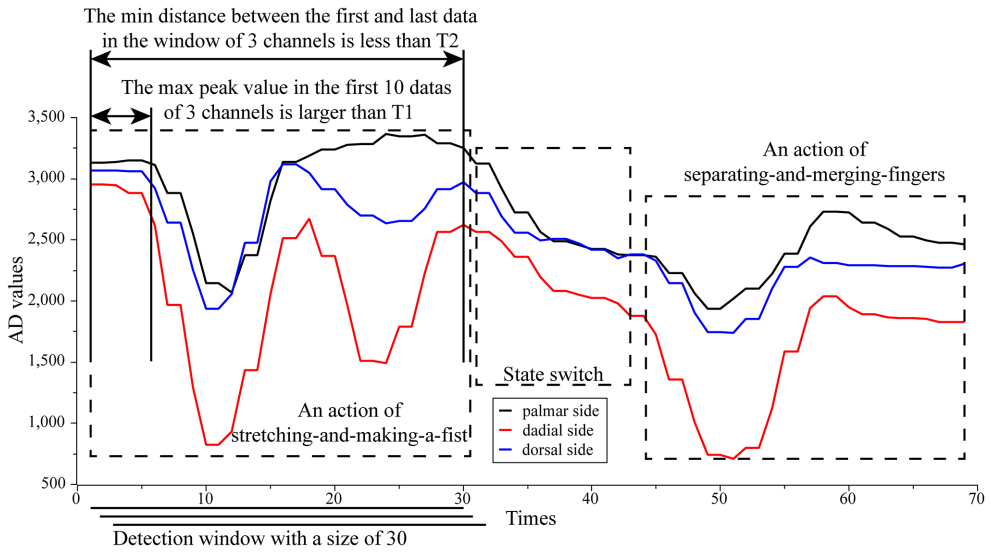

FIGURE 4
The schematic of the action pre-detection strategy. Only window data that meet the following two conditions will be considered as a rehabilitation training action and input to the classification algorithm for recognition. (1) The maximum peak value of the first 10 data of the three channels of the window is greater than the thresholdT_1, i.e., $\max_i\left\{\max_j\left\{ch_i(j)\right\}-\min_j\left\{ch_i(j)\right\}\right\}>T_1$. (2) The minimum head-to-tail AD distance of the three channels of the window is less than the thresholdT_2, i.e., $\min_i\left\{\left\|ch_i(1)-ch_i(30)\right\|\right\}<T_2$. Where the threshold values T_1 and T_2 are empirical values.

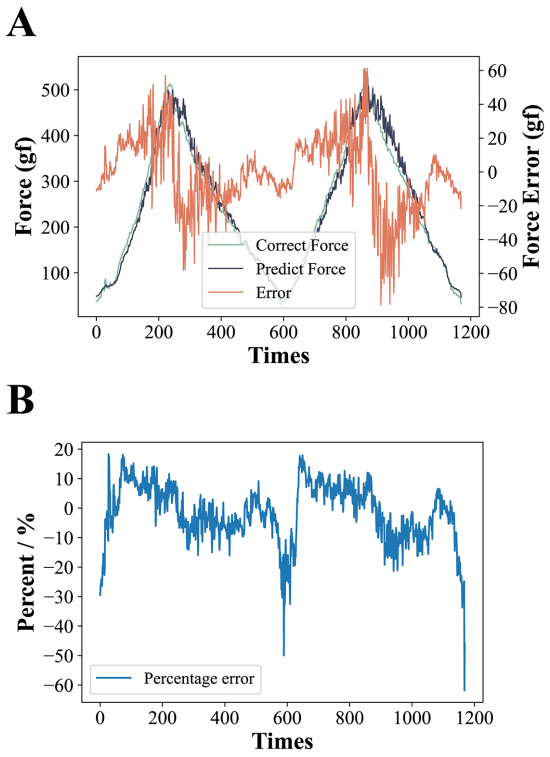

FIGURE 5
(A) Results of pressure calibration tests. The larger error at higher applied pressures is due to the fact that at higher pressures, the larger absolute value of the derivative of the pressure to the AD value results in larger predicted pressure changes from slight AD perturbations. **(B)** The error is expressed as a percentage. Except for individual spikes, the error is basically between ±20%.

3.2. Effect of the number of neurons in the hidden layer and output layer on the verification error of the autoencoder

In order to find the most suitable autoencoder structure for accurate feature extraction of the input data, we tested the effect of different numbers of neurons in hidden layers and output neurons on the validation error of the autoencoder. k-fold cross-validation, as an efficient method to test the performance analysis of networks with different hyperparameters, randomly disturbs the sample set and divides it equally into k subsets. In k times of loops, a different subset is selected as the validation set and the remaining subsets are used as the training set, and the error of the network completed by this loop training on the validation set is evaluated. After k loops, the average of the k test errors is used as a measure of the generalization ability of the network at the current hyperparameter setting. We choose a 10-fold cross-validation approach and let the number of neurons in the hidden layer increase from 10 to 60 in step of 10 and the number of neurons in the output layer increase from 5 to 40 in step of 5. The test results for all combinations are shown in Figure 6A. From the results, it can be seen that with the same number of neurons in the output layer, the average validation error shows a decreasing trend as the number of neurons in the hidden layer decreases, and with the same number of hidden layer neurons, the average validation error shows an increasing trend as the number of output layer neurons increases. Particularly, the network even has difficulty converging when the number of output neurons is larger than the hidden layer. Therefore, with a larger number of hidden layer neurons and a smaller number of output layer neurons, the autoencoder can reduce the dimensionality of the raw data with better accuracy. However, a larger number of hidden layer neurons implies an increase in the number of autoencoder parameters, which increases the execution time for the final deployment of the algorithm to the microcontroller, which is not conducive to real-time processing, while A smaller number of output neurons may lead to a one-sided extraction of features specific to the raw data set by the encoder, which can lead to a reduction in the generalization ability of the algorithm and make it difficult to guarantee its linear differentiation in low-dimensional spaces.

3.3. Effect of the number of neurons in the hidden layer and output layer on SVM classification

To further determine the appropriate size of the hidden layer and output layer of the autoencoder, we tested the effect of the number of neurons in the hidden layer and output layer on the SVM classification results for the above combination. In this test, we also use 10-fold cross-validation, and for each autoencoder structure, we encode all the original data using the autoencoder after training, then train 6 SVM classifiers using the encoded data, which do not use the kernel trick and have a C-value of 1. Finally, the final prediction of the algorithm is determined using the voting results of all SVMs on the encoded data. We use the prediction error rate as a measure of the algorithm's classification performance, which is expressed as the proportion of samples with incorrect predictions for all samples. The test results are shown in Figure 6B.

The results show that the number of hidden layer neurons shows a negative correlation with the recognition error rate. When the hidden layer is 30 neurons or more, the recognition error rate decreases and then increases with the increase of output layer size, and as the output layer size continues to increase, the error rate tends to saturate. The algorithm performs better with a larger hidden layer and a smaller output layer. As can be seen, the scale of the hidden layer plays a key role in the final performance of the algorithm. At the same time, as we expected, too small or too large an output layer leads to a reduced degree of linear separability after encoding the raw data, which is not entirely determined by the encoding performance of the autoencoder; for example, the autoencoder exhibits a high validation error when the number of neurons in the hidden layer and output layer is 50 and 15, respectively, but performs well in the final classification, and the opposite is true at their number of 60 and 25, respectively, although overall it remains that the lower encoding error leads to better classification performance.

3.4. Autoencoder training results

Considering the computing power of the microcontroller and the generalization capability of the model, we choose a final autoencoder structure with a hidden layer size of 40, an output layer size of 10, the Tanh function as the hidden layer activation function, and no activation function for the output layer. With this parameter setting, we randomly divide the original data into training and test sets

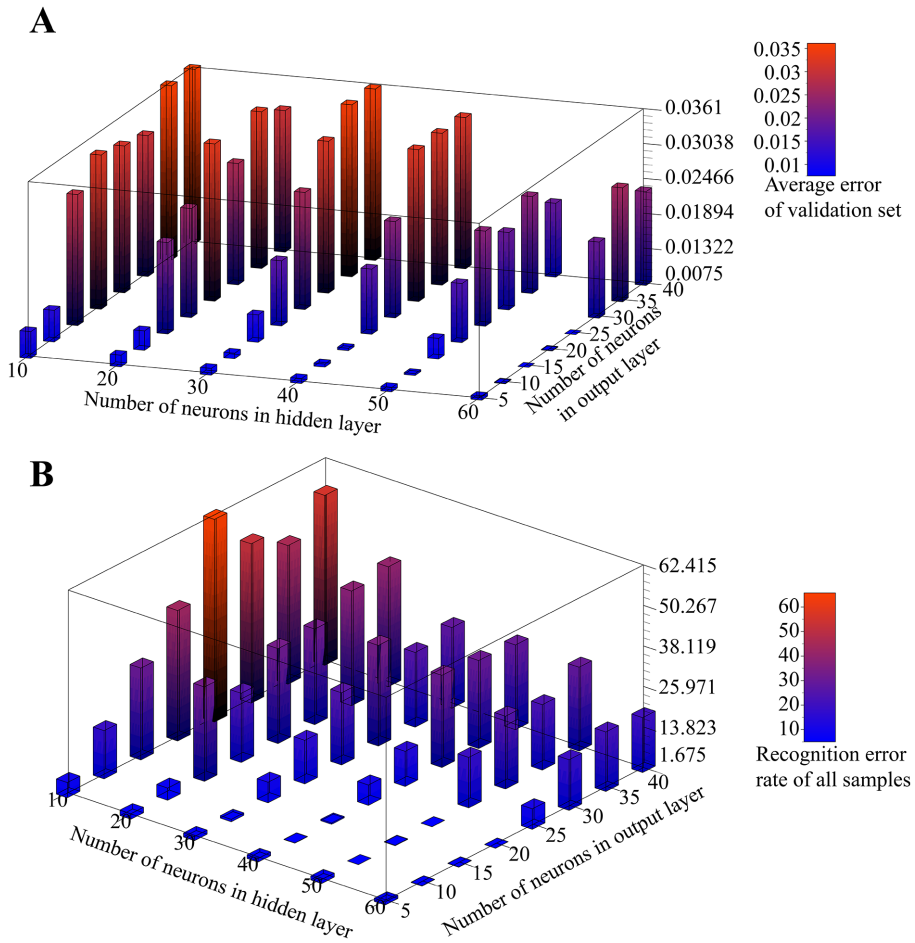

FIGURE 6
(A) Effect of the number of neurons in the hidden layer and output layer on the verification error of the autoencoder. **(B)** Effect of the number of neurons in the hidden layer and output layer on SVM classification.

according to 8:2, use Adam as the optimizer with each mini-batch size of 200, and select MSE as the loss function. The variation of the training set error and the test set error of the autoencoder with the training batch is shown in Figure 7A. It can be seen that during the training process, the test set and training set errors maintain the same downward trend and have very close values, characterizing the effective extraction of the raw data by the autoencoder. The raw data of the rehabilitation training actions and the corresponding fitted data of the autoencoder first encoded and then decoded are shown in Figure 7B.

3.5. Linear separability test after data encoding

After the autoencoder training is completed, we encode all the original data. According to our strategy, we are going to use six SVMs to vote on the categories of the encoded samples. Each SVM classifies two of the four classes of actions, such that the six classifiers are denoted as $S_{ij}\left(i=1,\ 2,\ 3,\ 4; j=i,\ldots 4\right)$, denoting the SVMs that classify class i with class j. Therefore, it is necessary to verify the degree of linear differentiability of the coded samples to justify our use of SVM. We propose a generalized k-fold cross-validation to assess the linear separability of the samples. The process is as follows: for the sample sets A and B to be classified, A is labeled as 1 and B is labeled as 0. Each of A and B is randomly disrupted and divided into k subsets as $A=A_1+A_2+\ldots+A_k$, $B=B_1+B_2+\ldots+B_k$. Unlike k-fold cross-validation, we only take a pair of subsets $A_i, \mathrm{B_i}$ as the training samples of SVM, and use the remaining samples $A-A_i$, $B-B_i$ as the test set, and finally calculate the misclassification rate of the test set under each combination and their mean values as the quantified index of the linear separability of the samples. If two sample sets have a high degree of linear differentiability in the sample space, it means that they have a larger distance and indicates that our SVM evaluation made based on the overall sample has a larger confidence level. A two-dimensional schematic of the generalized k-fold cross-validation process is shown in Figure 8. The test results for the six SVM classifiers using the generalized 5-fold cross-validation are shown in Figure 9. The stretching-and-making-a-fist and the ulnar-deviation actions and the separating-and-merging-fingers and the ulnar-deviation actions showed relatively high classification errors, indicating that they were close to each other in the sample space, especially between the separating-and-merging-fingers and the ulnar-deviation actions, which showed relatively high similarity in their pressure curves, leading to large classification errors, while the separating-and-merging-fingers and palm-flexion-and -dorsiflexion actions showed complete classification in all five subsets of the two sample sets, indicating that they were farthest apart in the sample space.

10.3389/fnins.2023.1238176

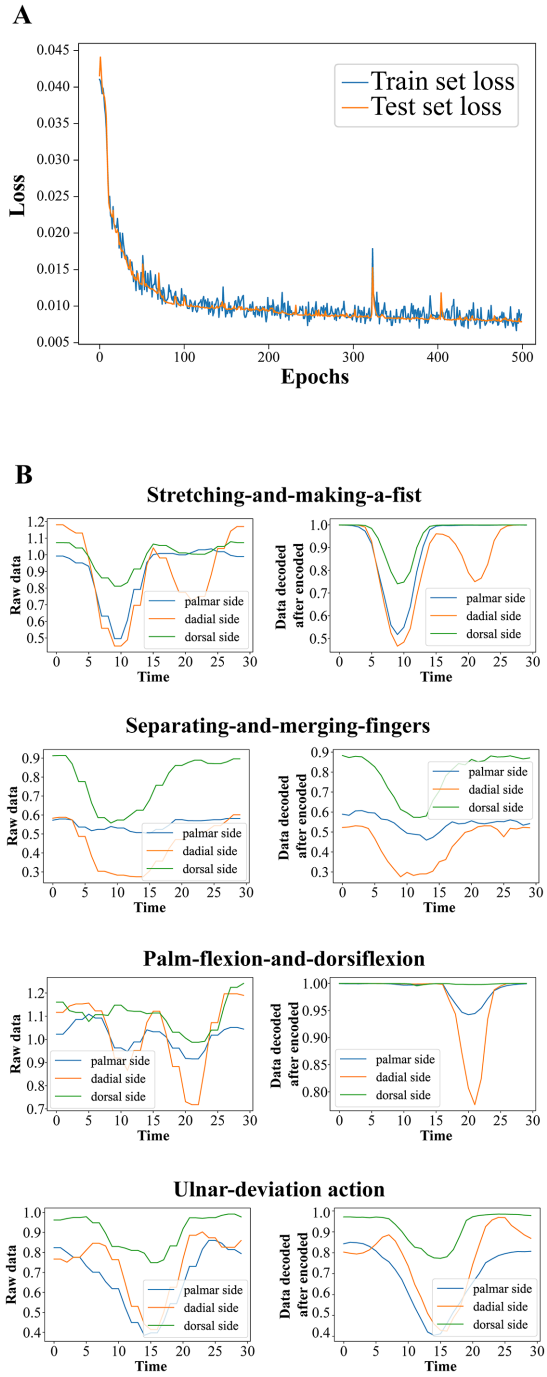

FIGURE 7
(A) The variation of the training set error and the test set error of the autoencoder with the training batch. **(B)** The raw data of the rehabilitation training actions and the corresponding fitted data of the autoencoder first encoded and then decoded.

3.6. Measured performance of the algorithm after deployment on the microcontroller

We deployed the entire classification algorithm trained on a microcontroller and tested it in practice. In addition to the five persons involved in the training set collection, we called five additional subjects to participate in the actual test, with each subject performing one round of testing. After the subject has tied the wristband and placed the elbow on the table with the arm upright and keeping the palm facing inward, the microcontroller first asks the user to stay relaxed and follow the instructions from the phone for the data acquisition of resting state, followed by the average calculation of the three-channel AD values. Thereafter, the microcontroller determines whether a rehabilitation action is coming according to the above action pre-detection strategy, and if so, classifies the action category, and if it is recognized as a rehabilitation action, sends a response message to the phone. Each subject performed 100 sets of each of the four types of rehabilitation training, with a supervisor counting manually on the side, and finally counting the number of differences between the rehabilitation training actions detected by the microcontroller and the actual actions performed. The confusion matrix was plotted based on the experimental results of each subject, and finally, the accuracy and recall of each rehabilitation training action recognition for each subject were counted.

The confusion matrix of 10 subjects is shown in Figure 10A, where the top row shows the test results of subjects who participated in the training set acquisition, and the bottom row shows the test results of subjects who did not participate in the training set acquisition. We counted the precision P, recall R, and f1 scores of each rehabilitation training action for each subject according to the confusion matrix, which was calculated by the following equations

$$P = \frac{TP}{TP + FP} \times 100\%$$

$$R = \frac{TP}{TP + FN} \times 100\%$$

$$f_1 = 2 \cdot \frac{P \cdot C}{P + C}$$

For the rehabilitation training action X, TP denotes the number of times the network correctly recognized X, FP denotes the number of times other actions were recognized as X, and FN denotes the number of times X was recognized as other actions or not recognized as any one action. The results show that the test results of the subjects who participated in the training set acquisition were generally good, indicating the effectiveness of the algorithm in classifying the four actions. Subjects who did not participate in the training set acquisition had slightly worse test results than the former but also showed sufficiently high generalization ability, indicating that the algorithm is generalized for feature extraction of the four actions.

The average precision and recall of the participants who participated in the training set acquisition and those who did not participate in the acquisition were counted separately on the four actions, and the results are shown in Figure 10B. On subjects participating in training set acquisition, the recognition accuracy and recall of the four rehabilitation actions were basically above 90% (except for palm-flexion-and-dorsiflexion action with 89.9% accuracy and extension grip with 88.4% recall), with extension grip having the highest accuracy of 98% and palmar dorsiflexion having the highest recall of 96%. On the subjects who were not involved in the training

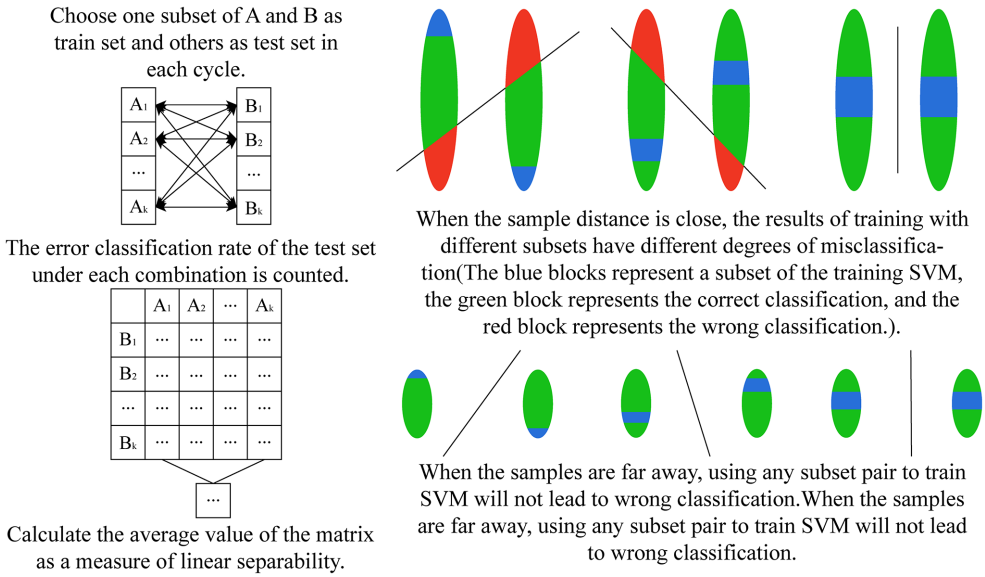

FIGURE 8
The schematic diagram of generalized k-fold cross-validation.

set acquisition, the recognition accuracy and recall rate of the four rehabilitation movements were above 82 and 84%, respectively, with the separating and merging fingers action having the highest accuracy of 90.24% and palm flexion and dorsiflexion action having the highest recall rate of 87.4%. And on all subjects, the average precision of the four rehabilitation movements recognition was 93.38, 91.22, 86.66, and 87.23%, and the average recall was 86.6, 89.9, 91.7, and 87.5%, respectively, and the total precision of the system's recognition of the four rehabilitation training movements was 89.62%, the total recall was 88.93%, f1 score was 89.27%.

4. Discussion

With the development of computers and the Internet, the medical system is gradually showing the trend of intelligence and digitalization. With the support of the Internet and smart devices, rehabilitation treatment is gradually evolving from the previous face-to-face communication between doctors and patients to a new mode of remote monitoring and management. For example, mHealth (Birkmeyer et al., 2021), defined as a medical and public health practice supported by mobile devices, has a large number of applications in clinical diagnosis or advice, improving patient compliance, parameterizing physiological parameters, and providing disease-related education (Rowland et al., 2020). mHealth, as a cell phone APP, can make full use of hardware resources and contains applications such as intelligent intervention, angle measurement (Pourahmadi et al., 2017; Modest et al., 2019; Ochen et al., 2020), intelligent monitoring, and rehabilitation games (Meijer et al., 2019, 2021) in assisting the rehabilitation training of distal radius fractures (Chen et al., 2020). Therefore, it has the advantage of low cost, but its simple architecture dictates that it cannot measure too many physiological parameters, so various terminals are needed to extend its functionality. As a sign of artificial intelligence, virtual reality (VR) technology is also increasingly used in the field of rehabilitation engineering, including assisted rehabilitation training for diseases such as cognitive impairment (Lei et al., 2019), arthritis (Byra and Czernicki, 2020), and chronic obstructive pulmonary disease (Rutkowski et al., 2020), and also in distal radius fractures (Kulkarni and Naqvi, 2021). VR technology in rehabilitation training is basically presented in the form of a serious game, which allows patients to play in the process with less pain caused by the disease and at the same time to carry out effective rehabilitation training, which greatly promotes the enthusiasm of patients in rehabilitation treatment. But playing VR games usually requires an empty space as well as an expensive headset, which makes it seem more appropriate for applications in specialized, centralized retreats rather than for individual users. There are some specialized integrated devices for rehabilitation training, which use surface EMG signals, inertial sensing units, flexible pressure sensors, and other means for physiological information acquisition from the affected area, and based on them for applications in the direction of clinical parameter assessment, movement posture detection, etc. These devices tend to achieve very high accuracy of assessment due to multimodal signal processing and can bring a greater variety of rehabilitation training options to patients. However, their high cost and the inconvenience of wearing them are still the main factors that prevent their popularity.

Our developed wristband for rehabilitation training of distal radius fracture directly detects the force on the palmar side, radial side, and dorsal side of the affected limb by means of a three-channel thin film pressure sensor with tying a rigid magic stick band around the outside. After the sensor is connected to the circuit, the rehabilitation training movement detection of the distal radius fracture recovery period can be performed. The measured data showed that the system achieved an f1 score of 89.27% for the recognition of the four rehabilitation actions. The demands placed on splint tightness in patients with distal radius fractures necessitated the use of a pressure sensor to quantitatively assess splint tightness. Pressure sensors can be categorized into piezoresistive, capacitive, optical fiber, resonant, and piezoelectric types based on different principles (Song et al., 2020), and all of them can be fabricated

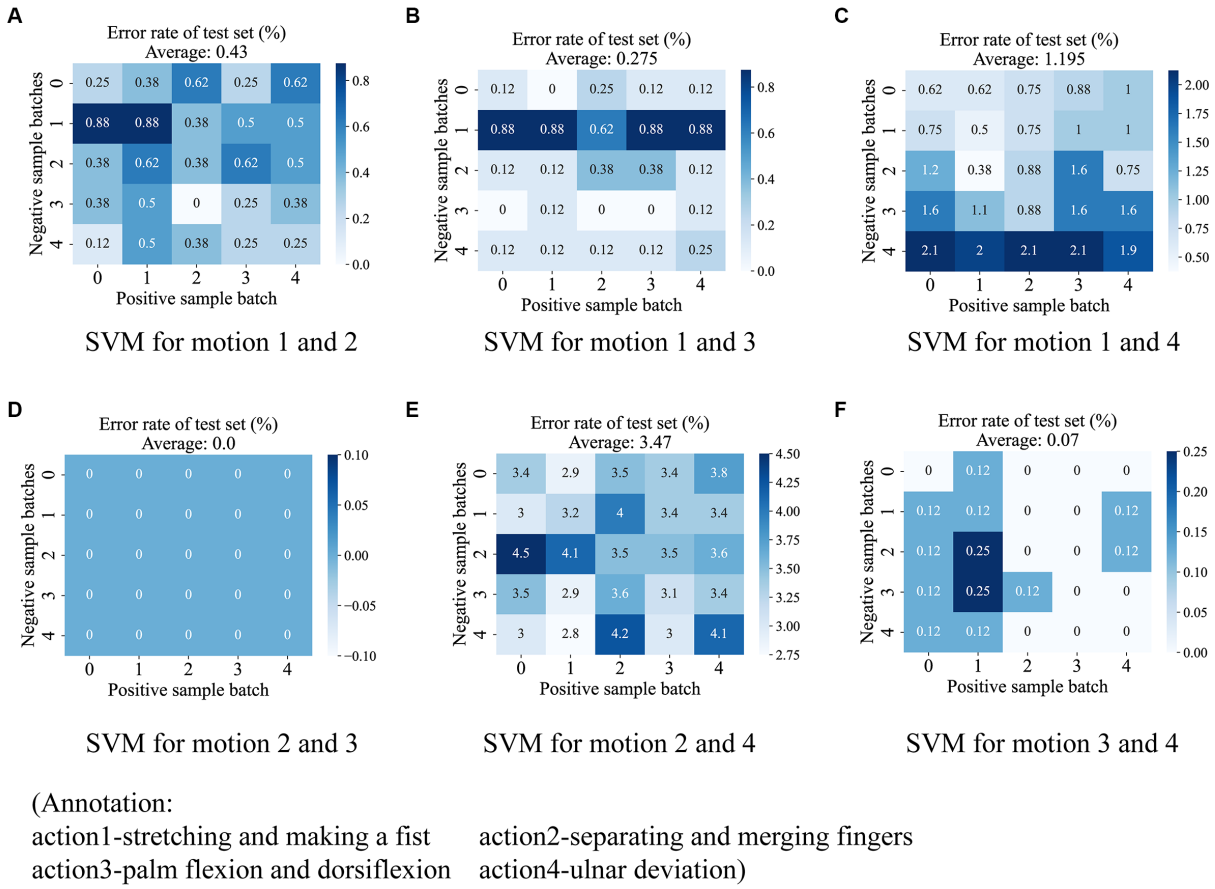

FIGURE 9
The test results for the six SVM classifiers using the generalized 5-fold cross-validation. The six subplots show the test results for each of the six SVM classifiers, including **(A)** between stretching-and-making-a-fist and seperating-and-merging-fingers, **(B)** between stretching-and-making-a-fist and palm-flexion-and-dorsiflexion, **(C)** between stretching-and-making-a-fist and ulnar-deviation action, **(D)** between seperating-and-merging-fingers and palm-flexion-and-dorsiflexion, **(E)** between seperating-and-merging-fingers and ulnar-deviation action, and **(F)** palm-flexion-and-dorsiflexion and ulnar-deviation action. The results show that there is a maximum linear separability between seperating-and-merging-fingers and palm-flexion-and-dorsiflexion **(D)**, however, there is a minimum between seperating-and-merging-fingers and ulnar-deviation action **(E)**. This is due to the fact that the two actions in the latter have a relatively high similarity in the data change curves.

with very small dimensions in the medical field (Chau and Wise, 1988; Kalvesten et al., 1998; Nemani et al., 2013). Due to the need for miniaturization of the system, we have abandoned the use of bulky sensors such as weighing sensors, despite their high accuracy. There are devices known as intelligent splints that are effective in maintaining pressure on the affected area for immobilization. Most of them use airbags for pressure regulation and quantify the tightness based on air pressure sensors, and this type of research is mainly taking place in China. However, none of the sensor arrangements in these systems directly detect the pressure at the fracture point, so we rule out this option as well. Taking all factors into account, we decided that flexible thin-film pressure sensors were the sensors that best met our requirements, as they are small enough that can be easily placed between the skin and the splint without the negative effects of splint immobilization. Flexible pressure sensors have gained wide application in wearable smart devices due to their high flexibility, high sensitivity, and small size (Xu et al., 2018; Huang et al., 2019). We chose a thin-film pressure sensor with a well-established market, costing less than 3 RMB. After the pressure calibration test, the results show that in our pressure acquisition circuit, the accuracy of the sensor is controlled at ±20%, which meets the accuracy standard of the sensor itself, indicating that our acquisition circuit is effective. It should be noted that the accuracy of our thin-film pressure sensor is far less than that of an accurate weighing sensor, but it is accurate enough to meet our splint pressure monitoring needs, and at the same time it is extremely low-cost, which makes it ideal for the Chinese market. The algorithm uses the average AD values of the initial relaxation state as the data benchmark, and the network input data of the training actions is the ratio of the original AD values relative to the data benchmark. Since each user wears the wristband with different degrees of looseness, this facilitates data normalization and thus improves system robustness and generalization. We designed an action pre-detection strategy. Some rehabilitation actions are divided into multiple phases, for example, stretching-and-making-a-fist action includes two phases, stretching and fisting. Since the data window uses sliding detection, in order to prevent data from the first stage from being passed into the classification algorithm once it enters the window, the strategy determines whether the beginning of the action data has moved close to the head of the window queue by judging the volatility of the data in the first third of the window. This strategy ensures that each window of data that enters the network is a complete rehabilitation training action. At the same time, switching between different rehabilitation actions can lead to strong changes in the pressure

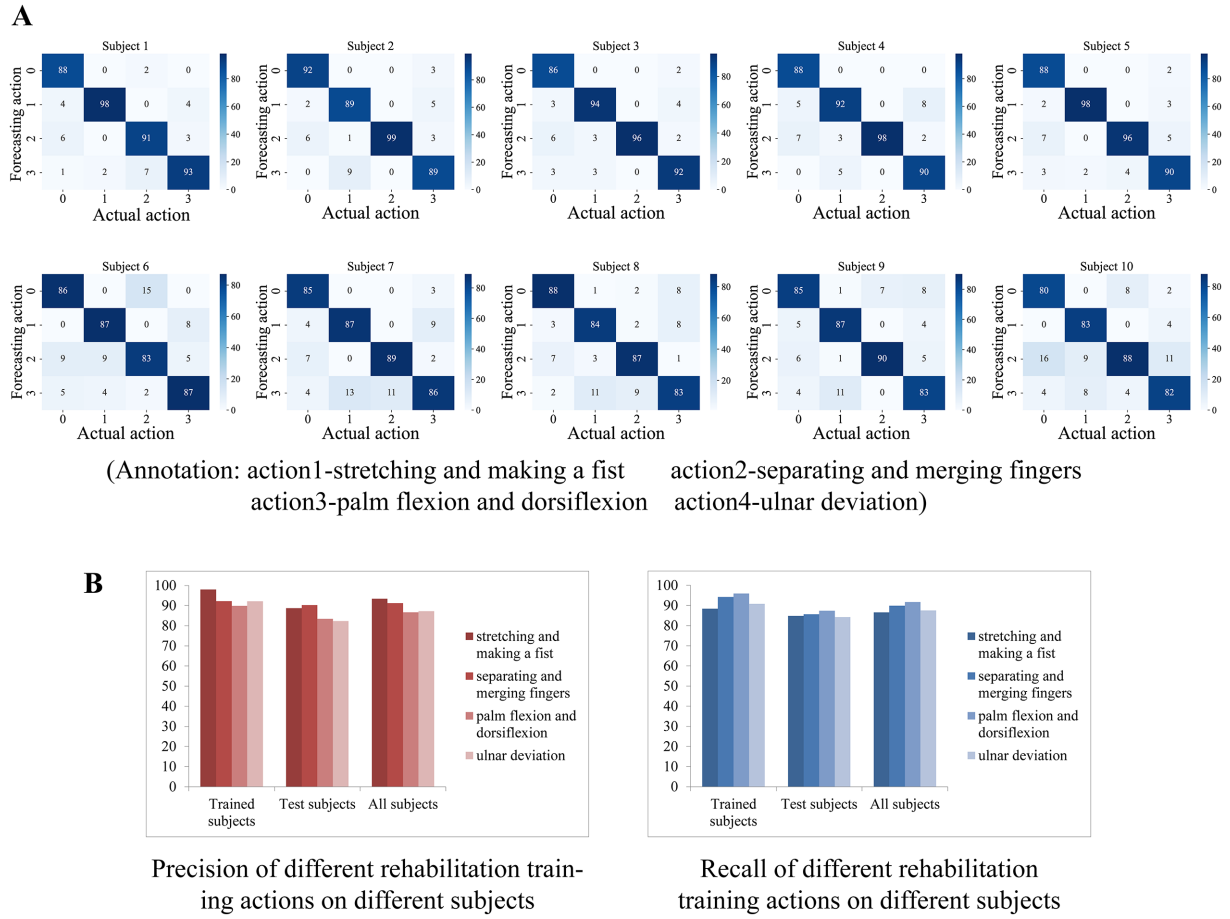

FIGURE 10
(A) The confusion matrix of 10 subjects. **(B)** The result of average precision and recall of the participants who participated in the training set acquisition versus those who did not.

data, for example, the initial hand gesture with a relaxed hand in the stretching-and-making-a-fist will result in a relatively low-pressure value, while the initial hand gesture with a tight hand in the separating-and-merging-fingers action will result in a relatively high-pressure value. Switching between these two actions produces a rising or falling slope of the pressure value signal. To prevent passing this switching process into the classification algorithm, the action pre-detection strategy excludes this state switching process by calculating the difference between the start and end values of the window pressure data, so that a complete rehabilitation action signal can be initially filtered by this strategy. In the classification algorithm, we first obtain the feature information after dimensionality reduction from the original action data by an autoencoder and then use six SVM linear classifiers to vote on the samples two by two, and the final prediction with the highest number of votes is used as the final classification output. We tested the linear separability of different action-coded data using a generalized k-fold cross-validation method, and the results show that the action-coded data of any two have good linear separability, proving the effectiveness of using the SVM linear classifier. In the actual test, the results showed that the system achieved a classification f1 score of 85.84% for subjects who did not participate in the training set acquisition, which shows the effectiveness of the system operation.

In addition, the rehabilitation wristband can be used independently in a variety of splinting (small splints, casts, thermoplastic splints, etc.) immobilization situations in the early stages of fracture patients. Its pressure sensor can accurately assess the degree of splint tightness by direct contact with the affected limb, which can largely reduce the dependence of splint fixation on physician experience. This gives the wristband the flexibility of application as it can alert users to the loosening of the splint during fixation (Naqvi, 2022). Through the Bluetooth interface of the rehabilitation training wristband, a variety of rehabilitation training software can be developed based on it, such as a database for recording and managing patients' daily rehabilitation training, and serious games for improving patients' motivation in rehabilitation training.

Data availability statement

The original contributions presented in the study are included in the article/Supplementary material, further inquiries can be directed to the corresponding authors.

Author contributions

XS and GZ designed and planned the study concept. QZ and ZX completed the system construction and algorithm and design drafted

the manuscript. XC provided medical guidance. All authors jointly revised the content of the study and agreed to submit the manuscript.

Funding

This work was supported by Science and Technology Program of Suzhou, China (No. SYG202019) and Science and Technology Program of Jiangsu Province, China (No. BE2021662).

Conflict of interest

The authors declare that the research was conducted in the absence of any commercial or financial relationships that could be construed as a potential conflict of interest.

Publisher's note

Supplementary material

The Supplementary material for this article can be found online at: https://www.frontiersin.org/articles/10.3389/fnins.2023.1238176/full#supplementary-material

References

Arora, S. P., and Naqvi, W. M. (2022). A research protocol on leap motion tracking device: a novel intervention method in distal radial fracture rehabilitation. *PLoS One* 17:e0267549. doi: 10.1371/journal.pone.0267549

Atitallah, B. B., Abbasi, M. B., Barioul, R., Bouchaala, D., Derbel, N., and Kanoun, O. (2020). Simultaneous pressure sensors monitoring system for hand gestures recognition. In 2020 IEEE Sensors (pp. 1–4). Rotterdam, Netherlands

Badwaik, N., Athawale, V., Dadgal, R., Wadhokar, O. C., and Kulkarni, C. A. (2021). Physiotherapy rehabilitation of distal radial fracture to enhance the activity of daily living. *J. Med. Pharm. Allied Sci.* 10, 3343–3345. doi: 10.22270/jmpas.V10I4.1270

Bhan, K., Hasan, K., Pawar, A. S., Patel, R., and Pawar, A. S. (2021). Rehabilitation following surgically treated distal radius fractures: do immobilization and physiotherapy affect the outcome? *Cureus* 13:e16230. doi: 10.7759/cureus.16230

Bilius, L. B., Pentiuc, Ş. G., and Vatavu, R. D. (2023). TIGER: a Tucker-based instrument for gesture recognition with inertial sensors. *Pattern Recogn. Lett.* 165, 84–90. doi: 10.1016/J.PATREC.2022.11.028

Birkmeyer, S., Wirtz, B. W., and Langer, P. F. (2021). Determinants of mHealth success: an empirical investigation of the user perspective. *Int. J. Inf. Manag.* 59:102351. doi: 10.1016/J.IJINFOMGT.2021.102351

Byra, J., and Czernicki, K. (2020). The effectiveness of virtual reality rehabilitation in patients with knee and hip osteoarthritis. *J. Clin. Med.* 9:2639. doi: 10.3390/JCM9082639

Chau, H. L., and Wise, K. D. (1988). An ultraminiature solid-state pressure sensor for a cardiovascular catheter. *IEEE Trans. Electron Devices* 35, 2355–2362. doi: 10.1109/16.8814

Chen, Y., Yu, Y., Lin, X., Han, Z., Feng, Z., Hua, X., et al. (2020). Intelligent rehabilitation assistance tools for distal radius fracture: a systematic review based on literatures and mobile application stores. *Comput. Math. Methods Med.* 2020, 1–9. doi: 10.1155/2020/7613569

Cheng, Y., Li, G., Yu, M., Jiang, D., Yun, J., Liu, Y., et al. (2021). Gesture recognition based on surface electromyography-feature image. *Concurr. Comput.* 33:e6051. doi: 10.1002/cpe.6051

Copaci, D., Arias, J., Gómez-Tomé, M., Moreno, L., and Blanco, D. (2022). sEMG-based gesture classifier for a rehabilitation glove. *Front. Neurorobot.* 16:750482. doi: 10.3389/fnbot.2022.750482

Debnath, B., O'brien, M., Yamaguchi, M., and Behera, A. (2022). A review of computer vision-based approaches for physical rehabilitation and assessment. *Multimed. Syst.* 28, 209–239. doi: 10.1007/S00530-021-00815-4

Dong, W., Yang, L., Gravina, R., and Fortino, G. (2021). Soft wrist-worn multi-functional sensor array for real-time hand gesture recognition. *IEEE Sensors J.* 22, 17505–17514. doi: 10.1109/JSEN.2021.3050175

Fang, B., Lv, Q., Shan, J., Sun, F., Liu, H., Guo, D., et al (2019). Dynamic gesture recognition using inertial sensors-based data gloves. In 2019 IEEE 4th international conference on advanced robotics and mechatronics (ICARM) (pp. 390–395). Toyonaka, Japan

Francisco, J. A., and Rodrigues, P. S. (2022). Computer vision based on a modular neural network for automatic assessment of physical therapy rehabilitation activities. *IEEE Trans. Neural Syst. Rehabil. Eng.* 31:2023, 2174–2183. doi: 10.1109/TNSRE.2022.3226459

Gao, Z., Xiao, X., Carlo, A. D., Yin, J., Wang, Y., Huang, L., et al. (2023). Advances in wearable strain sensors based on electrospun fibers. *Adv. Funct. Mater.* 33:2214265. doi: 10.1002/adfm.202214265

Guo, K., Zhang, S., Zhao, S., and Yang, H. (2021). Design and manufacture of data gloves for rehabilitation training and gesture recognition based on flexible sensors. *J. Healthc. Eng.* 2021, 1–9. doi: 10.1155/2021/6359403

Han, Y., Varadarajan, A., Kim, T., Zheng, G., Kitani, K., Kelliher, A., et al. (2022). Smart skin: vision-based soft pressure sensing system for in-home hand rehabilitation. *Soft Robot.* 9, 473–485. doi: 10.1089/soro.2020.0083

He, B., Tian, X., Ji, G., and Han, A. (2020). Comparison of outcomes between nonsurgical and surgical treatment of distal radius fracture: a systematic review update and meta-analysis. *Arch. Orthop. Trauma Surg.* 140, 1143–1153. doi: 10.1007/s00402-020-03487-3

Hellsten, T., Karlsson, J., Shamsuzzaman, M., and Pulkkis, G. (2021). The potential of computer vision-based marker-less human motion analysis for rehabilitation. *Rehabil. Process Outcome* 10:117957272110223. doi: 10.1177/11795727211022330

Hua, Z., Wang, J. W., Lu, Z. F., Ma, J. W., and Yin, H. (2018). The biomechanical analysis of three-dimensional distal radius fracture model with different fixed splints. *Technol. Health Care* 26, 329–341. doi: 10.3233/THC-171050

Huang, Y., Fan, X., Chen, S. C., and Zhao, N. (2019). Emerging technologies of flexible pressure sensors: materials, modeling, devices, and manufacturing. *Adv. Funct. Mater.* 29:1808509. doi: 10.1002/adfm.201808509

Huang, Q., Wu, W., Chen, X., Wu, B., Wu, L., Huang, X., et al. (2019). Evaluating the effect and mechanism of upper limb motor function recovery induced by immersive virtual-reality-based rehabilitation for subacute stroke subjects: study protocol for a randomized controlled trial. *Trials* 20, 104–109. doi: 10.1186/s13063-019-3177-y

Jeong, H., Feng, J., and Kim, J. (2022). 2.5 D laser-cutting-based customized fabrication of long-term wearable textile sEMG sensor: from design to intention recognition. *IEEE Robot Autom. Lett.* 7, 10367–10374. doi: 10.1109/LRA.2022.3190620

Kalvesten, E., Smith, L., Tenerz, L., and Stemme, G. (1998). The first surface micromachined pressure sensor for cardiovascular pressure measurements. In Proceedings MEMS 98. IEEE. Eleventh annual international workshop on Micro electro mechanical systems. An investigation of Micro structures, sensors, actuators, machines and systems cat. No. 98CH36176 (pp. 574–579). Heidelberg, Germany

Keskin, C., Kıraç, F., Kara, Y. E., and Akarun, L. (2012). Hand pose estimation and hand shape classification using multi-layered randomized decision forests. In Computer vision–ECCV 2012: 12th European conference on computer vision, Florence, Italy, October 7–13, 2012, proceedings, part VI 12 (pp. 852–863) Berlin Heidelberg

Kim, M., Cho, J., Lee, S., and Jung, Y. (2019). IMU sensor-based hand gesture recognition for human-machine interfaces. *Sensors* 19:3827. doi: 10.3390/s19183827

Kulkarni, C. A., and Naqvi, W. M. Impact of virtual reality on rehabilitation of distal radial fracture with head mounted device [internet]. Protocol exchange (2021) [cited 2021 Aug 11]. doi:10.21203/rs.3.pex-1341/v2

Lei, C., Sunzi, K., Dai, F., Liu, X., Wang, Y., Zhang, B., et al. (2019). Effects of virtual reality rehabilitation training on gait and balance in patients with Parkinson's disease: a systematic review. *PLoS One* 14:e0224819. doi: 10.1371/journal.pone.0224819

Li, T., Mi, M., Liu, H. B., Gao, Z. Q., Xiao, H. H., Zhou, Y., et al. (2020). Expert consensus on standardized painless closed manipulative reduction and cast immobilization for distal radius fracture based on enhanced recovery after surgery. Chinese journal of bone and joint. *Surgery* 13, 177–182[in Chinese]. doi: 10.3969/j.issn.2095-9958.2020.03.01

Li, Y., Yin, J., Liu, S., Xue, B., Shokoohi, C., Ge, G., et al. (2023). Learning hand kinematics for Parkinson's disease assessment using a multimodal sensor glove. *Adv. Sci.* 10:e2206982. doi: 10.1002/advs.202206982

Li, K., Zhuang, S., Liu, J., Guo, A., Wang, A., Lu, J., et al. (2021). Design of an intelligent medical splint with 3D printing and pressure detection. In 2021 IEEE 2nd international conference on big data, artificial intelligence and internet of things engineering (ICBAIE) (pp. 655–658). Nanchang, China

Meijer, H. A., Graafland, M., Obdeijn, M. C., Goslings, J. C., and Schijven, M. P. (2019). Face validity and content validity of a game for distal radius fracture rehabilitation. *J. Wrist Surg.* 8, 388–394. doi: 10.1055/s-0039-1688948

Meijer, H. A., Graafland, M., Obdeijn, M. C., van Dieren, S., Goslings, J. C., and Schijven, M. P. (2021). Serious game versus standard care for rehabilitation after distal radius fractures: a protocol for a multicentre randomised controlled trial. *BMJ Open* 11:e042629. doi: 10.1136/bmjopen-2020-042629

Meng, F., Liu, C., Li, Y., Hao, H., Li, Q., Lyu, C., et al. (2023). Personalized and safe soft glove for rehabilitation training. *Electronics* 12:2531. doi: 10.3390/electronics12112531

Modest, J., Clair, B., DeMasi, R., Meulenaere, S., Howley, A., Aubin, M., et al. (2019). Self-measured wrist range of motion by wrist-injured and wrist-healthy study participants using a built-in iPhone feature as compared with a universal goniometer. *J. Hand Ther.* 32, 507–514. doi: 10.1016/j.jht.2018.03.004

Moin, A., Zhou, A., Rahimi, A., Menon, A., Benatti, S., Alexandrov, G., et al. (2021). A wearable biosensing system with in-sensor adaptive machine learning for hand gesture recognition. *Nat. Electron.* 4, 54–63. doi: 10.1038/s41928-020-00510-8

Naqvi, W. M. (2022). Gamification in therapeutic rehabilitation of distal radial and ulnar fracture: a case report. *Cureus* 14:e28586. doi: 10.7759/cureus.28586

Nascimento, L. M. S. D., Bonfati, L. V., Freitas, M. L. B., Mendes Junior, J. J. A., Siqueira, H. V., and Stevan, S. L. Jr. (2020). Sensors and systems for physical rehabilitation and health monitoring—a review. *Sensors* 20:4063. doi: 10.3390/s20154063

Nemani, K. V., Moodie, K. L., Brennick, J. B., Su, A., and Gimi, B. (2013). In vitro and in vivo evaluation of SU-8 biocompatibility. *Mater. Sci. Eng. C* 33, 4453–4459. doi: 10.1016/j.msec.2013.07.001

Ochen, Y., Peek, J., van der Velde, D., Beeres, F. J. P., van Heijl, M., Groenwold, R. H. H., et al. (2020). Operative vs nonoperative treatment of distal radius fractures in adults: a systematic review and meta-analysis. *JAMA Netw. Open* 3:e203497. doi: 10.1001/jamanetworkopen.2020.3497

Østergaard, H. K., Mechlenburg, I., Launonen, A. P., Vestermark, M. T., Mattila, V. M., and Ponkilainen, V. T. (2021). The benefits and harms of early mobilization and supervised exercise therapy after non-surgically treated proximal humerus or distal radius fracture: a systematic review and meta-analysis. *Curr. Rev. Musculoskelet. Med.* 14, 107–129. doi: 10.1007/s12178-021-09697-5

Pierre Claver, U., and Zhao, G. (2021). Recent progress in flexible pressure sensors based electronic skin. *Adv. Eng. Mater.* 23:2001187. doi: 10.1002/adem.202001187

Pourahmadi, M. R., Ebrahimi Takamjani, I., Sarrafzadeh, J., Bahramian, M., Mohseni-Bandpei, M. A., Rajabzadeh, F., et al. (2017). Reliability and concurrent validity of a new iP hone® goniometric application for measuring active wrist range of motion: a cross-sectional study in asymptomatic subjects. *J. Anat.* 230, 484–495. doi: 10.1111/joa.12568

Prakash, A., Kumari, B., and Sharma, S. (2019). A low-cost, wearable sEMG sensor for upper limb prosthetic application. *J. Med. Eng. Technol.* 43, 235–247. doi: 10.1080/03091902.2019.1653391

Quadlbauer, S., Pezzei, C., Jurkowitsch, J., Rosenauer, R., Kolmayr, B., Keuchel, T., et al. (2020). Rehabilitation after distal radius fractures: is there a need for immobilization and physiotherapy? *Arch. Orthop. Trauma Surg.* 140, 651–663. doi: 10.1007/s00402-020-03367-w

Reid, S. A., Andersen, J. M., and Vicenzino, B. (2020). Adding mobilisation with movement to exercise and advice hastens the improvement in range, pain and function after non-operative cast immobilisation for distal radius fracture: a multicentre, randomised trial. *J. Physiother.* 66, 105–112. doi: 10.1016/j.jphys.2020.03.010

Rowland, S. P., Fitzgerald, J. E., Holme, T., Powell, J., and McGregor, A. (2020). What is the clinical value of mHealth for patients? *NPJ Digital Med.* 3:4. doi: 10.1038/s41746-019-0206-x

Rutkowski, S., Rutkowska, A., Kiper, P., Jastrzebski, D., Racheniuk, H., Turolla, A., et al. (2020). Virtual reality rehabilitation in patients with chronic obstructive pulmonary disease: a randomized controlled trial. *Int. J. Chron. Obstruct. Pulmon. Dis.* 15, 117–124. doi: 10.2147/COPD.S223592

Shen, M., and Lu, H. (2022). RARN: a real-time skeleton-based action recognition network for auxiliary rehabilitation therapy. In 2022 IEEE international symposium on circuits and systems (ISCAS), Austin, TX, USA, pp. 2482–2486

Sinha, A., Choi, C., and Ramani, K. (2016). Deephand: robust hand pose estimation by completing a matrix imputed with deep features. In Proceedings of the IEEE conference on computer vision and pattern recognition (pp. 4150–4158). Las Vegas, NV, USA

Song, P., Ma, Z., Ma, J., Yang, L., Wei, J., Zhao, Y., et al. (2020). Recent progress of miniature MEMS pressure sensors. *Micromachines* 11:56. doi: 10.3390/mi11010056

Sun, Y., Li, X., Wang, J., Li, D., and Zhu, Y. (2022). Research on upper limb rehabilitation action recognition method of unsupervised contrast learning based on time-domain multi-scale feature fusion. In 2022 5th international conference on intelligent robotics and control engineering (IRCE), Tianjin, China, pp. 103–107

Tang, D., Jin Chang, H., Tejani, A., and Kim, T. K. (2014). Latent regression forest: structured estimation of 3d articulated hand posture. In Proceedings of the IEEE conference on computer vision and pattern recognition (pp. 3786–3793).

Wan, C., Probst, T., Gool, L. V., and Yao, A., (2019). Self-supervised 3d hand pose estimation through training by fitting. In Proceedings of the IEEE/CVF conference on computer vision and pattern recognition (pp. 10853–10862). Long Beach, CA, USA

Weygers, I., Kok, M., Konings, M., Hallez, H., De Vroey, H., and Claeys, K. (2020). Inertial sensor-based lower limb joint kinematics: a methodological systematic review. *Sensors* 20:673. doi: 10.3390/s20030673

Wong, W. K., Juwono, F. H., and Khoo, B. T. T. (2021). Multi-features capacitive hand gesture recognition sensor: a machine learning approach. *IEEE Sensors J.* 21, 8441–8450. doi: 10.1109/JSEN.2021.3049273

Xiao, X., Yin, J., Chen, G., Shen, S., Nashalian, A., and Chen, J. (2022). Bioinspired acoustic textiles with nanoscale vibrations for wearable biomonitoring. *Matter* 5, 1342–1345. doi: 10.1016/j.matt.2022.03.014

Xu, H., Gao, L., Zhao, H., Huang, H., Wang, Y., Chen, G., et al. (2021). Stretchable and anti-impact iontronic pressure sensor with an ultrabroad linear range for biophysical monitoring and deep learning-aided knee rehabilitation. *Microsyst. Nanoeng.* 7:92. doi: 10.1038/s41378-021-00318-2

Xu, F., Li, X., Shi, Y., Li, L., Wang, W., He, L., et al. (2018). Recent developments for flexible pressure sensors: a review. *Micromachines* 9:580. doi: 10.3390/mi9110580

Yadav, S. K., Tiwari, K., Pandey, H. M., and Akbar, S. A. (2021). A review of multimodal human activity recognition with special emphasis on classification, applications, challenges and future directions. *Knowl. Based Syst.* 223:106970. doi: 10.1016/j.knosys.2021.106970

Zhang, Y., Liu, B., and Liu, Z. (2019). Recognizing hand gestures with pressure-sensor-based motion sensing. *IEEE Trans. Biomed. Circuits. Syst.* 13, 1425–1436. doi: 10.1109/TBCAS.2019.2940030

Zhu, Z. A., Lu, Y. C., You, C. H., and Chiang, C. K. (2019). Deep learning for sensor-based rehabilitation exercise recognition and evaluation. *Sensors* 19:887. doi: 10.3390/s19040887

frontiers | Frontiers in Neuroscience

TYPE Review
PUBLISHED 02 October 2023
DOI 10.3389/fnins.2023.1256682

OPEN ACCESS

EDITED BY
Lei Zhang,
Nanjing Normal University, China

REVIEWED BY
Alwin Poulose,
Indian Institute of Science Education and Research, Thiruvananthapuram, India
Ennio Gambi,
Marche Polytechnic University, Italy
Irina Mocanu,
Polytechnic University of Bucharest, Romania

*CORRESPONDENCE
Emanuele Torti
✉ emanuele.torti@unipv.it

RECEIVED 11 July 2023
ACCEPTED 18 September 2023
PUBLISHED 02 October 2023

CITATION
Guerra BMV, Torti E, Marenzi E, Schmid M, Ramat S, Leporati F and Danese G (2023) Ambient assisted living for frail people through human activity recognition: state-of-the-art, challenges and future directions.
Front. Neurosci. 17:1256682.
doi: 10.3389/fnins.2023.1256682

Ambient assisted living for frail people through human activity recognition: state-of-the-art, challenges and future directions

Bruna Maria Vittoria Guerra[1], Emanuele Torti[2]*, Elisa Marenzi[2], Micaela Schmid[1], Stefano Ramat[1], Francesco Leporati[2] and Giovanni Danese[2]

[1]Bioengineering Laboratory, Department of Electrical, Computer and Biomedical Engineering, University of Pavia, Pavia, Italy, [2]Custom Computing and Programmable Systems Laboratory, Department of Electrical, Computer and Biomedical Engineering, University of Pavia, Pavia, Italy

Ambient Assisted Living is a concept that focuses on using technology to support and enhance the quality of life and well-being of frail or elderly individuals in both indoor and outdoor environments. It aims at empowering individuals to maintain their independence and autonomy while ensuring their safety and providing assistance when needed. Human Activity Recognition is widely regarded as the most popular methodology within the field of Ambient Assisted Living. Human Activity Recognition involves automatically detecting and classifying the activities performed by individuals using sensor-based systems. Researchers have employed various methodologies, utilizing wearable and/or non-wearable sensors, and employing algorithms ranging from simple threshold-based techniques to more advanced deep learning approaches. In this review, literature from the past decade is critically examined, specifically exploring the technological aspects of Human Activity Recognition in Ambient Assisted Living. An exhaustive analysis of the methodologies adopted, highlighting their strengths and weaknesses is provided. Finally, challenges encountered in the field of Human Activity Recognition for Ambient Assisted Living are thoroughly discussed. These challenges encompass issues related to data collection, model training, real-time performance, generalizability, and user acceptance. Miniaturization, unobtrusiveness, energy harvesting and communication efficiency will be the crucial factors for new wearable solutions.

KEYWORDS

human activity recognition, ambient assisted living, wearable systems, frail people, deep learning

1. Introduction

Ambient Assisted Living (AAL) refers to the use of Information and Communication Technologies (ICT), assistive devices, and sensor network technologies to support, monitor and enhance the quality of life for individuals, particularly older adults, or people with disabilities, within their daily living and working environment. The primary goal of AAL is to provide individuals with increased independence, autonomy, and safety by incorporating technological solutions into their surroundings. These solutions can assist individuals in various activities of daily living, such as managing their health, monitoring

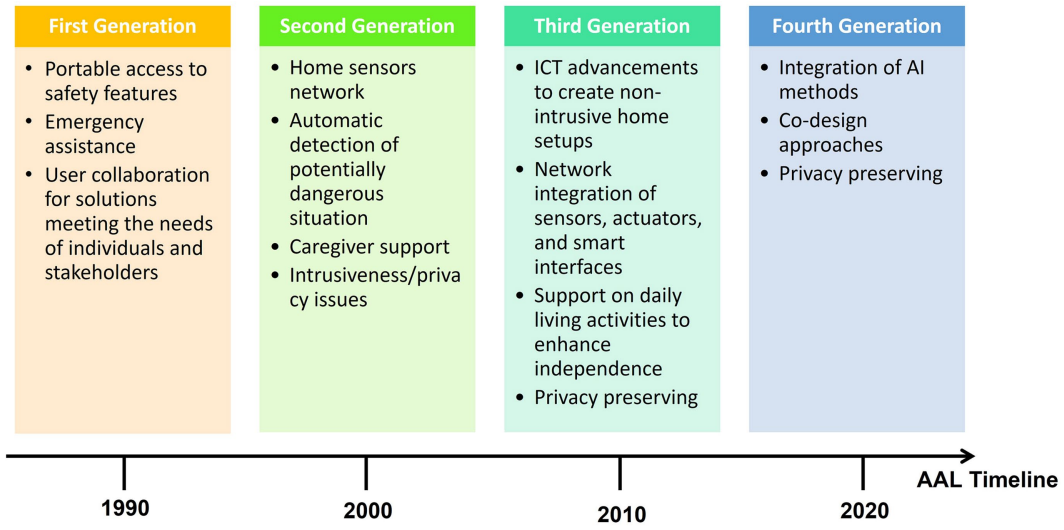

FIGURE 1
Evolution of AAL systems: four generations from the 1990s to the present day.

their safety, and improving their social interactions (Blackman et al., 2016; Stodczyk, 2020). One significant aspect of AAL is subject monitoring, which involves the continuous and unobtrusive tracking of an individual's activities, health parameters, and environment to ensure their safety and provide timely assistance when needed. Subject monitoring utilizes various sensors to collect data and analyze patterns, enabling caregivers and healthcare professionals to gain valuable insights into an individual's daily routines, health conditions, and potential risks. The choice of sensors can be made among two main groups: wearable and non-wearable sensors. The first one could be incorporated on clothing or worn by the user like accessories. Non-wearable sensors, on the other hand, are strategically placed on furniture, appliances, walls, doors, and other objects throughout the home. By integrating both types of sensors, through a so-called hybrid approach, a comprehensive monitoring solution can be created to effectively and efficiently monitor the subject (Calvaresi et al., 2017; Clapés et al., 2018).

The work of Aleksic et al. proposed a subdivision of AAL systems for subject monitoring into four distinct generations (see Figure 1) based on technological variations, highlighting the application of ICT, stand-alone assistive devices, and technologies for indoor environments within individuals' daily living and working environments (Al-Shaqi et al., 2016). These AAL systems actively encourage healthy lifestyles, contribute to disease prevention through personalized risk assessment and continuous monitoring, and primarily cater to frail individuals, by offering continuous support and actively promoting their independent and healthy living (Blackman et al., 2016; Calvaresi et al., 2017; Stodczyk, 2020; Cicirelli et al., 2021):

- *First Generation of AAL Systems*: the first generation of AAL systems primarily consists of alert and alarm systems using pendant or button devices worn by the monitored individuals. In the event of a dangerous situation, the individual would activate the button or pendant to send an alarm signal to a call center or caregiver. Examples of such solutions include the Salvalavita Beghelli[1] and LifeAlert.[2] While these devices offer several benefits, they also have specific limitations. For instance, individuals may be physically or mentally incapacitated, making them unable to trigger the alarm. Additionally, there are issues with individuals forgetting to wear or recharge the device.
- *Second Generation of AAL Systems*: the second generation of AAL systems involves more technologically advanced devices, installed in indoor spaces, incorporating sensors capable of automatically detecting dangerous conditions and triggering appropriate responses without relying on user activation. However, a weakness associated with this generation is that some users may perceive it as intrusive.
- *Third Generation of AAL Systems*: the third generation of AAL systems expands through advancements in ICT, introducing a more comprehensive concept of AAL. These systems encompass sensors designed to detect potentially dangerous situations and proactively prevent adverse scenarios, actuators providing support to the assisted individuals, and smart interfaces delivering information, assistance, and encouragement. The aim is to create minimally intrusive home setups comprising multiple sensors, actuators, and computing systems. These systems not only monitor the home environment but also track vital signs, changes in habits and activity patterns of frail individuals, and facilitate the execution of daily living activities (Mainetti et al., 2016).
- *Fourth Generation of AAL Systems*: the fourth generation of AAL systems incorporates Artificial Intelligence (AI) algorithms for data analysis within AAL solutions. These intelligent systems have the ability to learn from data and evolve over time, offering personalized assistance and support. The co-design approach is embraced, involving end-users, caregivers and stakeholders to

1 https://www.beghelli.it/salvalavita
2 http://www.lifealert.com

create users-centered and inclusive solutions (Siriwardhana et al., 2019; Bansal et al., 2021; Sophia et al., 2021; Gulati and Kaur, 2022; Rupasinghe and Maduranga, 2022; Warunsin and Phairoh, 2022).

1.1. Related works

By combining AAL with subject monitoring, it becomes possible to create personalized and proactive care solutions, promoting independent living while offering a safety net for vulnerable individuals. Subject monitoring can be conducted in both outdoor and indoor environments. Outdoor environments expose frail people to various risks, such as falls, extreme temperatures, and potential wandering or confusion in individuals with early symptoms of dementia. In this context, AAL systems aim to provide support to frail individuals by facilitating route checking, anomalous behavior recognition, motion activity evaluation, and other relevant functionalities (Fernandes et al., 2020; Lee, 2021). Since wearables are the only devices that can be employed outdoors, they acquire a fundamental importance. Smartwatches and smart wristbands are the most commonly used devices, while Inertial Measurement Units (IMUs) are typically the sensors chosen (the same used in indoor scenarios) (Bhargava et al., 2017; Iadarola et al., 2022). In literature, other solutions have been proposed that address alternative or complementary approaches (Sokullu et al., 2019; Kenfack Ngankam et al., 2020; Rupasinghe and Maduranga, 2022): for example, Global Navigation Satellite System (GNSS) sensors for outdoor localization (Junior et al., 2023); instrumented insoles (commercial or customized) as an aid for gait detection and consequently for pointing out unsteady walking or falls (Cristiani et al., 2014; Sivakumar et al., 2018) and sensors mounted on the body of a walker as a low-cost solution for people with limited mobility (Ding et al., 2022). Conversely, indoor scenarios present frail individuals with risks closely associated with their living spaces.

Notably, the indoor environment has been identified as a significant contributing element to falls (Lee, 2021), which are attributed to factors such as uneven or slippery floor surfaces (including carpets and mats), tripping obstacles, inadequate lighting, poorly designed or maintained stairs without handrails and unsuitable furniture. These criticalities increase the likelihood of tripping, falling, or slipping for frail individuals. Additional hazards arise from the absence of safety or preventive devices, such as night lights and grab rails (Carter et al., 1997; Lee, 2021). Indeed, the requirements of monitored subjects can vary significantly across different indoor scenarios. In private homes, where individuals live alone or with a caregiver, the primary focus of monitoring is on preventing domestic accidents and delivering essential healthcare services. On the other hand, in retirement residences where multiple individuals share common spaces, subject monitoring systems are primarily designed to facilitate group activities and controlled physical exercises (Nastac et al., 2019; Cicirelli et al., 2021).

Adapting the monitoring approach to suit the specific needs and dynamics of each indoor setting is crucial. This ensures that monitored subjects receive personalized support and care tailored to their circumstances. Additionally, it is important to recognize that AAL systems cannot remain static, as people's needs and habits evolve over time, along with the parameters that need to be observed. Consequently, data analysis methodologies must account for the evolving nature of these systems, allowing for the possibility of dynamically weighting or customizing certain parameters over others (Cicirelli et al., 2021). By embracing flexibility and adaptability, AAL systems can continue to provide effective and relevant support to individuals in various indoor environments.

The selection of appropriate sensors considers multiple factors, including the specific objectives of the AAL system, sensor cost, intrusiveness, user acceptability, and privacy concerns. However, more complex sensor networks, comprising environmental sensors, object sensors, cameras, and wearable sensors constitute the foundation of indoor AAL. The living facilities may be equipped with an array of interconnected sensors and actuators, enabling remote control and capable of detecting various environmental parameters such as door openings and room brightness. These sensors are strategically deployed to monitor the daily activities of individuals, ensuring security and safety. The selection of appropriate sensors considers multiple factors, including the specific objectives of the AAL system, sensor cost, intrusiveness, user acceptability, and privacy concerns. Communication protocols, such as ZigBee, Bluetooth, ZWave, USB, Ethernet, among others, are utilized to interconnect sensors, actuators, and smart devices throughout the environment (Tazari et al., 2011; Lloret et al., 2015; Babangida et al., 2022). Typically, raw or pre-processed data from sensors are transmitted to a collection center, either local or remote, where they undergo integration and analysis using robust algorithms (Plentz and De Pieri, 2018). A thorough and reliable data analysis becomes crucial in indoor scenarios equipped with automatic dangerous situation detection or capable of requesting help triggering alarms to third parties.

In the field of AAL, Human Activity Recognition (HAR) has emerged as a valuable tool with multifaceted utility. Within the AAL domain, HAR presents a range of solutions aimed at enhancing the quality of life of frail individuals (elderly and/or disabled people) and maintaining improved health and independence. Additionally, it provides also support to caregivers and medical professionals. HAR has garnered substantial interest as a prominent field of study in recent times. HAR methodologies are devised with the objective of autonomously detecting and classifying individuals' routine activities within defined contexts. Depending on the task and the employed technologies, two main methodologies are commonly adopted. The first approach relies on a threshold analysis method, which can suffice for triggering alerts when detecting dangerous events (Zdravevski et al., 2017; Al Machot et al., 2018a,b; Cicirelli et al., 2021). The second and more recent approach (see Figure 1, fourth generation), employs Artificial Intelligence (AI) solutions such as Machine Learning (ML) and Deep Learning (DL) algorithms for HAR (Aggarwal and Ryoo, 2011; Wang J. et al., 2019).

Among the various possible applications, human activities can be classified into four distinct groups based on the involvement of various body parts (Jegham et al., 2020; Minh Dang et al., 2020):

- *gestures* involve basic actions carried out by different parts of the human body, including hand gestures like the "okay" gesture or "thumbs up" gesture;
- *actions* refer to a collection of fundamental movements executed by an individual, such as walking, standing, sitting, running, and other similar activities;

- *interactions* encompass not only activities involving interactions between two individuals, but they can also involve the relationship between a person and an object. Examples of interactions include playing a guitar or hugging another person;
- *group of activities* are the most intricate category as they primarily involve a combination of gestures, actions, and interactions. Examples of group activities include group meetings or group walking, where multiple individuals engage in coordinated actions and interactions.

Detailed framework of the HAR process will be discussed in the upcoming section. Finally, the aim of this work is to provide an overview of recent literature of AAL systems focusing on HAR from a technological perspective, tackling emerging evidences, challenges and future directions (Stavropoulos et al., 2020).

Papers have been revised by searching published works in the last 10 years in the following databases: IEEE Xplore, PubMed, Scopus. A series of keywords have been used, alone or in combination: ambient assisted living, ambient assisted living technology, healthy ageing, human activity recognition, ambient sensors, wearable sensors, wearable technology, activity monitoring, machine learning, deep learning, frail person.

The rest of the paper is organized as follows: Section 2 describes the Monitoring Solutions, focusing on the main components of an AAL system and detailing wearable and non-wearable sensors. Section 3 presents the processing chain, outlining the most relevant methodologies for data acquisition, processing and analysis. Section 4 proposes a critical discussion that also addresses future directions of this research field.

2. Monitoring solutions

Monitoring solutions in AAL systems can be developed using a variety of technologies, depending on the specific application domains and requirements. Specifically, in the field of HAR different solutions can be employed (Cicirelli et al., 2021; Ranieri et al., 2021). The upcoming session will provide a detailed description of wearable and non-wearable sensor solutions for HAR within the context of AAL in indoor environments.

2.1. Wearable sensors

Wearable devices typically consist of small sensors that can be integrated into cloths, rings, shirts, watches or other garments and devices. Such sensors gather body and context information to be locally processed or directly transmitted, mainly wirelessly through appropriate communication protocols, to a central processing unit of an AAL system (Kumari et al., 2017).

In the last few years, most wearable devices have been miniaturized and have optimized their power consumption (Cicirelli et al., 2021). Wearable devices, especially fitness trackers, wristbands and smartwatches (Andò et al., 2016; Lutze, 2018; Xie et al., 2020), have various built-in/integrated sensors such as accelerometers, gyroscopes and orientation sensors. Smartphones represent an additional solution for their characteristics of cost effectiveness and high number of embedded sensors (Ramanujam et al., 2021). Moreover, smartphones' embedded sensors can be used alone or in combination with other wearable technology to evaluate posture and activities and to prevent falls, together with biological and behavioral monitoring (Haghi et al., 2019; Badgujar and Pillai, 2020; Nouredanesh et al., 2020). In this review, since users take their smartphone with them almost everywhere, even though they are not always in direct contact with the body, they are considered wearable devices at the same level as wristwatches, rings, glasses and necklaces, as opposed to environmental sensors and cameras. Apps for recording the device's sensors data can be run on all commercial operating systems (Android or iOS) and they can be combined with commercial smartwatches, self-developed smart bands or devices like Shimmer nodes (Sanchez-Comas et al., 2020). However, not all applications provide an integration with smartphones; instead, many studies considered custom-developed solutions of electronic components. A significant number of works developed technologies in the laboratory, whereas fewer studies used commercial devices. Inertial sensors are the most common wearable elements used for HAR in AAL; in some cases, accelerometers (Tay et al., 2023), gyroscopes, magnetometers, temperature and object sensors may be applied, mainly worn on the waist or the hip (Pierleoni et al., 2019; Sarabia-Jácome et al., 2020).

Identification of the user's position can be obtained even with passive RFID sensors or Bluetooth Low Energy (BLE) technology, that paved the way to the Bluetooth Smart for wearable devices (Ciabattoni et al., 2019; Paolini et al., 2019; Bilbao-Jayo et al., 2021). Also, wearables usually commercialized for fitness purposes have been evaluated for elderly wellbeing in the AAL domain (Piwek et al., 2016; Seneviratne et al., 2017; Cedillo et al., 2018; Surendran et al., 2018; Stavropoulos et al., 2020).

The majority of HAR systems in AAL are dedicated to the identification and management of falls, as confirmed by literature (Dhiman and Vishwakarma, 2019). In such systems, wearables are one of the key elements due to their mobility, portability, cost and availability and several studies have been conducted, mostly using a single wearable device (Wang X. et al., 2020). Even in this context, inertial sensors represent a large percentage of the research, whereas only a minority deployed other solutions (Bourke et al., 2007). Although Shimmer nodes, smartphones and smart watches often contain sensors like magnetometers, such elements were not normally used to detect falls; indeed, the only sensors embedded in smartphones used for this purpose are accelerometers and gyroscopes (Shi et al., 2016; Islam et al., 2017; Medrano et al., 2017; Chen et al., 2018).

Even combining multiple sensors into a single framework can provide valuable data for meaningful and complex predictions, thus achieving a more versatile, robust and trustworthy wearable system for HAR purposes. Moreover, commercial tools are widely used, such as Samsung Galaxy Gear Live (Faye et al., 2017), Microsoft Band 2 (Garcia-Ceja et al., 2018) and Intel Basis Peak (Kang and Larkin, 2017), as well as other alternatives like Empatica E3 (Clapés et al., 2018), Fitbit (Kang and Larkin, 2017), and Google Glass (Shewell et al., 2017; Clapés et al., 2018).

It is worth noticing that most of the time, wearable technology alone would be sufficient to assess activity recognition in indoor environments and AAL systems. This is an important advantage, combined with their low cost, portability and unobtrusiveness. However, a hybrid approach combining wearable and non-wearable

sensors often overcomes possible drawbacks due to users not wearing the device correctly, thus leading to low quality signals, not being comfortable in putting on a wearable that could excessively stand out, forgetting to charge it or even to wear it continuously.

2.2. Non-wearable sensors

Non-wearable sensor solutions for HAR encompass devices or systems that can detect and analyze human activities without needing to be directly attached to the body. These solutions play a crucial role in the functionality and effectiveness of AAL systems. Operating in a passive manner, these sensors autonomously monitor room occupants without the need for manual intervention. This eliminates the need for users to carry additional devices during their daily activities.

One example of a non-wearable sensor solution is radio-frequency-based systems, as demonstrated by (Fan et al., 2020). These systems utilize the analysis of radiofrequency (RF) signal reflections to monitor various activities performed by individuals. In this study, Radio Frequency sensors were embedded directly in the floor to capture the everyday activities of residents (Fan et al., 2020). As part of radiofrequency-based systems, radar and ultra-broadband technologies, as well as automotive-derived solutions, also emerged as interesting approaches for human activity recognition (Guendel et al., 2021; Senigagliesi et al., 2022).

Furthermore, contemporary monitoring and behavior analysis tasks can be facilitated by diverse image-based technologies.

Nowadays, low-cost cameras have emerged as viable options for monitoring individuals' daily activities, ensuring their well-being (Geman and Costin, 2014; Cebanov et al., 2019; Minh Dang et al., 2020; Ryselis et al., 2020; Bouchabou et al., 2021; Chen et al., 2021; Raeis et al., 2021). These devices enable continuous monitoring of individuals without requiring their active involvement. These include RGB, Depth, and RGB-D cameras, as well as IR (infrared) array sensors, known as thermal cameras.

RGB cameras, being widely available and affordable, provide information about the shape, color, and texture of the scene (Zerrouki et al., 2018). However, they have some drawbacks such as a limited field of view, complex calibration procedures, sensitivity to environmental variations (e.g., lighting conditions, type of illumination and cluttered background) and privacy concerns. To address this latter issue, depth cameras offer distance information from the sensor to elements in the scene, capturing detailed spatial information while maintaining heightened privacy protection (Jayaraj et al., 2019; Beddiar et al., 2020). Depth sensors also exhibit superior resilience to variations in illumination, color, and texture compared to RGB devices. However, noisy measurements can occasionally affect accurate object or subject identification, necessitating data processing and refinement. In recent years, low-cost devices integrating RGB and depth sensors, such as Kinect and Intel RealSense systems, have been employed as environmental sensors in AAL systems. Another alternative, IR array cameras, measure thermal energy emitted by the human body or other objects (Mashiyama et al., 2015; Spasova et al., 2016; Karayaneva et al., 2023). These low-resolution IR arrays offer advantages such as privacy preservation, low power consumption, insensitivity to ambient lighting variations, operation in complete darkness, fast response time, easy deployment, and straightforward image processing.

All these devices suffer from subject occlusion, which occurs when certain body parts of the subject are hidden or obscured by other objects or body parts within the room, leading to incomplete or inaccurate tracking of the subject's movements. To overcome the occlusion limitation, a practical solution is to employ a multiple camera setup that covers various areas of the room from different viewpoints. By using multiple cameras, the chances of occlusion can be reduced, as different cameras capture different perspectives of the scene. This approach allows for a more comprehensive view of the subject's activities and improves the accuracy of tracking. However, it is important to note that using multiple cameras increases HAR systems' costs and requires synchronization among them to ensure proper coordination and alignment of the captured data. Synchronizing the cameras enables the seamless integration of the captured images or depth data, allowing for a more complete understanding of the subject's movements and activities.

In the context of monitoring human activities, sensors can be also embedded in everyday objects within the environment. Contrary to wearable sensors, which directly measure human activities, these sensors enable the detection of movements and activities through the usage of specific objects, providing valuable insights into the daily lives of individuals (Bassoli et al., 2017; Rafferty et al., 2017). For instance, sensors can be integrated into furniture items such as carpets, beds, fridges, and more, allowing for unobtrusive monitoring of daily living activities. Presence statistics of users in different spaces can be gathered by monitoring the sensors embedded in furniture. Power meters can be employed to track appliance usage (Bianchi et al., 2019), such as monitoring TV sets, while smart pill box devices assist in checking medication intake (Keum et al., 2019). Roland et al. proposed the installation of an accelerometer attached to a smart drinking cup to efficiently identify the user's drinking movement (Roland et al., 2018). Bassoli et al. installed sensors directly on the furniture of the subject's house for HAR. Pressure pads are used to monitor bed or chair occupancy, while sensors inside the fridge provide indirect information about feeding habits (Marenzi et al., 2012, 2013a,b; Bassoli et al., 2017). Chaccour et al. developed a smart carpet with piezoresistive pressure sensors to detect falls of the inhabitant (Chaccour et al., 2015; Singh et al., 2020).

Everyday object sensors offer a less invasive and privacy-friendly alternative to cameras, as they are designed to specifically recognize human activities related to the intended use of the object. By focusing on that, these sensors can provide valuable insights and functionality while minimizing potential privacy concerns. Everyday object sensors can detect interactions with household appliances or devices, such as opening a refrigerator, without capturing or storing detailed visual information of individuals. Yue et al. proposed an RF-based system that accurately monitors sleep postures overnight in the user's own house. By analyzing RF reflections and distinguishing them from other signals, the system can identify different sleeping postures such as supine, left side, right side, and prone (Yue et al., 2020). This approach can help alleviate privacy concerns while still enabling the development of innovative and convenient technologies that enhance user experiences in a responsible and respectful manner.

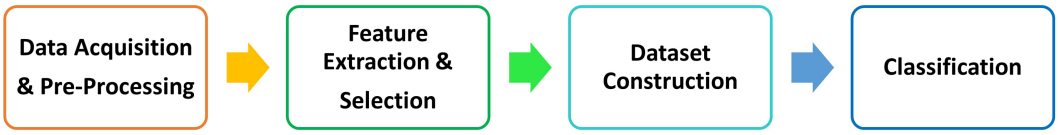

FIGURE 2
Processing chain illustrating the general steps of HAR.

3. HAR processing chain

Irrespective of the specific type of human activity being classified, the process of HAR typically adheres to a standard framework comprising several distinct phases. These phases are summarized in each block of Figure 2 and detailed in the following paragraphs, keeping the same names and order as in the Figure 2.

3.1. Data acquisition and pre-processing

Sensors and devices are characterized by outputs that are either punctual values (i.e., pixels in an image) or temporal series (i.e., position, acceleration). HAR applications could rely on raw data or need further pre-processing steps to enhance the signal quality (i.e., noise reduction, data normalization, segmentation) and/or to obtain derived data. For instance, from data captured by RGB-D cameras it is possible to estimate the position over time of specific points on the human body, often corresponding to anatomical points of repère or joints with respect to a specific coordinate system typically intrinsic to the device. This data processing stage is called skeleton tracking. Moreover, joint angles can be obtained starting from body joint positions (Jegham et al., 2020). Notably, in the context of AAL, it is common practice to store and analyze the skeleton tracking data instead of RGB or depth data to prioritize privacy preservation (Gasparrini et al., 2014; Tu et al., 2018; Li and Sun, 2021; Srimath et al., 2021). The pre-processing stage aims at noise reduction, data normalization and segmentation.

3.1.1. Noise reduction

Raw, noisy signals adversely affect signal segmentation and possible further computing steps (Deep et al., 2020). Noise can be removed in several ways: linear, averaging low-pass and high-pass filters (Amin et al., 2016). In some specific situations (e.g., inertial data and skeletal data), Kalman filters, moving average or adaptive filters are useful to correct distorted signals (Jeong et al., 2017; Beddiar et al., 2020; Ahad, 2021). The choice of an appropriate filter is critical, since it affects the quality of the filtered signals and of the successive steps of the processing chain. The Signal-to-Noise Ratio (SNR) is a crucial parameter in the identification of the most appropriate filter, together with the correlation coefficient (R) between the filtered and the reference signals, the cut-off frequency, the waveform delay, the filter size and the window length. The choice of the most suitable filter has to be a compromise among all these parameters. The components of the target signal that fall within the stop band of the filter are lost. At the same time filtering a signal introduces a delay (waveform delay), i.e., the output signal is shifted in time with respect to the input. This factor plays a critical role, especially when the responsiveness of the application is mandatory. The filtering of the signal at the same time as its acquisition is important in order not to accumulate delay between the filtered and raw signal. In other words, if the complete processing chain is designed to identify a potentially dangerous situation, the time shift should be compatible with this task, to ensure a prompt detection. Finally, a filter operates by allowing a specific range of frequencies to pass through. For instance, since frequency range of human activity is usually about 0–20 Hz (Antonsson and Mann, 1985; Grossman et al., 1988), the cut-off frequency is usually equal to at least twice such value (Castro et al., 2016; Wang et al., 2017; Ma et al., 2018; Minh Dang et al., 2020).

3.1.2. Data normalization

Data normalization is characterized by scaling or transforming the acquired data. This step is often necessary in HAR scenarios where data originated from different types of sensors and/or from people with various anthropometric characteristics. According to the type of data (e.g., RGB or depth, temporal or skeleton data) several normalization methods can be implemented (Pires et al., 2020; Ahad, 2021). Common normalization methods are min-max, mean, standardization and scaling to unit length. The first method scales the data in their maximum and minimum range: the minimum value is subtracted from each data point and the result is divided by the data range. In the second one the mean of all data samples is subtracted from the data vector, and the result is divided by the difference between the maximum and minimum samples. In the standardization method, the mean value of all data samples is subtracted from the data vector, and the result is divided by the standard deviation value. Finally, the last normalization technique scales all the data with respect to the sum of all elements of the data vector (Patro and Sahu, 2015; Mistry and Inden, 2018; Narkhede, 2019; Ahad, 2021).

When considering skeletal tracking data instead, there are also two other types of normalization methods. The first one is the Bounding-box normalization (referring to the border's coordinates that enclose the subject), in which all skeleton 3D joints coordinates are normalized using the maximum side-length of the bounding box of the skeleton (Cippitelli et al., 2016; Liu et al., 2020). In the second method data are normalized by dividing the 3D coordinates of the skeleton with respect to the length of a specific body segment (i.e., head, neck, torso and so on) or by the subject height. For example (Cippitelli et al., 2016), scaled joint position dividing each value by the Euclidean distance between the neck and torso joints.

3.1.3. Data segmentation

Data segmentation is strongly related to the type of data. When dealing with temporal sequences, it consists of partitioning the data into time windows. Otherwise, when RGB or depth images are analyzed, the segmentation involves the separation of the selected

target subject in the scene from the background. The data subdivision in time windows is principally done to overcome the limitations due to the difference between the duration of the action and the sampling rate imposed by the data acquisition device (Minh Dang et al., 2020; Ahad, 2021). The data segmentation can be categorized into Fixed size Non-overlapping Sliding Window (FNSW), Fixed-size Overlapping Sliding Window (FOSW) or Event-Driven Sliding Window (EDSW) (Bulling et al., 2014; Ahad, 2021). In FNSW and FOSW segmentations, the number of samples included in each window is fixed. The difference is that in FOSW consecutive analysis blocks of the time data are overlapped by the designated percentage of the time record, while in FNSW there is no overlapping. Concerning EDSW, it differs from the others since the number of samples included in the time window is not fixed (i.e., it features a variable window size) (Devanne et al., 2019). Generally, the window size has to always be carefully established to comprehend an adequate number of samples, at the same time avoiding prolonged execution times. When the HAR process is part of a system aiming at monitoring a person in the AAL environment, in which the promptness of the recognition is mandatory, smaller window segmentation is suitable (Buzzelli et al., 2020). It also reduces the complexity and the computational time of the HAR process. The overlapping technique can handle the transition between human activities more accurately, i.e., the transitions between sitting and standing postures, or between walking and running (Torti et al., 2019; Buzzelli et al., 2020; Khan and Ghani, 2021; Guerra et al., 2022, 2023). In case of RGB image, or depth image, the segmentation process is implemented using two different approaches: namely, the background subtraction and the foreground extraction. The first one consists in the extraction of the body silhouette in an image sequence captured from a static camera by comparing each incoming frame with a background model. A crucial step of this technique is to obtain a stable and accurate background model. The second one is recommended when the images are acquired by a moving camera, and it consists in the computation of the difference between consecutive image frames. The foreground extraction is more challenging than the background subtraction because, in addition to the motion of the target object, it also needs to consider the motion of the camera and the change of background (Ke et al., 2013; Babaee et al., 2018; Minh Dang et al., 2020; Mliki et al., 2020).

3.2. Feature extraction and selection

The feature extraction procedure consists in the definition of a set of parameters able to discriminate the activities to be classified. Based on the given data nature and characteristics, the features can be divided into several categories: time-domain, frequency-domain and kinematic features (Dhiman and Vishwakarma, 2019; Sousa Lima et al., 2019; Ahad, 2020, 2021). The time-domain features are usually defined to describe the data amplitude variation and distribution over time (for instance mean, variance and kurtosis). On the other hand, the frequency-domain features show the distribution of signal energy (i.e., Fast Fourier Transform, entropy and power spectral density). Kinematic features include all the characteristics of the subject's movements, acceleration and posture (joints positions and angles). The kinematic features describe geometric relations between body joints (Müller et al., 2005; Guerra et al., 2020).

In the case of images, usually global and local features are computed. The first ones describe the image frames as a whole, providing different types of information (spatial, temporal, frequency) (Ke et al., 2013). Local features extract information around a set of interest points or describe a selected image region, through techniques like histograms of oriented gradients (Aly and Sayed, 2019).

After feature extraction, the relevant ones are selected to achieve dimensionality reduction by finding the smallest subset of features which efficiently defines the data for the given problem (Blum and Langley, 1997; Chandrashekar and Sahin, 2014; Jindal and Kumar, 2017; Ayesha et al., 2020). It can be accomplished using different methods, such as filter, wrapper, embedded, and the more recent hybrid approach (Blum and Langley, 1997; Minh Dang et al., 2020; Zebari et al., 2020). Filter methods measure the relevance of features using statistical standards for evaluating a subset, they process data before the classification occurs and are independent from the latter. The features are ordered according to the ranking of importance (computed with suitable score metrics) and those below a certain threshold are removed. Among the different algorithms, the most used are: ReliefF, statistical techniques such as Principal Component Analysis, Independent Component Analysis, Neighborhood Component Analysis and Correlation Based filter (Suto et al., 2016; Alzahrani et al., 2019; Siddiqi and Alsirhani, 2022). Wrapper method selects the optimal features subset evaluating alternative sets by running the classification algorithm on the training data. It employs the classifier estimated accuracy as its metric (Bhavan and Aggarwal, 2018; Zebari et al., 2020). The most used iterative algorithms are the Recursive Feature Elimination with Support Vector Machine, the Sequential Feature Selection algorithm and the Genetic Algorithm (Liu and Shao, 2013; Guerra et al., 2022). Compared to the filter method, the wrapper method achieves better performance and higher accuracy, nevertheless it increases computing complexity due to the need to recall the learning process for each feature set considered (Jindal and Kumar, 2017; Zebari et al., 2020). In the embedded method, as the name suggests, the selection occurs within the learning algorithm. The most common are the tree-based algorithms like, for example, the Random Forest and the Decision Tree. Embedded methods can be used in multiclass and regression problems and compared to a wrapper method, it is computationally more effective while retaining similar performance (Negin et al., 2013). Finally, the hybrid approach combines filter and wrapper methods to achieve the benefits of both. Usually, the filter technique is first applied to reduce the search space and then, a wrapper model is used to acquire the best subset (Peng et al., 2010).

3.3. Dataset construction

Dataset construction concerns the process that divides the acquired data into training, validation and test sets. Generally, a set of data is required to train the classification model and a set of validation data is used to evaluate the performance of the model during training epochs for fine tuning the hyperparameters and to estimate if the model does not overfit, i.e., when a statistical model fits exactly against its training data at the expenses of its generalization abilities. Finally, test data, different from those involved in the training set, are used to evaluate the performance of the model (Bouchabou et al., 2021). The data contained in the training, validation and test could be described

by labels also called classes. As will be stressed in the next Section, this operation is of crucial importance for the classification algorithms. In HAR tasks, the classes represent the type of activity to be recognized (i.e., walking, sitting, lying down, and so on) (Sathya and Abraham, 2013; Sindhu Meena and Suriya, 2020).

In HAR, three methods have been used to divide the data into training, validation and test set. In the first one, called cross-subject, the subjects are divided into two groups. The data of the first group are used for the training phase, whereas those of the second one are involved in the validation and test phase (Khan and Ghani, 2021). The cross-subject method aims at guiding the learning process of the AI model so that it becomes as robust as possible, in order to adapt it to the heterogeneity of the subjects. The second splitting method is characterized by randomly dividing the whole dataset based on a percentage such as 70-30%, 80-20%, and so on. The larger portion is fed for training the model where the other portion is kept for validation and test (Ahad, 2021). This is the most used splitting criteria in the general problems of classification algorithms and have been reported in HAR with success. Alternatively, when data are acquired by multiple cameras with different points of view, a cross-view method can be used. In this case the data coming from one or more cameras are used for the training phase and those of the remaining ones for the validation and test phase (Wang L. et al., 2020).

3.4. Classification

The most critical step of HAR systems relies on classification algorithms. In the literature, two main categories can be identified, namely threshold-based and AI methods. Furthermore, AI algorithms can be divided into ML and DL techniques. In the following, these methods are analyzed, highlighting the main advantages and issues in their application for HAR data analysis.

3.4.1. Threshold-based methods

Threshold-based methods are the first introduced in the literature and they typically do not need feature extraction and selection. They are based on comparing the acquired values with a pre-defined threshold (Fetzer et al., 2018). If a signal value exceeds the threshold, then the algorithm identifies the targeted situation. More advanced threshold-based algorithms adopt adaptive thresholds (Madhu et al., 2021) or apply it on statistical indicators extracted from the original signals (Cola et al., 2017). Moreover, data fusion is employed when considering multiple sensors. A particular strategy uses only one of them to make a final decision: this is called partial fusion. An example is a fall detection system that employs a tri-axial accelerometer and an RGB-D camera: only when the measured signal exceeds a threshold, the camera is activated to capture the ongoing event (Kwolek and Kepski, 2014). One of the most important advantages of threshold-based algorithms is the low computational complexity. This allows the deployment of these algorithms directly on a small computation unit which typically also manages the data acquisition and pre-processing. Indeed, this solution is widely adopted for wearable devices which do not rely on external centralized processing (Jung et al., 2015; Cola et al., 2017). Concerning non-wearables, the preferred strategy is to send all the acquired data to a central host, which applies the threshold-based algorithm (Andò et al., 2016). The major drawback of these methods is the threshold selection since it depends on the monitored subject. Indeed, inter-subject movements show high variability and even the same person can perform a certain movement in different ways (intra-subject variability) depending on a multitude of factors, such as injuries or illness (Jegham et al., 2020). This affects the classification performance.

3.4.2. Machine learning methods

In the last decade, ML methods have been widely explored for HAR since they can automatically extract high level features and produce more affordable results than threshold-based approaches. In particular, the best results have been achieved by Support Vector Machines (SVMs), Artificial Neural Networks (ANNs), K-Nearest-Neighbours (KNN) and Complex Trees (Oniga and Suto, 2014; Hemmatpour et al., 2017; Su et al., 2017). SVMs and KNN rely on the concept of instances. First, they create sets of example data, in which each set is related to a specific class. Then the distances between the new data and the example data sets are computed. The aim is to find the example set with the minimum distance from the new data. Finally, the class of the minimum distance set is given to the new data. ANNs are based on the structure of biological neural networks. They are composed of elementary computational units, which perform a weighted sum of the inputs and apply a nonlinear function. These are organized into layers as Multi-Layer Perceptrons (MLP) and are used to map input data into output classes. Finally, Complex Trees build a decision-making diagram with a tree structure. The tree structure is based on the attribute values of the input data. The classification is obtained following the tree structure until a leaf is reached. Later, single algorithms have been combined in the so-called ensemble learning with different strategies such as boosting, stacking, bagging and majority voting to enhance the classification quality (Hasan et al., 2022).

These algorithms have been used both for data acquired by wearable and non-wearables devices. In both cases, the data are acquired and sent to a central unit for the classification step (Sheikh and Jilani, 2023). Therefore, the main drawback is related to data transmission since the communication rate should be high enough to guarantee continuous monitoring. Moreover, this represents a critical issue for wearable devices since wireless communication is the main power consuming process.

Concerning classification performance, it is affected by the quality of the dataset. AI methods need to be trained on significant examples, which should be balanced among the different classes conceived in the target application. It is worth noticing that an unbalanced training set negatively affects the model performance. A recent trend is to exploit data augmentation strategies to create synthetic data both to increase the training set size and to balance it (Um et al., 2017; Mathur et al., 2018; Steven Eyobu and Han, 2018). The main drawback is related to the choice of the augmentation techniques, since synthetic data can differ too much from the real ones.

3.4.3. Deep learning methods

DL emerged in recent years as the most powerful AI tool to automatically extract high level features and perform affordable classifications. The development of DL models has been enabled by the computing power offered by the technological evolution of devices such as multi-core processors and graphic processing units. Among the different DL methods used in HAR Convolutional

Neural Networks (CNNs), Long Short-Term Memory (LSTM) cells and Gated Recurrent Units (GRUs) (Torti et al., 2019; Ronald et al., 2021; Poulose et al., 2022; Guerra et al., 2023; Sonawani and Patil, 2023) emerged as suitable solutions. CNNs are mostly used to deal with visual data, since they roughly imitate human vision. The data is processed as a grid-like topology through the convolutional operator. They can be used both for images and for time series. On the other hand, LSTM and GRUs are mainly used for time series analysis. In fact, their main feature is to learn time dependencies.

These methods have been initially used for data coming from non-wearable devices, especially when vision-based sensors were employed. However, they are gaining popularity also for wearable devices (Torti et al., 2019; Goh et al., 2021; Luwe et al., 2022).

3.5. Computing power constraints

An important aspect related to HAR for frail people is the time needed by the AAL system to detect possible dangerous situations. This time is strictly related to the computational complexity of the adopted algorithms and to the computing power of the devices which perform the processing chain.

Threshold-based methods are the lowest computing power demanding techniques, since they are based on simple comparisons with a fixed value. Even in the case of threshold computed at runtime and/or applied to statistical indicators, the computational complexity can be easily managed by standard microcontrollers and does not have a critical impact on processing times.

AI methods are characterized by a higher computational complexity than threshold-based techniques. In particular, DL methods feature the highest computational complexity, not only for their training, which is run off-line and may require multiple CPU and/or GPU, but also for their implementation as a classifier once all the weights are determined. Therefore, their processing is typically performed by a centralized unit for both wearable and non-wearable devices. However, recently some researchers have designed DL algorithms on low power devices suitable for wearable applications.

Recent and very complex solutions exploited ensemble learning also with DL algorithms (Kumar and Suresh, 2023) enhancing the classification performance of single techniques.

The increasing popularity of AI solutions has led to the development of various software tools, libraries, and frameworks that facilitate the implementation of these algorithms on devices with limited resources. An example of such a tool is TensorFlow Lite for microcontroller[3] (TFLM), an open-source library designed to enable the implementation of AI methods (i.e., ANNs, LSTM, CNN and so on) on a wide variety of MCUs and Digital Signal Processors (DSPs). TFLM allows the execution of pre-trained algorithms developed using TensorFlow for on-device inference. Another prominent solution is X-Cube-AI, a software tool developed by STMicroelectronics.[4] It offers a comprehensive environment for generating and optimizing AI algorithms developed using popular ML and AI frameworks such as TensorFlow,[5] Keras,[6] or PyTorch.[7] X-Cube-AI is tailored for deployment on the STM32 family of MCUs, empowering developers to leverage familiar frameworks and simplify the integration of AI capabilities into their applications. In addition to these tools, there are cloud-based platforms like Edge Impulse, which provides a flexible environment for the development of AI models. Edge Impulse[8] supports various embedded platforms, including MCUs and smartphones, enabling developers to create AI models that cater to diverse hardware constraints. NanoEdge AI Studio[9] is another valuable tool that supports both learning and inference directly inside the MCUs. Notably, it offers the advantage of automatically selecting the most suitable machine learning libraries based on the provided data (Shumba et al., 2022).

Inference needs to be performed under real-time constraint, especially when a potentially dangerous condition needs to be identified. This means that the classification should be strictly performed prior to a fixed temporal deadline, which is defined by the acquisition time window. In other words, the system acquires a window of data and its pre-processing and classification should be performed before the end of acquisition of the following time window. The computational complexity of the algorithms and the computing units included in the system play a critical role in the real-time compliance (Avram and Pop, 2023; de la Cal et al., 2023; Gonçalves et al., 2023; Saliba et al., 2023; Zeng et al., 2023). Delayed or sluggish processing can hinder the effectiveness of AAL systems in providing timely assistance, which is crucial for ensuring the safety and well-being of individuals. Efficient algorithms and optimized implementations are necessary to overcome these constraints and enable real-time processing on resource-limited platforms. The computational unit controls the sampling and acquisition of data: usually this is performed by Commercial-Off-The-Shelf (COTS) low power and low cost microcontrollers, supporting interfaces and data transfer protocols (SPI, I2C…). When high speed, flexibility and control over the elements of the architecture are required, Field Programmable Gate Arrays (FPGAs) and Application-Specific Integrated Circuits (ASICs) can be used, with increased costs and higher time for development and/or production. The computational unit is equipped with initial signal conditioning and processing algorithms together with specific classification methods that perform data analysis for local decision making, real-time response and forwarding processed data to successive layers. Characteristics that can influence all these choices include power consumption, computational and storage capacity, complexity and results accuracy of the algorithms, privacy concerns and latency requirements. Pre-trained models using computationally efficient algorithms may be used for anomaly detection and the results can produce warnings or propose a course of action. Alternatively, a fraction of an ANN can perform partial on-device data processing, to forward only intermediate data, thus ensuring also the privacy of the user (Zhang et al., 2023). Lastly, after the elaboration and analysis of data, results,

3 https://www.tensorflow.org/lite/microcontrollers
4 https://www.st.com/content/st_com/en.html
5 https://www.tensorflow.org
6 https://keras.io
7 https://pytorch.org
8 https://www.edgeimpulse.com
9 https://www.st.com/en/development-tools/nanoedgeaistudio.html

inferences, or alarms are packaged and forwarded to the upper layers for further processing or management (Shumba et al., 2022).

4. Discussion

This review aims at providing an overview on the application of HAR process in the context of AAL systems, underlining their potential to support independent living for frail individuals.

Recent advances in AAL technologies and the reduced cost of sensors have encouraged the development of technological environments to enable frail people to live healthier and more independent lives and to support caregivers, medical personnel, thus limiting hospitalization, promoting personalized therapy and enhancing wellbeing. To provide such services, an AAL system has to be able to understand the daily activities of its residents. In general, the choice of technologies used for HAR purposes can include wearable sensors (IMUs, smartwatches, smartphones…), non-wearable sensors (environmental devices, objects, and cameras), or a combination of the two (hybrid approach). The sensor selection can be made especially depending on the individual's needs. Wearable sensors have numerous advantages, including their small size, low power consumption, direct acquisition of information on the subject's activity and full respect of the subject's privacy. At the same time, they also have some drawbacks. For example, they need to be worn by the subjects and to operate for long time periods. The latter could represent a significant problem for the monitored subject and for the battery life of the devices. Also, to fully capture the 3D motion associated with a human action, a single sensor may not be adequate. It may be necessary to utilize multiple configurations, thus increasing the intrusiveness of the devices worn by the subject (Wang Y. et al., 2019; Beddiar et al., 2020; Qiu et al., 2022). On the other hand, environmental and camera sensors offer the key advantage of being unobtrusive, as they do not require the individual to wear them. However, they also face certain challenges. One major issue is their reliance on infrastructure, which can limit their effectiveness in identifying specific movements or activities. Additionally, the utilization of environmental sensors is less frequent compared to wearable sensors due to higher costs and setup difficulties. Furthermore, similar to the wearable approach, this solution may not always be feasible as it requires users to interact with tagged objects or to remain within the environment where the sensors are installed. In particular, cameras suffer from drawbacks like occlusion, multiple-view variations and privacy issues (Minh Dang et al., 2020). A possible solution to handle occlusion relies on a multiple camera setup, even though these devices need to be synchronized among each other. Cameras are often perceived as the most intrusive technologies in terms of the privacy of the monitored individuals. The solution to this drawback may be RGB-D cameras, like the Kinect V2, which, through a data elaboration, are able to extract the "skeleton" of the subject from the depth image, i.e., the subject is represented as a set of body segments and joints, bypassing the need for using the RGB image for HAR purposes. These tools increase the person's acceptance towards the assistive technology, since they ensure privacy preservation (Gasparrini et al., 2014). Among non-wearable devices, object sensors are the least invasive and the most respectful of users' privacy, as they focus on recognizing human activities related only to the intended use of the object. For example, a smart cup recognizes drinking actions, and sensors embedded in cushions or beds identify specific sleeping postures.

To overcome the wearable and non-wearable limits a possible solution could be represented by a hybrid approach. Sensor fusion provides a more robust approach since multiple sensors may complement each other with their specific signals, producing a reliable system (Wang X. et al., 2020). Moreover, the likelihood of having missing data is progressively balanced out by increasing the number of sensors in the system. However, critical issues in AAL services stem from the integration of multiple technological types, mainly environmental and wearable sensors (Calvaresi et al., 2017). For instance, hybrid systems are characterized by sensors with different sampling frequencies. Thus, synchronization and interpolation of acquired data is mandatory for better correlation of output devices. Furthermore, some challenges can still be present; for example, security and privacy requirements need to be taken into consideration.

Independently from the adopted monitored system, HAR requires affordable processing chains to classify the target human activities. Typically, HAR should be performed meeting the real-time constraint, especially when frail people are monitored. While threshold algorithms are efficient for real-time processing, they may struggle with handling complex activities or adapting to dynamic contexts. These limits are overcome by AI methods, at the price of an increased computational complexity, which negatively impacts on classification time. For this reason, the optimal solution requires a suitable trade-off between classification quality and processing time to ensure real-time compliance. Common factors that determine real-time compliancy of a method are the computational complexity and the processing power of the system. It must be stressed that the computational complexity alone is not sufficient to determine if a method is real-time compliant. Indeed, the response time strictly depends on the processing power of the device. It is not trivial that very different processing units perform the same computation with significantly different times. Therefore, the choice of a suitable processing element covers a critical role in the real-time compliancy of a system. Moreover, datasets derived from real situations are not always available or sufficiently precise; in some cases, only simulated conditions are present, but this greatly compromises the results (Casilari and Silva, 2022). At the same time, prompt detection of dangerous conditions cannot be provided in some contexts.

Table 1 summarizes the type of activity, sensors, input data, datasets, main approaches and potential applicability in a real-life scenario, considered in the most relevant works in the field of Human Activity Recognition, already cited in the previous sections. It categorizes the papers into three main classes on the basis of their adopted technologies: wearable, hybrid and non-wearable solutions. In each row, among the labelled information previously reported, the type of activity is related to the target application of each proposed HAR system. Indeed, most of the works aim at recognizing falls and/or Activities of Daily Living (ADL), i.e., lying down, walking, sitting and so on. The input data type is labelled "Dynamic" in case of time series or "Static" otherwise. Concerning the datasets, publicly available ones present the corresponding reference paper, whereas custom Datasets report the number of involved subjects

10.3389/fnins.2023.1256682

TABLE 1 Summary of the analyzed literature.

Authors and year	Activity	Type of sensor	Input data type	Dataset	Approach	Real life scenario
Wearable solutions						
Andò et al. (2016)	ADL and Fall Detection	Tri-axial nano-accelerometer and gyroscope embedded in a smartphone	Static	Custom (10 healthy subjects; 6 activities)	Threshold-based Data Fusion	NO
Xie et al. (2020)	ADL and Fall Detection	Smart watch	Static	Custom (5 subjects; 9 activities)	Threshold-based SVM	NO
Badgujar and Pillai (2020)	Fall Detection	Tri-axial accelerometer	Static	SisFall (Sucerquia et al., 2017)	SVM and Decision Tree	NO
Nouredanesh et al. (2020)	Compensatory Balance Reactions (CBRs) for Fall Detection	IMU	Static	IMUFD (Aziz et al., 2017) and Custom (9 healthy subjects; 9 activities)	Random Forest	NO
Pierleoni et al. (2019)	Postural stability	IMU: tri-axial accelerometer, tri-axial gyroscope and tri-axial magnetometer	Static	Custom (6 healthy subjects; 3 activities)	Filter-based Data Fusion	NO
Sarabia-Jácome et al. (2020)	Fall Detection	Tri-axial accelerometer	Dynamic	SisFall (Sucerquia et al., 2017)	LSTM and GRU	NO
Bourke et al. (2007)	ADL and Fall Detection	Tri-axial accelerometer	Dynamic	Custom (a.10 healthy subjects; 8 activities b.10 elderly subjects; 8 activities)	Threshold	YES
Chen et al. (2018)	Fall Detection	Tri-axial accelerometer embedded in a smartphone	Static	Custom (10 healthy subjects; 13 activities)	SVM	NO
Islam et al. (2017)	Fall Detection	Tri-axial accelerometer embedded in a smartphone	Dynamic	Custom (7 healthy subjects; 4 activities)	Threshold	NO
Medrano et al. (2017)	ADL and Fall Detection	Tri-axial accelerometer embedded in a smartphone	Static	tFall (Medrano et al., 2014)	Threshold	NO
Garcia-Ceja et al. (2018)	ADL and Fall Detection	Sound and accelerometer data embedded in a smartphone and a wrist-band	Static	Custom (3 healthy subjects; 7 activities) Berkeley MHAD (Ofli et al., 2013), UTD-MHAD (Chen et al., 2015) and Opportunity (Roggen et al., 2010)	Random Forest	YES
Torti et al. (2019)	Fall Detection	Tri-axial accelerometer	Dynamic	SisFall (Sucerquia et al., 2017)	LSTM	NO
Cola et al. (2017)	Fall Detection	Barometer	Dynamic	Custom (6 subjects; 9 activities)	Threshold	NO
Jung et al. (2015)	ADL and Fall Detection	Tri-axial accelerometer	Dynamic	Custom (N. A. subjects; 5 activities)	Threshold	NO
Hemmatpour et al. (2017)	ADL	Tri-axial accelerometer embedded in a smart-watch	Static	Custom (22 subjects; 2 activities)	Multilayer Perceptron	NO
Sheikh and Jilani (2023)	Fall Detection	Tri-axial accelerometer and gyroscope	Static	SisFall (Sucerquia et al., 2017)	SVM	NO
Goh et al. (2021)	ADL	Tri-axial accelerometer and gyroscope	Dynamic	MotionSense (Malekzadeh et al., 2018), UCI-HAR (Garcia-Gonzalez et al., 2020) and USC-HAD (Zhang and Sawchuk, 2012)	1D-CNN and LSTM	YES

(Continued)

TABLE 1 (Continued)

Authors and year	Activity	Type of sensor	Input data type	Dataset	Approach	Real life scenario
Luwe et al. (2022)	ADL	Tri-axial accelerometer and gyroscope	Dynamic	MotionSense (Malekzadeh et al., 2018), UCI-HAR (Garcia-Gonzalez et al., 2020) and custom	1D-CNN and LSTM	YES
Kumar and Suresh (2023)	ADL	IMU: tri-axial accelerometer, tri-axial gyroscope and tri-axial magnetometer	Dynamic	WISDM (Kwapisz et al., 2011), PAMAP2 (Reiss and Stricker, 2012) and KU-HAR (Sikder and Nahid, 2021)	CNN and RNN	YES
de la Cal et al. (2023)	ADL and Fall Detection	Tri-axial accelerometer embedded in a wrist-band	Static	UMAFall (Casilari et al., 2017), UCIFall (Özdemir and Barshan, 2014) and FallAllD (Saleh et al., 2021)	KNN and K-Means	NO
Warunsin and Phairoh (2022)	ADL and Fall Detection	Tri-axial accelerometer	Static	MobiAct (Vavoulas et al., 2016)	Multilayer Perceptron	NO
Hybrid solutions						
Clapés et al. (2018)	ADL	Two RGB-depth cameras, accelerometer, gyroscope, and magnetometer	Static	Custom (14 elderly subjects; 6 activities)	SVM	YES
Geman and Costin (2014)	ADL	RGB-depth camera and tri-axial accelerometer	Static	Custom (88 subjects; 3 activities)	Multilayer Perceptron	YES
Kwolek and Kepski (2014)	Fall Detection	RGB-depth camera and tri-axial accelerometer	Dynamic	URFD (Kwolek and Kepski, 2014)	Threshold	YES
Non-wearable Solutions						
Fan et al. (2020)	ADL	Radio-frequency sensors embedded in the floor and RGB camera	Dynamic	Custom (N. A. subjects; 157 activities)	Attention- based LSTM	YES
Chen et al. (2021)	ADL	WiFi sensor network	Dynamic	Custom (1 subject; 7 activities)	SVM and GRU	YES
Zerrouki et al. (2018)	ADL	RGB cameras	Dynamic	URFD (Kwolek and Kepski, 2014) and UMAFall (Casilari et al., 2017)	AdaBoost	YES
Karayaneva et al. (2023)	ADL	Low-resolution infrared camera	Static and Dynamic	Custom (6 subjects; 15 activities)	SVM, random forest, k-NN, logistic regression, and convolutional LSTM	YES
Mashiyama et al. (2015)	ADL and Fall Detection	Low resolution infrared array sensor	Static	Custom (N. A. subjects; 5 activities)	Threshold-based SVM	NO
Spasova et al. (2016)	Fall Detection	Low resolution infrared array sensor	Static	Custom (5 subjects; 2 activities)	SVM	NO
Roland et al. (2018)	Drinking	Tri-axial accelerometer embedded in a cup	Static	Custom (N. A. subjects; 1 activities)	Multilayer Perceptron	YES
Chaccour et al. (2015)	ADL and Fall Detection	Piezoresistive pressure sensors	Static	Custom (3 subjects; 6 activities)	Threshold	NO
Yue et al. (2020)	Sleeping postures	FMCW radio equipped with an antenna array	Static	Custom (26 subjects; 4 activities)	Multilayer Perceptron	YES
Li and Sun (2021)	ADL	RGB-depth cameras	Dynamic	Florence3D-Action (Seidenari et al., 2013), Toyota Smarthome (Das et al., 2019) and NTU RGB + D (Shahroudy et al., 2016)	CNN	YES
Srimath et al. (2021)	ADL	RGB-depth cameras	Dynamic	UTD-MHAD (Chen et al., 2015), KTH (Schuldt et al., 2004) and UCF-Sports (Rodriguez et al., 2008)	1D-CNN	YES

(Continued)

TABLE 1 (Continued)

Authors and year	Activity	Type of sensor	Input data type	Dataset	Approach	Real life scenario
Tu et al. (2018)	ADL	RGB-depth cameras	Dynamic	SmartHome (Liu et al., 2017) and NTU RGB + D (Shahroudy et al., 2016)	3D-CNN	YES
Ma et al. (2018)	Hand gestures	RGB-depth camera	Dynamic	Custom (14 subjects; 28 activities)	LSTM	YES
Cippitelli et al. (2016)	ADL	RGB-depth camera	Static	KARD (Gaglio et al., 2015), CAD-60 (Sung et al., 2012), UTKinect (Xia et al., 2012), Florence3D-Action (Seidenari et al., 2013) and MSR Action3D (Li et al., 2010)	SVM	YES
Liu et al. (2020)	Hand gestures	RGB-depth camera	Static	Custom (30 subjects; 15 activities) and MSRA hand gesture (Sun et al., 2015)	3D-CNN	YES
Devanne et al. (2019)	ADL	RGB-depth camera	Dynamic	Watch-n-Patch (Wu et al., 2015)	LSTM	YES
Guerra et al. (2023)	ADL	RGB-depth camera	Dynamic	Custom (12 subjects; 4 activities)	GRU	YES
Guerra et al. (2022)	ADL	RGB-depth camera	Dynamic	Custom (12 subjects; 5 activities)	LSTM	YES
Guerra et al. (2020)	ADL	RGB-depth camera	Static	Custom (12 subjects; 3 activities)	Multilayer Perceptron	YES
Madhu et al. (2021)	ADL	RGB-depth camera	Static	MSR Action3D (Li et al., 2010)	Threshold-based SVM	YES
Su et al. (2017)	ADL	RGB-depth camera	Static	MSR Action3D (Li et al., 2010)	SVM	YES
Gonçalves et al. (2023)	ADL	RGB-depth camera	Static	Custom (15 subjects; 3 activities)	CNN	NO
Siriwardhana et al. (2019)	ADL	RGB-depth camera	Dynamic	Custom (17 subjects; 24 activities)	CNN-LSTM	YES
Poulose et al. (2022)	ADL	RGB camera	Static	Custom (10 subjects; 9 activities)	CNN	NO

and the amount of performed activities (if one or more parameters are not available, the acronym N.A. is indicated). The "Real life scenario" column is related to the system applicability outside the laboratory setting. It is labelled with "YES," in case of data acquisitions performed in an environment which considered not only ideal conditions (i.e., the subject is always directly in front of the camera or the falls are simulated only by young people).

5. Conclusion

In conclusion, it is significant to look toward the future of AAL systems, giving importance to HAR indoors and outdoors. The outdoor environment offers numerous activities that can contribute to preventing functional decline in frail individuals. However, monitoring outdoor activities presents different challenges, as non-wearable sensors may not be suitable and safety risks are increased. Therefore, wearables become crucial in this context. While user acceptance can sometimes be a challenging requirement to meet, the ease of use and unobtrusiveness of wearables greatly overcome this drawback. Wearable sensors enable continuous monitoring of indoor and outdoor activities, allowing for a more comprehensive assessment of an individual's daily life. By incorporating wearable technology into AAL systems, it becomes possible to gather valuable data and insights to support preventive measures and promote healthy lifestyles among frail individuals.

As research and technological advancements continue, it is important to explore and optimize the use of wearable sensors in AAL systems, considering the specific constraints and requirements posed by outdoor monitoring. Future research trends in wearables design could be an enhanced miniaturization of the sensors used nowadays leading to better unobtrusiveness and the possibility of integrating these sensors inside even smaller devices or directly into clothes. An example is the fast development of Micro Electro-Mechanical Systems (MEMS) which enabled the optimization of several sensors-based applications. Moreover, power efficiency will represent a crucial issue, since it impacts both on communication and battery life. Improvements on battery technology should also be coupled with energy harvesting methods to partially recharge the device. On the other hand, the technological evolution of processors and microcontrollers could enable the adoption of state of the art classification methods, overcoming the actual limitations on the models size related to the available amount of memory and of computational power. Finally, communication technologies such as 6G could represent the ideal technology to transmit data between acquisition points and data collection centers. By doing so, the

effectiveness of these systems can be enhanced in supporting independent living, improving safety, and preventing functional decline in the target population.

Author contributions

BG: Conceptualization, Investigation, Writing - original draft. ET: Conceptualization, Investigation, Writing – original draft. EM: Conceptualization, Investigation, Writing – original draft. MS: Writing – review & editing. SR: Writing – review & editing. FL: Writing – review & editing. GD: Writing – review & editing.

Funding

The author(s) declare that no financial support was received for the research, authorship, and/or publication of this article.

Conflict of interest

The authors declare that the research was conducted in the absence of any commercial or financial relationships that could be construed as a potential conflict of interest.

The author(s) declared that they were an editorial board member of Frontiers, at the time of submission. This had no impact on the peer review process and the final decision.

Publisher's note

References

Aggarwal, J. K., and Ryoo, M. S. (2011). Human activity analysis. *ACM Comput. Surv.* 43, 1–43. doi: 10.1145/1922649.1922653

Ahad, M. A. R. (2020). "Vision and sensor-based human activity recognition: challenges ahead" in *Advancements in instrumentation and control in applied system applications* (Pennsylvania: IGI Global), 17–35.

Ahad, A. R. (2021). *IoT sensor-based activity recognition*. 173.

Al Machot, F., Mosa, A. H., Ali, M., and Kyamakya, K. (2018a). Activity recognition in sensor data streams for active and assisted living environments. *IEEE Trans. Circuits Syst. Video Technol.* 28, 2933–2945. doi: 10.1109/TCSVT.2017.2764868

Al Machot, F., Ranasinghe, S., Plattner, J., and Jnoub, N. (2018b). Human activity recognition based on real life scenarios. 2018 IEEE international conference on pervasive computing and communications workshops (PerCom Workshops), Athens, Greece 3–8.

Al-Shaqi, R., Mourshed, M., and Rezgui, Y. (2016). Progress in ambient assisted systems for independent living by the elderly. *Springerplus* 5:624. doi: 10.1186/s40064-016-2272-8

Aly, S., and Sayed, A. (2019). Human action recognition using bag of global and local Zernike moment features. *Multimed. Tools Appl.* 78, 24923–24953. doi: 10.1007/s11042-019-7674-5

Alzahrani, M. S., Jarraya, S. K., Ben-Abdallah, H., and Ali, M. S. (2019). Comprehensive evaluation of skeleton features-based fall detection from Microsoft Kinect v2. *SIViP* 13, 1431–1439. doi: 10.1007/s11760-019-01490-9

Amin, M. G., Zhang, Y. D., Ahmad, F., and Ho, K. C. D. (2016). Radar signal processing for elderly fall detection: the future for in-home monitoring. *IEEE Signal Process. Mag.* 33, 71–80. doi: 10.1109/MSP.2015.2502784

Andò, B., Baglio, S., Lombardo, C. O., and Marletta, V. (2016). A multisensor data-fusion approach for ADL and fall classification. *IEEE Trans. Instrum. Meas.* 65, 1960–1967. doi: 10.1109/TIM.2016.2552678

Antonsson, E. K., and Mann, R. W. (1985). The frequency content of gait. *J. Biomech.* 18, 39–47. doi: 10.1016/0021-9290(85)90043-0

Avram, M.-R., and Pop, F. (2023). Real-time running workouts monitoring using Cloud–Edge computing. *Neural Comput. Applic.* 35, 13803–13822. doi: 10.1007/s00521-021-06675-3

Ayesha, S., Hanif, M. K., and Talib, R. (2020). Overview and comparative study of dimensionality reduction techniques for high dimensional data. *Informat. Fusion* 59, 44–58. doi: 10.1016/j.inffus.2020.01.005

Aziz, O., Musngi, M., Park, E. J., Mori, G., and Robinovitch, S. N. (2017). A comparison of accuracy of fall detection algorithms (threshold-based vs. machine learning) using waist-mounted tri-axial accelerometer signals from a comprehensive set of falls and non-fall trials. *Med. Biol. Eng. Comput.* 55, 45–55. doi: 10.1007/s11517-016-1504-y

Babaee, M., Dinh, D. T., and Rigoll, G. (2018). A deep convolutional neural network for video sequence background subtraction. *Pattern Recogn.* 76, 635–649. doi: 10.1016/j.patcog.2017.09.040

Babangida, L., Perumal, T., Mustapha, N., and Yaakob, R. (2022). Internet of things (IoT) based activity recognition strategies in smart homes: a review. *IEEE Sensors J.* 22, 8327–8336. doi: 10.1109/JSEN.2022.3161797

Badgujar, S., and Pillai, A. S. (2020). Fall detection for elderly people using machine learning. *2020 11th international conference on computing, communication and networking technologies (ICCCNT)*, Kharagpur, India 1–4.

Bansal, D., Khanna, K., Chhikara, R., Dua, R. K., and Malhotra, R. (2021). "A systematic literature review of deep learning for detecting dementia" in *Proceedings of the second international conference on information management and machine intelligence. Lecture notes in networks and systems*. eds. D. Goyal, A. K. Gupta, V. Piuri, M. Ganzha and M. Paprzycki, vol. *166* (Singapore: Springer)

Bassoli, M., Bianchi, V., De Munari, I., and Ciampolini, P. (2017). An IoT approach for an AAL Wi-fi-based monitoring system. *IEEE Trans. Instrum. Meas.* 66, 3200–3209. doi: 10.1109/TIM.2017.2753458

Beddiar, D. R., Nini, B., Sabokrou, M., and Hadid, A. (2020). Vision-based human activity recognition: a survey. *Multimed. Tools Appl.* 79, 30509–30555. doi: 10.1007/s11042-020-09004-3

Bhargava, K., McManus, G., and Ivanov, S. (2017). Fog-centric localization for ambient assisted living. *2017 international conference on engineering, technology and innovation (ICE/ITMC)*, 1424–1430. Madeira, Portugal

Bhavan, A., and Aggarwal, S. (2018). Stacked generalization with wrapper-based feature selection for human activity recognition. 2018 IEEE symposium series on computational intelligence (SSCI), 1064–1068. Bangalore, India

Bianchi, V., Ciampolini, P., and De Munari, I. (2019). RSSI-based indoor localization and identification for ZigBee wireless sensor networks in smart homes. *IEEE Trans. Instrum. Meas.* 68, 566–575. doi: 10.1109/TIM.2018.2851675

Bilbao-Jayo, A., Almeida, A., Sergi, I., Montanaro, T., Fasano, L., Emaldi, M., et al. (2021). Behavior modeling for a Beacon-based indoor location system. *Sensors* 21:4839. doi: 10.3390/s21144839

Blackman, S., Matlo, C., Bobrovitskiy, C., Waldoch, A., Fang, M. L., Jackson, P., et al. (2016). Ambient assisted living technologies for aging well: a scoping review. *J. Intell. Syst.* 25, 55–69. doi: 10.1515/jisys-2014-0136

Blum, A. L., and Langley, P. (1997). Selection of relevant features and examples in machine learning. *Artif. Intell.* 97, 245–271. doi: 10.1016/S0004-3702(97)00063-5

Bouchabou, D., Nguyen, S. M., Lohr, C., LeDuc, B., and Kanellos, I. (2021). A survey of human activity recognition in smart homes based on IoT sensors algorithms: taxonomies, challenges, and opportunities with deep learning. *Sensors* 21:6037. doi: 10.3390/s21186037

Bourke, A. K., O'Brien, J. V., and Lyons, G. M. (2007). Evaluation of a threshold-based tri-axial accelerometer fall detection algorithm. *Gait Posture* 26, 194–199. doi: 10.1016/j.gaitpost.2006.09.012

Bulling, A., Blanke, U., and Schiele, B. (2014). A tutorial on human activity recognition using body-worn inertial sensors. *ACM Comput. Surv.* 46, 1–33. doi: 10.1145/2499621

Buzzelli, M., Albé, A., and Ciocca, G. (2020). A vision-based system for monitoring elderly people at home. *Appl. Sci.* 10:374. doi: 10.3390/app10010374

Calvaresi, D., Cesarini, D., Sernani, P., Marinoni, M., Dragoni, A. F., and Sturm, A. (2017). Exploring the ambient assisted living domain: a systematic review. *J. Ambient. Intell. Humaniz. Comput.* 8, 239–257. doi: 10.1007/s12652-016-0374-3

Carter, S. E., Campbell, E. M., Sanson-Fisher, R. W., Redman, S., and Gillespie, W. J. (1997). Environmental hazards in the homes of older people. *Age Ageing* 26, 195–202. doi: 10.1093/ageing/26.3.195

Casilari, E., Santoyo-Ramón, J. A., and Cano-García, J. M. (2017). UMAFall: a multisensor dataset for the research on automatic fall detection. *Proc. Comput. Sci.* 110, 32–39. doi: 10.1016/j.procs.2017.06.110

Casilari, E., and Silva, C. A. (2022). An analytical comparison of datasets of real-world and simulated falls intended for the evaluation of wearable fall alerting systems. *Measurement* 202:111843. doi: 10.1016/j.measurement.2022.111843

Castro, H. F., Correia, V., Sowade, E., Mitra, K. Y., Rocha, J. G., Baumann, R. R., et al. (2016). All-inkjet-printed low-pass filters with adjustable cutoff frequency consisting of resistors, inductors and transistors for sensor applications. *Org. Electron.* 38, 205–212. doi: 10.1016/j.orgel.2016.08.025

Cebanov, E., Dobre, C., Gradinaru, A., Ciobanu, R.-I., and Stanciu, V.-D. (2019). Activity recognition for ambient assisted living using off-the-shelf motion sensing input devices. 2019 Global IoT Summit (GIoTS), Aarhus, Denmark 1–6.

Cedillo, P., Sanchez, C., Campos, K., and Bermeo, A. (2018). A Systematic Literature Review on Devices and Systems for Ambient Assisted Living: Solutions and Trends from Different User Perspectives. *2018 International Conference on eDemocracy and eGovernment (ICEDEG)*. 59–66. doi: 10.1109/ICEDEG.2018.8372367

Chaccour, K., Darazi, R., Hajjam el Hassans, A., and Andres, E. (2015). "Smart carpet using differential piezoresistive pressure sensors for elderly fall detection" in *2015 IEEE 11th international conference on wireless and mobile computing, networking and communications (WiMob)*, 225–229. doi: 10.1109/WiMOB.2015.7347965

Chandrashekar, G., and Sahin, F. (2014). A survey on feature selection methods. *Comput. Electr. Engin.* 40, 16–28. doi: 10.1016/j.compeleceng.2013.11.024

Chen, K.-H., Hsu, Y.-W., Yang, J.-J., and Jaw, F.-S. (2018). Evaluating the specifications of built-in accelerometers in smartphones on fall detection performance. *Instrumentat. Sci. Technol.* 46, 194–206. doi: 10.1080/10739149.2017.1363054

Chen, J., Huang, X., Jiang, H., and Miao, X. (2021). Low-cost and device-free human activity recognition based on hierarchical learning model. *Sensors* 21:2359. doi: 10.3390/s21072359

Chen, C., Jafari, R., and Kehtarnavaz, N. (2015). UTD-MHAD: a multimodal dataset for human action recognition utilizing a depth camera and a wearable inertial sensor. 2015 IEEE international conference on image processing (ICIP), 168–172 Quebec City, QC

Ciabattoni, L., Foresi, G., Monteriù, A., Pepa, L., Pagnotta, D. P., Spalazzi, L., et al. (2019). Real time indoor localization integrating a model based pedestrian dead reckoning on smartphone and BLE beacons. *J. Ambient. Intell. Humaniz. Comput.* 10, 1–12. doi: 10.1007/s12652-017-0579-0

Cicirelli, G., Marani, R., Petitti, A., Milella, A., and D'Orazio, T. (2021). Ambient assisted living: a review of technologies, methodologies and future perspectives for healthy aging of population. *Sensors* 21:3549. doi: 10.3390/s21103549

Cippitelli, E., Gasparrini, S., Gambi, E., and Spinsante, S. (2016). A human activity Recognition system using skeleton data from RGBD sensors. *Comput. Intell. Neurosci.* 2016, 1–14. doi: 10.1155/2016/4351435

Clapés, A., Pardo, À., Pujol Vila, O., and Escalera, S. (2018). Action detection fusing multiple Kinects and a WIMU: an application to in-home assistive technology for the elderly. *Mach. Vis. Appl.* 29, 765–788. doi: 10.1007/s00138-018-0931-1

Cola, G., Avvenuti, M., Piazza, P., and Vecchio, A. (2017). Fall detection using a head-worn barometer. Proceedings of the international conference on wireless mobile communication and healthcare (MCH' 17), Springer, Cham (pp. 217–224)

Cristiani, A. M., Bertolotti, G. M., Marenzi, E., and Ramat, S. (2014). An instrumented insole for long term monitoring movement, comfort, and ergonomics. *IEEE Sensors J.* 14, 1564–1572. doi: 10.1109/JSEN.2014.2299063

Das, S., Dai, R., Koperski, M., Minciullo, L., Garattoni, L., Bremond, F., et al. (2019). Toyota smarthome: real-world activities of daily living. 2019 IEEE/CVF international conference on computer vision (ICCV), Seoul, Korea 833–842.

de la Cal, E. A., Fáñez, M., Villar, M., Villar, J. R., and González, V. M. (2023). A low-power HAR method for fall and high-intensity ADLs identification using wrist-worn accelerometer devices. *Logic J. IGPL* 31, 375–389. doi: 10.1093/jigpal/jzac025

Deep, S., Zheng, X., Karmakar, C., Yu, D., Hamey, L. G. C., and Jin, J. (2020). A survey on anomalous behavior detection for elderly care using dense-sensing networks. *IEEE Communicat. Surv. Tutor.* 22, 352–370. doi: 10.1109/COMST.2019.2948204

Devanne, M., Papadakis, P., and Nguyen, S. M. (2019). Recognition of activities of daily living via hierarchical long-short term memory networks. 2019 IEEE international conference on systems, man and cybernetics (SMC), Bari, Italy 3318–3324

Dhiman, C., and Vishwakarma, D. K. (2019). A review of state-of-the-art techniques for abnormal human activity recognition. *Eng. Appl. Artif. Intell.* 77, 21–45. doi: 10.1016/j.engappai.2018.08.014

Ding, D.-M., Wang, Y.-G., Zhang, W., and Chen, Q. (2022). Fall detection system on smart Walker based on multisensor data fusion and SPRT method. *IEEE Access* 10, 80932–80948. doi: 10.1109/ACCESS.2022.3195674

Fan, L., Li, T., Yuan, Y., and Katabi, D. (2020). In-home daily-life captioning using radio signals. Computer vision – ECCV 2020: 16th European conference, Glasgow, UK, 105–123.

Faye, S., Bronzi, W., Tahirou, I., and Engel, T. (2017). Characterizing user mobility using mobile sensing systems. *Int. J. Distrib. Sens. Netw.* 13:155014771772631. doi: 10.1177/1550147717726310

Fernandes, C. D., Depari, A., Sisinni, E., Ferrari, P., Flammini, A., Rinaldi, S., et al. (2020). Hybrid indoor and outdoor localization for elderly care applications with LoRaWAN. 2020 IEEE international symposium on medical measurements and applications (MeMeA), 1–6. Bari, Italy

Fetzer, T., Ebner, F., Bullmann, M., Deinzer, F., and Grzegorzek, M. (2018). Smartphone-based indoor localization within a 13th century historic building. *Sensors* 18:4095. doi: 10.3390/s18124095

Gaglio, S., Re, G. L., and Morana, M. (2015). Human activity Recognition process using 3-D posture data. *IEEE Trans. Hum.-Mach. Syst.* 45, 586–597. doi: 10.1109/THMS.2014.2377111

Garcia-Ceja, E., Galván-Tejada, C. E., and Brena, R. (2018). Multi-view stacking for activity recognition with sound and accelerometer data. *Inf. Fusion* 40, 45–56. doi: 10.1016/j.inffus.2017.06.004

Garcia-Gonzalez, D., Rivero, D., Fernandez-Blanco, E., and Luaces, M. R. (2020). A public domain dataset for real-life human activity recognition using smartphone sensors. *Sensors* 20:2200. doi: 10.3390/s20082200

Gasparrini, S., Cippitelli, E., Spinsante, S., and Gambi, E. (2014). Depth cameras in AAL environments: technology and real-world applications. *Assistive technologies for physical and cognitive disabilities* Pennsylvania, United States: IGI Global 22–41.

Geman, O., and Costin, H. (2014). Automatic assessing of tremor severity using nonlinear dynamics, artificial neural networks and neuro-fuzzy classifier. *Adv. Electr. Comput. Eng.* 14, 133–138. doi: 10.4316/AECE.2014.01020

Goh, J. X., Lim, K. M., and Lee, C. P. (2021). 1D convolutional neural network with long short-term memory for human activity recognition. 2021 IEEE international conference on artificial intelligence in engineering and technology (IICAIET), Kota Kinabalu, Malaysia. 1–6.

Gonçalves, C., Lopes, J. M., Moccia, S., Berardini, D., Migliorelli, L., and Santos, C. P. (2023). Deep learning-based approaches for human motion decoding in smart walkers for rehabilitation. *Expert Syst. Appl.* 228:120288. doi: 10.1016/j.eswa.2023.120288

Grossman, G. E., Leigh, R. J., Abel, L. A., Lanska, D. J., and Thurston, S. E. (1988). Frequency and velocity of rotational head perturbations during locomotion. *Exp. Brain Res.* 70, 470–476. doi: 10.1007/BF00247595

Guendel, R. G., Unterhorst, M., Gambi, E., Fioranelli, F., and Yarovoy, A. (2021). Continuous human activity recognition for arbitrary directions with distributed radars. 2021 IEEE radar conference (RadarConf21). Atlanta, GA, USA. 1–6.

Guerra, B. M. V., Ramat, S., Beltrami, G., and Schmid, M. (2020). Automatic pose Recognition for monitoring dangerous situations in ambient-assisted living. *Front. Bioeng. Biotechnol.* 8:415. doi: 10.3389/fbioe.2020.00415

Guerra, B. M. V., Ramat, S., Beltrami, G., and Schmid, M. (2023). Recurrent network solutions for human posture recognition based on Kinect skeletal data. *Sensors* 23:5260. doi: 10.3390/s23115260

Guerra, B. M. V., Schmid, M., Beltrami, G., and Ramat, S. (2022). Neural networks for automatic posture recognition in ambient-assisted living. *Sensors* 22:2609. doi: 10.3390/s22072609

Gulati, N., and Kaur, P. D. (2022). FriendCare-AAL: a robust social IoT based alert generation system for ambient assisted living. *J. Ambient. Intell. Humaniz. Comput.* 13, 1735–1762. doi: 10.1007/s12652-021-03236-3

Haghi, M., Geissler, A., Fleischer, H., Stoll, N., and Thurow, K. (2019). Ubiqsense: a personal wearable in ambient parameters monitoring based on IoT platform. 2019 international conference on sensing and instrumentation in IoT era (ISSI), Lisbon, Portugal. 1–6

Hasan, T., Bin Karim, M. F., Mahadi, M. K., Nishat, M. M., and Faisal, F. (2022). Employment of ensemble machine learning methods for human activity Recognition. *J. Healthcare Engin.* 2022, 1–18. doi: 10.1155/2022/6963891

Hemmatpour, M., Ferrero, R., Montrucchio, B., and Rebaudengo, M. (2017). "A neural network model based on co-occurrence matrix for fall prediction" in *Wireless mobile communication and healthcare. MobiHealth 2016. Lecture notes of the institute for computer sciences, social informatics and telecommunications engineering*. eds. P. Perego, G. Andreoni and G. Rizzo, vol. *192* (Cham: Springer), 241–248.

Iadarola, G., Disha, D., De Santis, A., Spinsante, S., and Gambi, E. (2022). Global positioning system measurements: comparison of IoT wearable devices. 2022 IEEE 9th international workshop on metrology for AeroSpace (MetroAeroSpace), 213–218. Pisa, Italy

Islam, Z. Z., Tazwar, S. M., and Islam, M Z., Serikawa, S., & Ahad, M A R. (2017). Automatic fall detection system of unsupervised elderly people using smartphone. Proceedings of the 5th IIAE international conference on industrial application engineering 2017, 418–424.

Jayaraj, R. L., Azimullah, S., Beiram, R., Jalal, F. Y., and Rosenberg, G. A. (2019). Neuroinflammation: friend and foe for ischemic stroke. *J. Neuroinflammation* 16:142. doi: 10.1186/s12974-019-1516-2

Jegham, I., Ben Khalifa, A., Alouani, I., and Mahjoub, M. A. (2020). Vision-based human action recognition: An overview and real world challenges. *Foren. Sci. Internat.* 32:200901. doi: 10.1016/j.fsidi.2019.200901

Jeong, S. Y., Choi, M. S., Kang, S. J., and Lee, H.-W. (2017). Homecare kit platform supporting multiple bio-signals acquisition and analysis in daily-life. 2017 IEEE international conference on big data and smart computing (BigComp), Jeju, Korea 64–68.

Jindal, P., and Kumar, D. (2017). A review on dimensionality reduction techniques. *Int. J. Comput. Applicat.* 173, 42–46. doi: 10.5120/ijca2017915260

Jung, S., Hong, S., Kim, J., Lee, S., Hyeon, T., Lee, M., et al. (2015). Wearable fall detector using integrated sensors and energy devices. *Sci. Rep.* 5:17081. doi: 10.1038/srep17081

Junior, A. P., Díez, L. E., Bahillo, A., and Eyobu, O. S. (2023). Remote pedestrian localization systems for resource-constrained environments: a systematic review. *IEEE Access* 11, 36865–36889. doi: 10.1109/ACCESS.2023.3266957

Kang, J., and Larkin, H. (2017). Application of an emergency alarm system for physiological sensors utilizing smart devices. *Technologies* 5:26. doi: 10.3390/technologies5020026

Karayaneva, Y., Sharifzadeh, S., Jing, Y., and Tan, B. (2023). Human activity recognition for AI-enabled healthcare using low-resolution infrared sensor data. *Sensors* 23:478. doi: 10.3390/s23010478

Ke, S.-R., Thuc, H., Lee, Y.-J., Hwang, J.-N., Yoo, J.-H., and Choi, K.-H. (2013). A review on video-based human activity recognition. *Computers* 2, 88–131. doi: 10.3390/computers2020088

Kenfack Ngankam, H., Pigot, H., Lorrain, D., Viens, I., and Giroux, S. (2020). Context awareness architecture for ambient-assisted living applications: case study of nighttime wandering. *J. Rehabilit. Assist. Technol. Eng.* 7:205566831988786. doi: 10.1177/2055668319887864

Keum, S. S., Lee, C. H., and Kang, S. J. (2019). Device to device collaboration architecture for real- time identification of user and abnormal activities in home. 2019 29th international telecommunication networks and applications conference (ITNAC), 1–3

Khan, N. S., and Ghani, M. S. (2021). A survey of deep learning based models for human activity recognition. *Wirel. Pers. Commun.* 120, 1593–1635. doi: 10.1007/s11277-021-08525-w

Kumar, P., and Suresh, S. (2023). Deep-HAR: an ensemble deep learning model for recognizing the simple, complex, and heterogeneous human activities. *Multimed. Tools Appl.* doi: 10.1007/s11042-023-14492-0

Kumari, P., Mathew, L., and Syal, P. (2017). Increasing trend of wearables and multimodal interface for human activity monitoring: a review. *Biosens. Bioelectron.* 90, 298–307. doi: 10.1016/j.bios.2016.12.001

Kwapisz, J. R., Weiss, G. M., and Moore, S. A. (2011). Activity recognition using cell phone accelerometers. *ACM SIGKDD Explorat. Newsl.* 12, 74–82. doi: 10.1145/1964897.1964918

Kwolek, B., and Kepski, M. (2014). Human fall detection on embedded platform using depth maps and wireless accelerometer. *Comput. Methods Prog. Biomed.* 117, 489–501. doi: 10.1016/j.cmpb.2014.09.005

Lee, S. (2021). Falls associated with indoor and outdoor environmental hazards among community-dwelling older adults between men and women. *BMC Geriatr.* 21:547. doi: 10.1186/s12877-021-02499-x

Li, M., and Sun, Q. (2021). 3D skeletal human action recognition using a CNN fusion model. *Math. Probl. Eng.* 2021, 1–11. doi: 10.1155/2021/6650632

Li, W., Zhang, Z., and Liu, Z. (2010). Action recognition based on a bag of 3D points. 2010 IEEE computer society conference on computer vision and pattern recognition – workshops San Francisco, CA, USA, 9–14

Liu, M., Liu, H., and Chen, C. (2017). Enhanced skeleton visualization for view invariant human action recognition. *Pattern Recogn.* 68, 346–362. doi: 10.1016/j.patcog.2017.02.030

Liu, L., and Shao, L. (2013). Learning discriminative representations from RGB-D video data. *Proceedings of the twenty-third international joint conference on artificial intelligence*, Beijing, China, AAAI Press 1493–1500.

Liu, J., Wang, Y., Liu, Y., Xiang, S., and Pan, C. (2020). 3D PostureNet: a unified framework for skeleton-based posture recognition. *Pattern Recogn. Lett.* 140, 143–149. doi: 10.1016/j.patrec.2020.09.029

Lloret, J., Canovas, A., Sendra, S., and Parra, L. (2015). A smart communication architecture for ambient assisted living. *IEEE Commun. Mag.* 53, 26–33. doi: 10.1109/MCOM.2015.7010512

Lutze, R. (2018). Practicality of smartwatch apps for supporting elderly people – a comprehensive survey. 2018 IEEE international conference on engineering, technology and innovation (ICE/ITMC), Stuttgart, Germany 1–7

Luwe, Y. J., Lee, C. P., and Lim, K. M. (2022). Wearable sensor-based human activity recognition with hybrid deep learning model. *Informatics* 9:56. doi: 10.3390/informatics9030056

Ma, C., Wang, A., Chen, G., and Xu, C. (2018). Hand joints-based gesture recognition for noisy dataset using nested interval unscented Kalman filter with LSTM network. *Vis. Comput.* 34, 1053–1063. doi: 10.1007/s00371-018-1556-0

Madhu, B., Mukherjee, A., Islam, M. Z., Mamun-Al-Imran, G. M., Roy, R., and Ali, L. E. (2021). "Depth motion map based human action recognition using adaptive threshold technique" in *2021 5th international conference on electrical information and communication technology (EICT)*, Khulna, Bangladesh, 1–6.

Mainetti, L., Manco, L., Patrono, L., Secco, A., Sergi, I., and Vergallo, R. (2016). An ambient assisted living system for elderly assistance applications. 2016 IEEE 27th annual international symposium on personal, indoor, and mobile radio communications (PIMRC), Valencia, Spain 1–6

Malekzadeh, M., Clegg, R. G., Cavallaro, A., and Haddadi, H. (2018). Protecting sensory data against sensitive inferences. Proceedings of the 1st workshop on privacy by design in distributed systems, Porto, Portugal 1–6

Marenzi, E., Bertolotti, G. M., Cristiani, A., De Donno, F., Leporati, F., Danese, G., et al. (2013a). Identification and evaluation of parameters for the prevention of pressure ulcers in hospitalized patients. IEEE EuroCon 2013. Zagreb, Croatia

Marenzi, E., Bertolotti, G. M., Leporati, F., and Danese, G. (2013b). Capacitive sensors matrix for interface pressure measurement in clinical, ergonomic and automotive environments. Proceedings – 16th Euromicro Conference on Digital System Design, DSD 2013. Los Alamitos, CA, USA

Marenzi, E., Lombardi, R., Bertolotti, G. M., Cristiani, A., and Cabras, B. (2012). Design and development of a novel capacitive sensor matrix for measuring pressure distribution. 2012 IEEE sensors applications symposium, SAS 2012 – proceedings. Brescia, Italy

Mashiyama, S., Hong, J., and Ohtsuki, T. (2015). Activity recognition using low resolution infrared array sensor. 2015 IEEE international conference on communications (ICC), London, UK 495–500

Mathur, A., Zhang, T., Bhattacharya, S., Velickovic, P., Joffe, L., Lane, N. D., et al. (2018). Using deep data augmentation training to address software and hardware heterogeneities in wearable and smartphone sensing devices. 2018 17th ACM/IEEE international conference on information processing in sensor networks (IPSN), Porto, Portugal 200–211.

Medrano, C., Igual, R., García-Magariño, I., Plaza, I., and Azuara, G. (2017). Combining novelty detectors to improve accelerometer-based fall detection. *Med. Biol. Eng. Comput.* 55, 1849–1858. doi: 10.1007/s11517-017-1632-z

Medrano, C., Igual, R., Plaza, I., and Castro, M. (2014). Detecting falls as novelties in acceleration patterns acquired with smartphones. *PLoS One* 9:e94811. doi: 10.1371/journal.pone.0094811

Minh Dang, L., Min, K., Wang, H., Piran, M., and Lee, C. (2020). Sensor-based and vision-based human activity recognition: a comprehensive survey. *Pattern Recogn.* 108:107561. doi: 10.1016/j.patcog.2020.107561

Mistry, J., and Inden, B. (2018). An approach to sign language translation using the Intel RealSense camera. 2018 10th computer science and electronic engineering (CEEC), Colchester, UK 219–224

Mliki, H., Bouhlel, F., and Hammami, M. (2020). Human activity recognition from UAV-captured video sequences. *Pattern Recogn.* 100:107140. doi: 10.1016/j.patcog.2019.107140

Müller, M., Röder, T., and Clausen, M. (2005). Efficient content-based retrieval of motion capture data. *ACM Trans. Graph.* 24, 677–685. doi: 10.1145/1073204.1073247

Narkhede, A. H. (2019). *Human activity recognition based on multimodal body sensing* San Jose, CA [San Jose State University

Nastac, D. I., Arsene, O., Dragoi, M., Stanciu, I. D., and Mocanu, I. (2019). An AAL scenario involving automatic data collection and robotic manipulation. 3rd IET international conference on technologies for active and assisted living (TechAAL 2019), London, UK 1–6.

Negin, F., Ozdemir, F., Yuksel, K. A., Akgul, C. B., and Ercil, A. (2013). A decision forest based feature selection framework for action recognition from RGB-depth cameras. 2013 21st signal processing and communications applications conference (SIU), Haspolat, Turkey 1–4.

Nouredanesh, M., Gordt, K., Schwenk, M., and Tung, J. (2020). Automated detection of multidirectional compensatory balance reactions: a step towards tracking naturally occurring near falls. *IEEE Trans. Neural Syst. Rehabil. Eng.* 28, 478–487. doi: 10.1109/TNSRE.2019.2956487

Ofli, F., Chaudhry, R., Kurillo, G., Vidal, R., and Bajcsy, R. (2013). Berkeley MHAD: a comprehensive multimodal human action database. 2013 IEEE workshop on applications of computer vision (WACV), Clearwater Beach, FL, USA 53–60

Oniga, S., and Suto, J. (2014). Human activity recognition using neural networks. Proceedings of the 2014 15th international carpathian control conference (ICCC), Velke Karlovice, Czech Republic 403–406.

Özdemir, A., and Barshan, B. (2014). Detecting falls with wearable sensors using machine learning techniques. *Sensors* 14, 10691–10708. doi: 10.3390/s140610691

Paolini, G., Masotti, D., Antoniazzi, F., Salmon Cinotti, T., and Costanzo, A. (2019). Fall detection and 3-D indoor localization by a custom RFID reader embedded in a smart e-health platform. *IEEE Transact. Microw. Theory Techniq.* 67, 5329–5339. doi: 10.1109/TMTT.2019.2939807

Patro, S. G. K., and Sahu, K. K. (2015). Normalization: a preprocessing stage. *IARJSET* 2, 20–22. doi: 10.17148/IARJSET.2015.2305

Peng, Y., Wu, Z., and Jiang, J. (2010). A novel feature selection approach for biomedical data classification. *J. Biomed. Inform.* 43, 15–23. doi: 10.1016/j.jbi.2009.07.008

Pierleoni, P., Belli, A., Palma, L., Paoletti, M., Raggiunto, S., and Pinti, F. (2019). Postural stability evaluation using wearable wireless sensor. *2019 IEEE 23rd international symposium on consumer technologies (ISCT)*, Ancona, Italy 256–260

Pires, I. M., Hussain, F., Garcia, N. M., Lameski, P., and Zdravevski, E. (2020). Homogeneous data normalization and deep learning: a case study in human activity classification. *Fut. Internet* 12:194. doi: 10.3390/fi12110194

Piwek, L., Ellis, D. A., Andrews, S., and Joinson, A. (2016). The rise of consumer health wearables: promises and barriers. *PLoS Med.* 13:e1001953. doi: 10.1371/journal.pmed.1001953

Plentz, P. D. M., and De Pieri, E. R. (2018). An overview on real-time constraints for ambient intelligence (AmI). *2018 IEEE/ACS 15th international conference on computer systems and applications (AICCSA)*, Aqaba, Jordan 1–7.

Poulose, A., Kim, J. H., and Han, D. S. (2022). HIT HAR: human image threshing machine for human activity recognition using deep learning models. *Comput. Intell. Neurosci.* 2022, 1–21. doi: 10.1155/2022/1808990

Qiu, S., Zhao, H., Jiang, N., Wang, Z., Liu, L., An, Y., et al. (2022). Multi-sensor information fusion based on machine learning for real applications in human activity recognition: state-of-the-art and research challenges. *Informat. Fusion* 80, 241–265. doi: 10.1016/j.inffus.2021.11.006

Raeis, H., Kazemi, M., and Shirmohammadi, S. (2021). Human activity recognition with device-free sensors for well-being assessment in smart homes. *IEEE Instrument. Measur. Magaz.* 24, 46–57. doi: 10.1109/MIM.2021.9513637

Rafferty, J., Nugent, C. D., Liu, J., and Chen, L. (2017). From activity Recognition to intention Recognition for assisted living within smart homes. *IEEE Trans. Hum. Mach. Syst.* 47, 368–379. doi: 10.1109/THMS.2016.2641388

Ramanujam, E., Perumal, T., and Padmavathi, S. (2021). Human activity recognition with smartphone and wearable sensors using deep learning techniques: a review. *IEEE Sensors J.* 21, 13029–13040. doi: 10.1109/JSEN.2021.3069927

Ranieri, C. M., MacLeod, S., Dragone, M., Vargas, P. A., and Romero, R. A. F. (2021). Activity recognition for ambient assisted living with videos, inertial units and ambient sensors. *Sensors* 21:768. doi: 10.3390/s21030768

Reiss, A., and Stricker, D. (2012). Introducing a new benchmarked dataset for activity monitoring. 2012 16th international symposium on wearable computers, 108–109.

Rodriguez, M. D., Ahmed, J., and Shah, M. (2008). Action MACH a spatio-temporal maximum average correlation height filter for action recognition. 2008 IEEE conference on computer vision and pattern recognition, Newcastle, UK 1–8

Roggen, D., Calatroni, A., Rossi, M., Holleczek, T., Forster, K., Troster, G., et al. (2010). Collecting complex activity datasets in highly rich networked sensor environments. 2010 seventh international conference on networked sensing systems (INSS), Kassel, Germany 233–240

Roland, L., Lidauer, L., Sattlecker, G., Kickinger, F., Auer, W., Sturm, V., et al. (2018). Monitoring drinking behavior in bucket-fed dairy calves using an ear-attached tri-axial accelerometer: a pilot study. *Comput. Electron. Agric.* 145, 298–301. doi: 10.1016/j.compag.2018.01.008

Ronald, M., Poulose, A., and Han, D. S. (2021). iSPLInception: An inception-ResNet Deep learning architecture for human activity Recognition. IEEE. *Access* 9, 68985–69001. doi: 10.1109/ACCESS.2021.3078184

Rupasinghe, I. D. M. S., and Maduranga, M. W. P. (2022). Towards ambient assisted living (AAL): design of an IoT-based elderly activity monitoring system. *Int. J. Eng. Manufact.* 12, 1–10. doi: 10.5815/ijem.2022.02.01

Ryselis, K., Petkus, T., Blažauskas, T., Maskeliūnas, R., and Damaševičius, R. (2020). Multiple Kinect based system to monitor and analyze key performance indicators of physical training. *HCIS* 10:51. doi: 10.1186/s13673-020-00256-4

Saleh, M., Abbas, M., and Le Jeannes, R. B. (2021). FallAllD: an open dataset of human falls and activities of daily living for classical and Deep learning applications. *IEEE Sensors J.* 21, 1849–1858. doi: 10.1109/JSEN.2020.3018335

Saliba, M., Drapeau, N., Skime, M., Hu, X., Accardi, C. J., Athreya, A. P., et al. (2023). PISTACHIo (PreemptIon of diSrupTive behAvior in CHIldren): real-time monitoring of sleep and behavior of children 3–7 years old receiving parent–child interaction therapy augment with artificial intelligence — the study protocol, pilot study. *Pilot Feasibility Stud.* 9:23. doi: 10.1186/s40814-023-01254-w

Sanchez-Comas, A., Synnes, K., and Hallberg, J. (2020). Hardware for recognition of human activities: a review of smart home and AAL related technologies. *Sensors* 20:4227. doi: 10.3390/s20154227

Sarabia-Jácome, D., Usach, R., Palau, C. E., and Esteve, M. (2020). Highly-efficient fog-based deep learning AAL fall detection system. *Internet Things* 11:100185. doi: 10.1016/j.iot.2020.100185

Sathya, R., and Abraham, A. (2013). Comparison of supervised and unsupervised learning algorithms for pattern classification. *Int. J. Adv. Res. Artif. Intellig.* 2, 34–38. doi: 10.14569/IJARAI.2013.020206

Schuldt, C., Laptev, I., and Caputo, B. (2004). Recognizing human actions: a local SVM approach. Proceedings of the 17th international conference on pattern recognition, 2004. ICPR 2004. Cambridge, UK, 3, 32–36.

Seidenari, L., Varano, V., Berretti, S., Del Bimbo, A., and Pala, P. (2013). Recognizing actions from depth cameras as weakly aligned multi-part bag-of-poses. Proceedings of the IEEE conference on computer vision and pattern recognition (CVPR) workshops Portland, OR, USA. doi: 10.1109/CVPRW.2013.77

Seneviratne, S., Hu, Y., Nguyen, T., Lan, G., Khalifa, S., Thilakarathna, K., et al. (2017). A survey of wearable devices and challenges. *IEEE Commun. Surv. Tutor.* 19, 2573–2620. doi: 10.1109/COMST.2017.2731979

Senigagliesi, L., Ciattaglia, G., Disha, D., and Gambi, E. (2022). Classification of human activities based on automotive radar spectral images using machine learning techniques: a case study. 2022 IEEE radar conference (RadarConf22), New York City, NY, USA 1–6.

Shahroudy, A., Liu, J., Ng, T.-T., and Wang, G. (2016). NTU RGB+D: a large scale dataset for 3D human activity analysis. 2016 IEEE conference on computer vision and pattern recognition (CVPR), Las Vegas, NV, USA 1010–1019.

Sheikh, S. Y., and Jilani, M. T. (2023). A ubiquitous wheelchair fall detection system using low-cost embedded inertial sensors and unsupervised one-class SVM. *J. Ambient. Intell. Humaniz. Comput.* 14, 147–162. doi: 10.1007/s12652-021-03279-6

Shewell, C., Nugent, C., Donnelly, M., Wang, H., and Espinilla, M. (2017). Indoor localisation through object detection within multiple environments utilising a single wearable camera. *Heal. Technol.* 7, 51–60. doi: 10.1007/s12553-016-0159-x

Shi, T., Sun, X., Xia, Z., Chen, L., and Liu, J. (2016). Fall detection algorithm based on Triaxial accelerometer and magnetometer. *Eng. Lett.* 24, 157–163.

Shumba, A.-T., Montanaro, T., Sergi, I., Fachechi, L., De Vittorio, M., and Patrono, L. (2022). Leveraging IoT-aware technologies and AI techniques for real-time critical healthcare applications. *Sensors* 22:7675. doi: 10.3390/s22197675

Siddiqi, M. H., and Alsirhani, A. (2022). An efficient feature selection method for video-based activity recognition systems. *Math. Probl. Eng.* 2022, 1–13. doi: 10.1155/2022/5486004

Sikder, N., and Nahid, A.-A. (2021). KU-HAR: an open dataset for heterogeneous human activity recognition. *Pattern Recogn. Lett.* 146, 46–54. doi: 10.1016/j.patrec.2021.02.024

Sindhu Meena, K., and Suriya, S. (2020). "A survey on supervised and unsupervised learning techniques" in *Proceedings of international conference on artificial intelligence, smart grid and smart city applications* (Cham: Springer International Publishing), 627–644.

Singh, A., Rehman, S. U., Yongchareon, S., and Chong, P. H. J. (2020). Sensor technologies for fall detection systems: a review. *IEEE Sensors J.* 20, 6889–6919. doi: 10.1109/JSEN.2020.2976554

Siriwardhana, C., Madhuranga, D., Madushan, R., and Gunasekera, K. (2019). "Classification of activities of daily living based on depth sequences and audio" in *2019 14th conference on industrial and information systems (ICIIS)* (Kandy, Sri Lanka), 278–283.

Sivakumar, S., Gopalai, A. A., Gouwanda, D., and Lim, K. H. (2018). Estimation of joint angle from ground reaction force in human gait. 2018 IEEE-EMBS conference on biomedical engineering and sciences (IECBES), Sarawak, Malaysia, 623–628.

Sokullu, R., Balcı, A., and Demir, E. (2019). "The role of drones in ambient assisted living systems for the elderly" in *Enhanced living environments. Lecture notes in computer science*. eds. I. Ganchev, N. Garcia, C. Dobre, C. Mavromoustakis and R. Goleva, vol. *11369* (Cham: Springer), 295–321.

Sonawani, S., and Patil, K. (2023). Air quality measurement, prediction and warning using transfer learning based IOT system for ambient assisted living. *Int. J. Pervas. Comput. Communicat.* doi: 10.1108/IJPCC-07-2022-0271

Sophia, S., Sridevi, U. K., Boselin, P. S. R., and Thamaraiselvi, P. (2021). "Ambient-assisted living of disabled elderly in an intelligent home using behavior prediction—a reliable Deep learning prediction system" in *Computational analysis and deep learning for medical care* (Hoboken: Wiley), 329–342.

Sousa Lima, W., Souto, E., El-Khatib, K., Jalali, R., and Gama, J. (2019). Human activity recognition using inertial sensors in a smartphone: an overview. *Sensors* 19:3213. doi: 10.3390/s19143213

Spasova, V., Iliev, I., and Petrova, G. (2016). Privacy preserving fall detection based on simple human silhouette extraction and a linear support vector machine. *Int. J. Bioautomat.* 20, 237–252.

Srimath, S., Ye, Y., Sarker, K., and Sunderraman, R., & Ji, S. (2021). Human activity Recognition from RGB video streams using 1D-CNNs. 2021 IEEE SmartWorld, ubiquitous intelligence & computing, advanced & trusted computing, scalable computing & communications, internet of people and smart city innovation (SmartWorld/SCALCOM/UIC/ATC/IOP/SCI), 295–302.

Stavropoulos, T. G., Papastergiou, A., Mpaltadoros, L., Nikolopoulos, S., and Kompatsiaris, I. (2020). IoT wearable sensors and devices in elderly care: a literature review. *Sensors* 20:2826. doi: 10.3390/s20102826

Steven Eyobu, O., and Han, D. (2018). Feature representation and data augmentation for human activity classification based on wearable IMU sensor data using a deep LSTM neural network. *Sensors* 18:2892. doi: 10.3390/s18092892

Stodczyk, R. (2020). Ambient assisted living an overview of current applications, end-users and acceptance. *Biomed. J. Sci. Techn. Res.* 30, 23374–23384. doi: 10.26717/BJSTR.2020.30.004949

Su, B., Wu, H., and Sheng, M. (2017). Human action recognition method based on hierarchical framework via Kinect skeleton data. 2017 international conference on machine learning and cybernetics (ICMLC), Ningbo, China 83–90.

Sucerquia, A., López, J., and Vargas-Bonilla, J. (2017). SisFall: a fall and movement dataset. *Sensors* 17:198. doi: 10.3390/s17010198

Sun, X., Wei, Y., Liang, Shuang, Tang, X., and Sun, J. (2015). Cascaded hand pose regression. 2015 IEEE conference on computer vision and pattern recognition (CVPR), Boston, MA, USA 824–832.

Sung, Jaeyong, Ponce, C., Selman, B., and Saxena, A. (2012). Unstructured human activity detection from RGBD images. 2012 IEEE international conference on robotics and automation, 842–849. Saint Paul, MN

Surendran, D., Janet, J., Prabha, D., and Anisha, E. (2018). A study on devices for assisting Alzheimer patients. 2018 2nd international conference on I-SMAC (IoT in social, mobile, analytics and cloud) (I-SMAC), Palladam, India 620–625.

Suto, J., Oniga, S., and Sitar, Petrica Pop (2016). Comparison of wrapper and filter feature selection algorithms on human activity recognition. Available at: https://ieeexplore.ieee.org/abstract/document/7496749/ (Accessed September 16, 2022).

Tay, N. C., Connie, T., Ong, T. S., Teoh, A. B. J., and Teh, P. S. (2023). A review of abnormal behavior detection in activities of daily living. *IEEE Access* 11, 5069–5088. doi: 10.1109/ACCESS.2023.3234974

Tazari, M. R., Wichert, R., and Norgall, T. (2011). "Towards a unified ambient assisted living and personal health environment" in *Ambient assisted living* (Berlin Heidelberg: Springer), 141–155.

Torti, E., Fontanella, A., Musci, M., Blago, N., Pau, D., Leporati, F., et al. (2019). Embedding recurrent neural networks in wearable systems for real-time fall detection. *Microprocess. Microsyst.* 71:102895. doi: 10.1016/j.micpro.2019.102895

Tu, J., Liu, M., and Liu, H. (2018). Skeleton-based human action recognition using spatial temporal 3D convolutional neural networks. 2018 IEEE international conference on multimedia and expo (ICME), San Diego, CA, USA 1–6.

Um, T. T., Pfister, F. M. J., Pichler, D., Endo, S., Lang, M., Hirche, S., et al. (2017). "Data augmentation of wearable sensor data for parkinson's disease monitoring using convolutional neural networks" in *Proceedings of the 19th ACM international conference on multimodal interaction*. eds. E. Lank, A. Vinciarelli, E. Hoggan, S. Subramanian and S. A. Brewster (New York: Association for Computing Machinery), 216–220.

Vavoulas, G., Chatzaki, C., Malliotakis, T., Pediaditis, M., and Tsiknakis, M. (2016). The MobiAct dataset: recognition of activities of daily living using smartphones. Proceedings of the international conference on information and communication technologies for ageing well and e-health, Rome, Italy 143–151.

Wang, Y., Cang, S., and Yu, H. (2019). A survey on wearable sensor modality centred human activity recognition in health care. *Expert Syst. Appl.* 137, 167–190. doi: 10.1016/j.eswa.2019.04.057

Wang, J., Chen, Y., Hao, S., Peng, X., and Hu, L. (2019). Deep learning for sensor-based activity recognition: a survey. *Pattern Recogn. Lett.* 119, 3–11. doi: 10.1016/j.patrec.2018.02.010

Wang, X., Ellul, J., and Azzopardi, G. (2020). Elderly fall detection systems: a literature survey. *Front. Robot. AI* 7:71. doi: 10.3389/frobt.2020.00071

Wang, L., Huynh, D. Q., and Koniusz, P. (2020). A comparative review of recent Kinect-based action Recognition algorithms. *IEEE Transact. Image Proc.* 29, 15–28. doi: 10.1109/TIP.2019.2925285

Wang, S., Zhang, X., Liu, X., Zhang, J., Ma, S., and Gao, W. (2017). Utility-driven adaptive preprocessing for screen content video compression. *IEEE Trans. Multimed.* 19, 660–667. doi: 10.1109/TMM.2016.2625276

Warunsin, K., and Phairoh, T. (2022). Wristband fall detection system using deep learning. *2022 7th international conference on computer and communication systems (ICCCS)*, Wuhan, China 223–227.

Wu, C., Zhang, J., Savarese, S., and Saxena, A. (2015). Watch-n-patch: unsupervised understanding of actions and relations. 2015 IEEE conference on computer vision and pattern recognition (CVPR), Boston, MA, USA 4362–4370.

Xia, L., Chen, C.-C., and Aggarwal, J. K. (2012). View invariant human action recognition using histograms of 3D joints. 2012 IEEE computer society conference on computer vision and pattern recognition workshops, 20–27. Providence, RI, USA

Xie, J., Guo, K., Zhou, Z., Yan, Y., and Yang, P. (2020). ART: adaptive and real-time fall detection using COTS smart watch. 2020 6th international conference on big data computing and communications (BIGCOM), Deqing, China 33–40.

Yue, S., Yang, Y., Wang, H., Rahul, H., and Katabi, D. (2020). BodyCompass. *Proc. ACM Interact. Mobile Wearable Ubiquitous Technol.* 4, 1–25. doi: 10.1145/3397311

Zdravevski, E., Lameski, P., Trajkovik, V., Kulakov, A., Chorbev, I., Goleva, R., et al. (2017). Improving activity recognition accuracy in ambient-assisted living systems by automated feature engineering. *IEEE Access* 5, 5262–5280. doi: 10.1109/ACCESS.2017.2684913

Zebari, R. R., Mohsin Abdulazeez, A., Zeebaree, D. Q., Zebari, D. A., and Saeed, J. N. (2020). A comprehensive review of dimensionality reduction techniques for feature selection and feature extraction. *J. Appl. Sci. Technol. Trends* 1, 56–70. doi: 10.38094/jastt1224

Zeng, L., Duan, X., Pan, Y., and Deng, M. (2023). Research on the algorithm of helmet-wearing detection based on the optimized yolov4. *Vis. Comput.* 39, 2165–2175. doi: 10.1007/s00371-022-02471-9

Zerrouki, N., Harrou, F., Sun, Y., and Houacine, A. (2018). Vision-based human action classification using adaptive boosting algorithm. *IEEE Sensors J.* 18, 5115–5121. doi: 10.1109/JSEN.2018.2830743

Zhang, Y., Chen, Y., Wang, J., and Pan, Z. (2023). Unsupervised deep anomaly detection for multi-sensor time-series signals. *IEEE Trans. Knowl. Data Eng.* 35, 2118–2132. doi: 10.1109/TKDE.2021.3102110

Zhang, M., and Sawchuk, A. A. (2012). USC-Had. Proceedings of the 2012 ACM conference on ubiquitous computing, Pittsburgh, PA, USA 1036–1043.

Frontiers in Neuroscience

Provides a holistic understanding of brain function from genes to behavior

Part of the most cited neuroscience journal series which explores the brain - from the new eras of causation and anatomical neurosciences to neuroeconomics and neuroenergetics.

Discover the latest Research Topics

See more →

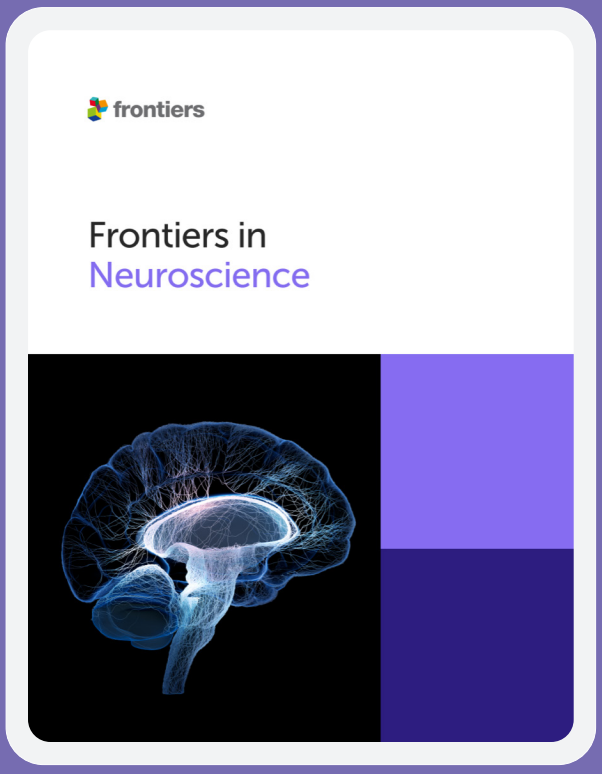

Frontiers

Avenue du Tribunal-Fédéral 34
1005 Lausanne, Switzerland
frontiersin.org

Contact us

+41 (0)21 510 17 00
frontiersin.org/about/contact